

SYNTHESIS AND APPLICATIONS OF HIERARCHICALLY POROUS  
METAL AND METAL OXIDE MONOLITHIC MATERIALS

by

FRANCHESSA MADDOX SAYLER

MARTIN G. BAKKER, COMMITTEE CHAIR

MICHAEL K. BOWMAN, Ph.D.

SHANLIN PAN, Ph.D.

SHANE C. STREET, Ph.D.

MIKA LINDÉN, Ph.D.

A DISSERTATION

Submitted in partial fulfillment of the requirements  
for the degree of Doctor of Philosophy  
in the Department of Chemistry  
in the Graduate School of  
The University of Alabama

TUSCALOOSA, ALABAMA

2013

Copyright Franchessa Maddox Sayler 2013  
ALL RIGHTS RESERVED

## ABSTRACT

A nanocasting method for synthesizing a broad range of hierarchically porous, high surface area metal and metal oxide monolithic materials was developed. The importance of a well-connected hard template was established based on conductivity measurements. A hierarchically porous, silica monolith prepared with 7% octadecyltrimethylammonium bromide was found to be the optimum silica template. Several different factors were found to regulate how well the silica template was replicated. When the connectivity of the silica template, contents of the metal salt solution, impregnation method, temperature, atmosphere, and template removal are all controlled, a good replica of the original silica monolith can be attained in different metals or metal oxides. These metal and metal oxide monoliths were used in catalysis and liquid chromatography.

## DEDICATION

This dissertation is dedicated to my husband, Todd Saylor, for his loving encouragement, understanding and assistance throughout this work. Without his unfaltering love and support, none of this would have been possible.

I would also like to dedicate this dissertation to my mother, Karen Brown, for teaching me how to persevere and always urging me to succeed, and to my father, DeWitt Maddox, and to grandparents, Joe and Rita Griffin, for their love and support through the years.

## LIST OF ABBREVIATIONS AND SYMBOLS

$^{\circ}\text{C}$	degrees Celsius
%	percent
$2\theta$	diffraction angle in degrees
<i>3-D</i>	three-dimensional
<i>A</i>	ampere
<i>A</i>	Eddy diffusion term
<i>AU</i>	absorbance unit
<i>B</i>	diffusion coefficient
<i>BET</i>	Brunauer-Emmett-Teller
<i>BJH</i>	<i>Barret-Joyner-Halenda</i>
<i>b.p.</i>	boiling point
<i>C</i>	resistance to mass transfer
<i>C<sub>14</sub>TAB</i>	tetradecyltrimethylammonium bromide
<i>C<sub>16</sub>TAB</i>	hexadecyltrimethylammonium bromide
<i>C<sub>18</sub>TAB</i>	octadecyltrimethylammonium bromide
<i>ca.</i>	circa (around)
<i>cm</i>	centimeter
<i>CMC</i>	critical micelle concentration
<i>cts.</i>	counts
<i>d</i>	diameter
<i>d<sub>surf</sub></i>	surfactant pore diameter
<i>dV(d)</i>	derivative of volume with respect to diameter

<i>EDS</i>	energy dispersive X-ray spectroscopy
<i>e.g.</i>	<i>exempli gratia</i> (for example)
<i>et al.</i>	et alia (and others)
<i>etc.</i>	et cetera (and so on)
<i>FIB</i>	focused ion beam
<i>g</i>	grams
<i>h</i>	hour
<i>H</i>	height equivalent to a theoretical plate
<i>hr</i>	hour
<i>i.e.</i>	in est (in other words)
<i>K</i>	Kelvin
<i>k</i>	rate constant
<i>keV</i>	kiloelectron volt
<i>kg</i>	kilogram
<i>kPa</i>	kilopascal
<i>L</i>	liters
<i>M</i>	molarity
<i>MΩ</i>	megaohm
<i>mAU</i>	milli-absorbance unit
<i>mg</i>	milligram
<i>min</i>	minute
<i>mL</i>	milliliter
<i>mm</i>	millimeter

<i>mol</i>	mole
<i>m.p.</i>	melting point
<i>MW</i>	molecular weight
<i>nm</i>	nanometer
<i>NLDFT</i>	non-local density functional theory
<i>OTAB</i>	octadecyltrimethylammonium bromide
<i>P</i>	pressure
$P_o$	initial pressure
$P_0$	initial pressure
<i>Pa</i>	Pascal
<i>PEG</i>	polyethylene glycol
$P/P_o$	partial pressure
<i>ppm</i>	parts per million
<i>psi</i>	pounds per square inch
<i>RH</i>	relative humidity
<i>s</i>	second
<i>SEM</i>	scanning electron microscope
<i>TEM</i>	transmission electron microscope
<i>TEOS</i>	tetraethoxysilane
<i>u</i>	linear velocity
$U_{s-m}$	chemical energy of the silica-metal or metal oxide interaction
<i>V</i>	volt
<i>V</i>	volume

$V_{macro}$	macropore volume
<i>vs.</i>	versus
$V_{surf}$	surfactant pore volume
$V_{text}$	textural pore volume
$V_{total}$	total pore volume
<i>wt%</i>	weight percent
<i>XRD</i>	X-ray diffractometer
$\mu L$	microliter
$\mu m$	micrometer
$\mu S$	microsiemens
$\Omega$	ohm
$\sigma_f$	free energy of formation
$\sigma_m$	free energy of the metal/metal oxide interface
$\sigma_{s-m}$	interfacial free energy of the metal or metal oxide in contact with silica
$\sigma_{m-g}$	surface energy of the metal/metal oxide in a given gaseous atmosphere
$\sigma_{s-g}$	surface energy of the silica in the given gaseous atmosphere

## ACKNOWLEDGEMENTS

I would like to begin by thanking my research advisor, Prof. Martin G Bakker, for his guidance and encouragement during the course of this work. He has had a significant role in both my scientific and personal development during my graduate career and has encouraged me to follow my dream of starting my own business. I must also thank Prof. Jan-Henrik Smått and Prof. Mika Lindén for hosting me at Åbo Akademi University in Turku, Finland for two summers and Prof. Susanne Wiedmer for their valuable insights in this work. I also would like to thank Prof. Michael Bowman, Prof. Shanlin Pan, Prof. Shane Street, and Prof. Mika Lindén for serving as my dissertation committee and for their valuable suggestions and comments.

I also must thank Ms. Amy Grano for her help on this project and her help in the analysis of many of the materials produced here. The valuable advice and support of my group members: Dr. Nik Cordes, Mr. Chris Redden, and Ms. Katrina Staggemeier are gratefully acknowledged.

Instrumentation access and assistance was provided to me by The University of Alabama Central Analytical Facility. Training and advice on the SEM was provided by Rich Martens and Johnny Goodwin. Training and guidance on the XRD was provided by Rob Holler.

I would also like to thank numerous undergraduate co-workers who have provided help and support through the years to allow this work to be completed. Ms. Elizabeth Junkin spent a summer in Finland along with several years in Tuscaloosa working on this project. Mr. Jake Mimms has also been of great assistance in much of this work. Additional undergraduates that worked on this project include: Keana Graves, Sonja Gregorowicz, Allison Hu, Rodney Littlejohn, Allison Osama, Kate Price, Pasha Sanders, Blake Whitley, and Shuwen Yue.

Funding for this research was provided by the National Science Foundation through grant CHE-0719398(MGB).

## CONTENTS

ABSTRACT .....	ii
DEDICATION .....	iii
LIST OF ABBREVIATIONS AND SYMBOLS .....	iv
ACKNOWLEDGEMENTS .....	viii
LIST OF TABLES .....	xv
LIST OF SCHEMES .....	xv
LIST OF FIGURES .....	xvi
CHAPTER 1 BACKGROUND AND INTRODUCTION .....	1
1.1 Background .....	1
1.2 Introduction .....	2
1.3 References .....	9
CHAPTER 2 CORRELATION BETWEEN ELECTRICAL CONDUCTIVITY, RELATIVE HUMIDITY AND PORE CONNECTIVITY IN MESOPOROUS SILICA MONOLITHS .....	10
2.1 Abstract .....	10
2.2 Introduction .....	10
2.3 Experimental Methods .....	13
2.3.1 Materials and Synthesis .....	13
2.3.2 Characterization .....	14
2.3.3 Conductivity .....	15
2.4 Results .....	16
2.4.1 Platinum Replication .....	16

2.4.2	Nitrogen Physisorption and Mercury Intrusion Porosimetry .....	17
2.4.3	Water Vapor Sorption .....	20
2.4.4	Conductivity.....	23
2.5	Discussion .....	24
2.6	Conclusions.....	30
2.7	Acknowledgements.....	31
2.8	References.....	32
2.9	Supplemental Information .....	34
CHAPTER 3	US PATENT APPLICATION 13/405714: METHODS FOR PREPARING AND USING METAL AND/OR METAL OXIDE POROUS MATERIALS.....	39
3.1	Abstract .....	39
3.2	Field .....	39
3.3	Background .....	39
3.4	Summary .....	42
3.5	Brief Description of Figures .....	42
3.6	Detailed Description .....	43
3.7	General Definitions .....	44
3.8	Methods.....	48
3.9	Compositions .....	59
3.10	Applications .....	64
3.11	Examples.....	69
3.11.1	Example 1 .....	70
3.11.2	Example 2 .....	70

3.11.3	Example 3 .....	71
3.11.4	Example 4 .....	71
3.11.5	Example 5 .....	71
3.11.6	Example 6 .....	72
3.11.7	Example 7 .....	72
3.12	Claims .....	74
3.13	Figures.....	77
3.14	Acknowledgements.....	84
3.15	References.....	85
CHAPTER 4	<b>NANOCASTING OF HIERARCHICALLY POROUS NiO, Co<sub>3</sub>O<sub>4</sub>, Ni, Co, AND Ag MONOLITHS: IMPACT OF PROCESSING CONDITIONS ON FIDELITY OF REPLICATION .....</b>	<b>87</b>
4.1	Abstract .....	87
4.2	Introduction.....	87
4.3	Experimental .....	91
4.4	Results.....	93
4.4.1	SiO <sub>2</sub> Monolith .....	94
4.4.2	Co <sub>3</sub> O <sub>4</sub> Monolith .....	97
4.4.3	Cobalt Metal Monolith Synthesis .....	99
4.4.4	Synthesis of Nickel Oxide Monolith.....	103
4.4.5	Synthesis of Nickel Monolith .....	106
4.4.6	Synthesis of Silver Monolith .....	107
4.5	Discussion .....	108
4.5.1	Solution Infiltration.....	109

4.5.2	Thermal Decomposition.....	109
4.5.3	Movement of Metal and Metal Oxides .....	110
4.5.4	Metal Monolith Replication and Impact of Annealing.....	114
4.5.5	Metal Oxide Monolith Replication .....	117
4.6	Conclusions.....	118
4.7	Acknowledgements.....	119
4.8	References.....	121
4.9	Supplemental Information .....	125
CHAPTER 5	<b>FORMATION OF HIERARCHICALLY POROUS METAL OXIDE AND METAL MONOLITHS BY NANOCASTING INTO SILICA MONOLITHS.....</b>	<b>130</b>
5.1	Abstract .....	130
5.2	Introduction.....	130
5.2.1	Formation of Porous Silica and Metal Oxide Monoliths by Spinodal Decomposition .....	132
5.2.2	Nanocasting to Form Other Hierarchically Porous Materials .....	134
5.3	Experimental.....	139
5.3.1	Preparation of Hierarchically Porous Silica Monoliths.....	139
5.3.2	Preparation of $\text{Co}_3\text{O}_4$ Monoliths (Varying the Gas Atmosphere).....	140
5.3.3	Preparation of $\text{Fe}_2\text{O}_3$ Monoliths.....	140
5.3.4	Preparation of $\text{ZrO}_2$ Monoliths .....	141
5.3.5	Preparation of Ag Monoliths .....	141
5.3.6	Preparation of NiO and Ni Monoliths.....	142

5.3.7	Characterization Methods .....	142
5.4	Results and Discussion .....	143
5.4.1	SiO <sub>2</sub> Template Monoliths .....	143
5.4.2	Co <sub>3</sub> O <sub>4</sub> Monoliths (Varying the Gas Atmosphere) .....	146
5.4.3	Fe <sub>2</sub> O <sub>3</sub> Monoliths.....	150
5.4.4	ZrO <sub>2</sub> Monoliths .....	153
5.4.5	Ag Monoliths .....	157
5.4.6	Nickel Oxide and Nickel Monolith.....	160
5.4.7	Impact of Monolith Type .....	163
5.5	Conclusions.....	163
5.6	Acknowledgements.....	164
5.7	References.....	165
5.8	Supporting Information.....	170
CHAPTER 6	FORMATION AND APPLICATIONS OF HIERARCHICALLY POROUS CARBON, METALS, AND METAL OXIDES FORMED BY NANOCASTING.....	174
6.1	Abstract .....	174
6.2	Introduction.....	174
6.3	Experimental .....	175
6.3.1	Synthesis of Monolithic Silica Templates, Nickel and Carbon Monoliths .....	175
6.3.2	Catalysis Experiments.....	177
6.3.3	Preparation of Porous Electrodes.....	177
6.4	Results and Discussion .....	178

6.4.1	Catalysis.....	178
6.4.2	Porous Electrodes.....	179
6.5	Conclusions.....	183
6.6	Acknowledgements.....	183
6.7	References.....	184
CHAPTER 7	APPLICATION OF 3-D HIERARCHICALLY POROUS SILVER, COBALT OXIDE, AND ZINC OXIDE MONOLITHS TO CHROMATOGRAPHIC SEPARATIONS .....	185
7.1	Abstract .....	185
7.2	Introduction.....	185
7.3	Experimental .....	186
7.4	Results and Discussion .....	188
7.5	Conclusions.....	192
7.6	Acknowledgements.....	192
7.7	References.....	193
CHAPTER 8	CONCLUSIONS AND FUTURE WORK .....	194
8.1	Conclusions.....	194
8.2	Future Work.....	196

## LIST OF TABLES

Table 2.1	Aqueous Molar Composition of Monoliths .....	14
Table 2.2	Mercury Intrusion and Nitrogen Physisorption Data for Native Monoliths .....	20
Table 2.3	Water Vapor Sorption Data for Native and $\text{Co}(\text{NO}_3)_2$ Impregnated Monoliths .....	22
Table 4.1	Nitrogen Sorption and X-ray Diffraction Data .....	96
Table 4.2	Melting Temperatures .....	111
Table 5.1	Replica Monoliths. Summary of Textural Properties of the Starting Silica Monoliths and the Different Replica Samples.....	145

## LIST OF SCHEMES

Scheme 5.1	The Hierarchical Nature of the Monolithic Silica Templates Used in This Study.....	133
Scheme 5.2	An Overview of the Different Steps That are Involved in the Nanocasting Process .....	135

## LIST OF FIGURES

Figure 1.1	Nanocasting Variables .....	3
Figure 1.2	Comparison of Silica Template and Carbon Replica at Different Length Scales. ....	4
Figure 2.1	Silica Monolith.....	11
Figure 2.2	Images of Native Monoliths and Platinum Replicas.....	17
Figure 2.3	Nitrogen Physisorption Isotherms of Native Monoliths .....	18
Figure 2.4	Water Vapor Sorption Isotherms of Native Monoliths.....	21
Figure 2.5	Water Vapor Sorption Isotherms of 0.02 M Cobalt Nitrate Impregnated Monoliths.....	22
Figure 2.6	Measured Electrical Conductivity with Increasing Relative Humidity.....	23
Figure 2.7	Comparison of Water Adsorption and Conductivity Curves .....	27
Figure 2.8	Electrical Conductivity of Monoliths as a Function of Percent Surfactant Templated Mesopore.....	28
Figure 2.S1	Nitrogen Physisorption Isotherms of 0.02 M $\text{Co}(\text{NO}_3)_2$ Impregnated Monoliths.....	34
Figure 2.S2	NLDFT Pore Size Distribution Plot of Native Monoliths .....	35
Figure 2.S3	NLDFT Pore Size Distribution Plot of 0.02 M $\text{Co}(\text{NO}_3)_2$ Impregnated Monoliths.....	36
Figure 2.S4	Mercury Porosimetry Cumulative Pore Volume Plot.....	37
Figure 2.S5	Measured Electrical Conductivity with Increasing Relative Humidity on C16-9 Containing Varied Salt Concentrations. ....	38
Figure 3.1(a)	Cartoon of Porous Materials Prepared.....	77
Figure 3.1(b)	Empirical Schematic Representation of a Bicontinuous Structure.....	77

Figure 3.2	SEM Image of Cobalt Metal Monolith .....	78
Figure 3.3	SEM Image of Copper Metal Monolith.....	79
Figure 3.4	SEM Image of Sterling Silver Monolith.....	80
Figure 3.5	SEM Image of Macropores in Nickel Oxide Monolith .....	81
Figure 3.6	SEM Image of Hollow Fiber Cobalt Monolith.....	82
Figure 3.7	SEM Image of Macropores in Nickel Metal Monolith.....	83
Figure 3.8	SEM and TEM Images of Cobalt Oxide Monolith Macropores and Highly Ordered Mesopores.....	84
Figure 4.1	Parent Silica Monolith and Replicas.....	94
Figure 4.2	SEM Images of Silica, Cobalt Oxide, and Nickel Oxide Monoliths at Micrometer and Nanometer Scales .....	95
Figure 4.3	SEM Images of Nickel, Cobalt, and Silver Replica Monoliths at Micrometer and Nanometer Scales .....	100
Figure 4.4	XRD of Replicas .....	101
Figure 4.5	Nitrogen Physisorption Isotherms and NLDFT Pore Size Distributions for Silica, Cobalt Oxide and Nickel Oxide Monoliths.....	102
Figure 4.6	Nitrogen Physisorption Isotherms and NLDFT Pore Size Distributions for Cobalt, Nickel and Silver Monoliths.....	104
Figure 4.S1	Nitrogen Sorption Isotherms and NLDFT Pore Size Distributions for Cobalt Oxide Composites and Replicas Before and After Annealing.....	125
Figure 4.S2	Nitrogen Sorption Isotherms and NLDFT Pore Size Distributions for Cobalt Metal Composites and Replicas Before and After Annealing.....	126
Figure 4.S3	Nitrogen Sorption Isotherms and NLDFT Pore Size Distributions for Nickel Oxide Composites and Replicas Before and After Annealing.....	127

Figure 4.S4	Nitrogen Sorption Isotherms and NLDFT Pore Size Distributions for Nickel Metal Composites and Replicas Before and After Annealing.....	128
Figure 4.S5	Nitrogen Sorption Isotherms and NLDFT Pore Size Distributions for Silver Composite and Replica.....	129
Figure 5.1	SEM Image of a Silica Monolith with Silver Crystallites in the Macropore Structure .....	137
Figure 5.2	Pore Size Distribution Plots of the Different Silica Monoliths Used as Templates in This Study. ....	144
Figure 5.3	SEM Images Showing the Influence of the Morphology of the $\text{Co}_3\text{O}_4$ Macropore Walls by Different Gas Atmospheres .....	146
Figure 5.4	Nitrogen Physisorption Isotherms of $\text{Co}_3\text{O}_4$ Replicas Prepared under Different Gas Atmospheres .....	147
Figure 5.5	SEM Images of Samples $\text{Fe}_2\text{O}_3$ -B2 and $\text{ZrO}_2$ -M1.....	151
Figure 5.6	XRD Measurements of $\text{Fe}_2\text{O}_3$ , $\text{ZrO}_2$ , Ag and Ni Monoliths.....	152
Figure 5.7	Nitrogen Physisorption Measurements on the $\text{Fe}_2\text{O}_3$ -B2 Replica, the $\text{SiO}_2/\text{ZrO}_2$ -M1 Composite and the $\text{ZrO}_2$ -M1 Replica Monoliths.....	153
Figure 5.8	Photograph Showing Etched ( $\text{ZrO}_2$ ) and Non-Etched ( $\text{ZrO}_2/\text{SiO}_2$ ) Composites .....	154
Figure 5.9	TEM Images of Sample $\text{ZrO}_2$ -M2 .....	155
Figure 5.10	FT-Raman Measurement of Sample $\text{ZrO}_2$ -M2 Showing Both Monoclinic (m) and Tetragonal (t) Peaks .....	157
Figure 5.11	SEM Images of Ag-B3-vacuum and Ag-B3-air .....	158
Figure 5.12	SEM Images $\text{NiO}$ -B1, Ni-B1-post- $\text{H}_2$ , and Ni-B2- $\text{H}_2$ .....	161
Figure 5.13	Nitrogen Physisorption of Nickel Oxide and Nickel Monoliths.....	161
Figure 5.S1	Nitrogen Physisorption Isotherms of the Different Silica Templates.....	171

Figure 5.S2	Nitrogen Physisorption Results of Ag-B3-air and Ag-B3-vac Samples .....	172
Figure 5.S3	EDS Results for the Different Silver Samples.....	173
Figure 6.1	SEM Images of Hierarchically Porous Carbon Monoliths Produced by "Nanocasting" into Porous Silica Templates.....	176
Figure 6.2	SEM Images of Manganese Dioxide Coated Hierarchically Porous Carbon Monoliths .....	180
Figure 6.3	Cyclic Voltammogram of Bare Carbon Monolith and Manganese Dioxide Coated Carbon Monolith .....	180
Figure 6.4	SEM Images of Carbon Monoliths Coated with Iron Oxide .....	181
Figure 6.5	Cyclic Voltammogram of Bare Carbon Monolith and Iron Oxide Coated Carbon Monolith.....	182
Figure 7.1	SEM Image of Cobalt Oxide Produced by Nanocasting into a Monolithic Silica Template.....	187
Figure 7.2	Completed Chromatography Column Incorporating Monolithic Cobalt Oxide .....	187
Figure 7.3	Chromatogram of a Standard Solution from Phenomonex <sup>®</sup> on a Sterling Silver Column.....	189
Figure 7.4	Chromatograms on Cobalt Oxide and Zinc Oxide Columns.....	189
Figure 7.5	Van Deemter Plot of Pyridine Retention on Cobalt Oxide .....	191

## Chapter 1

### Background and Introduction

#### 1.1 Background

Mesoporous materials (having pores between 2 and 50 nm in diameter) have been of great interest to the heterogeneous catalysis community for quite some time.<sup>1</sup> Over the last twenty years, monolithic materials that possess both mesopores and macropores (pores greater than 50 nm in diameter) have been developed. While particles have sizes from the 50 nm to 100's of microns range, monoliths are a single, continuous entity with a homogenous microstructure, such that the size of the monolith is on the centimeter to meter range. These materials are referred to as being hierarchically porous and can have highly interconnected pore systems. The pore systems can be ordered, such that all of the pores of one size are aligned in the same direction, or disordered, consisting of a network of randomly oriented pores. The most well-known disordered, hierarchically porous monolithic material is silica. The invention of the silica monolith in 1997 by Kazuki Nakanishi<sup>2</sup> has revolutionized the field of chromatography, transforming HPLC from High *Pressure* Liquid Chromatography to High *Performance* Liquid Chromatography. These materials provide superior flow properties, while the tortuous nature of the pore system enhances interactions between liquid and gas phases with the solid phase. Utilization of this monolithic silica in other applications has been limited due to acid/base sensitivity and lack of electrical and thermal conductivity.

Hierarchically porous, high surface area, monolithic metal and metal oxide materials are of great interest to many fields due to the wide range of applications including, but not limited to catalysis, batteries, super capacitors, sensors, and separations. The specific surface area required for most chromatographic applications is generally in the range of 150-400 m<sup>2</sup>/g, but the highest

surface area for commercial metal foam is approximately  $1 \text{ m}^2/\text{g}$ . Producing monolithic metal oxides directly using solution-gelation (sol-gel) chemistry involves complicated self-assembly mechanisms in which the rate of formation of the oxide must be well controlled. This is very difficult to accomplish and has only been successful with group 4 transition metal oxides. Furthermore, sol-gel techniques do not currently have the capability to generate metal monoliths and it is not clear that it is feasible. Therefore, an alternative approach must be developed that enables the production of these materials. The research presented here involves the development of a robust, patent pending method to produce various hierarchically porous, high surface area metal and metal oxide monoliths. The application of select metal and metal oxide monoliths in liquid chromatography and catalysis will be also be presented.

## **1.2 Introduction**

After several different avenues for designing metal and metal oxide monoliths were investigated, including electrodepositing nanostructure onto foam metal and electrodeposition into mesoporous silica monoliths, the most promising approach was determined to be nanocasting into mesoporous silica monoliths. Nanocasting is a method generally used to replicate mesoporous nanoparticles such that a negative copy (similar to a negative in photography) of the original structure is created at the nanometer scale after the mesoporous template is removed. The process of nanocasting commonly involves infiltration of a fluid precursor into the nanopores, followed by chemical conversion to the final desired material, and concluding with the removal of the original hard template. Silica particles are the most commonly employed hard template as they are inexpensive and easy to produce. It is relatively straightforward to control most of the properties of the silica monolith such as pore size and surface area during synthesis as well as the dimensions of the monolith itself. Ideally, the

resulting structure after removal of the silica will be a replica of the original monolith with all of the macro, micro, and nanostructure in place. While, nanocasting into mesoporous silica monoliths to generate  $\text{Co}_3\text{O}_4$ ,  $\text{SnO}_2$ ,  $\text{MnO}_2$  and  $\text{Mn}_2\text{O}_3$  was previously achieved by our collaborator, Professor Jan-Henrik Smått, only modest surface areas of 30-70  $\text{m}^2/\text{g}$  were obtained from silica monoliths having surface areas of 240-940  $\text{m}^2/\text{g}$ .<sup>3</sup>

Nanocasting to replicate monoliths is more complicated than replicating particles. When a particle is not completely replicated, the result is simply a particle that is smaller in diameter than the original. When a monolith is not completely replicated, the resulting material is particulate as opposed to monolithic. Through much experimentation, it was found that there are many variables, as seen in Figure 1.1, that must be considered in order to make a well replicated, monolithic metal or metal oxide.

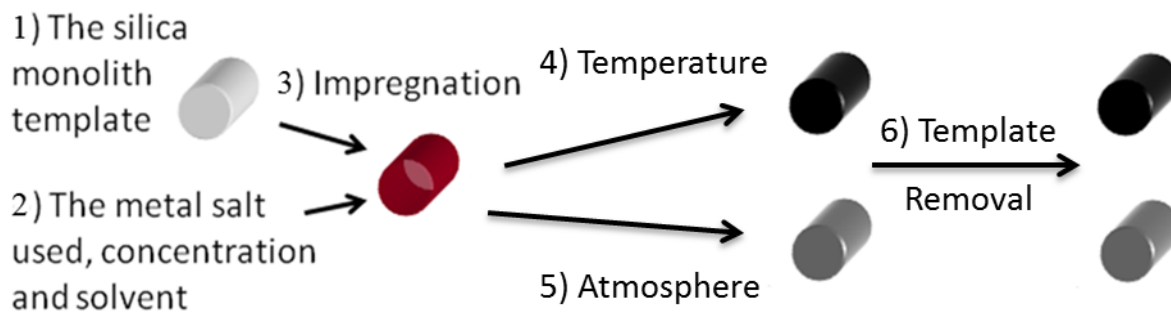


**Figure 1.1.** Nanocasting Variables

The schematic presented here may be thought of as a bottom-up approach where capillary forces allow filling of the smallest mesopores first. The process is then repeated until the templated silica mesopores are filled. The final structure forms a negative replica of the mesopores and a positive replica of the macropores. Figure 1.2 depicts the positive replica formed at the millimeter and micrometer length scales while a negative replica is seen at the nanometer length scale.<sup>4</sup>

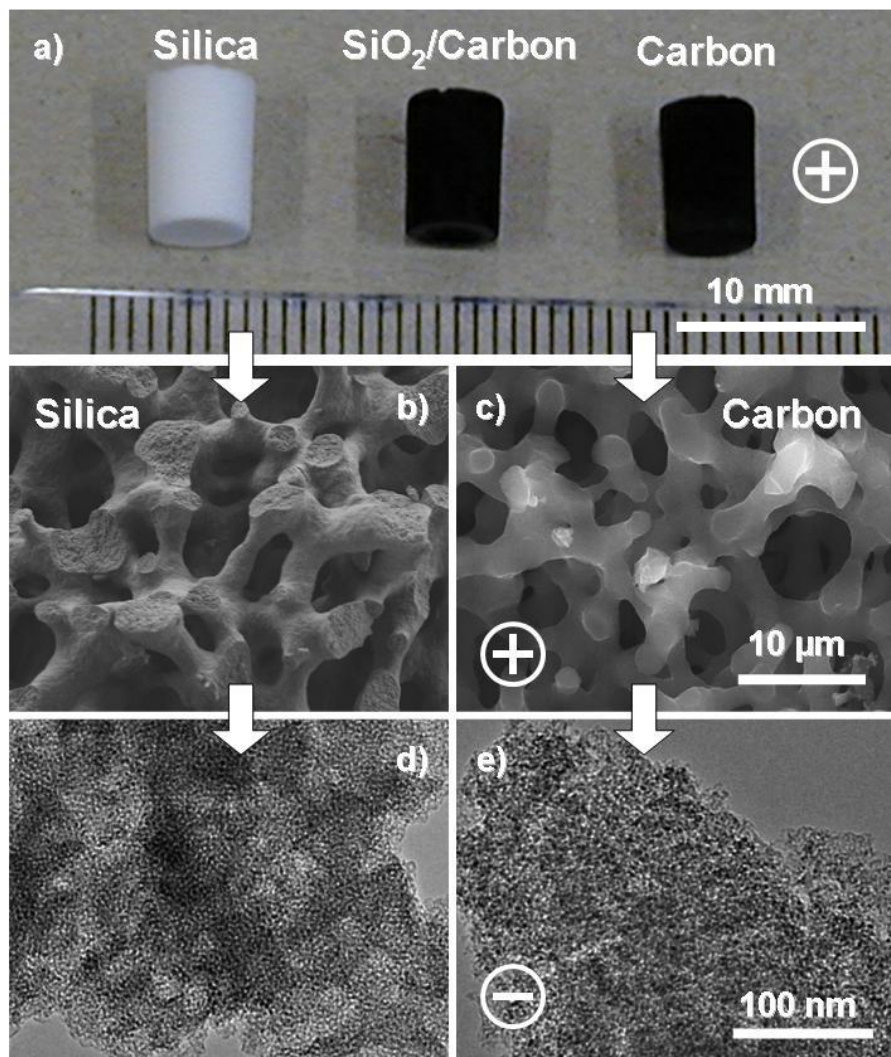


**Figure 1.2.** Comparison of Silica Template and Carbon Replica at Different Length Scales. a) Photograph of silica template, silica-carbon composite, and carbon replica, b) Scanning Electron Microscope (SEM) image of silica, c) SEM image of carbon replica, d) Transmission Electron Microscope (TEM) image of silica, e) TEM image of carbon replica.<sup>4</sup>

First, a well-connected silica mesopore system is needed to ensure that a robust monolithic replica is produced. It was hypothesized that lack of connectivity between the mesopores in the silica monolith template lead to the poor replication seen by Smått et al. Since connectivity of disordered porous materials is difficult to infer without neutron scattering or transmission electron microscope tomography, an experiment was designed specifically to

measure mesopore connectivity in our silica system. Hierarchically porous silica monoliths were synthesized according to methods reported by Småtå and co-workers possessing macropores, generated by the addition of polyethylene glycol to the solution, and different sizes of surfactant templated mesopores, generated by the addition of tetradecyl-, hexadecyl-, and octadecyl-trimethylammonium bromide salts referred to as C<sub>14</sub>TAB, C<sub>16</sub>TAB, and C<sub>18</sub>TAB, respectively, to the solution.<sup>5</sup> The silica monoliths were impregnated with 0.02 M aqueous Co(NO<sub>3</sub>)<sub>2</sub> solution, dried, and the resistance was measured as a function of relative humidity (RH). As RH increases, a monolayer will form and then pores will fill with water from smallest to largest. The initial idea was to find which type of monolith structure best enables the travel of ions through the system.

A distinct dissimilarity was found between all monoliths made with merely a two carbon difference in alkyl chain length. By comparing the conductance with nitrogen physisorption and water adsorption measurements, it was discovered that the C<sub>14</sub>TAB surfactant templated mesopores had to be completely filled before any conductivity could be measured. C<sub>16</sub>TAB had measurable conductance, but did not display any sharp increases until the surfactant templated pores were filled with water. However, C<sub>18</sub>TAB monoliths showed increasing conductance at 20% relative humidity and exhibited sharply increasing conductance at 70%. Monoliths with no surfactant templated mesopores, monomodal samples, showed no conductance until they were completely wet.<sup>6</sup> Småtå et al. used monomodal and C<sub>16</sub>TAB templated silica.<sup>3</sup> Based on these results, nanocasting should better replicate the structure of C<sub>18</sub>TAB type monoliths and ensure minimum loss of porosity.

The second factor is related to the metal or metal oxide precursor liquid. The most common types of precursors are metal nitrate salts because they tend to have high solubility in water, low melting points, and low decomposition temperatures. The number of times the

infiltration-decomposition/reduction cycle is repeated is dictated by the initial concentration of the precursor and the change in density when the salt is converted into metal or metal oxide. When a nearly saturated solution of metal nitrate salt is used, the number of cycles needed is ~3-5 to produce a metal oxide replica and 5-8 for a metal replica. However, we have demonstrated that in some cases, the use of melted metal nitrate salts alone can be used to significantly reduce the number of re-infiltration cycles needed to produce a replicate. The utilization of a nitrate melt can reduce the number of cycles required to produce a metal oxide replica to 2-3 and 3-5 for a metal replica.<sup>7,8</sup>

Another factor that greatly influences replication is the method of impregnation. A common method, referred to as “incipient wetness”, involves adding a volume of solution that equals the volume of the templated silica mesopores. Since capillary forces will favor filling the mesopores rather than the macropores, the infiltration solution will be limited to only the mesopores. Another approach is to use a more dilute solution and allow evaporation to concentrate the precursors in the mesopores. This method requires careful control of the initial concentration as salt may precipitate in the macropores if the solution reaches saturation before the solvent has evaporated from the macropores. The best method we have found is vacuum infiltration, where the entire monolith is placed under vacuum and then filled with a degassed, concentrated aqueous solution. In this case, all of the void volume is filled with liquid.

The fourth and probably most critical variable is temperature. If the silica monolith is infiltrated with a concentrated salt solution and the salt is allowed to dry too slowly, then large salt crystals may grow in the macropores causing the entire monolith to crack and, in some cases, turn into powder. If the infiltrated silica monolith is heated too high initially, then macroscopic migration occurs radially and the end result is a monolith with a hole through the center. It

seems that the optimum initial temperature for nitrates salts is 150 °C. After holding at this temperature for a given amount of time for the different metals, the temperature can then be increased to complete the transformation to the desired oxide or metal. This final temperature must be high enough to complete the transformation, but still lower than the mobility temperatures for the final product. These mobility temperatures for nanostructures are defined as the Hüttig temperature, the temperature at which atoms from defect sites become mobile ( $\sim 1/3 T_{\text{bulk melting}}$ ) and the Tammann temperature, the temperature at which nanoparticles become mobile on a surface ( $\sim 1/2 T_{\text{bulk melting}}$ ).<sup>9</sup>

Another critical variable is atmosphere, which determines not only whether the final product is an oxide or metal, but also how well the product replicates the silica mesostructure. Most metal nitrate salts produce a metal oxide when decomposed in air, oxygen, or an inert atmosphere. A detailed study was performed comparing  $\text{Co}_3\text{O}_4$  produced under vacuum, air, helium, nitrogen, and argon. It was found that the  $\text{Co}_3\text{O}_4$  monolith produced under argon resulted in the highest surface area replica.<sup>8</sup> Metal replicas can be made when decomposition occurs in a reducing atmosphere such as hydrogen, ethylene glycol, or methanol. Care must be taken to avoid exposing certain metal replicas to air as they are very reactive and can be pyrophoric. However, this high reactivity has some advantages, particularly in the field of catalysis.

Finally, once the nanocasting process is complete, the hard silica template needs to be removed via etching. Generally this is performed with either an aqueous hydroxide solution or hydrofluoric acid etchant. Unfortunately, certain metal oxides are soluble in both etchant solutions, e.g. zinc oxide, and others will react with the etchant to produce a hydroxylated surface. An etchant that is able to circumvent these limitations will be presented.<sup>7</sup>

Nickel monoliths produced in the manner discussed above have been tested as catalysts. The catalytic activity of a nickel monolith reduced with hydrogen and a nickel monolith reduced with methanol were compared to that of Raney® Ni. The catalytic hydrogenation of cyclohexanone to cyclohexanol was investigated using these nickel materials. It was found that 96% conversion was achieved with Raney® Ni, 80% conversion with the nickel monolith reduced with methanol, and 69% conversion with the nickel monolith reduced with hydrogen.<sup>10</sup>

These metal and metal oxide monolithic materials have also been tested in liquid chromatographic separations. Monolithic sterling silver, zinc oxide, and cobalt oxide chromatography columns were produced. The sterling silver column showed some evidence of separation of a mixture of hydrophobic and hydrophilic components purchased from Phenomenex®, although resolution of each component was not achieved. Retention of several different small analytes was demonstrated on the zinc oxide and cobalt oxide columns. No separation of a mixture of analytes was successful due to the short length of the oxide columns. These oxide columns were half the length of the sterling silver column because of cracking that occurred during processing.<sup>11</sup>

A general method for producing highly porous, high surface area metal and metal oxide materials was developed. Select metal and metal oxide monoliths were utilized in catalysis and chromatographic separations. In both of these applications, further refinement of the monolithic structure is necessary to achieve optimum results. In the case of application to liquid chromatography, much more column characterization is needed to study the nature of these unique stationary phases and their interactions with a broad range of analytes from small molecules to large proteins.

### 1.3 References

- (1) Biz, S.; Occelli, M. L.; *Catal. Rev.* **1998**, *40*, 329-407.
- (2) Nakanishi, K. *J. Porous. Mat.* **1997**, *4*, 67-112.
- (3) Smått, J.-H.; Weidenthaler, C.; Rosenholm, J. B.; Lindén, M. *Chem. Mater.* **2006**, *18*, 1443-1450.
- (4) Smått, J.-H. Hierarchically porous silica, carbon and metal oxide monoliths – synthesis and characterization. A Dissertation, Åbo Akademi University, Åbo, Finland **2006**.
- (5) Smått, J.-H.; Schunk, S. A.; Lindén, M. *Chem. Mater.* **2003**, *15*, 2354-2361.
- (6) Maddox Sayler, F.; Bakker, M. G.; Smått, J.-H.; Lindén, M. *J. Phys. Chem. C* **2010**, *114*, 8710-8716.
- (7) Bakker, M.; Sayler, F. M.; Grano, A.; Smått, J.-H. Methods for preparing and using metal and/or metal oxide porous materials. U.S. Patent Application 13/405,714, Aug 30, 2012.
- (8) Smått, J.-H.; Sayler, F. M.; Grano, A. J.; Bakker, M. G. *Adv. Eng. Mater.* **2012**, *14*, 1059-1073.
- (9) Moulijn, J. A.; van Diepen, A. E.; Kapteijn, F. *App. Catal. A* **2001**, *212*, 3.
- (10) Sayler, F. M.; Grano, A. J.; Scogin, W.; Sanders, P.; Smatt, J.-H.; Shaughnessy, K.; Bakker, M. G. *MRS Proceedings*, **2012**, *1389*, g05-05.
- (11) Sayler, F. M.; Grano, A.; Wiedmer, S.; Smått, J.-H.; Bakker, M. G. *MRS Proceedings*, **2012**, *1389*, g03-16.

## Chapter 2

### Correlation between Electrical Conductivity, Relative Humidity and Pore Connectivity in Mesoporous Silica Monoliths

#### 2.1 Abstract

Incipient wetness was used to load cobalt nitrate into the pores of a set of silica monoliths with pores arranged in a hierarchal fashion, either in the form of a bimodal pore structure containing only macropores and textural mesopores, or trimodal pore structures with additional mesopores as a result of surfactant templating. The volume and diameter of the surfactant templated mesopores was controlled by varying concentration and using surfactants of different chain length, tetradecyl-, hexadecyl-, and octadecyltrimethylammonium bromide ( $C_{14}TAB$ ,  $C_{16}TAB$ , and  $C_{18}TAB$ , respectively.) Platinum replication of samples made with  $C_{14}TAB$  and  $C_{18}TAB$  was performed. The native and the cobalt nitrate impregnated monoliths were characterized with nitrogen physisorption, water sorption and electron microscopy. The electrical conductivity of the cobalt nitrate impregnated monoliths was measured as a function of relative humidity. The presence of the surfactant templated mesopores resulted in significantly higher conductivity at all relative humidities, and generally the conductivity increased as a function of surfactant chain length (going from  $C_{14}TAB$  to  $C_{18}TAB$  surfactants), and with increasing surfactant concentration in the precursor sols. The findings are suggested to originate from differences in the macroscopic mesopore connectivity throughout the monoliths, a property which is otherwise difficult to assess by other characterization techniques.

#### 2.2. Introduction

Mesoporous silica has become increasingly popular for applications ranging from drug delivery<sup>1</sup> and chemical separations to electrochemical sensor arrays.<sup>2</sup> Silica monoliths containing both macropores and mesopores have been developed as the stationary phase in

commercially available chromatography columns.<sup>3,4</sup> Mesoporous silica is attractive for many applications in various fields due to properties such as high surface area, large void volume, and tunable surface chemistry. The ease and low cost with which it can be produced adds to the appeal of using mesoporous silica in sensor based devices.

Mesoporous, monolithic silica can be easily prepared via sol-gel techniques. Hierarchical porosity containing both macropores and mesopores, pores greater than 50 nm in diameter and pore diameters between 2 and 50 nm respectively, can be achieved by combining polymerization induced phase separation and surfactant templating.<sup>5-8</sup> Figure 2.1 shows the typical hierarchical structure seen in these monoliths. The size and shape of the monoliths were fully determined by the outline of the synthesis vessel, while the macropores seen in Figure 2.1(b) were formed by the addition of a polymer, in this case, polyethylene glycol. The SEM image in Figure 2.1(c) reveals the textural mesopores formed by the space between silica particle agglomerates that form the macropore structure. The addition of a surfactant gives rise to surfactant mesopores within the individual particles seen in Figure 2.1(c). The chain length of the surfactant used as the porogen determines the pore diameter of the mesopores. Using a surfactant that differs in

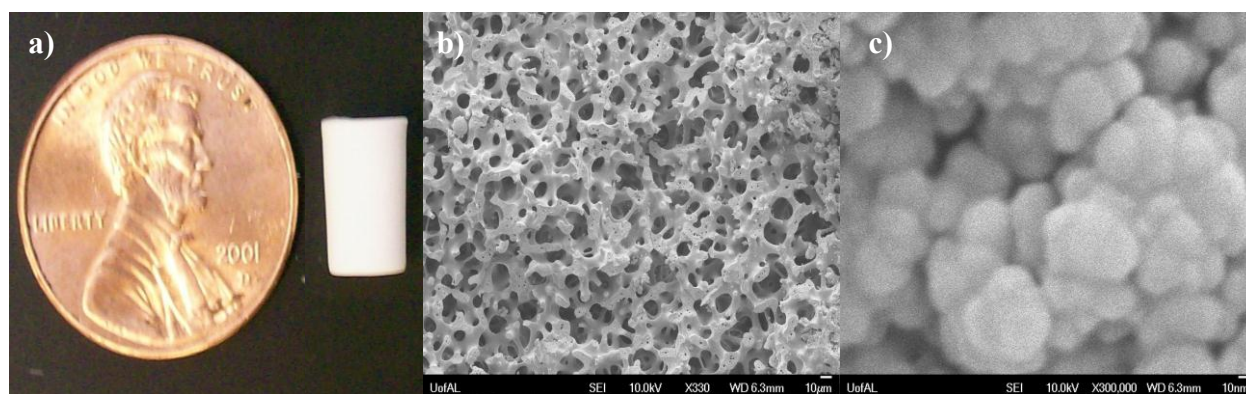


**Figure 2.1.** Silica Monolith (a) Photo of a cylindrical monolith (the size of the coin is 19 mm) (b) SEM image of the macropore structure (c) SEM image of agglomerates creating the textural pores.

alkyl chain length by a mere two carbons alters pore size and surface area.<sup>6</sup> The connectivity of the surfactant templated mesopore network is also significant for many applications, predominantly those such as separations that involve mass transport through the monolith. This is an aspect of mesoporous silica that has received rather limited investigation, and is a challenging problem to address.

Current electron microscopy techniques cannot give sufficient information about the connectivity of a mesopore network with appropriate resolution. Small angle X-ray scattering and neutron scattering techniques give information about the periodicity and ordering of mesoporous systems, but do not report well on connectivity. Tomography techniques are potentially useful in giving connectivity information. TEM tomography, particularly using high angle annular dark field detection, has shown the ability to image small sections of mesoporous silica particles in great detail.<sup>9-12</sup> However, TEM tomography cannot image sufficiently large regions of a sample to address the connectivity at the macroscopic level. Conversely, tomography based on Focused Ion Beam (FIB) imaging combined with ion-milling, has only 25 nm lateral resolution,<sup>13</sup> which is likely not adequate to address the mesopore connectivity on a macroscopic length scale. Replication approaches have been carried out to study the connectivity of mesopores on a mesoscopic length scale. For instance, the pore structures of various ordered mesoporous silica materials, including SBA-15<sup>14</sup> and KIT-6,<sup>15</sup> have been investigated using Pt replication. The higher contrast of Pt compared to SiO<sub>2</sub> facilitates direct TEM observation and a stable replica structure suggests an interconnected network of mesopores in the original silica material. The problem for similar studies on the macroscopic level is the potential for deposition outside the mesoporous network, making it difficult to discuss mesopore connectivity on a macroscopic level based solely on the mechanical integrity of the replicas.

One technique that potentially can be used to gain insight into the connectivity of the pores in monolithic silica is electrical conductivity. For a given relative humidity, the better the overall connectivity of the mesopores and macropores, the higher the conductivity expected. By studying the electrical conductivity as a function of relative humidity, further insight into pore connectivity can be obtained. Specifically, as the relative humidity rises pores will be filled in ascending order according to size. Once an unobstructed path is available, ions will be able to move freely. This approach has recently been used for studying proton conduction in mesoporous silica monoliths<sup>16</sup> and thin films.<sup>17,18</sup> By exploring the changes in conductivity with relative humidity for a range of different preparations, the observed trends have been found to give interesting new insight into the connectivity of the various types of monoliths.

## **2.3. Experimental Methods**

### **2.3.1 Materials and Synthesis**

Monoliths were prepared using a method described by Småtå et al.<sup>6</sup> Tetraethoxysilane 98% purchased from Aldrich (TEOS), polyethylene glycol 35,000 g/mol (PEG) purchased from Merck, and a 30% nitric acid solution were mixed with a specific molar composition (see Table 2.1) to produce monoliths with a bimodal pore structure. Trimodal monoliths with additional surfactant templated mesopores were produced by the addition of an alkyltrimethylammonium bromide surfactant with varying alkyl chain lengths. Tetradecyl-, hexadecyl-, and octadecyl-alkyl chain lengths were used in 0.229 M, 0.276 M, and 0.196 M concentrations, which correspond to 7, 9, and 7 wt% of the starting sol, respectively. Furthermore, a series of different C<sub>18</sub>TAB concentrations, corresponding to 7, 5, and 3 wt%, was also prepared. Tetradecyl- and octadecyltrimethylammonium bromide were purchased from Fluka and hexadecyltrimethylammonium bromide was purchased from Merck. The resulting monoliths

**Table 2.1.** Aqueous Molar Composition of Monoliths

monolith	HNO <sub>3</sub>	PEG 35,000	TEOS	C <sub>n</sub> TAB
C0-0	0.51	1.38x10 <sup>-3</sup>	2.02	0.00
C14-7	0.51	1.15x10 <sup>-3</sup>	2.02	0.229
C16-9	0.51	8.74x10 <sup>-4</sup>	2.02	0.276
C18-7	0.51	8.74x10 <sup>-4</sup>	2.02	0.196
C18-5	0.51	1.08x10 <sup>-3</sup>	2.02	0.138
C18-3	0.51	1.28x10 <sup>-3</sup>	2.02	0.082

have been denoted C<sub>x</sub>-<sub>y</sub>, where x denotes the chain length (x = 14 – 18) and y indicates the wt% (y = 0 – 9) of the surfactant that has been used in the synthesis. According to earlier work, the amount of PEG has been adjusted to obtain monoliths with similar macropore structure regardless of the surfactant concentration.<sup>6</sup>

Samples were allowed to gel for 8 hours and then aged for 72 hours at 40 °C after which, solvent exchange was performed with 1.0 M ammonium hydroxide at 90 °C for 8 hours. Monoliths were then neutralized in 0.1 M nitric acid, washed with water and acetone, and dried at 40 °C. Finally, monoliths were calcined at 550 °C for 5 hours using a ramp of 1 °C/min.

### 2.3.2 Characterization

Nitrogen physisorption isotherms were taken of each type of monolith at 77 K with a NOVA 2200e surface area and pore size analyzer purchased from Quantachrome. Pore size was analyzed using the adsorption branch with Non-Local Density Functional Theory (NLDFT) based on a cylindrical pore model. Non-impregnated monoliths were degassed overnight at 250 °C, while impregnated monoliths were degassed for at least 72 hours at 45 °C. Mercury intrusion

was measured on a Pascal 140/440 mercury porosimeter purchased from Thermo Fisher Scientific. Water sorption isotherms were measured at 25 °C using a Hydrosorb 1000 vapor sorption system purchased from Quantachrome. SEM images were collected on a JEOL 7000 Scanning Electron Microscope equipped with an Oxford Instruments INCAx-sight Energy Dispersive X-ray Spectrometer (EDS) for elemental analysis. A thin (ca. 2 nm thick) gold layer was sputtered onto the sample to minimize charging of the sample.

Platinum replication of C14-7 and C18-7 containing 40 and 60 wt% Pt was carried out according to methods described by Shin.<sup>19</sup> Monoliths were first ground into a fine powder in an attempt to avoid macropore replication. Replicas containing 40 wt% and 60 wt% Pt used hexachloroplatinic acid, purchased from Aldrich, as a Pt precursor. Samples were reduced at 250 °C with a heating ramp of 10 °C/min under a flow of 5% H<sub>2</sub> in N<sub>2</sub> for 24 hours. The resulting black powder was etched at 90 °C in 4 M NaOH for 24 hours to remove the silica. SEM images were collected. TEM samples were sonicated for 1 hour in ethanol, dispersed onto a carbon coated copper grid, and subjected to Argon ion etching to thin the samples. TEM images were collected on a FEI Tecnai F-20 Transmission Electron Microscope.

### 2.3.3 Conductivity

In order to test electrical conductivity, monoliths were impregnated with 0.02 M cobalt nitrate hexahydrate (98%, purchased from Fluka) solution via incipient wetness.<sup>20</sup> After impregnation, the monoliths were dried under vacuum for 48 hours at 45 °C and weighed. Complete drying of the impregnated sample was indicated by a color change from pink to blue caused by the transition of cobalt nitrate hexahydrate to anhydrous cobalt nitrate. The difference in the mass of the monoliths before and after impregnation was not significant. Monoliths impregnated with 0.02 M cobalt nitrate are denoted C<sub>x</sub>-y-Co. The cylindrical monoliths used

were 5 mm in height and 4 mm in diameter. Monoliths were positioned between two copper plates, which had been cleaned with 1.0 M hydrochloric acid, and placed inside of a controlled humidity chamber. The humidity was controlled by changing the balance between a stream of dry air, controlled by an Agilent H<sub>2</sub>O trap, and one of water vapor saturated air, designed in house. This system was reliably able to control the humidity from 5% up to 90% relative humidity as measured by a Vaisala MI70 humidity meter. A wire was affixed to each plate and the resistance between the two plates was measured in duplicate at different relative humidities using a Fluke 8020B multimeter. Measurements were carried out using alternating current. Preliminary experiments utilizing direct current, showed evidence of ion migration within the monolith. Measurable resistance values were in the range of 20 M $\Omega$  to 200  $\Omega$ . At low relative humidity (RH) the resistances exceeded the range of the multimeter. As the humidity was raised, the monolith was allowed to equilibrate at each RH value for 15 minutes. This time was determined by plotting resistance at different time intervals while keeping the RH constant, and was found to be sufficient for the monoliths to have equilibrated. Resistance was converted to units of conductivity.

## **2.4 Results**

### **2.4.1 Platinum Replication**

SEM and TEM images of C14-7, C18-7, and their Pt replicas can be seen in Figure 2.2. Complete reduction of the Pt precursor was confirmed by EDS analysis. The SEM images comparing the native monoliths, Figure 2.2a-b, with their 40 wt% Pt replicas, Figure 2.2c-d, do indicate that mesopores have been replicated. Notice in Figures 2.2c and 2.2d, there are Pt ligaments that are much smaller in width than the space between the silica agglomerates seen in

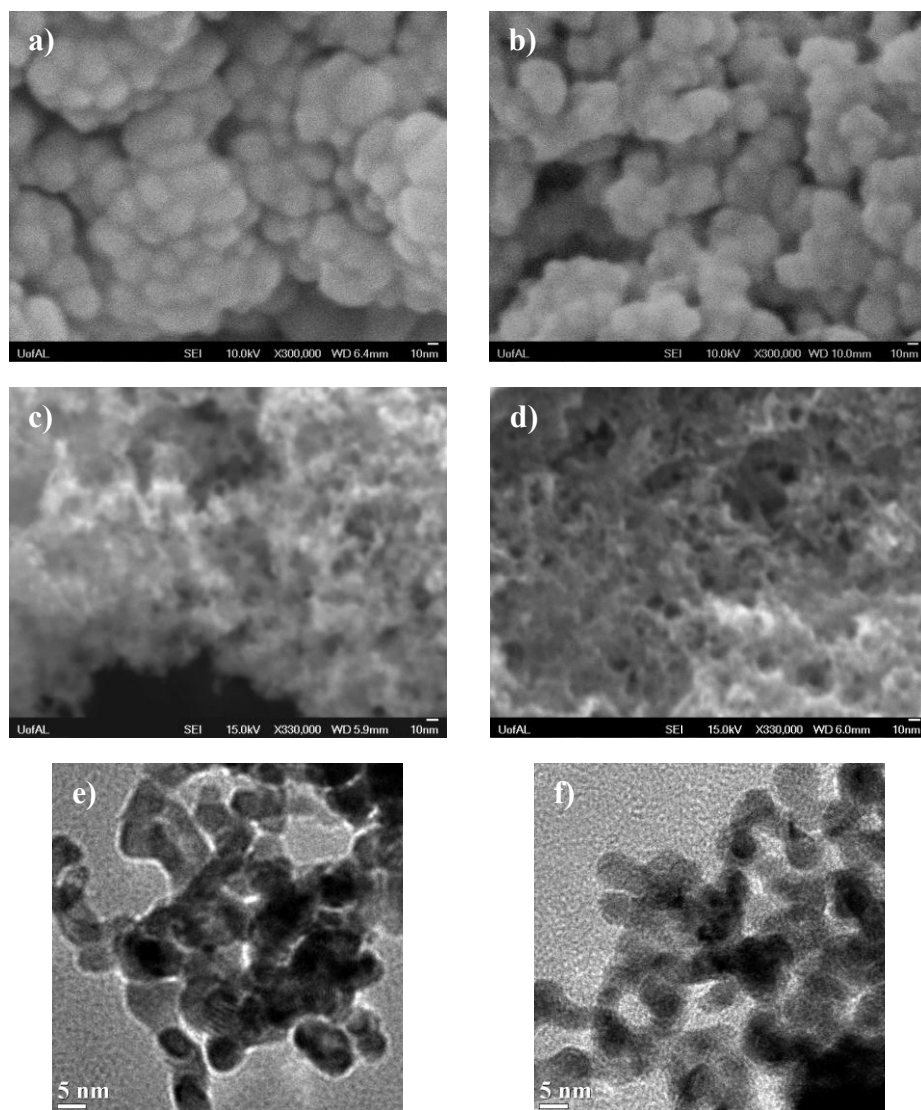


**Figure 2.2.** Images of Native Monoliths and Platinum Replicas. SEM images of (a) C14-7 (b) C18-7 (c) C14-7 40 wt% Pt replica (d) C18-7 40 wt% Pt replica. TEM images of (e) C14-7 60 wt% Pt replica (f) C18-7 60 wt% Pt replica.

Figures 2.2a and 2.2b. However, it appears that in addition to the surfactant mesopores, the textual mesopores have been replicated at these high Pt loadings, resulting in thicker Pt ligaments among the fine structure of the replica. These samples were much too thick to obtain high quality TEM images. The TEM images Figure 2.2e-f, were obtained from the fringes of the samples which were sufficiently thin to have some transparency. The TEM images show

agglomerated particles approximately 5 nm in diameter. It is not clear how representative of the sample as a whole these images are, as relatively few areas show significant transparency.

#### 2.4.2 Nitrogen Physisorption and Mercury Intrusion Porosimetry

Nitrogen adsorption isotherms for the native monoliths are shown in Figure 2.3. All samples display a steep nitrogen uptake at a relative pressure above 0.9 indicating the presence of textural mesopores. In the surfactant templated samples capillary condensation also takes

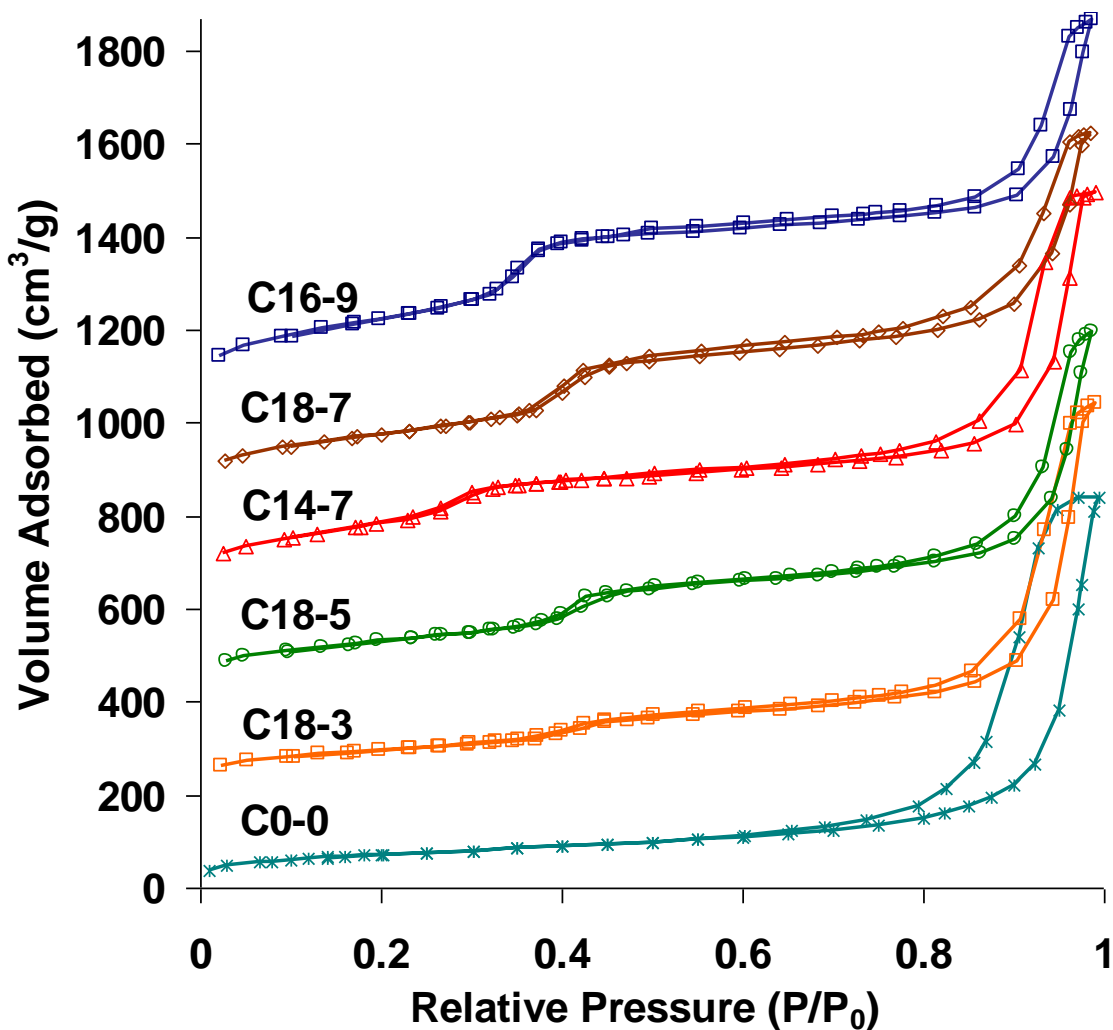


**Figure 2.3.** Nitrogen Physisorption Isotherms of Native Monoliths. C18-3 is offset by 200  $\text{cm}^3/\text{g}$ , C18-5 is offset by 400  $\text{cm}^3/\text{g}$ , C14-7 is offset by 600  $\text{cm}^3/\text{g}$ , C18-7 is offset by 800  $\text{cm}^3/\text{g}$ , and C16-9 is offset by 1000  $\text{cm}^3/\text{g}$  for clarity.

place in the relative pressure range between 0.30 and 0.45 indicating that these monoliths also contain smaller mesopores, which is in agreement with previously published data.<sup>6</sup> A slight hysteresis is present in the surfactant templated mesopore region. However, this was found experimentally to be a function of equilibration time with very lengthy equilibration times needed to remove these effects. Nitrogen isotherms for cobalt nitrate impregnated monoliths and NLDFT pore size distributions for all monoliths can be found in the supporting information, Figures 2.S1-S3. A small difference was found between native and impregnated samples; nonetheless, the overall trend was the same. The derived surface areas, pore diameters, and pore volumes of native monoliths obtained from nitrogen adsorption and mercury intrusion are summarized in Table 2.2. The samples were checked for microporosity using the t-plot method, but no significant volume of micropores was found. Mercury intrusion curves for native monoliths are also included in the supporting information section, Figure 2.S4. Even though some deviations in the macropore structure can be observed, we can assume that this will not have any effect on the conductivity under the studied relative humidities.

As anticipated, BET analysis reported much higher surface areas when surfactants were used. NLDFT analysis indicated the expected pore size distribution for all surfactant templated samples; with the average pore size increasing from 3.7 nm for the C<sub>14</sub>TAB to 4.6 nm for the C<sub>18</sub>TAB. Additionally, total mesopore volumes ( $V_{\text{surf}} + V_{\text{text}}$ ) of monoliths prepared with surfactants were also similar with values lying between 1.3 and 1.5 cm<sup>3</sup>/g. When the monoliths were impregnated with 0.02 M cobalt nitrate salt solution, the BET specific surface areas decreased in all cases. NLDFT analysis showed no significant shift in pore size distribution after impregnation. There was a consistent decrease in the volume of the surfactant templated pores

upon addition of the salt. This decrease is visible upon comparison of the NLDFT pore size distribution plots located in supporting information (Figures 2.S2 and 2.S3).

**Table 2.2.** Mercury Intrusion and Nitrogen Physisorption Data for Native Monoliths

Monolith type	BET specific surface area (m <sup>2</sup> /g)	d <sub>surf</sub> <sup>1</sup> (nm)	V <sub>surf</sub> <sup>2</sup> (cm <sup>3</sup> /g)	V <sub>text</sub> <sup>3</sup> (cm <sup>3</sup> /g)	V <sub>macro</sub> <sup>3</sup> (cm <sup>3</sup> /g)	V <sub>total</sub> (cm <sup>3</sup> /g)
C0-0	197	–	–	1.05	2.39	3.44
C14-7	667	3.7	0.46	1.01	2.84	4.31
C16-9	810	4.1	0.65	0.71	3.08	4.44
C18-7	665	4.6	0.55	0.86	3.32	4.73
C18-5	484	4.6	0.40	0.86	3.31	4.57
C18-3	340	4.6	0.28	0.99	2.76	4.03

<sup>1</sup> Determined from NLDFT pore size distribution (cylindrical pore model)

<sup>2</sup> Determined from nitrogen adsorption isotherm  $P/P_0 \leq 0.6$

<sup>3</sup> Determined from mercury intrusion porosimetry

### 2.4.3 Water Vapor Sorption

Water vapor sorption data for native and impregnated monoliths are shown in Figures 2.4 and 2.5, respectively. The monomodal monolith showed low water adsorption due to the lack of surfactant mesopores. The surfactant templated pore volumes seen in Table 2.3 were slightly less than that obtained from nitrogen adsorption. The lower value found from water adsorption likely reflects assumptions made in the choice of water contact angle (0°) on the silica surface.<sup>21</sup> It is not clear what an appropriate value would be for the empty mesoporous silica, nor for cobalt nitrate impregnated silica. We therefore are not concerned about the apparent discrepancy, as the general trends are consistent and useful. The increase in volume for C16-9 samples upon impregnation was likely due to samples being drawn from different batches. Generally, upon

impregnation, peak pore size distribution and pore volume decreased. The circled points of inflection in Figure 2.5 represent the relative pressure and volume at which the surfactant templated mesopores are completely filled.

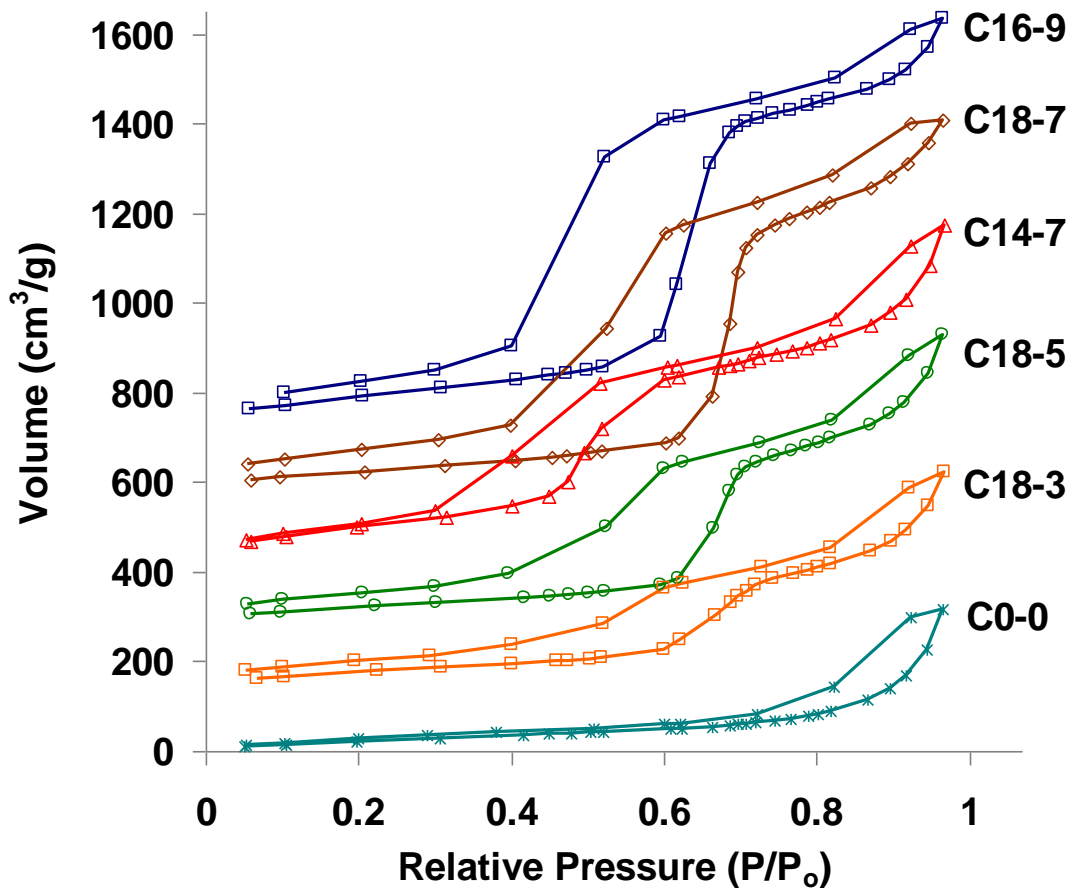


**Figure 2.4.** Water Vapor Sorption Isotherms of Native Monoliths. C18-3 is offset by 150  $\text{cm}^3/\text{g}$ , C18-5 is offset by 300  $\text{cm}^3/\text{g}$ , C14-7 is offset by 450  $\text{cm}^3/\text{g}$ , C18-7 is offset by 600  $\text{cm}^3/\text{g}$ , and C16-9 is offset by 750  $\text{cm}^3/\text{g}$  for clarity.

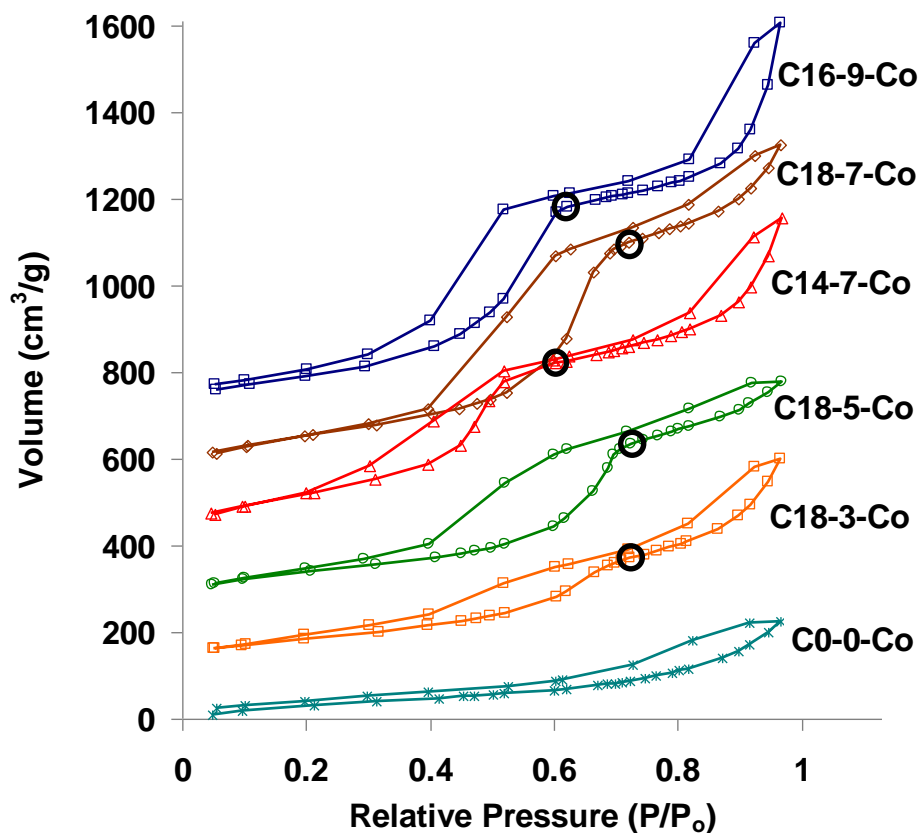


**Figure 2.5.** Water Vapor Sorption Isotherms of 0.02 M Cobalt Nitrate Impregnated Monoliths. C18-3-Co is offset by 150 cm<sup>3</sup>/g, C18-5-Co is offset by 300 cm<sup>3</sup>/g, C14-7-Co is offset by 450 cm<sup>3</sup>/g, C18-7-Co by 600 cm<sup>3</sup>/g, and C16-9-Co by 750 cm<sup>3</sup>/g for clarity.

**Table 2.3.** Water Vapor Sorption Data for Native and Co(NO<sub>3</sub>)<sub>2</sub> Impregnated Monoliths

Monolith type	V <sub>surf</sub> <sup>1</sup> (cm <sup>3</sup> /g)		V <sub>total</sub> <sup>2</sup> (cm <sup>3</sup> /g)	
	native	Co(NO <sub>3</sub> ) <sub>2</sub>	native	Co(NO <sub>3</sub> ) <sub>2</sub>
C0-0	–	–	0.26	0.18
C14-7	0.31	0.30	0.58	0.57
C16-9	0.53	0.35	0.71	0.69
C18-7	0.45	0.40	0.65	0.58
C18-5	0.28	0.27	0.51	0.39
C18-3	0.18	0.18	0.38	0.36

<sup>1</sup> Pore volume after surfactant pores filled

<sup>2</sup> Total volume of water at 0.97 P/P<sub>0</sub>

## 2.4.4 Conductivity

Initial studies comparing different concentrations of impregnated salt can be found in the supporting information, Figure 2.S5. From these studies, the optimal salt concentration was found to be 0.02 M  $\text{Co}(\text{NO}_3)_2$ . No measurable conductance was observed in native monoliths. Comparison of the conductivity for different types of monoliths impregnated with 0.02 M cobalt nitrate, seen in Figure 2.6, is illuminating. Sample C0-0-Co, the monolith without surfactant templated mesopores, showed no conductance until the RH was fairly high, approximately 75%. Monoliths with both surfactant and textural mesopore structure began to exhibit conductivity at much lower relative humidity. Initial onset of measurable conductance for C18-7-Co was 50% RH, followed by C18-5-Co and C16-9-Co at 58% and 60%, respectively. Onset of measurable conductivity was found to be 65% for C18-3-Co and 75% for C14-7-Co. Even at very high humidity the conductance at a given humidity shows the corresponding trend: highest for the

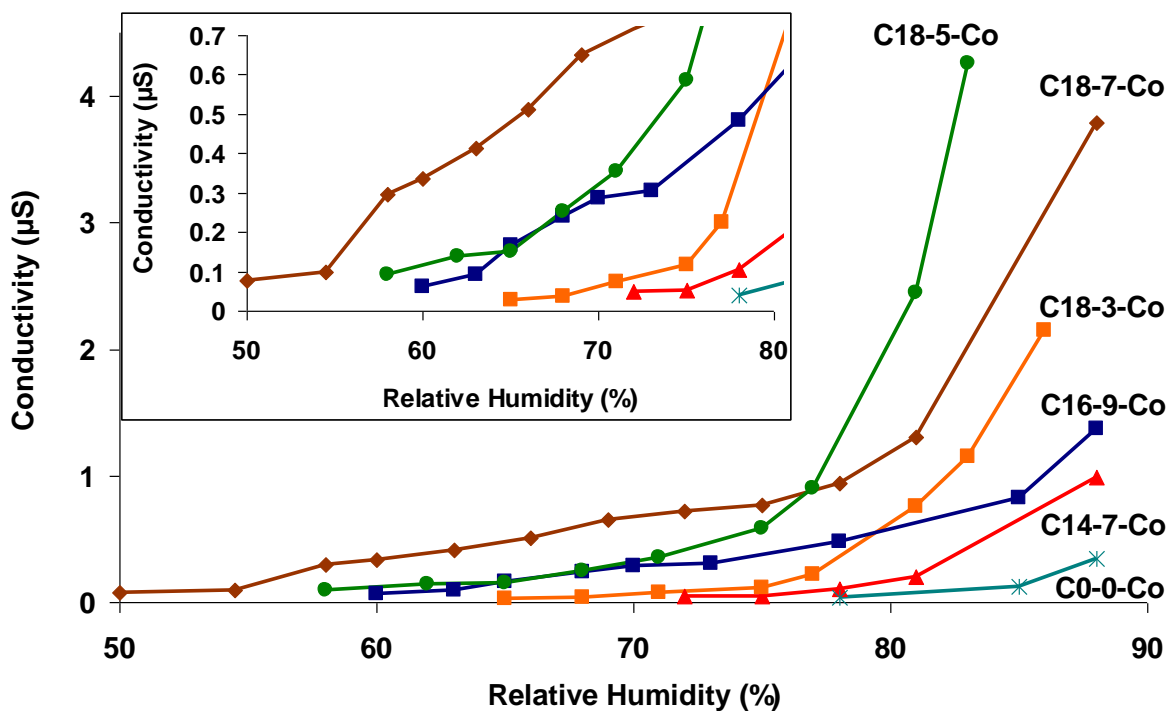


**Figure 2.6.** Measured Electrical Conductivity with Increasing Relative Humidity.

C18-7-Co, lower for C16-9-Co and lowest for C14-7-Co. When comparing monoliths prepared with differing amounts of the same surfactant (C18-3-Co, C18-5-Co, C18-7-Co) it is clear that not only the mesopore dimension, but also the actual number of mesopores influences conductance. In these monoliths, as the amount of C<sub>18</sub>TAB added is increased, the pore size distribution remains relatively constant; however, the pore volume increases which indicates a higher concentration of mesopores inside the silica matrix.

## 2.5 Discussion

As shown in Figure 2.6 above, significant differences in electrical conductivity as a function of RH are observed for the different types of monoliths. To understand how the monolith structure impacts the measured conductivity, the factors that can impact the measured conductivity will be considered. Under conditions of less than 100% RH, the macropores in the monoliths will not be filled with liquid, and current must flow through a multitude of parallel pathways along the macropore framework. The textural mesopores and the surfactant mesopores are contained within the macropore walls. The resistance of any one section of conductance path will depend upon the concentration of ions, the length of the path and cross-section of the path. Although it would be convenient to assume that the concentration of cobalt nitrate will be the same everywhere, it is not clear that this assumption can be made. Because of the nature of the experiment it is possible that the cobalt nitrate may be distributed unevenly within the different types of pores of a monolith and that this distribution might be different for different types of monolith.

The incipient wetness method merely fills the void volume of a porous material with a solution. For impregnating hierarchically porous materials with a salt, water desorption occurs by evaporation from the largest pores first. Water will evaporate from the macropores leaving a

more concentrated salt solution in the mesopores contained within the silica ligaments. As water continues to evaporate, it will leave the smallest pores filled until last. Since there is no microporosity, it is reasonable to assume that most of the cobalt salt is in fact located somewhere inside the surfactant templated mesopores upon drying.

To further confirm that the salt is confined to the surfactant mesopores, both the solubility of cobalt nitrate and the nature of the silica surface must be considered. Based on the pore volumes of native samples measured by mercury intrusion porosimetry and nitrogen physisorption, it is simple to calculate where the salt will begin to precipitate onto the silica surface. As dehydration takes place, the solubility limit for cobalt nitrate hexahydrate, which is reported to be 133.8 g/100 mL water for cold water<sup>20</sup>, is not reached in the macropores nor in the textural pores. The solubility limit is only just reached in C14-7-Co and C18-7-Co when the surfactant mesopores remain filled and the solubility limit is not reached in the surfactant pores in C16-9-Co. This is not to say that there could not be isolated pools of solution in the textural mesopores, which do not have adequate access to surfactant pores for the salt to be concentrated in these pores and this could result in significant precipitation of cobalt nitrate outside the surfactant mesopores. However, given this mechanism for water desorption, it is reasonable to assume that the salt does in fact remain mostly in the surfactant templated mesopores upon dehydration. Additionally, if the ionic strength of the impregnating solution was high it could greatly influence the surface chemistry of the monolith and result in considerable salt adsorption onto the entire silica surface, which is what was seen in the Pt replicas. Fortunately, the ionic strength of the cobalt nitrate solution was 0.06 M, which would allow for no substantial salt effects until the salt was confined to the mesopores. Furthermore, the dilute impregnating solution used in these experiments was mildly acidic. The point of zero charge for mesoporous

silica has been reported to be approximately pH 4.<sup>23</sup> In order for electrostatic ion adsorption to occur, the impregnating solution would need to be very basic and therefore deprotonate the silanol surface.<sup>24</sup> Similar filling behavior was observed when using the same type of silica monoliths as templates for making carbon replicas as the dilute carbon precursor (furfuryl alcohol) was preferentially loaded into the surfactant templated mesopores.<sup>25</sup> Accordingly, we believe that relatively little cobalt nitrate occurs outside the surfactant mesopores for the surfactant templated monoliths.

In the discussion that follows we will neglect any conductivity due to proton conduction, either in water or along the surface of the silica. Given the conductances reported by Xiong and Nogami<sup>16</sup>, and that the conductivity of our monoliths without added salt was below the range we could measure, we consider this a reasonable assumption. The presence of cobalt nitrate is expected to determine the electrical conductivity. Although the ionic mobilities of the cobalt and nitrate ions are significantly lower than that of protons, the concentrations are also five orders of magnitude higher.

When water condenses into the mesopores as relative humidity rises, the ions become hydrated and are able to move freely within the local water pool. How far the ions are able to move, and therefore conduct electricity, depends on how well the mesopores are connected, both inside a particle aggregate, and between different particle agglomerates. If the individual mesopores are not in contact with each other or if they exist in isolated networks, there will be effectively no conductance until the textural mesopores and macropores begin to fill with water. The latter does not occur under our experimental conditions. If the surfactant mesopores form completely connected networks and are at least partially filled with water, significant electrical conductivity would occur.

A direct comparison of water sorption data with the conductivity of C14-7-Co and C18-7-Co is made in Figure 2.7a and 2.7b, respectively. These graphs allow a direct comparison of conductivity and water adsorption. The points of inflection in the water sorption isotherm, circled in Figure 2.5, correspond to filling of the surfactant templated mesopores. It is easy to

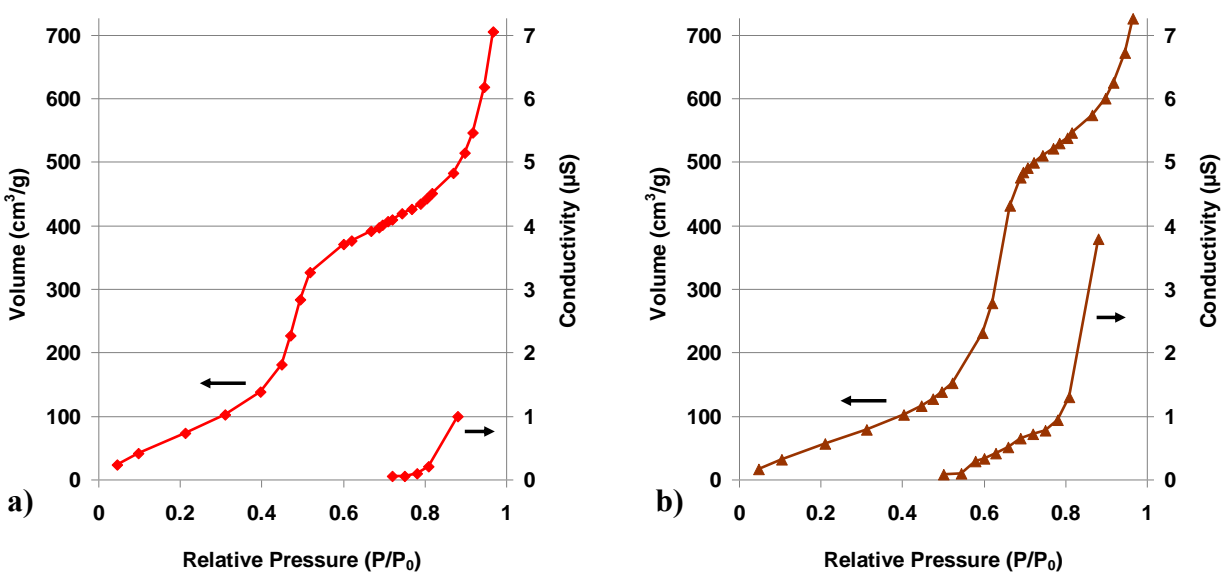


**Figure 2.7.** Comparison of Water Adsorption and Conductivity Curves a) Sample C14-7-Co b) Sample C18-7-Co.

see that the onset of conductivity for C14-7-Co does not occur until the surfactant mesopores are completely filled, at a relative pressure of 0.75  $P/P_0$ . However, the onset of conductivity for C18-7-Co appears at a relative pressure of 0.5  $P/P_0$ , which is at the point where the surfactant pores begin to fill. Then C18-7-Co shows a close to linear rise in conductivity when the mesopores are being filled with water. This is followed by a rapid rise in conductivity as the filling of the surfactant templated mesopores is completed. On the other hand, C14-7-Co shows a “J” shaped curve, with the rise in conductivity occurring in a narrow range of water condensation once the surfactant pores are filled. These observations can not be ascribed to differences in the local concentration of cobalt nitrate. From Table 2.2 it can be seen that the

volume of the surfactant mesopores only changes over a factor of two, between the different types of surfactant templated mesopores.

It is simple to extrapolate the volume of condensate at each relative humidity data point, and therefore calculate the percentage of the total volume of water it takes to completely fill the surfactant pores. Figure 2.8 displays this relationship of pore filling and conductivity more clearly, illustrating that by relating the measured electrical conductivity to the percent surfactant templated mesopore filling, insight into the connectivity of the mesoporous network is gained. When considered on this percentage basis, the difference between the samples is even more striking. C14-7-Co did not exhibit any conductance until the templated mesopores were completely filled, while C18-7-Co gave measurable conductivity with merely 30% of the surfactant templated mesopores filled. Of course, 30% of a filled pore would not be expected to conduct ions unless there was in fact a highly connected pore system in which conductance could

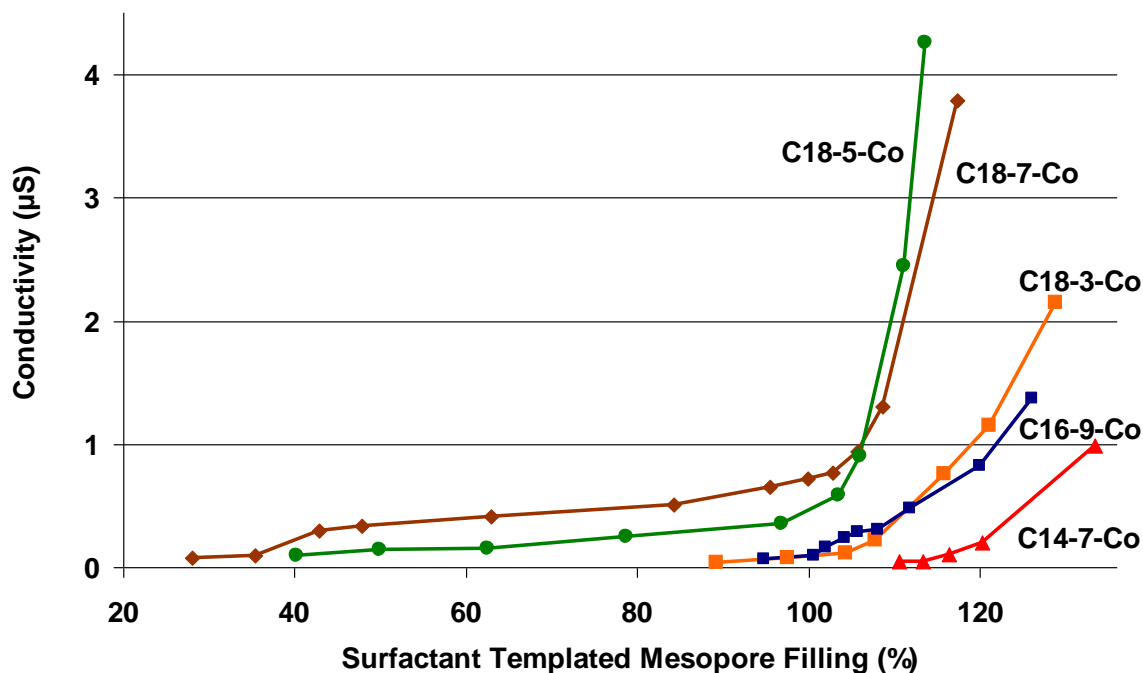


**Figure 2.8.** Electrical Conductivity of Monoliths as a Function of Percent Surfactant Templated Mesopore

occur after multilayer water formation took place. Very similar behavior is seen in C18-5-Co where initial conductance is seen at 40% pore filling. C16-9-Co and C18-3-Co are intermediate, with a late onset of conductivity and followed by a rapid rise after the surfactant mesopores are completely filled.

We interpret these observations as suggesting that in C14-7 monoliths the surfactant templated mesopores exist as mostly isolated pores or isolated sections of particle aggregates, which remain relatively isolated until the textural pores begin to fill, at which point the conductivity begins to rise rapidly. For C16-9, the surfactant mesopores must have some small degree of connectivity to produce the rising conductivity observed between 90 and 100% filled pores, but it is not until the textural mesopores begin to fill that the conductivity rises sharply. In C18-7, the surfactant mesopores do not seem to be isolated at all and C18-5 are isolated only at very low relative humidity. In C18-3 samples, the presence of fewer surfactant mesopores increases the probability that individual pores are isolated, resulting in conductance that is similar to that of C16-9 and C14-7. As conductivity rises with increasing humidity this likely reflects both a larger accessible volume available for conducting electricity, as well as steadily increasing connectivity. This again indicates that the C<sub>18</sub>TAB surfactant gives more connected pore networks, than do C<sub>16</sub>TAB and C<sub>14</sub>TAB.

The electrical conductivity in these monoliths displays classic percolation properties<sup>26</sup>; rising rapidly once a threshold relative humidity is reached. However, the question remains: what produces this threshold behavior and how does it relate to the actual structure of the monoliths? We believe that a start to answering this question can be seen in Figure 2.2a and 2.2b, which show SEM images of cross-sections of C14-7 and C18-7 monoliths. These monoliths form by agglomeration of mesoporous particles of approximately 20-50 nm in

diameter. Between these loosely packed particles, the textural mesopores appear. Collections of these agglomerated particles then combine to define the macropore walls. For the C14-7, it is clear from Figure 2.8 that the threshold for detectable electrical conductivity occurs once the surfactant mesopores are completely filled and the textural pores begin to fill. This is not the case for the other surfactant templated monoliths, where the threshold is significantly lower suggesting that there must be another mechanism for connecting those surfactant mesopores containing solution. Our hypothesis is that this mechanism might be direct connectivity between the surfactant mesopores network in adjoining particles. The longer surfactant chains do not simply produce larger pores; they also result in a higher driving force for self-assembly.<sup>27</sup> We would suggest that when two mesoporous silica particles encounter each other, if the particles contain C<sub>18</sub>TAB, there is a higher probability that elongated rod micelles will produce mesopores that span from one particle into the other. That is, the longer the hydrocarbon tail on a surfactant, the higher the likelihood of mesopores forming that extend from one particle to another, thereby producing a further connected mesopore system.

## **2.6 Conclusions**

Using electrical conductivity we have demonstrated that hierarchically porous monoliths templated with surfactants of differing chain length have significantly different electrical conductivity, which we postulate comes from differences in connectivity between mesopores. Monoliths without surfactant templated mesopores exhibit no electrical conductivity until the humidity is high enough for the textural mesopores to begin to fill. For C<sub>18</sub>TAB templated silica the mesopores form extensive networks, which fill at low relative humidity to provide a continuous path for electrical conductivity over macroscopic distances. In C<sub>16</sub>TAB templated monoliths the degree of interconnectivity between the mesopores is significantly lower than for

the C<sub>18</sub>TAB monoliths, but still sufficient to give measurable conductivity at moderate relative humidity. For silica monoliths templated with C<sub>14</sub>TAB surfactant, the degree of interconnectivity is too low for significant conductivity. It is only once the textural pores start to fill that conductivity can occur over macroscopic lengths.

We believe that we have demonstrated at least a portion of the potential insight into the connectivity in silica monoliths that can be gained by the application of electrical conductivity and control of relative humidity.

## **2.7 Acknowledgements**

The primary support of this work by National Science Foundation CHE-0719398 is gratefully acknowledged. This work used the Central Analytical Facility, which is supported by The University of Alabama. We would like to acknowledge Ms. Amy Grano for her work on the TEM. Additional support was provided through the Academy of Finland (project number 127919).

Supporting Information Available: Figures displaying nitrogen adsorption isotherms for 0.02 M Co(NO<sub>3</sub>)<sub>2</sub> impregnated monoliths (Figure 2.S1), NLDFT pore size distribution plots of native (Figure 2.S2) and 0.02 M Co(NO<sub>3</sub>)<sub>2</sub> impregnated monoliths (Figure 2.S3), mercury porosimetry data (Figure 2.S4), and electrical conductivity of monoliths impregnated with 2 M, 0.2 M, and 0.02 M Co(NO<sub>3</sub>)<sub>2</sub> (Figure 2.S5) are located in supporting information.

This work was completed with co-authors Professor Jan-Henrik Smått, Professor Mika Lindén, and Professor Martin Bakker.

## 2.8 References

- (1) Trewyn, B. G.; Slowing, I. I.; Giri, S.; Chen, H.-T.; Lin, V. S.-Y. *Acc. Chem. Res.* **2007**, *40*, 846-853.
- (2) Walcarius, A.; Kuhn, A. *Trends Anal. Chem.* **2008**, *27*, 593-603.
- (3) Leinweber, F. C.; Lubda, D.; Cabrera, K.; Tallarek, U. *Anal. Chem.* **2002**, *74*, 2470-2477.
- (4) Tanaka, N.; Kobayashi, H.; Ishizuka, N.; Minakuchi, H.; Nakanishi, K.; Hosoya, K.; Ikegami, T. *J. Chromatogr. A* **2002**, *965*, 35-49.
- (5) Nakanishi, K. *J. Porous Mat.* **1997**, *4*, 67-112.
- (6) Smått, J.-H.; Schunk, S. A.; Lindén, M. *Chem. Mater.* **2003**, *15*, 2354-2361.
- (7) Amatani, T.; Nakanishi, K.; Hirao, K.; Kodaira, T. *Chem. Mater.* **2005**, *17*, 2114-2119.
- (8) Brandhuber, D.; Torma, V.; Raab, C.; Peterlik, H.; Kulak, A.; Husing, N. *Chem. Mater.* **2005**, *17*, 4262-4271.
- (9) Friedrich, H.; Sietsma, J. R. A.; de Jongh, P. E.; Verkleij, A. J.; de Jong, K. P. *J. Am. Chem. Soc.* **2007**, *129*, 10249-10254.
- (10) Li, Z.; Kübel, C.; Parvulescu, V. I.; Richards, R. *ACS Nano* **2008**, *2*, 1205-1212.
- (11) Ward, E. P. W.; Yates, T. J. V.; Fernandez, J.-J.; Vaughan, D. E. W.; Midgley, P. A. *J. Phys. Chem. C* **2007**, *111*, 11501-11505.
- (12) Thomas, J. M.; Midgley, P. A.; Yates, T. J. V.; Barnard, J. S.; Raja, R.; Arslan, I.; Weyland, M. *Angew. Chem. Int. Ed.* **2004**, *43*, 6745-6747.
- (13) Dunn, D. N.; Shiflet, G. J.; Hull, R. *Rev. Sci. Instrum.* **2002**, *73*, 330-334.
- (14) Ryoo, R.; Ko, C. H.; Kruk, M.; Antochshuk, V.; Jaroniec, M. *J. Phys. Chem. B* **2000**, *104*, 11465-11471.
- (15) Kleitz, F.; Choi, S. H.; Ryoo, R. *Chem. Commun.* **2003**, 2136-2137.
- (16) Xiong, L.; Nogami, M. *Chem. Lett.* **2006**, *35*, 972-973.
- (17) Bearzotti, A. *J. Phys. D: Appl. Phys.* **2008**, *41*, 015105 (5 pp).
- (18) Innocenzi, P.; Falcaro, P.; Bertolo, J. M.; Bearzotti, A.; Amenitsch, H. *J. Non-Cryst. Solids* **2005**, *351*, 1980-1986.

- (19) Shin, H. J.; Ryoo, R.; Liu, Z.; Terasaki, O. *J. Am. Chem. Soc.* **2001**, *123*, 1246-1247.
- (20) Taguchi, A.; Smått, J.-H.; Lindén, M. *Adv. Mater.* **2003**, *15*, 1209-1211.
- (21) Gusev, V. Y. *Langmuir* **1994**, *10*, 235-240.
- (22) Lide, D. R. *CRC Handbook of Chemistry and Physics: A Ready-reference Book of Chemical and Physical Data*, 85 ed.; CRC Press: London, 2004.
- (23) Jiao, L.; Regalbuto, J. R. *J. Catal.* **2008**, *260*, 342-350.
- (24) Miller, J. T.; Schreier, M.; Kropf, A. J.; Regalbuto, J. R. *J. Catal.* **2004**, *225*, 203-212.
- (25) Lu, A.-H.; Smått, J.-H.; Backlund, S.; Lindén, M. *Micropor. Mesopor. Mater.* **2004**, *72*, 59-65.
- (26) Stauffer, D.; Aharony, A. *Introduction to Percolation Theory*, 2nd ed.; Taylor and Francis: Washington, D.C., 1992.
- (27) Mata, J.; Varade, D.; Bahadur, P. *Thermochim. Acta* **2004**, *428*, 147-155.

## 2.9 Supplemental Information

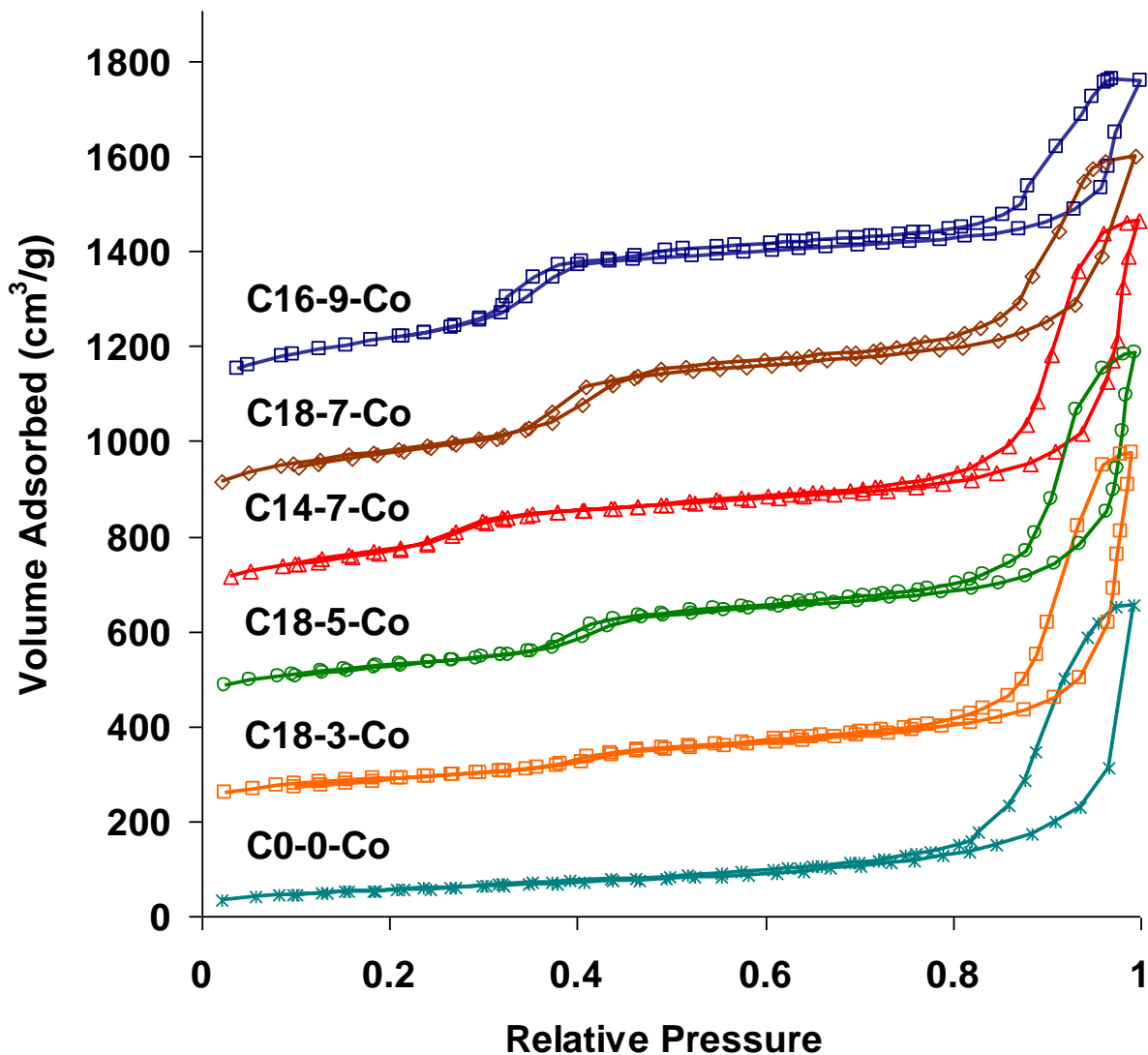


**Figure 2.S1.** Nitrogen Physisorption Isotherms of 0.02 M  $\text{Co}(\text{NO}_3)_2$  Impregnated Monoliths. C18-3-Co is offset by 200  $\text{cm}^3/\text{g}$ , C18-5-Co is offset by 400  $\text{cm}^3/\text{g}$ , C14-7-Co is offset by 600  $\text{cm}^3/\text{g}$ , C18-7-Co is offset by 800  $\text{cm}^3/\text{g}$ , and C16-9-Co is offset by 1000  $\text{cm}^3/\text{g}$  for clarity.

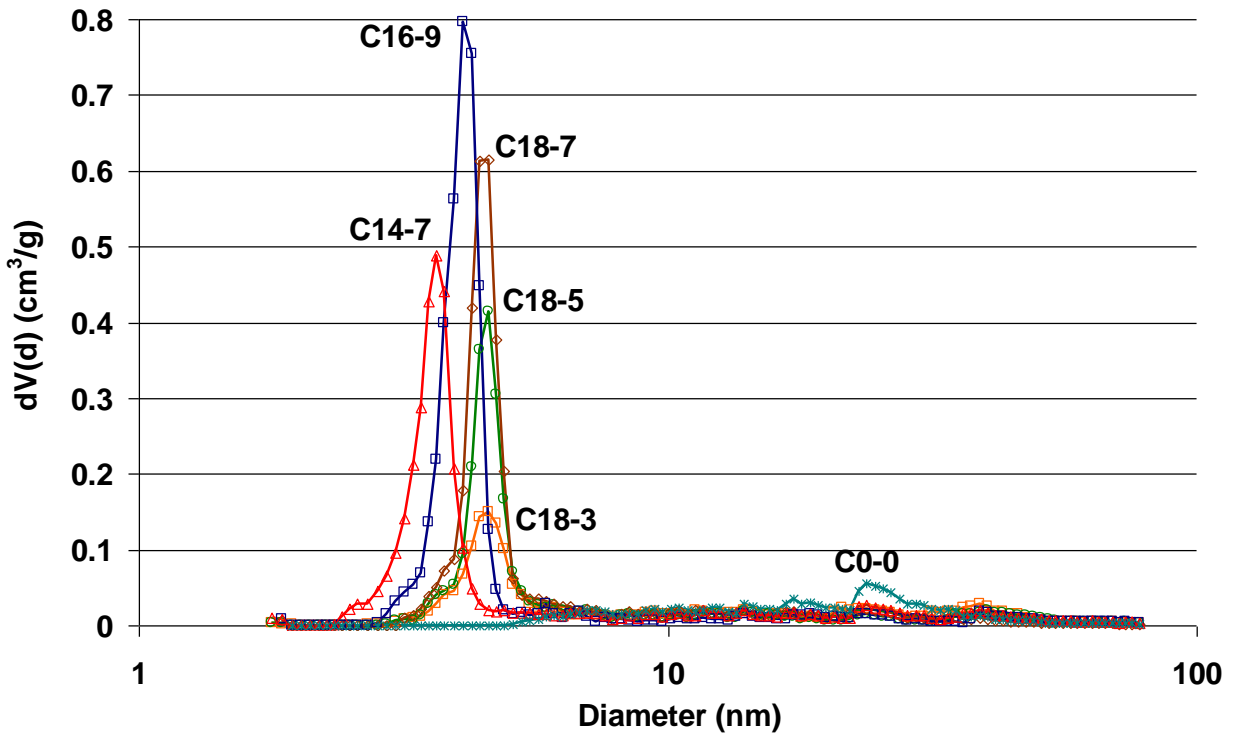


Figure 2.S2. NLDFT Pore Size Distribution Plot of Native Monoliths.

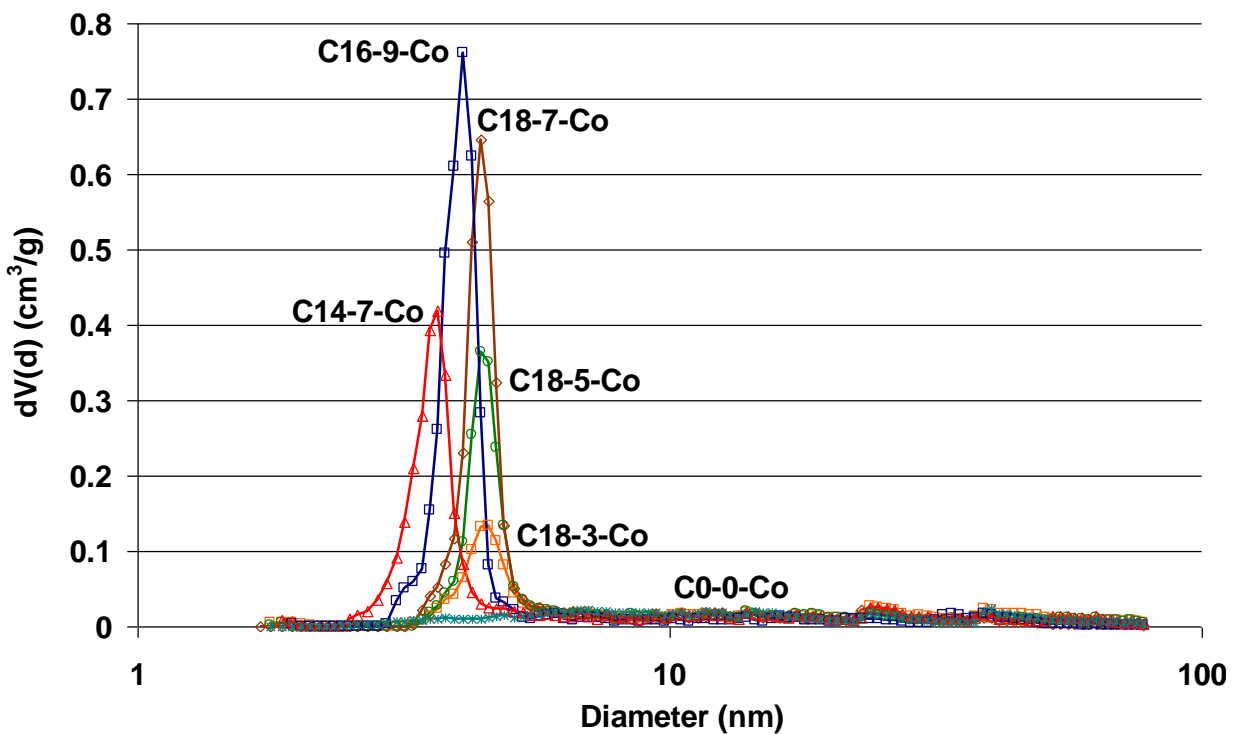


Figure 2.S3. NLDFT Pore Size Distribution Plot of 0.02 M  $\text{Co}(\text{NO}_3)_2$  Impregnated Monoliths.

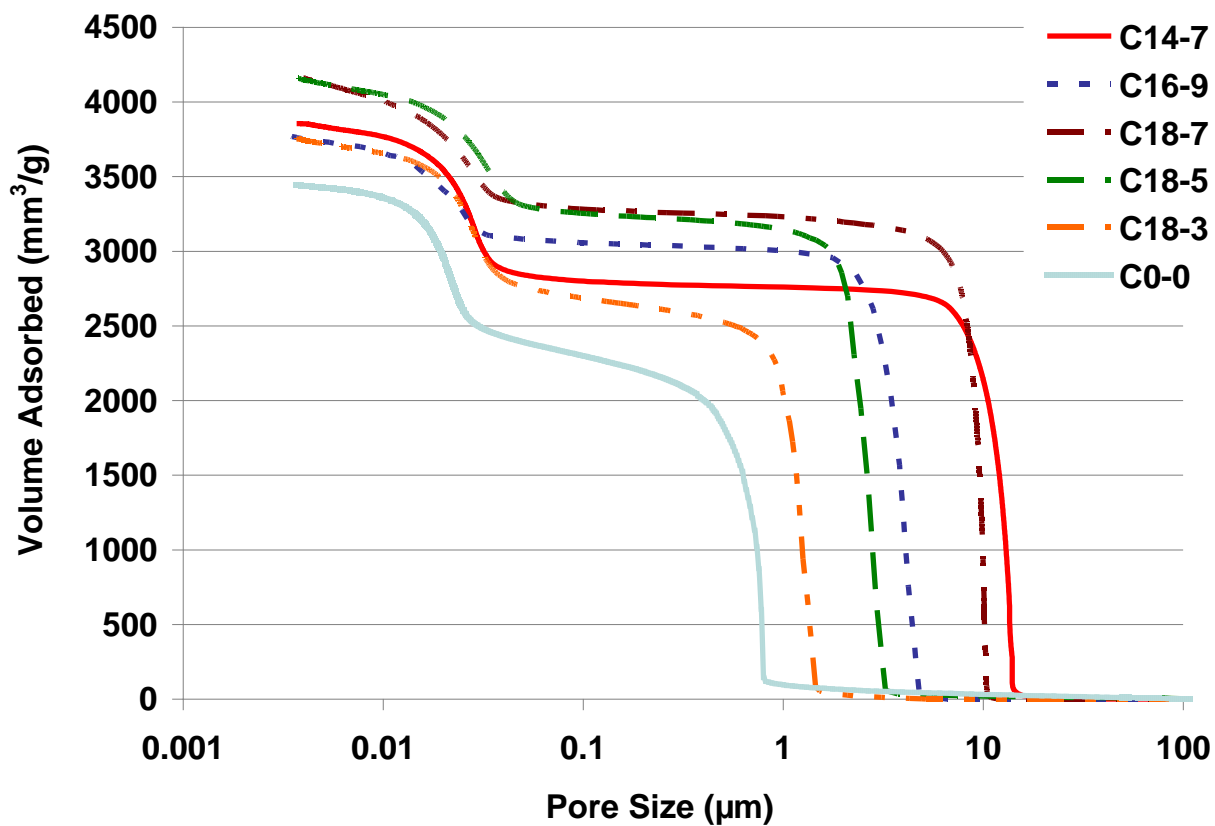
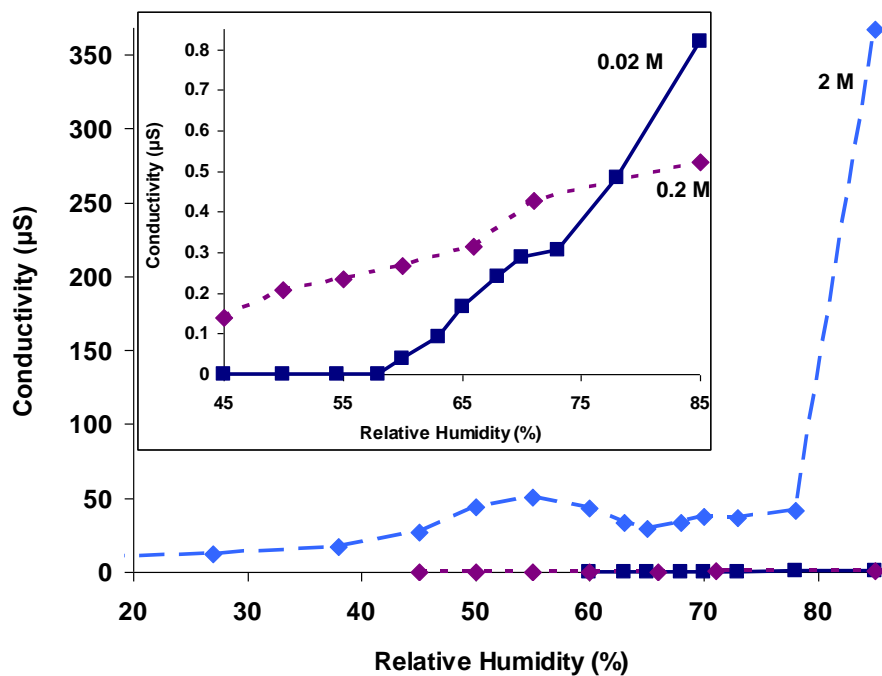


Figure 2.S4. Mercury Porosimetry Cumulative Pore Volume Plot (intrusion branch).



**Figure 2.S5.** Measured Electrical Conductivity with Increasing Relative Humidity on C16-9 Containing Varied Salt Concentrations. Note that sample containing 0.02 M  $\text{Co}(\text{NO}_3)_2$  was from a different batch than 0.2 M and 2 M.

## Chapter 3

### US Patent Application 13/405714: Methods for Preparing and Using Metal and/or Metal Oxide Porous Materials

#### 3.1 Abstract

Disclosed are methods for producing carbon, metal and/or metal oxide porous materials that have precisely controlled structures on the nanometer and micrometer scales. The methods involve the single or repeated infiltration of porous templates with metal salts at controlled temperatures, the controlled drying and decomposition of the metal salts under reducing conditions, and optionally the removal of the template. The carbon porous materials involve the infiltration of a carbon precursor into a porous template, followed by polymerization and pyrolysis. These porous materials have utility in separations, catalysis, among others.

#### 3.2 Field

The subject matter disclosed herein relates to methods for producing metal and/or metal oxide porous materials. Metal and/or metal oxide porous materials and methods of using them are also disclosed herein.

#### 3.3 Background

A number of methods have been advanced to produce controlled porosity on micrometer and millimeter length scales. Principal among these methods is the use of colloidal templating in which micrometer sized beads of silica or polymers such as polystyrene are used as template for sol-gel mixtures, primarily silica. The sol-gel mixture may or may not include a structure directing agent to give porosity on the nanometer scale. After the removal of the polymer and nanostructure directing agent by dissolution or combustion, a three dimensional replica is produced. These replicas have regular, highly

ordered micropore networks, are typically not mechanically very strong, and are difficult to produce in large bodies. The need for polymer or silica beads increases the cost of this synthesis and limits the range of structures available. The need for infiltration of the sol-gel precursor through the material also limits the applicability of this approach. The material formed by this approach has been used as a template for the formation of metal oxide and metals. Such materials have low surface areas.

Other methods for producing porous metal materials known as metal foams include bubbling gas through molten metal, generating gas during an exothermic reaction that melts the metal or that reduces and melts the metal, and generating gas during electrodeposition of the metal. Such processes generally produce large pore size distributions, are not compatible with the simultaneous formation of nanopores, are typically not very mechanically robust, and often have significant amounts of organic impurities. Other methods of making metal foams involve electrodeposition or metal condensation onto carbon skeletons. These approaches typically are not capable of generating small pore diameters and large bodies.

Other methods have been developed for producing porous metal oxide particles. Yue et al. disclose that metal nitrates can be introduced into mesoporous silica particles by grinding the metal nitrate and mesoporous silica particles in a crucible and then heating the material at a rate of 1 °C/min to 500 °C where the temperature is maintained for 5 hours.<sup>1</sup> Yue et al. teach that the metal nitrate melted and entered the pores of the silica. They disclose images of small (<150 nm) sized particles. Yue et al.'s disclosure demonstrates a limitation of that method for preparing larger bodies. For example, the grinding step reduces the size of the mesoporous silica particles limiting the size of replica particle that can be produced. The grinding step would result in the destruction of a larger body. The heating ramp used also constitutes a limit on the size of replica that can be achieved as it provides

insufficient time for transport of materials within the mesopores. As such, these methods have not been applied to larger porous bodies.<sup>1,2</sup>

Moreover, while the decomposition of metal nitrates has been much studied, the results have been contradictory. As the temperature of a nitrate melt is raised towards the decomposition temperature of the nitrate, water of hydration can be lost producing compounds that may either be a liquid or a solid and so may or may not be able to move within a mesopore. The loss of water is determined by the pressure of any ambient atmosphere and by the rate of transport of the water vapor through the mesopores. This can be illustrated by considering the nickel nitrate system which is among the most studied metal nitrates. Heating nickel nitrate is reported to go through a series of dehydration steps.<sup>3-7</sup> Various mechanisms of decomposition of the nickel nitrate to nickel oxides are reported.<sup>3,4,8,9</sup> Further, the products and the mechanism are both reported to depend upon the atmosphere under which the heating to decomposition takes place. Sun et al. teach that even the shape of the container in which an amount of porous silica particles containing a metal nitrate melt is heated can change the structure of the metal oxide formed within the porous silica particles.<sup>10</sup> Seitsma et al. teach that carrying out heating of nickel nitrate under different atmospheres can affect the extent of migration of the nickel oxide product from the mesopores in silica particles onto the exterior of the particle.<sup>8,9</sup> The effect of such variability in the decomposition and migration of metal nitrates has meant that these techniques have only been applied to particles, where the effects, though present, are more manageable and have less effect on the small scales seen with particle products. Such methods have not been applied for the preparation of larger porous materials.

Accordingly, there are no known methods for generating porous metal and/or metal oxide materials in which the spatial distribution of different metals and metal oxides within

one material can be controlled. The methods disclosed herein can produce metal and/or metal oxide porous materials (e.g. bodies) having precisely controlled microstructure and nanostructure that includes control over the spatial distribution of a number of metal and metal oxides within the same material. The disclosed porous materials can be used in a variety of applications and can also incorporate carbon or silica present in some templates.

### **3.4 Summary**

In accordance with the purposes of the disclosed materials, compounds, compositions, articles, devices, and methods, as embodied and broadly described herein, the disclosed subject matter, in one aspect, relates to methods for producing metal and/or metal oxide porous materials. Metal and/or metal oxide porous materials, with or without a template, are also disclosed, as are methods of using the disclosed materials.

Additional advantages of the subject matter described herein will be set forth in part in the description that follows, and in part will be obvious from the description, or can be learned by practice of the aspects described below. The advantages described below will be realized and attained by means of the elements and combinations particularly pointed out in the appended claims. It is to be understood that both the foregoing general description and the following detailed description are exemplary and explanatory only and are not restrictive.

### **3.5 Brief Description of the Figures**

The accompanying Figures, which are incorporated in and constitute a part of this specification, illustrate several aspects of the invention and together with the description serve to explain the principles of the invention.

Figure 3.1(a) is a cartoon of a porous material prepared by the methods disclosed herein. The porous material has a bimacroporous, “hollow” system in which two bicontinuous macroporous networks are separated by a 100-500 nanometer thick membrane

(the membrane can also be referred to as a “wall” of the macropore). This membrane can be mesoporous and/or microporous or can be continuous (i.e., without porosity). The membrane can be metal, metal oxide, silica, carbon, or other material (e.g. sulfides). If the membrane is porous then the porous material has utility as “hollow fiber” membranes also known as contactors. If the membrane is not porous but is, for example, all metal, it can have utility as a heat exchanger, or if, for example, it comprises various metal oxides, which are oxygen permeable (generally as oxide) it can be used as an oxygen filter membrane. Figure 3.1(b) is an empirical, schematic representation of a bicontinuous structure.

Figure 3.2 is a SEM image of macropores in cobalt metal monolith. Figure 3.3 is a SEM image of macropores in copper metal monolith. Figure 3.4 is a SEM image of macropores in sterling silver monolith. Figure 3.5 is a SEM image of macropores in nickel oxide monolith. Figure 3.6 is a SEM image of hollow fiber cobalt monolith with two separate macroporous networks. Figure 3.7 is a SEM image of macropores in nickel metal monolith. Figure 3.8 is a group of SEM and TEM images of cobalt oxide monolith macropores (5 micrometer scale bar image) and highly ordered mesopores (100 and 10 nm scale bar images).

### **3.6 Detailed Description**

The materials, compounds, compositions, articles, devices, and methods described herein may be understood more readily by reference to the following detailed description of specific aspects of the disclosed subject matter and the Examples and Figures included therein.

Before the present materials, compounds, compositions, and methods are disclosed and described, it is to be understood that the aspects described below are not limited to specific synthetic methods or specific reagents, as such may, of course, vary. It is also to be

understood that the terminology used herein is for the purpose of describing particular aspects only and is not intended to be limiting.

Also, throughout this specification, various publications are referenced. The disclosures of these publications in their entireties are hereby incorporated by reference into this application in order to more fully describe the state of the art to which the disclosed matter pertains. The references disclosed are also individually and specifically incorporated by reference herein for the material contained in them that is discussed in the sentence in which the reference is relied upon.

### **3.7 General Definitions**

In this specification and in the claims that follow, reference will be made to a number of terms, which shall be defined to have the following meanings:

Throughout the description and claims of this specification the word “comprise” and other forms of the word, such as “comprising” and “comprises,” means including but not limited to, and is not intended to exclude, for example, other additives, components, integers, or steps.

As used in the description and the appended claims, the singular forms “a,” “an,” and “the” include plural referents unless the context clearly dictates otherwise. Thus, for example, reference to “a metal salt” includes mixtures of two or more such metal salts, reference to “an agent” includes mixtures of two or more such agents, reference to “the porous material” includes mixtures of two or more such porous materials, and the like. “Optional” or “optionally” means that the subsequently described event or circumstance can or cannot occur, and that the description includes instances where the event or circumstance occurs and instances where it does not.

Ranges can be expressed herein as from “about” one particular value, and/or to

“about” another particular value. When such a range is expressed, another aspect includes from the one particular value and/or to the other particular value. Similarly, when values are expressed as approximations, by use of the antecedent “about,” it will be understood that the particular value forms another aspect. It will be further understood that the endpoints of each of the ranges are significant both in relation to the other endpoint, and independently of the other endpoint.

References in the specification and concluding claims to parts by weight of a particular element or component in a composition denotes the weight relationship between the element or component and any other elements or components in the composition or article for which a part by weight is expressed. Thus, in a compound containing 2 parts by weight of component X and 5 parts by weight component Y, X and Y are present at a weight ratio of 2:5, and are present in such ratio regardless of whether additional components are contained in the compound.

A weight percent (wt%) of a component, unless specifically stated to the contrary, is based on the total weight of the formulation or composition in which the component is included.

By “continuous” is meant a phase such that all points within the phase are directly connected, so that for any two points within a continuous phase there exists a path which connects the two points and does not leave the phase. A “phase” in this context can refer to a pore, void, or a metal or metal oxide layer. A “bicontinuous” material contains two separate continuous phases such that each phase is continuous, and in which the two phases are interpenetrating as shown schematically in Figure 3.1(b). It is impossible to separate the two structures without tearing one of the structures. Another example of a system with this property is the gyroid phase of block copolymers.<sup>11</sup>

By “tortuous” is meant when phases have only short straight line distances so that moving within the phase requires continuing changes in direction.

By “hollow” is meant when two continuous (void) network phases completely separated by a third continuous phase that prevents any direct contact between the two continuous void network phases. In a large body, material cannot travel from one continuous void phase to the other continuous void phase without passing through the third continuous separating phase.

By “hierarchical pores” and other forms of the phrase like “hierarchically porous material” is meant having pores that span a number of different length scales. As used herein materials with hierarchal pores have pores that span two or more length scales. Typically, there will be a distribution of pore diameters at each length scale, where often the distribution of pore diameters are sufficiently narrow that there is little or no overlap between the pore size distributions; there are some pore sizes for which few or no pores are present in such a hierarchically porous material.

By “constant diameter” is meant when the smallest distance across a continuous phase is constant, i.e., less than one standard deviation.

By the word "body" is meant a macroscopic, single piece of solid material typically with dimensions (length, width, and/or height) exceeding about 1 mm. A body is distinguished from a particle, where the dimensions of the material are typically much less than that for a body.

By “partial infiltration” is meant that the metal salt or carbon precursor infiltrates and contacts less than all of the volume of the porous template. Generally, partial infiltration is when from about 10 to about 90, from about 25 to about 75, or about 50% of the template is filled with the metal salt or carbon precursor.

Also, disclosed herein are materials, compounds, compositions, and components that can be used for, can be used in conjunction with, can be used in preparation for, or are products of the disclosed methods and compositions. These and other materials are disclosed herein, and it is understood that when combinations, subsets, interactions, groups, etc. of these materials are disclosed that while specific reference of each various individual and collective combinations and permutation of these compounds may not be explicitly disclosed, each is specifically contemplated and described herein. For example, if a composition is disclosed and a number of modifications that can be made to a number of components of the composition are discussed, each and every combination and permutation that are possible are specifically contemplated unless specifically indicated to the contrary. Thus, if a class of components A, B, and C are disclosed as well as a class of components D, E, and F and an example of a composition A-D is disclosed, then even if each is not individually recited, each is individually and collectively contemplated. Thus, in this example, each of the combinations A-E, A-F, B-D, B-E, B-F, C-D, C-E, and C-F are specifically contemplated and should be considered disclosed from disclosure of A, B, and C; D, E, and F; and the example combination A-D. Likewise, any subset or combination of these is also specifically contemplated and disclosed. Thus, for example, the sub-group of A-E, B-F, and C-E are specifically contemplated and should be considered disclosed from disclosure of A, B, and C; D, E, and F; and the example combination A-D. This concept applies to all aspects of this disclosure including, but not limited to, steps in methods of making and using the disclosed compositions. Thus, if there are a variety of additional steps that can be performed it is understood that each of these additional steps can be performed with any specific aspect or combination of aspects of the disclosed methods, and that each such combination is specifically contemplated and should be considered disclosed.

Reference will now be made in detail to specific aspects of the disclosed materials, compounds, compositions, articles, and methods, examples of which are illustrated in the accompanying Examples and Figures.

### **3.8 Methods**

The methods disclosed herein relate, in certain aspects, to the production of metal and/or metal oxide porous materials (e.g. bodies) by a single or repeated introduction of one or more metal salts into a porous template, and controlled thermal decomposition of the metal salt under reducing conditions or to convert the metal salt to metal. In another aspect, disclosed herein are methods for the production of metal and/or metal oxide porous materials by a single or repeated introduction of one or more metal salts into a porous template, and controlled heating of a metal nitrate under in an inert or oxidizing atmosphere, followed by thermal decomposition or reduction to convert the metal salt or metal oxide, respectively, to metal. These methods can also be used to produce metal and/or metal oxide nanowires. Generally, the disclosed methods comprise combining a composition comprising a metal salt (e.g. a neat metal salt, metal salt hydrate, metal salt solution, or melt) with a porous template to form a mixture; maintaining the mixture at below the decomposition temperature of the metal salt until a desired spatial distribution of the metal salt in the template is obtained; and then heating the mixture to above the decomposition temperature of the metal salt in the presence of a reducing agent or inert atmosphere to produce the metal and/or metal oxide porous material. These steps can optionally, be repeated with the same metal salt (e.g. a neat metal salt, metal salt hydrate, metal salt solution, or melt) or with a different metal salt. These steps can also, optionally, be followed by removal of the template.

Alternatively, disclosed herein is a method that comprises combining a composition comprising a metal nitrate (e.g. a neat metal nitrate, metal nitrate hydrate, or metal nitrate

solution) with a porous template to form a mixture; maintaining the mixture at below the decomposition temperature of the metal nitrate until a desired spatial distribution of the metal nitrate in the template is obtained; and then heating the mixture to above the decomposition temperature of the metal nitrate in the presence of a reducing agent, inert atmosphere, or oxidizing atmosphere to produce the metal or metal oxide porous material. If the metal oxide is prepared the porous material the oxide can be reduced to prepare a metal porous material.

The disclosed methods involve the infiltration of metal salts as described herein into a suitable porous template to form a mixture. This occurs by contacting a composition comprising the metal salt with the porous template. The metal salt can be used in solution, hydrate or solvate form, or neat. When using a metal salt hydrate, solvate or neat salt, infiltration can be accomplished by contacting the porous template with the metal salt at above the salt's melt temperature, though below the salt's decomposition temperature. Alternatively, the metal salt can be part of a solution, i.e., the composition can comprise the metal salt and a solvent. For convenience, reference to the "metal salt" means either a neat metal salt, metal salt hydrate, metal salt solvate, or a metal salt solution, unless the context clearly refers to one or the other. Contacting the metal salt with the porous template can be performed by, for example, adding the porous template to the metal salt or by adding the metal salt solution to the porous template. Contacting can also be performed by slowly mixing one component with the other or by drop-wise addition of one component into the other. Agitation (e.g. stirring, shaking, or ultrasonic agitation) can be used to facilitate the contacting of the metal salt with the porous template.

The metal salts that are suitable for use in the disclosed methods can comprise one or more transition metals, alkaline metals, alkaline earth metals, or lanthanide metals. For example, a suitable metal salt can comprise a metal selected from the group consisting of Li,

Be, Na, Mg, Al, K, Ca, Sc, Ti, V, Cr, Mn, Fe, Co, Ni, Cu, Zn, Ga, Rb, Sr, Y, Zr, Nb, Mo, Tc, Ru, Rh, Pd, Ag, Cd, In, Sn, Sb, Cs, Ba, La, Ce, Pr, Nd, Pm, Sm, Eu, Gd, Tb, Dy, Ho, Er, Tm, Yb, Lu, Hf, Ta, W, Re, Os, Ir, Pt, Au, Tl, Pb, and Bi. The counterion of the metal salt can be a nitrate, acetate, sulfate, or chloride. Other suitable counterions can be organic or inorganic ions such as carbonate, nitrile, bromide, iodide, phosphate, sulfite, phosphite, nitrite, and the like. Some particularly preferred metal salts are transition metal, alkaline metal, alkaline earth metal, or lanthanide metal nitrate, acetate, sulfate, or chloride.

Metal salts suitable for use herein can be readily obtained from commercial suppliers or synthesized by methods known in the art. Similarly metal salt hydrates and metal salt solutions can be prepared by methods known in the art or obtained from commercial sources. Metal salts for use herein have a decomposition temperature and a melting temperature. When using a composition comprising the metal salt hydrate, solvate, or neat metal salt the composition is heated above the melt temperature of the metal salt, but below the decomposition temperature of the metal salt. When using a composition comprising a metal salt and a solvent, the solvent can be any suitable solvent that dissolves the particular metal salt being used. In certain aspects, water is used as the solvent. Other aqueous solvents can be used, such as water/organic solvent mixtures. Suitable water/organic solvent mixtures contain water and an organic solvent that is at least partially miscible with water. For example, as aqueous alcohols, aqueous polyols, aqueous carboxylic acids, aqueous esters, aqueous aldehydes, aqueous ketones, and the like can be used. In other examples, carboxylic acids, alcohols, polyols, ketones, or aldehydes can be used and are advantageous solvents because they can also act as the reducing agent. The use of aqueous metal salt solutions is particularly advantageous as aqueous solutions effectively wet certain porous templates (e.g. silica templates), producing good penetration of the metal salt solution into the porous

template. When a solution of a metal salt is used, the weight or molar ratio of metal salt to solvent can be from about 1:10 to about 10:1. For example, the weight ratio of metal salt to solution can be from about 1:10, 2:10, 3:10, 4:10, 5:10, 6:10, 7:10, 8:10, 9:10, 10:9, 10:8, 10:7, 10:6, 10:5, 10:4, 10:3, 10:2, 10:1, or 1:1. In other examples, the molar ratio of metal salt to solution can be from about 1:10, 2:10, 3:10, 4:10, 5:10, 6:10, 7:10, 8:10, 9:10, 10:9, 10:8, 10:7, 10:6, 10:5, 10:4, 10:3, 10:2, 10:1, or 1:1. A neat metal salt can be used as well, i.e., where there is no solvent. Further, metal salt hydrates and solvates can also be used. Such hydrates or solvates typically contain from 1 to 10 water or solvent molecules per metal center.

In a preferred aspect, a composition comprising an aqueous metal nitrate or metal nitrate hydrate is used. The use of the metal nitrate salts can be advantageous since such salts have high solubility in water. As metal nitrate hydrates, many metal nitrates also have a liquid range that allows for continued movement of the salt, improving the fidelity of the replication of the porous template, and increasing the surface area of the final product.

In preferred aspects, the composition comprising the metal salt is not a sol-gel or a metal foam.

The porous template can be a monolithic body. When the decomposition is under reducing conditions, the template can also be a particular template. The form and shape of the porous template used, as well as the amount and degree of infiltration of the metal salt into the porous template, affect the final form of the metal and/or metal oxide porous material. When using a monolithic form of porous template, the resulting metal and/or metal oxide porous material can be a bicontinuous monolithic body.

Suitable porous templates can be obtained commercially or can be prepared according to methods described in the art. For example, a number of groups have used colloidal crystal

templating or self-assembly of polymer or silica beads to give a relatively hard template into which the metal salts disclosed herein can be infiltrated to create the disclosed metal and/or metal oxide porous material.<sup>12,13</sup> Infiltration of a sol-gel precursor including a surfactant as template can be used to induce ordered mesopores in the macropore walls of these materials.<sup>14</sup> The major drawback of this approach is the expense of the polymeric beads for macroscopic pieces. A number of other methods of producing suitable porous templates have been developed using microemulsions,<sup>15</sup> bicontinuous polymer foams,<sup>16</sup> salt crystals,<sup>17</sup> bacteria,<sup>18</sup> cellulose,<sup>19, 20</sup> sugars,<sup>21</sup> or ice<sup>22</sup> as templates for macrostructure, and foaming of the sol-gel silica.<sup>23</sup> Each of these articles is incorporated herein by reference for their teaching of processes for producing porous templates.

Suitable porous templates for use herein can comprise silica, carbon, metal, or metal oxide. In other examples, the porous template comprises a combination or composite of one or more of silica, carbon, metal, or metal oxide. In a preferred aspect, the porous template is a mesoporous and/or microporous silica. The use of a silica template is particularly advantageous since porous silica templates of controlled structure on the micrometer and nanometer scales are readily available.

A particularly suitable porous templates are hierarchically porous silica monoliths as prepared by the methods of Nakanishi et al.<sup>12</sup> and Småt et al.<sup>24</sup> which are incorporated by reference herein for their teaching of templates and their method of preparation and use.

When using a metal salt solution with the porous template, a portion of the solvent can be removed. This is done to concentrate the metal salt solution, thus forming a concentrated mixture of the metal salt solution and porous template. All of the solvent should not be removed, however, as enough solvent should remain in the concentrated mixture for maintaining the metal salt solution as a liquid.

The mixture of the composition comprising a metal salt and the porous template can be maintained at below the decomposition temperature of the metal salt (and in the case of a metal salt hydrate, solvate or neat salt above the melt temperature of the metal salt) for a sufficient period of time to allow the infiltration of the metal salt into the porous template to proceed to the desired degree of distribution. The melt temperature and the decomposition temperature of a metal salt is a value that can readily be determined based on the particular metal salt used. By controlling the temperature the degree of infiltration can be controlled.

Rapid heating ramps should be avoided in that the metal salt can decompose prematurely, before it has infiltrated the template to the desired degree. The pressure of the system can also be controlled, as well as the equilibration time, to control the degree of penetration of the metal salts into the porous template. Thus by controlling the pressure and time, one can only partially replicate the porous template or fully replicate the porous template, whichever is desired. Partial replication of the porous template can produce a second set of voids on a micrometer length scale.

The use of vacuum (e.g. from at or below about 1 Torr) to remove all air from the template and dissolved gases from the metal salt solution can produce an even spatial distribution of the metal salt and, consequently, metal and/or metal oxides in the porous template, because it prevents blockage of meso and micropores by air or dissolved gas. For example, the pressure can be at or below about 1 Torr, 0.1 Torr,  $10^{-2}$  Torr,  $10^{-3}$  Torr,  $10^{-4}$  Torr,  $10^{-5}$  Torr, or  $10^{-6}$  Torr, where any of the stated values can form an upper or lower endpoint of a range. The use of reduced pressure therefore allows the metal salt to completely infiltrate the meso and/or micropores of the porous template. Increasing the time of contact and reducing the temperature during contact can also be used to achieve complete infiltration of the metal salt into the porous template.

When a vacuum is not applied at this step, or when pressure is increased, one can produce a metal and/or metal oxide porous material with a “hollow core” structure. A hollow core structure is when the mesoporous and/or microporous membrane of a porous template is only partially infiltrated by the metal salt. Thus, infiltration of the metal salt occurs into only surface mesopores. In other words, when walls of the macropores themselves contain mesopores and/or macropores, infiltration of the metal salt can be controlled with weaker vacuum or increased pressure so that the metal salt does not go completely through the meso and/or micropore. This results in spaces along the mesopores and/or micropores with no metal and/or metal oxide. Partial infiltration to produce a hollow core structure can also be achieved by shortening the time of contact between the metal salt and the porous template or by increasing the temperature during contact. Such partial replication of only a portion of the porous template can be used to produce useful and unique structures.

Once the desired spatial distribution of the metal salt in the porous template is attained, the mixture of the metal salt and porous template can then be heated to above the decomposition temperature of the metal salt under appropriate reducing conditions to convert the metal salt to a metal or metal oxide. Heating under reducing conditions can involve heating the mixture in the presence of a reducing agent. The reducing agent can be added to the mixture by any method known in the art or described herein. Suitable reducing agents can be hydrogen gas or alcohols, e.g. methanol, ethanol, and ethylene glycol, carboxylic acids (e.g. acetic acid), aldehydes, hydrazine, hydrides, ketones, boranes, and the like.

Decomposition should be carried out at the lowest temperature possible to prevent migration of the metal or metal oxide from nanometer sized pores into larger pores.

Carrying out the decomposition under an atmosphere of hydrogen can convert the metal salt into metal. The presence of the hydrogen can assist in decreasing the mobility of

the metal oxide and metal oxynitride intermediates produced in the reaction. This can improve the fidelity of the replication and increases the surface area of the final product. The use of reductants allows the decomposition of the metal salt to be carried out at lower temperature, improving the fidelity of replication and alleviating the use of hydrogen gas which in some cases can represent a safety concern. The resulting porous material can be cooled after the decomposition step under nitrogen, and then stored under nitrogen or degassed water or similar solvent. This can prevent reaction with oxygen to form the oxide. The decomposition step can also be conducted under inert or oxidizing atmosphere. An inert atmosphere can be helium or argon. An oxidizing atmosphere can be synthesis gas or CO<sub>2</sub>. This can produce a metal porous material or metal oxide porous material, respectively. Metal oxide porous materials can be reduced to metal porous materials by addition of a suitable reducing agent. The reducing agent can be added to the mixture by any method known in the art or described herein. Suitable reducing agents can be hydrogen gas or alcohols, e.g. methanol, ethanol, and ethylene glycol, carboxylic acids (e.g. acetic acid), aldehydes, hydrazine, hydrides, ketones, boranes, and the like.

The steps of the disclosed methods can optionally be repeated one or more times in order to control the nature of the microstructure and nanostructure of the porous material. This allows the production of mechanically robust metal and/or metal oxide porous materials with high surface area. The material can be kept under a chemically inert atmosphere or degassed solvent between steps or, alternatively, the material can be kept under air between steps.

In certain aspects, one or more of the steps disclosed herein can be performed under inert atmosphere, under air, at reduced pressure, at atmospheric pressure, or at about atmospheric pressure. Also, different metal salts can be used at each repetition cycle to

produce different distributions of different metals and/or metal oxides in the final material.

Also, when the desired degree of replication is achieved the template can optionally be removed.

As another additional and optional step, the disclosed methods can include adding an additional metal to the metal and/or metal oxide porous materials by electrodeposition, electroless deposition, or by displacement deposition.

The disclosed methods involving metal salt infiltration into a porous template, thermal decomposition of the metal salt under reducing condition, and removal of the template, can result in metal and/or metal oxide porous materials (e.g. porous particles or porous body). The disclosed methods can, with high fidelity, replicate the porous template's structure with metal and/or metal oxide. The resulting metal and/or metal oxide porous material is thus a high surface area metal and/or metal oxide composition.

Similar procedures to those disclosed herein for making metal and/or metal oxide porous materials can be used to produce porous carbon materials with similar structures and useful properties. There are a number of procedures known in the art for introducing carbon precursors into mesoporous silica templates and hierarchically porous silica templates, which are incorporated herein for their teaching of carbon precursors, silica templates, and methods of using thereof.<sup>25-28</sup> In general they involve infiltration of a carbon precursor such as a polymer precursor, where polymerization is thermally initiated. Subsequent pyrolysis under an inert atmosphere converts the polymer into carbon. The resultant replica can be produced in one infiltration cycle and has very significant microporosity. The electrical conductivity of the replica is dependent upon the temperature, with temperatures of 800-1000 °C being necessary to produce highly conducting carbon. These methods do not produce the hollow hierarchically porous structures as are disclosed herein. Such hierarchically porous carbon

structures are produced by the methods disclosed herein and involve increasing the viscosity of the infiltrating carbon precursor solution, and by increasing the rate at which the polymerization of the carbon precursor occurs.

Disclosed herein is a method for producing a hollow, carbon porous material that comprises contacting a porous template, such as those disclosed herein, in particular a hierarchical porous template, and a polymerizable carbon precursor to form a mixture. This contacting step is performed such that the precursor does not infiltrate through the entire template and is referred to herein as partial infiltration. Then the mixture is heated to polymerize the precursor. Further heating is then performed to pyrolyze the polymerized precursor, thereby producing a carbon porous material. These steps can be repeated with the same carbon precursor or with a different precursor. The disclosed process can be used to prepare hollow carbon porous materials.

In these methods, particular infiltration can be accomplished by varying the time of contact, rate of polymerization, and viscosity of the precursor. The carbon precursor can be of increased viscosity so that it does not penetrate as far or as quickly as a low viscosity precursor. Specifying the exact viscosity of the carbon precursor is not possible since the desirable viscosity will depend on the size and type of template, the type of carbon precursor (which affects the rate of polymerization), the time the precursor is contacted with the template, and the desired level of infiltration. More viscous precursors allowed to contact the template for a longer period of time can produce similar structures as a less viscous precursor allowed to contact the template for a shorter period of time. Thus, the practitioner can determine a sufficient viscosity for a given precursor by simple experimentation, raising or lowering the viscosity or time of contact with the template as needed to obtain the desired level of infiltration. If more viscous precursors are needed, additives such as sugars,

alcohols, glycols, and alkanes can be added. Other suitable methods for increasing the viscosity include allowing the carbon precursor to undergo some polymerization prior to introduction to the hierarchically porous silica template.

Further, the rate of polymerization of the precursor can be varied to provide a desired level of infiltration. More rapid polymerization means that the polymerizable carbon precursor would not infiltrate as far as a slower polymerization rate. Suitable methods for increasing the rate of the polymerization of the precursor prior to introduction to the porous template include, but are not limited to addition of crosslinking agents or polymerization initiators.

The carbon precursor can be for example, furfuryl alcohol, poly(furfuryl alcohol), formaldehyde, resorcinol, phenol, 1,2,3-trihydroxybenzene, 1,5-dihydroxynaphthalene, polyvinyl chloride-acrylate terpolymer, phenol resin, acrylonitrile-methyl methacrylate copolymer, polyimide, polypyrrolone, polyaromatic resin, polydivinylbenzene, sucrose, or mixtures thereof. Further examples of suitable carbon precursors are disclosed in Lu et al., which is incorporated by reference herein for its teachings of carbon precursors, templates and nanocasting techniques.<sup>29</sup>

The use of silica templates, for the metal, metal oxide, or carbon based methods disclosed herein, allows for the use of well-defined chemistry to remove the template. For example, the porous material can be immersed in concentrated aqueous hydroxide solution at from about 25 °C to about 110 °C. For example, the material can be immersed for a period of about 4 to about 12 hours in 1-3 M aqueous sodium or potassium hydroxide solution. Alternatively, the material can be immersed in hydrofluoric acid. For metals such as copper and metal oxides such as zinc oxide, which are dissolved or corroded by exposure to aqueous hydroxide or hydrofluoric acid, the metal and/or metal oxide porous material can be

immersed in a solution of basic alcohol such as a solution of sodium hydroxide or potassium hydroxide in dry methyl alcohol or ethyl alcohol in order to remove a silica template. In one example with copper, the corrosion of copper by aqueous potassium hydroxide solutions can be prevented by applying a small (0.3-3.0 Volt) anodic potential to the copper during the dissolution of the silica. However, the use of alcoholic base as described herein is more convenient and bypasses difficulties with contacting the copper.

### **3.9 Compositions**

The metal and/or metal oxide porous materials produced according to the methods disclosed herein are porous. Similarly the carbon materials produced according to the methods disclosed herein are porous. The term “porous” as used herein means a material having a plurality of pores, holes, and/or channels, each of which may or may not extend throughout the entire length of the material. However, the pores can interconnect, resulting in a network of pores or voids that spans the material, permitting the flow of liquid or gas into and through the material, i.e. a continuous phase of pores or voids.

The disclosed materials can have two or more continuous phases, e.g. a bicontinuous structure. By “bicontinuous” is meant that both the voids/pores phase and the metal, metal oxide or carbon phase are continuous throughout the material. In other words, for a metal the metal surface is continuous and the materials can thus be electrically conductive. Similarly, the voids or pores are continuous so that a fluid (gas or liquid) can pass through the porous material. Bicontinuous can also refer to different porous networks, e.g. two or more continuous pore/void phases. This occurs when there are, for example, a macroporous network and a mesoporous network, both of which are continuous. Thus the disclosed materials can be bicontinuous by reference to the various pores or void phases that are continuous.

The disclosed materials can also be hollow in that two continuous void phases are completely separated by a third continuous phase that prevents any direct contact between the two continuous phases. To illustrate this characteristic, the disclosed materials can have a continuous phase made up of a non-porous oxygen conducting ceramic where air would enter through one continuous void network, the oxygen would pass through the ceramic and exit through the other continuous void network, and would leave behind the other components of air. A second illustrative example is when the third continuous, separating phase, was itself porous on a much smaller scale, such that only ions or molecules less than a given size could penetrate the third continuous separating phase. A solution containing a mixture of ions or molecules of various sizes could then enter through one continuous void phase, the selected ions or molecules could travel through the third separating geometry and exit through the second continuous void phase. Such geometries can therefore serve as filters.

When the disclosed materials have a hollow geometry they can be even-walled. By “even-walled” is meant where a third continuous phase separates two continuous void phases and the shortest distance between one continuous void phase and the other continuous void phase is constant. Equivalently, if the thickness of the third continuous separating phase is constant this material can be referred to as "even-walled". For filters and similar devices the property "even-walled" can be advantageous because it affects how fast material is transported across the third continuous phase, and it also impacts the pressure drop across this phase as material is transported through the phase. Materials with large variations in wall thickness, i.e., those which are not "even-walled," can have significant differences in the rate at which materials transport through the third continuous phase at different positions, this can lead to decreased selectivity in filter applications.

The disclosed materials can also be said to have hierarchical pores. As noted above, a

material with hierarchical pores has pores that span two or more length scales. For example, the material can have both macropores and mesopores, both macropores and micropores, both mesopores and micropores, or macropores, mesopores and micropores.

Thus, in certain examples, the materials disclosed herein can have a macroporous system. This means the porous material has a plurality of pores, holes, and/or channels greater than about 0.1  $\mu\text{m}$  in diameter, i.e., macropores. For example, the macropores can have a diameter of from about 0.5  $\mu\text{m}$  to about 30  $\mu\text{m}$ , from about 1  $\mu\text{m}$  to about 20  $\mu\text{m}$ , from about 5  $\mu\text{m}$  to about 15  $\mu\text{m}$ , from about 10  $\mu\text{m}$  to about 30  $\mu\text{m}$ , or from about 0.5  $\mu\text{m}$  to about 15  $\mu\text{m}$  in diameter.

The walls of the macropores (also termed the “membrane”) can be from about 50 nm to about 15  $\mu\text{m}$ , for example, from about 50 nm to about 600 nm, 100 nm to about 500 nm, from about 200 to about 400 nm, from about 50 to about 200, from about 300 to about 600 nm, from about 500 nm to about 5  $\mu\text{m}$ , from about 5  $\mu\text{m}$  to about 10  $\mu\text{m}$ , or from about 5  $\mu\text{m}$  to about 15  $\mu\text{m}$  thick. In one aspect, the walls of the macropores are continuous, i.e., without porosity. In another aspect, the walls of the macropores are themselves porous.

These pores, holes, and/or channels within the macropore walls can be from about 2 nm to about 30 nm, from about 10 nm to about 20 nm, from about 15 nm to about 50 nm, or from about 2 nm to about 15 nm in diameter, i.e., mesopores. Still further, the walls of the macropores can contain pores, holes, and/or channels that are less than about 2 nm, i.e., micropores. In a preferred aspect, the porous materials disclosed herein have macropores as well as meso and/or micropores, which exist in the membrane or macropore wall. This presence of pores of more than one length scale in one material is characterized as a hierarchical pore structure. In one aspect, the macropores lying within the membrane are themselves continuous. Such materials are hollow, hierarchically porous structures. In this

aspect the macroporous phase lying within the membrane is completely separated from the macroporous phase lying outside the membrane. A cartoon showing a porous material as disclosed herein with both macropores and meso and/or micropores is shown in Figure 3.1(a).

The structure of these hollow hierarchically porous bodies is such that the material is tortuous and contains three interpenetrating phases. All three phases are continuous. In certain aspects, two phases are voids and the third is solid and separates the two void phases such that any continuous path that joins any point in one void region to any point in the other void region must pass through the third region. This geometry therefore functions as a filter or membrane.

Notably, this geometry is distinct from other porous materials and hierarchically porous materials. This is shown by comparing the disclosed materials to other types of porous materials: Three dimensionally ordered materials (also known as 3-DOM, or colloid crystal templated materials) contain only two continuous phases, one solid the other void.

Therefore, these structures are not hollow as that term is defined herein. These phases are tortuous and interpenetrating. But the absence of a third, continuous, separate void region means that these materials do not have the same features as the disclosed hollow hierarchically porous materials, which can be prepared by the methods disclosed herein. 3-DOM structures have distinctly different properties than the materials disclosed herein. The largest and smallest diameters of the void phase in 3-DOM materials are generally significantly different. As such, the disclosed materials can, in contrast to 3-DOM materials, have more than two continuous regions and narrow pore diameter distribution (e.g. less than 1 standard deviation in diameter).

Aerogels, ambigels, and xerogels are classes of materials prepared by sol-gel chemistry with removal of the solvent in different manners. The structure of these materials

typically contains an agglomeration of small particles. The distribution of pore sizes is typically broad with pores as small as 2-5 nm to as large as 400-4000 nm. The materials have no order, and they may not be completely or even largely bicontinuous. These materials also do not have the property of being hollow. The materials disclosed herein are not aerogels, ambigels, and xerogels because, unlike those structures, they are bicontinuous, hollow and have a narrow distribution of pore sizes.

Foams are typically of two forms. In closed-cell foams the regions of one material are completely enclosed within a continuous region of a second material. While open-cell foam can be bicontinuous, the void network is disordered and the diameters of the void network show a large range, with large spherical voids separated from each other by small windows. The materials disclosed herein are not foams.

The disclosed materials can, in certain examples, be described as tortuous, interpenetrating, and not hollow. Generally they have a smaller range of void network diameters than 3-DOM, foams, or aerogel materials, and have a narrower range of smallest dimensions across the solid material.

The disclosed porous materials can comprise one or more metals, metal oxides, or a combination thereof, wherein the metals are selected from the group consisting of Li, Be, Na, Mg, Al, K, Ca, Sc, Ti, V, Cr, Mn, Fe, Co, Ni, Cu, Zn, Ga, Rb, Sr, Y, Zr, Nb, Mo, Tc, Ru, Rh, Pd, Ag, Cd, In, Sn, Sb, Cs, Ba, La, Ce, Pr, Nd, Pm, Sm, Eu, Gd, Tb, Dy, Ho, Er, Tm, Yb, Lu, Hf, Ta, W, Re, Os, Ir, Pt, Au, Tl, Pb, and Bi. When magnetic metals or metal oxides are present in the disclosed materials, the material can be magnetic.

The disclosed porous materials can have very high surface area, approaching that of nanoparticles. For example, the surface area can be greater than about 5, 10, 15, 20, 25, 30, 35, 40, 45, 50, 55, 60, 65, 70, 75, 80, 85, 90, 95, or 100 m<sup>2</sup>/g, where any of the stated values

can form an upper or lower endpoint of a range. In some examples, porous materials with a surface area up to about 200 m<sup>2</sup>/g are disclosed.

When the disclosed porous material is a carbon porous material the surface area can be even greater than that described for the metal and/or metal oxide porous materials. For example, in these materials the surface area can be greater than about 200, 400, 600, 800, 1000, 1200, or 1600 m<sup>2</sup>/g, where any of the stated values can form an upper or lower endpoint of a range.

Further, the disclosed porous materials, in certain aspects, do not release nanoparticles of metal when used. This can be environmentally advantageous.

Additional components can be added to the disclosed metal and/or metal oxide porous materials, such as catalysts. The disclosed porous materials are not etch materials whereby ionizing radiation is used to form the pores. The disclosed materials can be substantially free (i.e., having less than about 1% by weight of the porous material) of surfactant. The disclosed materials can be substantially free (having less than about 1, 0.1, or 0.01% by weight of the porous material) of silica.

Also disclosed herein are compositions that comprise the metal and/or metal oxide porous materials disclosed herein and a carbon nanotube.

### **3.10 Applications**

The disclosed methods allow the control of the spatial distribution of different metals and/or metal oxides simultaneously within the same porous material, and formation of metal and/or metal oxide nanowires. The metal and/or metal oxide porous materials produced by the methods disclosed herein can be used as packing materials in chromatography, as catalysts, or as electrocatalysts. The disclosed materials can be used for chemical conversions such as combustion of liquid and gaseous fuels, conversion of liquid and gaseous

fuels to electricity, and conversion of electricity to liquid and gaseous fuels.

The disclosed materials can be used to assist heat transfer or to store and release electrical charge. The disclosed materials can be used to convert light to electric energy.

In particular, any process that uses a metal or metal oxide catalyst can be adapted by using the metal or metal oxide porous materials disclosed herein. For example, nickel is used as a reduction catalyst. A porous material as disclosed herein comprising nickel can be likewise used as a reduction catalyst in similar processes. Similarly, the disclosed metal and/or metal oxide porous materials can be used as catalysts in other reactions where traditional metal and metal oxide catalysts are used, such as hydrogenation of carbon-carbon and carbon-heteroatom pi bonds (alkenes, alkynes, nitriles, imines, carbonyls, etc.), reduction of carbon-nitrogen or carbon-oxygen pi bonds to give alcohols and amines, Fischer-Tropsch type chemistry to make hydrocarbons from CO/H<sub>2</sub>, hydrogenolysis of alcohols, hydrogen production from biomass, Pauson-Khand reactions (alkyne + alkene + CO to give cyclopentanones), and dechlorination of aromatic compounds. Further, the disclosed porous materials would be advantageous over traditional heterogeneous catalysts given their high surface area, which would aid efficiency, and their monolithic structure, which would simplify separation of the catalyst and make continuous flow reactions an option.

In a preferred use, the disclosed materials can be used as starting materials for deposition of carbon nanotubes and other charge storage materials, and the like. The growth of carbon nanotubes on porous substrates is known. These processes can be adapted by using the metal and/or metal oxide porous materials disclosed herein as substrates for the carbon nanotubes. As such, disclosed herein are compositions that comprise the disclosed metal and/or metal porous materials and a carbon nanotube.

The disclosed materials can also be used in the production of metal and metal oxide

nanowires for use in electrically and thermally conducting fabric, metal and metal oxide nanowires for use in catalysis and electrocatalysis, metal and metal oxide nanowires for use in information storage and the like. By controlling the level of infiltration of the metal salt into a porous template, thermal decomposition of the metal under reducing conditions or inert atmosphere, and removal of the porous template, a nanowire can be formed. The disclosed process also allows one to form large quantities of nanowires. As such disclosed herein are charge storage materials, nanowires, conducting fabric, catalysts, and information storage media comprising the porous materials disclosed herein.

Certain aspects of the disclosed methods can also be applied to the formation of porous carbon materials. The disclosed methods can also be applied to the production of microstructured and nanostructured porous carbon materials as templates for other materials, microstructured and nanostructured porous carbon bodies as catalyst support, microstructured, and nanostructured porous carbon bodies as current collectors in capacitors and batteries, microstructured and nanostructured porous carbon bodies as filters, microstructured and nanostructured porous carbon bodies as combined catalyst support and filter.

In a preferred use, the disclosed materials can be used as filters. There are many situations in which it is desirable to be able to separate or analyze an analyte or target molecule from a given sample or to remove impurities from a sample. For example, in disease diagnoses there is often a particular analyte that is produced by or part of a pathogen, and physicians use the presence or absence of that analyte to determine whether the patient is infected with the pathogen.

Described herein are methods for separating one or more target molecules present in a sample. "Separating a target from a sample" means removing the target molecule from the

sample. In one aspect, the method involves passing the sample through a porous material as disclosed herein. When the sample is passed through the porous material, the target molecules can be localized on or in the porous material. The porous materials disclosed herein can permit the flow of liquid through or into the material. In certain embodiments, the target molecules are reversibly localized and in other embodiments the localization is irreversible.

Often it is desirable to detect the target molecules that have been localized, by for example, viewing them directly or assaying for some type of label that has been associated with the target molecule. Once the target molecule has been localized near the surface of the porous material, further processing steps may be performed. The target molecules can also be, for example, amplified, detected, or isolated. For example, the target molecules can also be counted, correlated, purified, or collected. One way of categorizing target molecule is by their size, relative to the pore size of the disclosed porous material used. For example, the target molecule can have a contour length or globular diameter at least 1.5 times, two times, three times, four times, six times, eight times, ten times, or twenty times the diameter of the pores in the porous material. Any target molecule that has the properties necessary for localization on the disclosed porous material can be targeted or manipulated. For example, the target molecule can be a protein, peptide, polypeptide (e.g. antibody, enzyme), carbohydrate, sugar, nucleic acid, phospholipid, detergent, or surfactant or a combination thereof.

Similarly, it is possible to use the disclosed porous materials as filters to remove impurities from a sample. This can be done by contacting a sample with impurities to the disclosed porous materials. The impurities can be trapped, adsorbed, and/or degraded by the porous material, thus resulting in the removal of the impurities from the sample. This method

can be used to separate gaseous impurities from gaseous or liquid samples. It can also be used to separate liquid impurities from gaseous or liquid samples. For example, the disclosed porous materials can be used as solid state oxygen filters, and gas/liquid separators.

The disclosed porous materials can also be used in chromatography, for example, gas, HPLC, flash, or thin-layer chromatography, as the stationary phase. The chromatography can also involve the use of applied potential to control localization of target molecules, such as in electrochemical chromatography and electromodulated or electrochemically modulated chromatography. Because the disclosed porous materials have such high surface area and can be conductive, they are particularly well suited for these uses.

In another aspect, the disclosed porous materials can be used in fuel cells as a fuel cell separator. Thus, fuel cells comprising the disclosed porous materials are also contemplated herein.

In still another aspect, the disclosed porous materials can be used in environmental remediation. For example, the metal surface of the porous materials can be an active site to decompose hazardous materials. This can be useful for general remediation or waste water filtration. The material is also beneficial in that it can be retrofit into existing filtration systems and incorporated into existing industrial processes.

In still other examples, the disclosed porous materials have such high surface areas that they can be used for heat dissipation applications. For example, they can be used in heat exchanges, heat sinks (e.g. in computers and gaming consoles), thermal conduits, and the like. The disclosed porous material can be adapted to be positioned in a heat conducting relationship with an electronic module to be cooled. As another example, the disclosed porous materials can be used in cookware.

### 3.11 Examples

The following examples are set forth below to illustrate the methods and results according to the disclosed subject matter. These examples are not intended to be inclusive of all aspects of the subject matter disclosed herein, but rather to illustrate representative methods and results. These examples are not intended to exclude equivalents and variations of the present invention which are apparent to one skilled in the art.

Efforts have been made to ensure accuracy with respect to numbers (e.g. amounts, temperature, etc.) but some errors and deviations should be accounted for. Unless indicated otherwise, parts are parts by weight, temperature is in °C or is at ambient temperature, and pressure is at or near atmospheric. There are numerous variations and combinations of reaction conditions, e.g. component concentrations, temperatures, pressures, and other reaction ranges and conditions that can be used to optimize the product purity and yield obtained from the described process. Only reasonable and routine experimentation will be required to optimize such process conditions.

The silica monoliths used in these examples were produced using the methods disclosed by US Patent 6,911,192, Nakanishi and Smått et al.<sup>12, 13, 24</sup>

In a typical synthesis tetraethylorthosilicate (TCI America), 30% nitric acid, deionized water, polyethylene glycol MW = 35,000 g/mol (Sigma-Aldrich), and OTAB (Alfa Aesar) were mixed in the following molar ratios, 1:0.25:14.7:0.43:0.1, respectively. The solution was transferred into a template and allowed to gel for 72 hours at 40 °C. Monoliths were then aged in 1 M ammonium hydroxide at 90 °C overnight followed by neutralization in 0.1 M nitric acid, rinsing three times with deionized water, three times with acetone, and dried at 40 °C for 72 hours. Finally, the silica monoliths were calcined at 550 °C for 5 hours with a ramp rate of 1 °C/min.

### 3.11.1 Example 1

A concentrated solution comprising 77.7 g of  $\text{Co}(\text{NO}_3)_2 \cdot 6\text{H}_2\text{O}$  dissolved in 59.0 g of de-ionized water (4.5 mol/ kg solvent) was prepared. Silica monoliths containing large pores, 1-5  $\mu\text{m}$  in diameter, and much smaller pores, 4.5 nm in diameter, were dried under vacuum for 20 minutes and filled with the solution above. Monoliths became translucent and excess solution was removed from the outside. Filled monoliths were heated at 150 °C for 10 hours and then heated up to 400 °C over 4 hours and held at 400 °C for 30 hours while flowing 5%  $\text{H}_2$  in  $\text{N}_2$ . The filling and heating steps were repeated 4 times. The silica was removed by soaking the composite in an aqueous potassium hydroxide solution (3 mol/liter water) overnight. This resulted in a free standing, porous cobalt metal monolith.

Electron microscopy confirmed positive replication of the large pores and can be seen in Figure 3.2. X-ray Diffraction confirmed the presence of cobalt metal. Replication of the small pores was confirmed by nitrogen adsorption measurements where the porosity, before removal of the silica, at 4.5 nm was nearly absent and after silica removal pores larger than 20 nm in diameter remain. The resulting specific surface area of this material was no less than 40  $\text{m}^2/\text{g}$ .

### 3.11.2 Example 2

In the same manner as Example 1, a concentrated solution consisting of 137.8 g of  $\text{Cu}(\text{NO}_3)_2 \cdot 3\text{H}_2\text{O}$  diluted to 100 mL with de-ionized water (5.7 mol/ liter solution) was prepared and used to fill the pores of the silica monolith. Filled monoliths were dried under nitrogen atmosphere at 150 °C for 10 hours, and then heated up to 310 °C for an hour under a flow of nitrogen bubbled through methanol. The filling and heating cycles were repeated 3 times. The silica was removed by soaking the composite in a solution of potassium hydroxide (3 mol/liter) in dry methanol at 80 °C overnight. This resulted in a free standing,

porous copper metal monolith. The same characterization methods were used as in Example 1. The resulting monolith gave a brilliant rose color and a SEM image can be seen in Figure 3.3. The specific surface area of the resulting material was 10 m<sup>2</sup>/g or greater.

#### 3.11.3 Example 3

In the same manner as Example 1, a solution of 23.5 g AgNO<sub>3</sub>, 2.7 g Cu(NO<sub>3</sub>)<sub>2</sub>·3H<sub>2</sub>O, and 5 mL water was prepared and used to fill the pores of the silica monolith. Filled monoliths were dried at 150 °C for 10 hours, and then heated under an ethylene glycol atmosphere to reduce to the metal. The filling and heating cycle was done twice. The silica was removed by soaking the composite in an aqueous potassium hydroxide solution (3 mol/liter water) for several hours. This resulted in a free standing, porous sterling silver monolith and the SEM image can be seen in Figure 3.4. The same characterization methods were used as in Example 1. The resulting specific surface area of this material was 2 m<sup>2</sup>/g and greater.

#### 3.11.4 Example 4

In the same manner as Example 1, a concentrated solution of 59.6 g Ni(NO<sub>3</sub>)<sub>2</sub>·6H<sub>2</sub>O diluted to 50 mL with de-ionized water was prepared and used to fill the silica pores. Filled monoliths are heated at 150 °C for 10 hours, and then at 250 °C for four hours to ensure complete decomposition. The filling and heating cycle was done three times. The monoliths were then heated to 600 °C for 5 hours. The silica was removed by soaking the composite in a solution of potassium hydroxide (3 mol/liter) in dry methanol at 90 °C overnight. This resulted in a free standing, porous nickel oxide monolith. The monoliths were grayish green in color and a SEM image can be seen in Figure 3.5. The same characterization methods were used as in Example 1. The resulting specific surface area of this material was 32 m<sup>2</sup>/g.

#### 3.11.5 Example 5

A mixture of Co(NO<sub>3</sub>)<sub>2</sub>·6H<sub>2</sub>O and water (16.5 M) was prepared. The mixture was

then heated to 60 °C, which is above the melting point of the salt, and kept there. Silica monoliths containing large pores, 1-5 µm in diameter, and much smaller pores, 4.5 nm in diameter, were placed in the solution and allowed to soak overnight, and were translucent in color the next day. The monoliths were then removed from the solution, placed in a 60 °C furnace so that the salt would not crystallize in the monoliths, and excess solution was removed. The monoliths were then heated for 10 hours at 150 °C for 10 hours under flow of 5% H<sub>2</sub> in N<sub>2</sub>, and then at 400 °C for 24 hours under the same atmosphere. This process was repeated twice. The silica was removed in the same manner as Example 1. This resulted in a free standing, porous cobalt monolith.

Electron microscopy was used to confirm replication. These monoliths exhibited the same positive replica of the large pores, but also contained hollow ligaments within the walls, as seen in 3.6. This gave a specific surface area of 65 m<sup>2</sup>/g.

#### 3.11.6 Example 6

The solution from Example 4 was used and introduced into the silica as in Example 1. The filled monolith was heated at 150 °C for 10 hours under flow of 5% H<sub>2</sub> in N<sub>2</sub>, and then at 350 °C for 10 hours under the same atmosphere. This process was repeated 4 times. However, great care was taken not to expose the samples to oxygen. They were kept under deoxygenated water or nitrogen gas the entire time. The silica was removed in deoxygenated potassium hydroxide solution (3 mol/L). The same characterization methods were used as in Example 1 and a SEM image of the nickel replica can be seen in Figure 3.7. The specific surface area of this nickel metal replica was 15 m<sup>2</sup>/g or better.

#### 3.11.7 Example 7

The solution from Example 1 was used and introduced into the silica as in Example 1. The silica monoliths contained large pores, 1-5 µm in diameter, and much smaller pores,

about 8 nm in diameter, that are ordered in orientation. The filled monoliths were heated at 150 °C for 10 hours under N<sub>2</sub> flow and then at 250 °C for 1 hour under the same atmosphere. This process was repeated twice. The silica was removed in the same manner as in Example 1. This resulted in a free standing, porous cobalt oxide monolith containing ordered pores of about 4 nm. The same characterization methods were used as in Example 1 and electron microscope images of the ordered cobalt oxide replica can be seen in Figure 3.8. The specific surface area of this cobalt oxide replica was 120 m<sup>2</sup>/g or better.

As described, according to the disclosed methods it is possible to produce porous bodies composed of metals and metal oxides and mixtures of various metals and metal oxides that have structure at a number of length scales, where the structure is determined by the template used and the precise procedure carried out. Applications of such materials include, but are not limited to chromatography and other separations methods, catalysis and electrocatalysis, energy storage and energy conversion.

Other advantages which are obvious and which are inherent to the invention will be evident to one skilled in the art. It will be understood that certain features and sub-combinations are of utility and may be employed without reference to other features and sub-combinations. This is contemplated by and is within the scope of the claims. Since many possible aspects may be made of the invention without departing from the scope thereof, it is to be understood that all matter herein set forth is to be interpreted as illustrative and not in a limiting sense.

### 3.12 Claims

1. A bicontinuous porous body, comprising: a plurality of macropores having a diameter of from greater than about 0.1  $\mu\text{m}$ , wherein the macropores interconnect, forming a continuous network of pores that spans the material, permitting the flow of liquid or gas into and through the material, and wherein the wall of the macropores comprise a continuous layer of metal and/or metal oxide.
2. The body of claim 1, wherein the macropores have a diameter of from about 0.5  $\mu\text{m}$  to about 30  $\mu\text{m}$ .
3. The body of claim 1, wherein the walls of the macropores are not porous.
4. The body of claim 1, wherein the walls of the macropores have a plurality of mesopores having a diameter of from about 2 nm to about 50 nm thereby resulting in a bicontinuous porous material with hierarchical pores.
5. The body of claim 1, wherein the walls of the macropores have a plurality of micropores having a diameter of from less than about 2 nm thereby resulting in a bicontinuous porous material with hierarchical pores.
6. The body of claim 1, wherein the body is a hollow body.
7. The body of claim 1, wherein the material comprises one or more metals, metal oxides, or a combination thereof, wherein the metals are selected from the group consisting of Li, Be, Na, Mg, Al, K, Ca, Sc, Ti, V, Cr, Mn, Fe, Co, Ni, Cu, Zn, Ga, Rb, Sr, Y, Zr, Nb, Mo, Tc, Ru, Rh, Pd, Ag, Cd, In, Sn, Sb, Cs, Ba, La, Ce, Pr, Nd, Pm, Sm, Eu, Gd, Tb, Dy, Ho, Er, Tm, Yb, Lu, Hf, Ta, W, Re, Os, Ir, Pt, Au, Tl, Pb, and Bi.
8. A method for producing a metal and/or metal oxide porous body, comprising:
  - (i) contacting a porous template and a composition comprising a metal salt to form a

- mixture, wherein the metal salt has a decomposition temperature;
- (ii) maintaining the mixture below the decomposition temperature of the metal salt until a desired spatial distribution of the metal salt in the porous template is obtained; and then
  - (iii) heating the mixture to above the decomposition temperature of the metal salt in the presence of a reducing agent or inert atmosphere to produce the metal and/or metal oxide porous material; and optionally repeating steps (i)-(iii) with the same metal salt or with a different metal salt.
9. The method of claim 8, wherein the metal salt comprises a metal selected from the group consisting of Li, Be, Na, Mg, Al, K, Ca, Sc, Ti, V, Cr, Fe, Cu, Ga, Rb, Sr, Y, Zr, Nb, Mo, Tc, Ru, Rh, Pd, Cd, In, Sb, Cs, Ba, La, Ce, Pr, Nd, Pm, Sm, Eu, Gd, Tb, Dy, Ho, Er, Tm, Yb, Lu, Hf, Ta, W, Re, Os, Ir, Pt, Au, Tl, Pb, and Bi.
10. The method of claim 8, wherein the metal salt comprises a metal selected from the group consisting of Ni, Co, Mn, Ag, Zn, and Sn.
11. The method of claim 8, wherein the composition comprising the metal salt is a neat metal salt or a metal salt hydrate.
12. The method of claim 8, wherein the composition comprising the metal salt further comprises a solvent.
13. The method of claim 12, wherein the solvent is water.
14. The method of claim 12, wherein the solvent is an aqueous alcohol, aqueous polyol, aqueous carboxylic acid, aqueous ester, or aqueous aldehyde.
15. The method of claim 12, wherein the ratio of metal salt to solvent in the composition is from 1:10 to 10:1.

16. The method of claim 8, wherein the composition comprising the metal salt comprises a metal nitrate hydrate or an aqueous metal nitrate.
17. The method of claim 8, wherein the porous template is monolithic or particulate.
18. The method of claim 8, wherein the porous template comprises a composite of one or more of silica, carbon, metal, or metal oxide.
19. The method of claim 8, wherein the porous template comprises silica.
20. The method of claim 8, wherein the porous template comprises macropores having a diameter of from greater than about 0.1  $\mu\text{m}$  in diameter and mesopores having a diameter of from about 2 nm to about 30 nm.
21. The method of claim 8, wherein the reducing agent comprises hydrogen gas, alcohol, polyol, carboxylic acid, aldehyde, hydrazine, hydride, ketone, or borane.
22. The method of claim 8, further comprising removing the porous template.
23. The method of claim 22, wherein the porous template comprises silica and the silica is removed by immersing the porous material from step (iii) in an aqueous hydroxide solution at from about 25  $^{\circ}\text{C}$  to about 110  $^{\circ}\text{C}$ .
24. The method of claim 22, wherein the porous template comprises silica and the silica is removed by immersing the porous material from step (iii) in hydrofluoric acid.
25. The method of claim 22, wherein the porous template comprises silica and the silica is removed by immersing the porous material from step (iii) in a solution of basic alcohol.
26. The method of claim 8, further comprising adding an additional metal to the metal and/or metal oxide porous material by electrodeposition, by electroless deposition, or by displacement deposition.

3.13 Figures

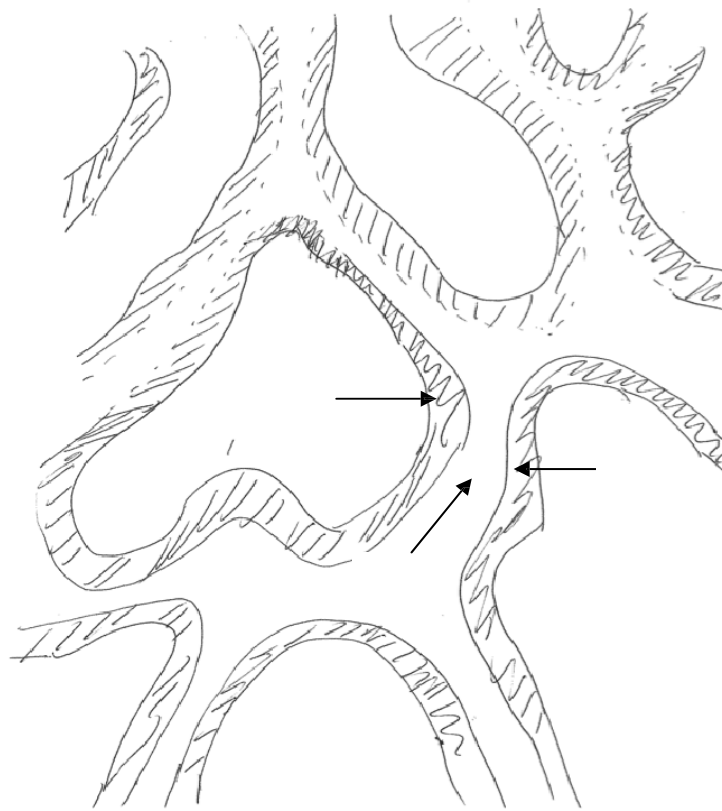


Figure 3.1(a). Cartoon of Porous Materials Prepared.

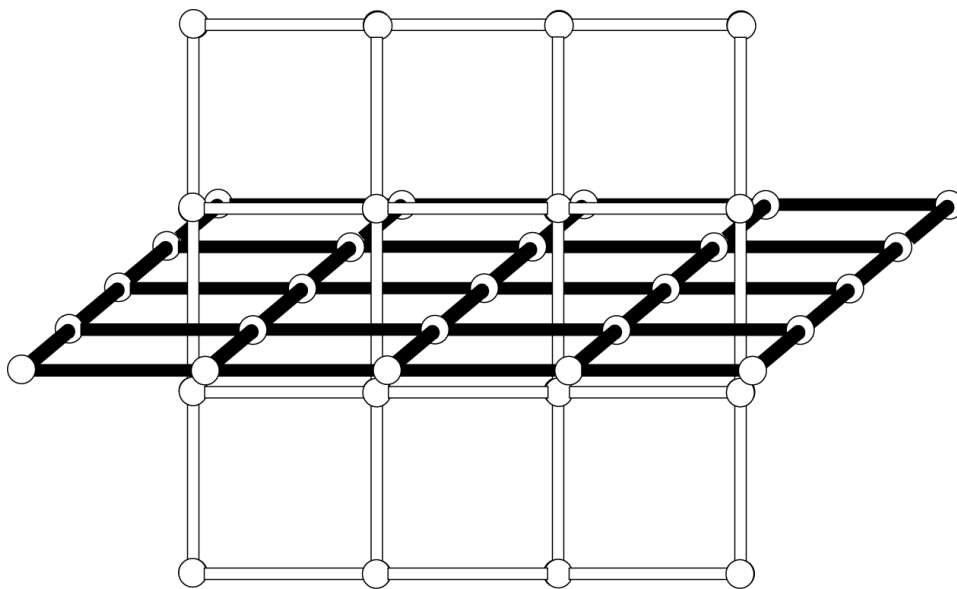
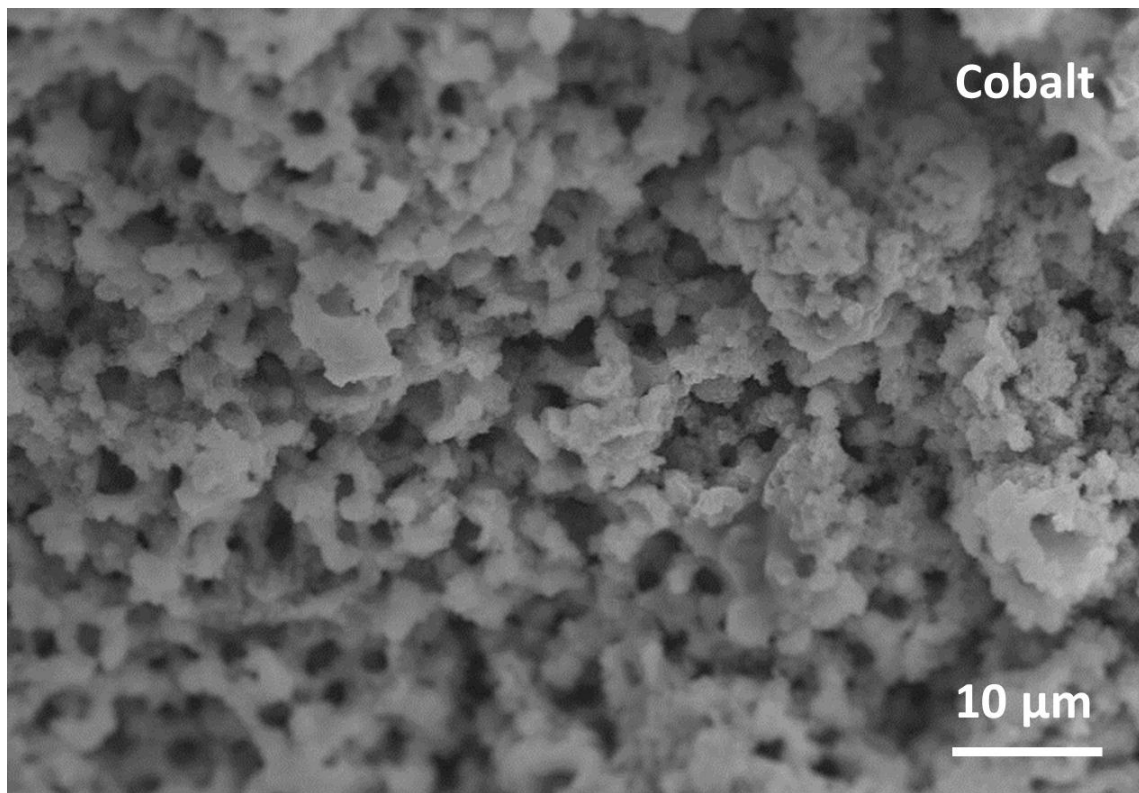
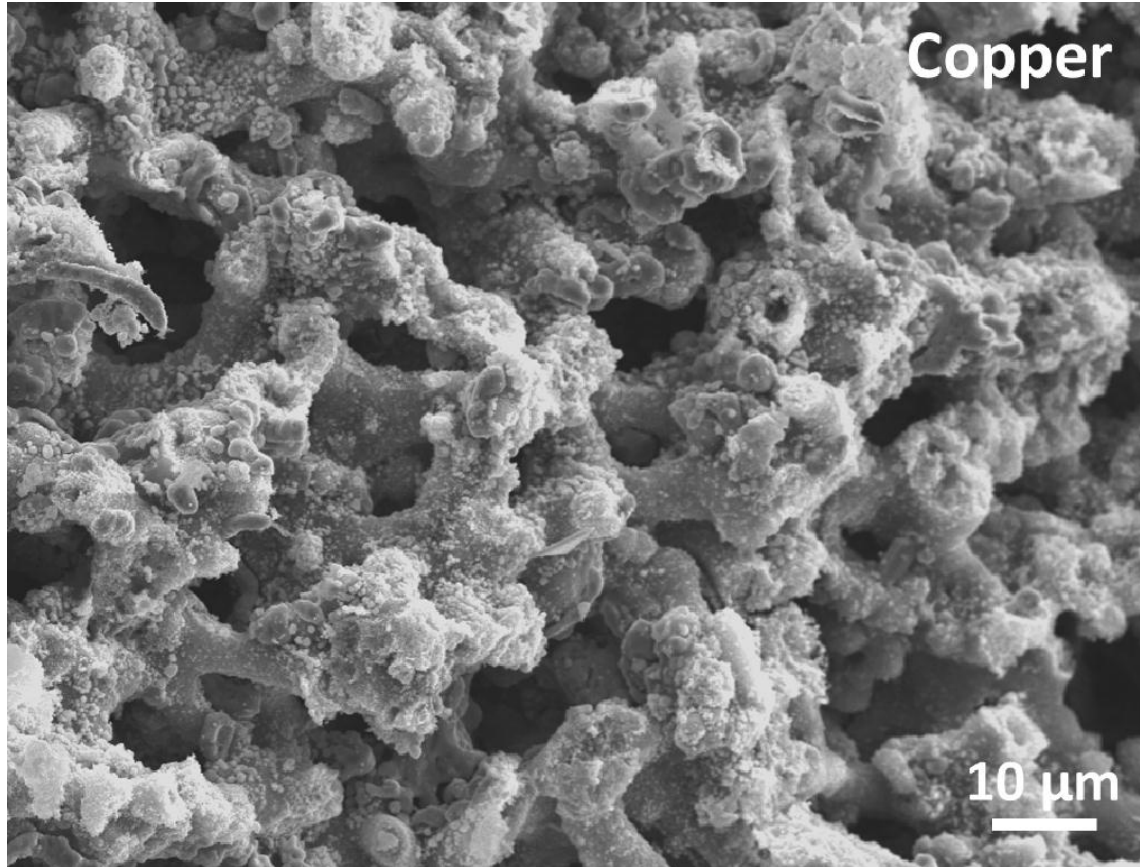


Figure 3.1(b). Empirical Schematic Representation of a Bicontinuous Structure.



**Figure 3.2.** SEM Image of Cobalt Metal Monolith.



**Figure 3.3.** SEM Image of Copper Metal Monolith.

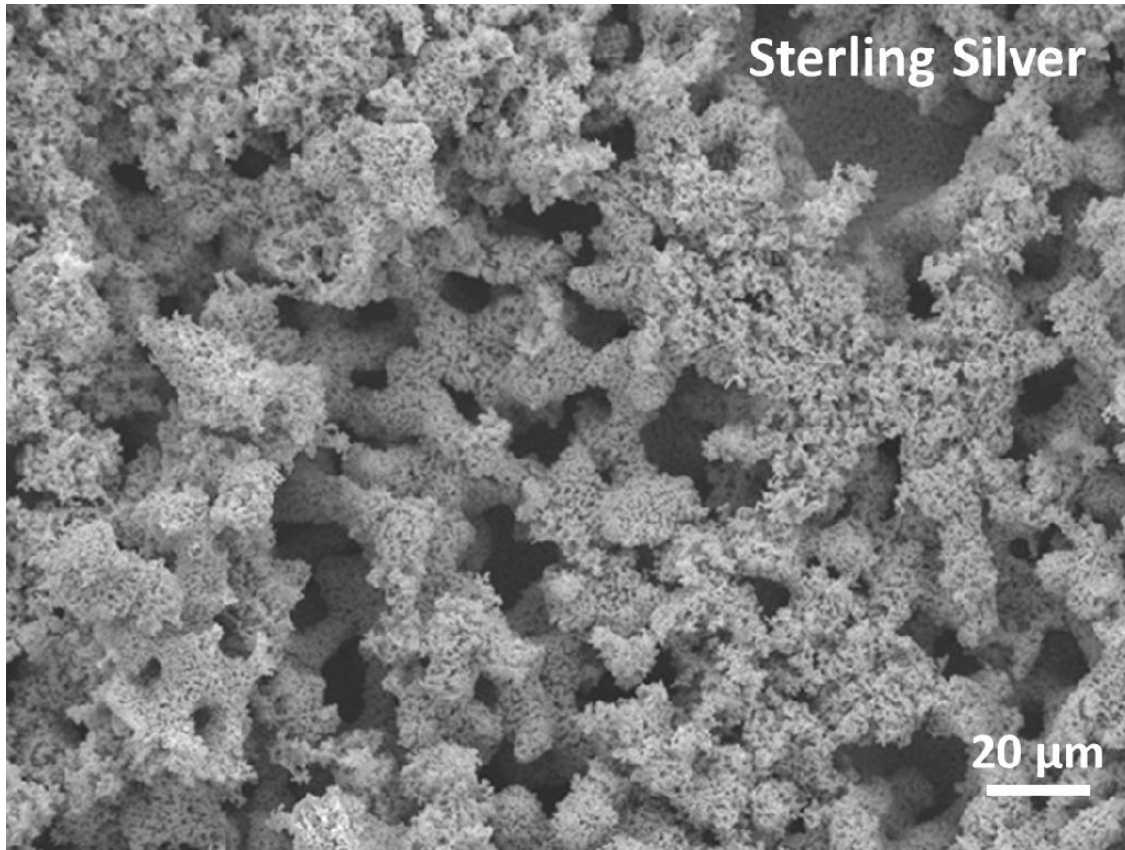


**Figure 3.4.** SEM Image of Sterling Silver Monolith.

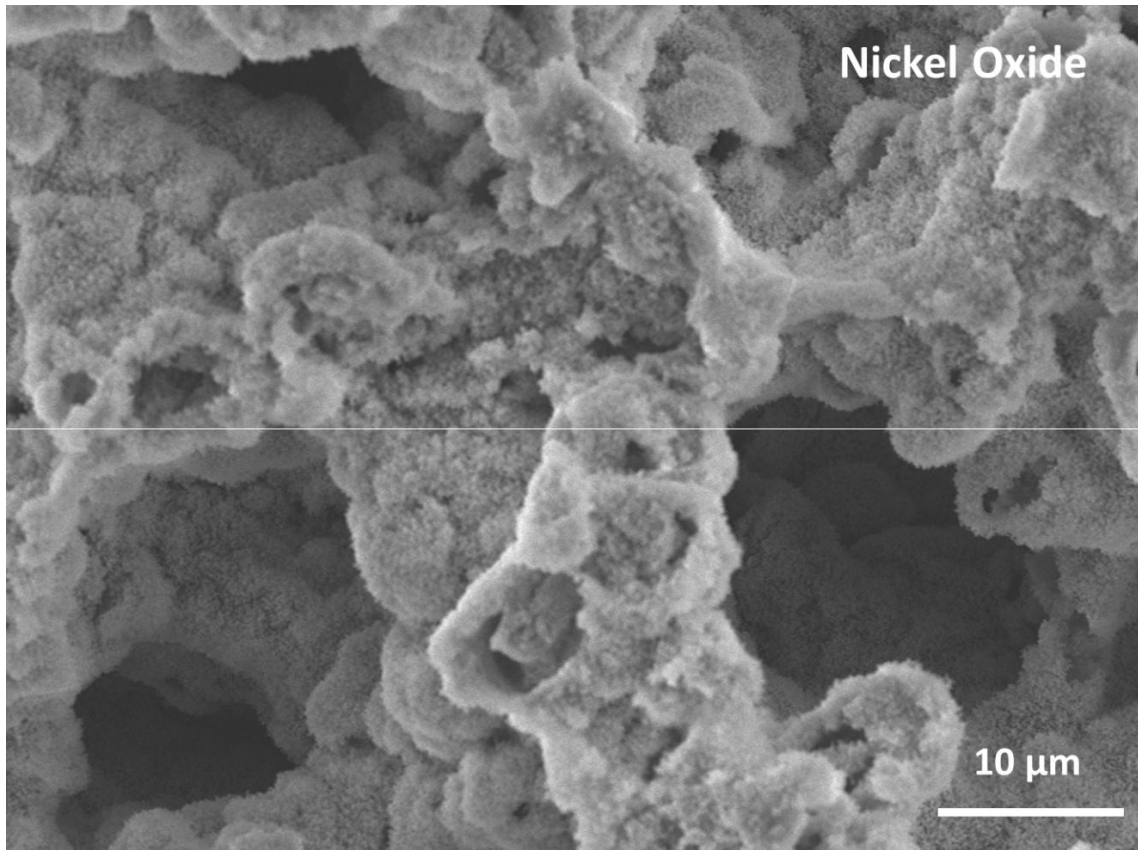


**Figure 3.5.** SEM Image of Macropores in Nickel Oxide Monolith.

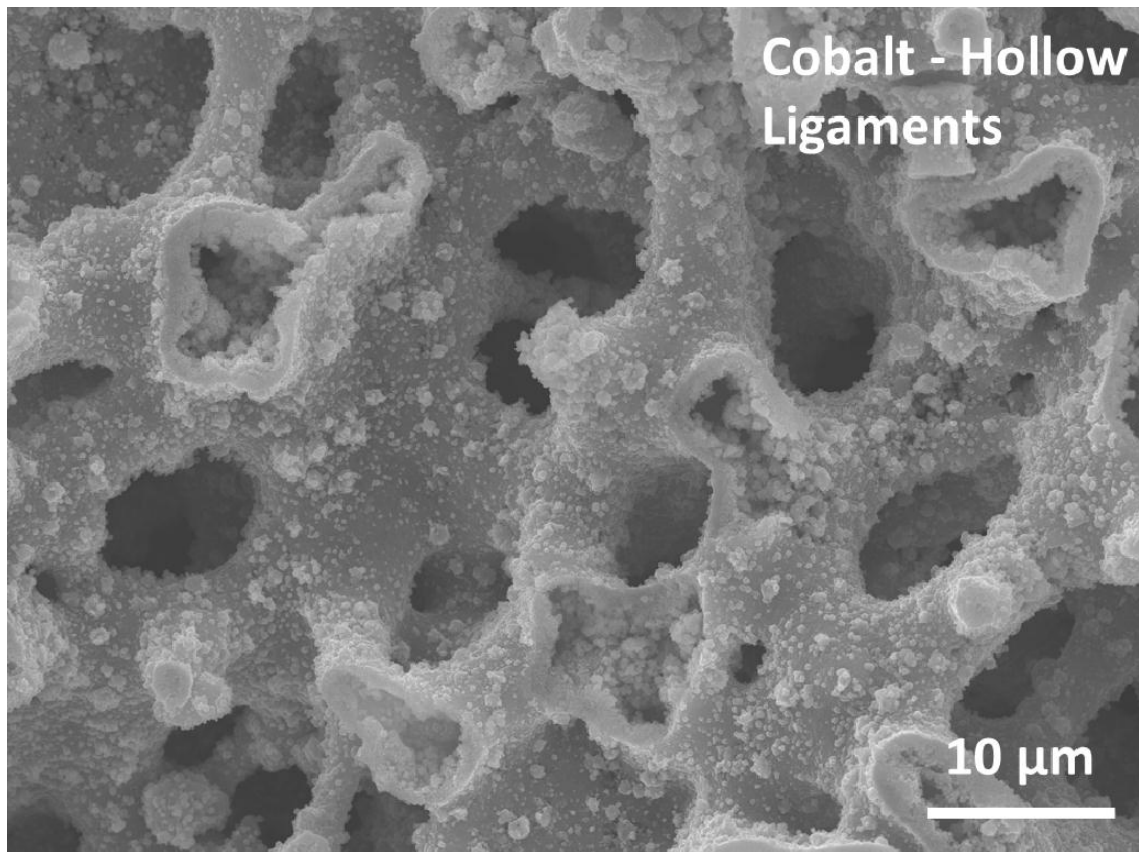


**Figure 3.6.** SEM Image of Hollow Fiber Cobalt Monolith.

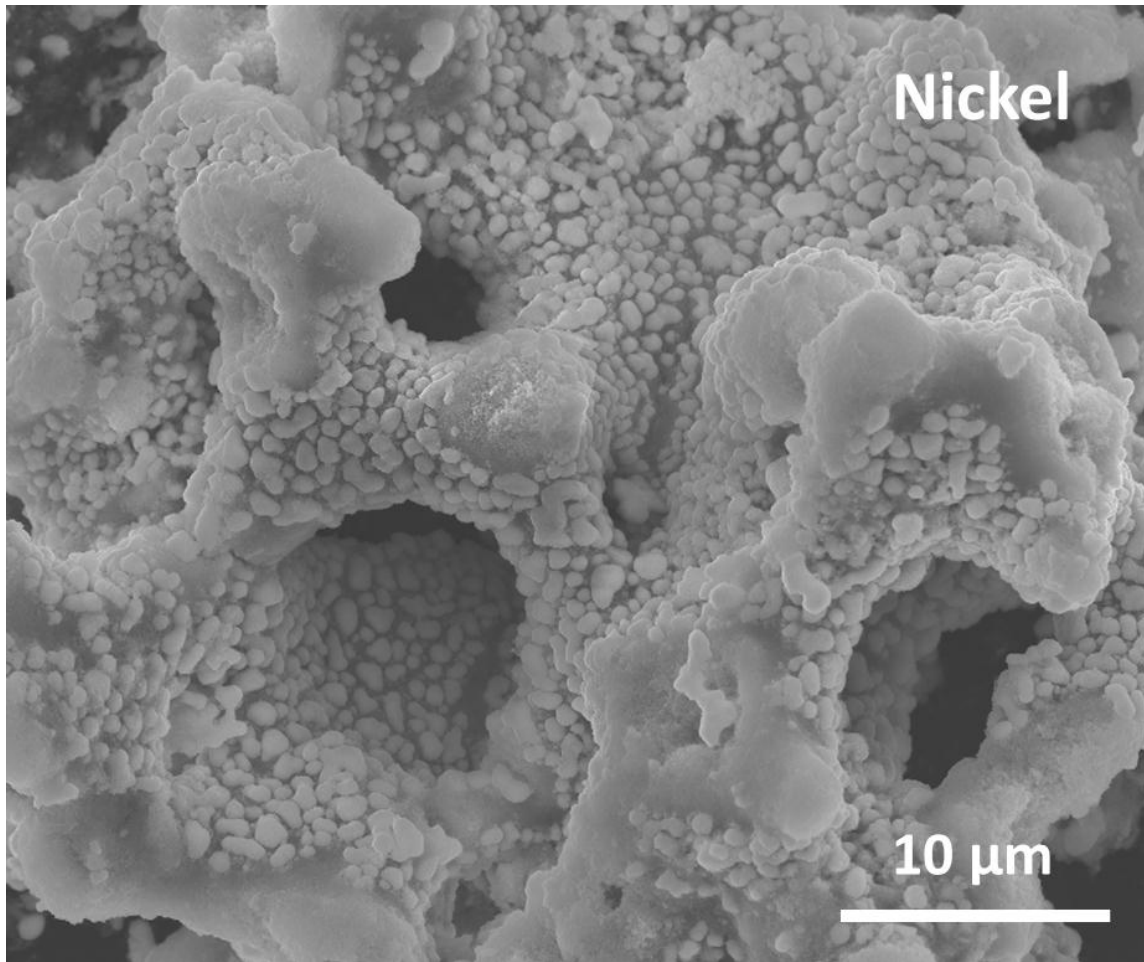


**Figure 3.7.** SEM Image of Macropores in Nickel Metal Monolith.

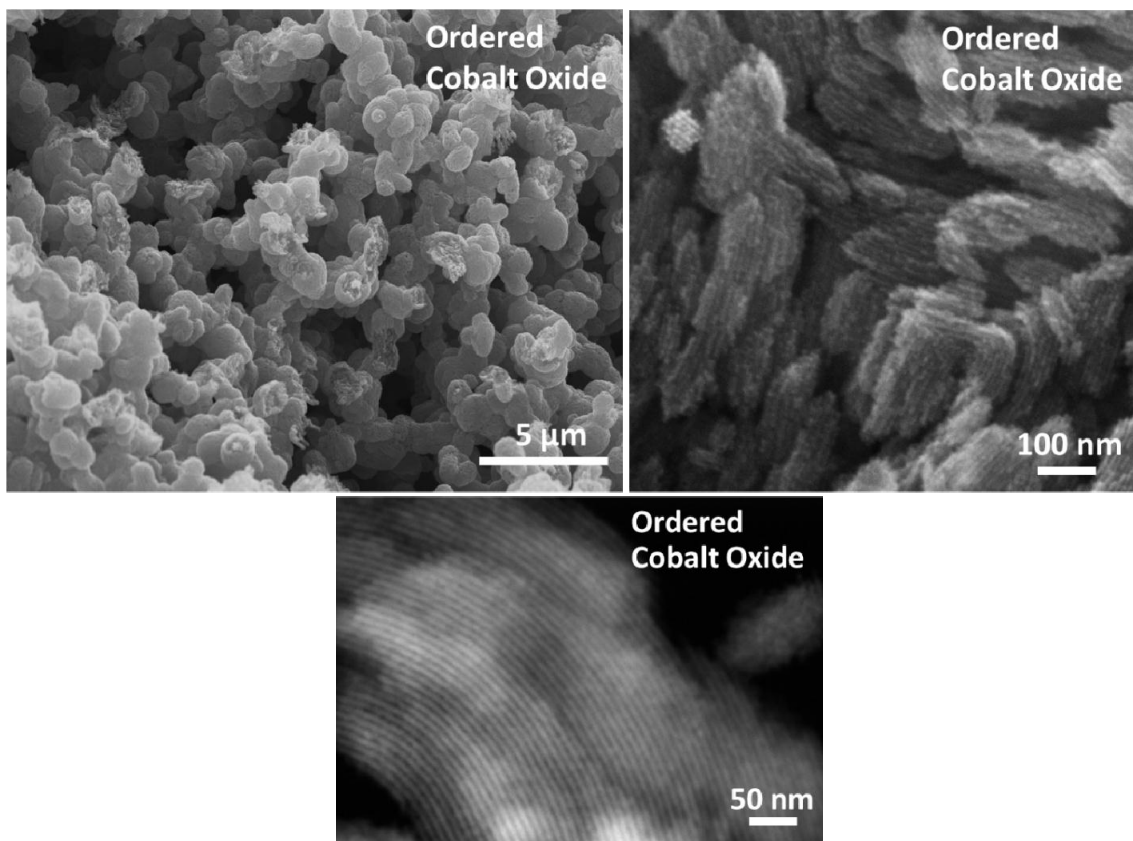


**Figure 3.8.** SEM and TEM Images of Cobalt Oxide Monolith Macropores and Highly Ordered Mesopores.

### 3.14 Acknowledgements

This work was performed with co-inventors Professor Martin Bakker, Ms. Amy Grano, and Professor Jan-Henrik Smått.

### 3.15 References

- (1) Yue, W.; Zhou, W. *Chem. Mater.* **2007**, *19*, 2359-2363.
- (2) Yue, W. B.; Zhou, W. Z. *Studies Surf. Sci. Catal.* **2007**, *170*, 1755-1762.
- (3) Brockner, W.; Ehrhardt, C.; Gjika, M. *Thermochim. Acta* **2007**, *456*, 64-68.
- (4) Llewellyn, P. L.; Chevrot, V.; Ragai, J.; Cerclier, O.; Estienne, J.; Rouquerol, F. *Solid State Ionics* **1997**, *101-103*, 1293-1298.
- (5) Mansour, S. A. A. *Thermochim. Acta* **1993**, *228*, 173-189.
- (6) Paulik, F.; Paulik, J.; Arnold, M. *Thermochim. Acta* **1987**, *121*, 137-149.
- (7) Estelle, J.; Salagre, P.; Cesteros, Y.; Serra, M.; Medina, F.; Sueiras, J. E. *Solid State Ionics* **2003**, *156*, 233-243.
- (8) Sietsma, J. R. A.; Meeldijk, J. D.; Versluijs-Helder, M.; Broersma, A.; van Dillen, A. J.; de Jongh, P. E.; de Jong, K. P. *Chem. Mater.* **2008**, *20*, 2921-2931.
- (9) Sietsma, J. R. A.; Friedrich, H.; Broersma, A.; Versluijs-Helder, M.; van Dillen, A. J.; de Jongh, P. E.; de Jong, K. P. *J. Catal.* **2008**, *260*, 227-235.
- (10) Sun, X.; Shi, Y.; Zhang, P.; Zheng, C.; Zheng, X.; Zhang, F.; Zhang, Y.; Guan, N.; Zhao, D.; Stucky, G. D. *J. Am. Chem. Soc.* **2011**, *133*, 14542-14545.
- (11) Bates, F. S.; Fredrickson, G. H. *Physics Today* **1999**, *52*, 32-38.
- (12) Nakanishi, K. *Method for Preparing Inorganic Porous Material*. U. S. Patent 6,911,192, June 28, 2002.
- (13) Nakanishi, K. *J. Porous Mater.* **1997**, *4*, 67-112.
- (14) Li, F.; Wang, Z.; Ergang, N. S.; Fyfe, C. A.; Stein, A. *Langmuir* **2007**, *23*, 3996-4004.
- (15) Carn, F.; Colin, A.; Achard, M.-F.; Deleuze, H.; Sellier, E.; Birot, M.; Backov, R. *J. Mater. Chem.* **2004**, *14*, 1370-1376.
- (16) Maekawa, H.; Esquena, J.; Bishop, S.; Solans, C.; Chmelka, B. F. *Adv. Mat.* **2003**, *15*, 591-596.
- (17) Zhao D. Y.; Yang P. D.; Chmelka B. F.; Stucky, G. D. *Chem. Mater.* **1999**, *11*, 1174-1178.
- (18) Davis, S. A.; Burkett, S. L.; Mendelson, N. H.; Mann, S. *Nature* **1997**, *385*, 420-423.

- (19) Caruso, R. A.; Schattka, J. H. *Adv. Mat.* **2000**, *12*, 1921-1923.
- (20) Caruso, R.A.; Antonietti, M. *Adv. Funct. Mater.* **2002**, *12*, 307-312.
- (21) Walsh, D.; Arcelli, L.; Ikoma, T.; Tanaka, J.; Mann, S. *Nat. Mat.* **2003**, *2*, 386-390.
- (22) Nishihara, H.; Mukai, S. R.; Yamashita, D.; Tamon, H. *Chem. Mater.* **2005**, *17*, 683.
- (23) Suzuki, K.; Ikari, K.; Imai, H. *J. Mater. Chem.* **2003**, *13*, 1812-1816.
- (24) Smått, J.-H.; Schunk, S. A.; Lindén, M. *Chem. Mater.* **2003**, *15*, 2354-2361.
- (25) Ryoo, R.; Joo, S. H.; Kruk, M.; Jaroniec, M. *Adv. Mat.* **2001**, *13*, 677-681.
- (26) Lu, A.-H.; Kiefer, A.; Schmidt, W.; Schuth, F. *Chem. Mater.* **2004**, *16*, 100.
- (27) Yang, H. F.; Zhao, D. Y. *J. Mater. Chem.* **2005**, *15*, 1217-1231.
- (28) Hu, Y.-S.; Adelhelm, P.; Smarsly, B. M.; Hore, S.; Antonietti, M.; Maier, J. *Adv. Funct. Mater.* **2007**, *17*, 1873-1878.
- (29) Lu, A.-H.; Zhao, D.; Wan, Y. *Nanocasting: A Versatile Strategy for Creating Nanostructured Porous Materials*, Royal Society of Chemistry, Cambridge, U. K., 2010.

## Chapter 4

### Nanocasting of Hierarchically Porous NiO, Co<sub>3</sub>O<sub>4</sub>, Ni, Co and Ag Monoliths: Impact of Processing Conditions on Fidelity of Replication

#### 4.1 Abstract

Porous silica monoliths with bicontinuous pore structure at the micrometer scale and 4.4 nm surfactant templated pores were used as templates for preparing NiO, Co<sub>3</sub>O<sub>4</sub>, as well as nickel, cobalt and silver metal monoliths. Aqueous solutions of metal nitrates were repeatedly infiltrated into the porous silica templates and the nitrate thermally decomposed. Thermal decomposition in air produced porous NiO and Co<sub>3</sub>O<sub>4</sub> oxide monoliths. Thermal decomposition under an atmosphere of 5% hydrogen in 95% nitrogen produced porous monoliths of nickel, cobalt and silver. Repeated solution infiltration, drying and thermal decomposition followed by removal of the silica using aqueous sodium or potassium hydroxide solutions produced free standing hierarchically porous nickel oxide, cobalt oxide, nickel, cobalt and silver monoliths. The surface areas of the materials determined by nitrogen adsorption were 141 m<sup>2</sup>/g for Co<sub>3</sub>O<sub>4</sub>, 42 m<sup>2</sup>/g for cobalt, 32 m<sup>2</sup>/g for NiO, 13.7 m<sup>2</sup>/g for nickel and 2.2 m<sup>2</sup>/g for silver. The impact of an additional annealing step was found to adversely affect replication. The surface area, pore size distribution, morphology of the samples and fidelity of the replication are discussed within the framework of a comprehensive model for nanocasting within porous monoliths.

#### 4.2 Introduction

High surface area metal/metal oxide materials are of great importance to many applications including catalysis,<sup>1</sup> energy storage<sup>2,3</sup> and utilization,<sup>4</sup> sensors,<sup>5</sup> and separations. Many applications require good mass transport of reactants, products, electrons, and/or ions combined with high surface area. To meet these requirements, materials need to be hierarchically porous having continuous pores at multiple length scales. For some applications

the material also needs to be available as macroscopic individual pieces referred to as monoliths. Various approaches have been explored to make such materials. Metal foams<sup>6-8</sup> are examples of hierarchically porous monoliths that generally consist of large (micrometer scale) macropores with a broad pore size distribution, and have relatively low surface areas due to the absence of nanometer scale structures. So called "nanofoams" have been produced that have much higher surface areas,<sup>9</sup> but again the pore size distributions are very broad and mass transport is less than ideal. Another approach that has been used to produce hierarchically porous metal oxides is sol-gel chemistry, which has been used to make a wide range of aerogels,<sup>10,11</sup> again with a broad size pore size distribution. Addition of various templates to sol-gel systems can be used to better controlled porosity;<sup>12-20</sup> however, the fast condensation kinetics typical for metal oxide sol-gel systems makes control difficult, so that each different metal oxide needs careful, individual adjustment. Many applications require formation of heterostructured materials, i.e. where two or more materials are present and where the structure and spatial location of each phase needs to be controlled. This has been accomplished in the formation of nickel oxide catalyst on porous titanium;<sup>21</sup> however, the extra complexity both complicates the synthesis and makes it more difficult to control the final structure.

A parallel approach to direct synthesis of hierarchically porous monoliths is the use of nanocasting into a template generated by another synthesis method such as sol-gel derived silica structures. Nanocasting involves infiltrating a precursor into the template, performing the appropriate chemistry to obtain the desired material, and then repeating these steps as necessary to essentially build up a complete replica structure at the nanoscale. This approach has the advantage of utilizing the very well developed structure control provided by a broad range of silica based syntheses, and so simplifying the problem to one of controlling the chemistry of the

metal or metal oxide being nanocast. When nanocasting into silica, once the composite is formed, the silica can be removed with either hydrofluoric acid or base etching. This does limit nanocasting to materials that are stable in either acid or base. For carbon templates the carbon can be burned off in air, limiting application to air stable materials, particularly metal oxides. The literature on nanocasting into mesoporous silica particles is extensive, including nanocasting to make mesoporous polymers, carbons, metal oxides and metals.<sup>13</sup> There has also been a significant number of reports of nanocasting into mesoporous carbon particles. Ryoo and co-workers reported the first mesoporous metallic replica of a silica powder producing platinum nanowires.<sup>22</sup> Other groups subsequently replicated mesoporous silica powder in gold, palladium, and osmium.<sup>23-25</sup> Successful replication of monolithic silica by nanocasting is a demanding process that has been achieved for several metal oxides and for carbon.<sup>26-29</sup> In order for the replica to be free standing and mechanically robust a continuous replica needs to be produced. The extent of replication must be controlled to balance mechanical stability (favored by addition of material) against surface area (which tends to be favored by lower levels of material addition). As the nanocast material begins to form continuous domains, mechanical stresses due to differences in coefficient of thermal expansion also become important. For nanocasting into mesoporous particles mechanical fracturing of the template is generally not a concern as the nanocast product is itself a (smaller) particle. For replication of a single monolithic piece a single fracture leads to two pieces instead of a full replicate of the starting monolith. Nanocasting of monoliths also requires that the template be continuous and fully connected. If the pore system is not connected, the resulting nanocast replica will not possess any mechanical

strength and be merely aggregated<sup>1</sup> nanoparticles, nanowires, or pieces of wormlike nanostructures once the silica is removed.

In this study we give the first detailed report of the formation of high surface area mesoporous metal monoliths (nickel, cobalt and silver) by nanocasting into hierarchically porous silica monoliths as well as the nanocasting of NiO and Co<sub>3</sub>O<sub>4</sub> into such templates. The silica template used includes extensive mesopores networks produced by inclusion of 7% octadecyltrimethylammonium bromide (OTAB) during the synthesis which we have previously shown<sup>30</sup> to produce a well-connected mesopore structure. The high surface area of the nickel and cobalt metal monoliths leads to rapid oxidization. In preliminary work we have shown that such nickel monoliths can be reduced by hydrogen to give catalytically active surfaces with sufficient mechanical strength to allow their use as catalysts.<sup>31</sup>

We also assess the impact of annealing the monoliths during nanocasting. Such annealing improves the mechanical stability of the nanocast monoliths, but adversely impacts the surface area and fidelity of the replication. These and other properties are evaluated in terms of a comprehensive model for nanocasting into mesoporous silica templates which draws from the well developed literature of supported catalysts to provide a unifying model for such processes. The monolithic nature of the template allows for the assessment of how transport of reactants and products within such hierarchically porous materials impacts the final product. The importance of such transport phenomena in nanocasting has recently been highlighted by nanocasting into powders, where such seemingly arbitrary details as the shape of the container

---

<sup>1</sup> In this article, the terms aggregate and agglomerate will refer to the IUPAC definition used in catalysis. Therefore, an aggregate is defined as a cluster of the smallest identifiable particles fused together such that they are resistant to breakage by mechanical means. An assemblage of aggregates is an agglomerate. Such agglomerates *can* be mechanically disrupted into their constituent aggregates.

was found to alter the nature of the products observed.<sup>32</sup> The control of transport properties available in monolithic templates provides an excellent foundation for systematically exploring such effects.

### 4.3 Experimental

Silica monoliths were prepared according to the methods of Småt et al.<sup>33</sup> Tetraethylorthosilicate (TCI America), 30% nitric acid, deionized water, polyethylene glycol, MW = 35,000 g/mol (Sigma-Aldrich), and OTAB (Alfa Aesar) were mixed in the following molar ratio, 1:0.25:14.7:5.4 x 10<sup>-4</sup>:0.1. The solution was transferred into a mold and allowed to gel for 72 hours at 40 °C. Monoliths were then aged in 1 M ammonium hydroxide at 90 °C overnight followed by neutralization in 0.1 M nitric acid, rinsing three times with deionized water, three times with acetone, and dried at 40 °C for 72 hours. Finally, the silica monoliths were calcined at 550 °C for 5 hours with a ramp rate of 1 °C/min.

Aqueous solutions of nickel nitrate hexahydrate (Fisher), cobalt nitrate hexahydrate (Fisher), and silver nitrate (Alfa Aesar) were prepared having concentrations of 4.6 M, 4.5 M, and 6.6 M, respectively. Silica monoliths to be impregnated were degassed and held under vacuum during solution infiltration. After the first impregnation, monoliths appeared translucent and any excess solution was removed.

The impregnated monoliths were dried at 150 °C for 10 hours either under air or N<sub>2</sub> flow to produce the oxides, or under 5% H<sub>2</sub> in N<sub>2</sub> if the final product was to be the metal. For formation of oxide monoliths, the cobalt nitrate or nickel nitrate impregnated monoliths were then heated to 250 °C for 4 hours under nitrogen or air flow, respectively. Preliminary experiments for producing metal replicas indicated that in order to maintain the best replication for each metal and prevent excessive sintering, different conditions were needed for each metal.

The dried cobalt nitrate impregnated replicas were heated at a rate of 1 °C/min to 400 °C for 20 hours. Nickel nitrate impregnated monoliths were heated at a rate of 1 °C/min to 350 °C and held for 10 hours. Silver nitrate impregnated monoliths were heated at a rate of 1 °C/min to 250 °C held for 10 hours.

These steps of vacuum solution infiltration, drying, and decomposition/reduction cycles were repeated until the surfactant mesopore volume was theoretically filled. The amount of theoretical filling of the silica surfactant mesopores was based on the volume of nitrogen adsorbed at 0.6  $P/P_0$  in nitrogen physisorption measurements for the bare silica monolith. Adjustments for the change in density from the impregnated salt to the metal/metal oxide were made. This required 5 cycles for the nickel and cobalt replicas, 3 cycles for the oxide replicas, and 2 cycles for the silver replica. An annealing step was added to some materials to observe the effects of additional heating on replication. Samples were heated to 550 °C at 1 °C/min and held at 550 °C for 5 hours in air to produce cobalt oxide and 5 %  $H_2$  in  $N_2$  for metals. NiO replicas were prepared by heating to 600 °C for 4 hours at a rate of 1 °C/min in air to obtain the green stoichiometric oxide.

The silica template was removed with a 3 M aqueous KOH etch at room temperature for 24 hours for all replicas except nickel oxide. KOH was chosen because it etches away the silica at room temperature, which made working with the metal replicas under nitrogen less difficult. The etchant for nickel oxide was 1 M NaOH at 80 °C to reduce the amount of nickel hydroxide formed. The etching step was repeated to ensure complete silica removal and the replicas were rinsed until a neutral pH was achieved. Special care was taken to minimize the amount of oxygen exposure of the metal replicas.

Each sample was characterized by Scanning Electron Microscopy (SEM) on a JEOL-7000 FE SEM equipped with an Oxford Energy Dispersive Spectroscopy (EDS) detector for elemental analysis. Further analysis was performed using X-ray Diffraction (XRD) with a Bruker D8 Discover with GADDS X-ray diffractometer (wavelength Co K $\alpha$ ).

Additional surface characterization was performed via nitrogen physisorption at 77 K in helium mode with a NOVA 2200e surface area and pore analyzer purchased from Quantachrome Instruments. Isotherms were analyzed with Quantachrome's NovaWin software version 10.01. The linear region of the BET equation between 0.05 and 0.3 P/P<sub>0</sub> was used to determine specific surface area and the silica Non-Local Density Functional Theory (NLDFT) cylindrical pore kernel was applied to the adsorption branch to determine the pore size distribution. The fitting errors between the NLDFT model used and our measured samples were less than 1% in all cases, and thus deemed appropriate for our materials.<sup>34</sup> Surfactant mesopore volume, templated mesopore volume, and total pore volume were determined at 0.6, 0.8, and 0.99 P/P<sub>0</sub>, respectively.<sup>2\*</sup>

#### **4.4 Results**

Figure 4.1 shows images of the parent silica monoliths and the oxide and metal replicas. Some shrinkage is noticeable, particularly in the case of the metals. All replicas were mechanically stable although the green nickel oxide monolith, produced by annealing at 600 °C, fell apart upon etching and resulted in large (mm-sized) pieces. The cobalt and nickel replicas were mechanically robust, while the silver replica was very soft, with simple finger pressure being sufficient to deform the monolith. However, the nickel and cobalt replicas were both very

---

<sup>2</sup> Gas adsorption isotherms for the various materials composites described are available in supplementary information. Where referred to in the text these figures are cited as "Figure 4.S#".

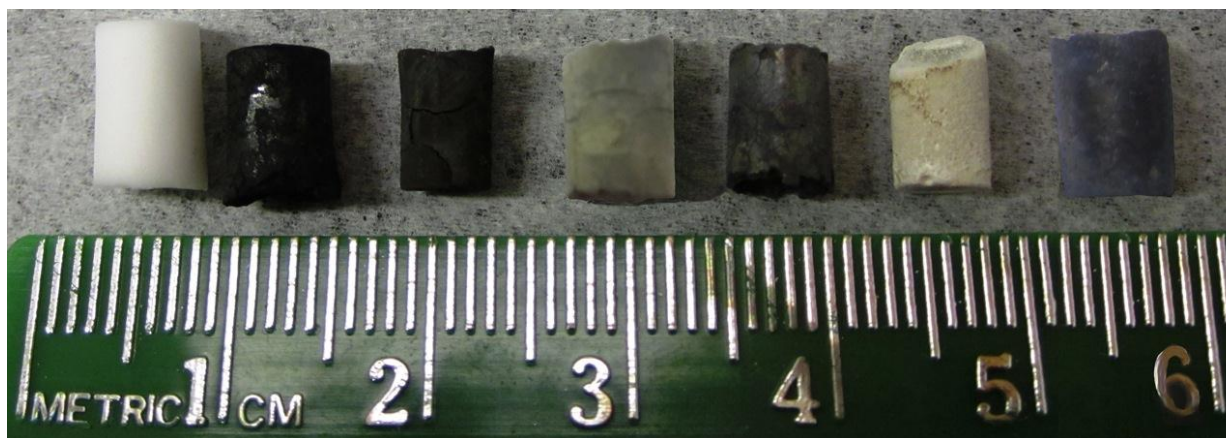


**Figure 4.1.** Parent Silica Monolith and Replicas. Order from left to right: silica, cobalt oxide, cobalt, stoichiometric nickel oxide composite, nickel, silver and non-stoichiometric nickel oxide.

oxygen sensitive and oxidized quickly if exposed to air. This oxidation produced a considerable amount of heat, which causes cracks to form on the surface of the monolith. The results pertaining to the silica monolith and each type of replica are listed in individual sections below. SEM images of the parent silica monolith and the  $\text{Co}_3\text{O}_4$  and nickel oxide replicas can be seen in Figure 4.2. Figure 4.3 contains the SEM images of the metal replicas. XRD data for each replica is graphed in Figure 4.4. Nitrogen sorption isotherms and NLDFT pore size distributions for the silica monolith and the oxide replicas are located in Figure 4.5, and those for the metal replicas in Figure 4.6. BET surface area, pore volume, and the NLDFT pore size distribution for the parent silica monolith and the replicas are listed in Table 4.1.

#### 4.4.1 $\text{SiO}_2$ Monolith

Silica macropores, visible in the SEM image in Figure 4.2a, are composed of mesoporous particles. The crevices between these mesoporous particles form the textural mesopores, which can be seen in the SEM image in Figure 4.2b. The silica isotherm, shown in Figure 4.5, exhibits two regions of increased capillary condensation. The first in the low pressure range is due to the

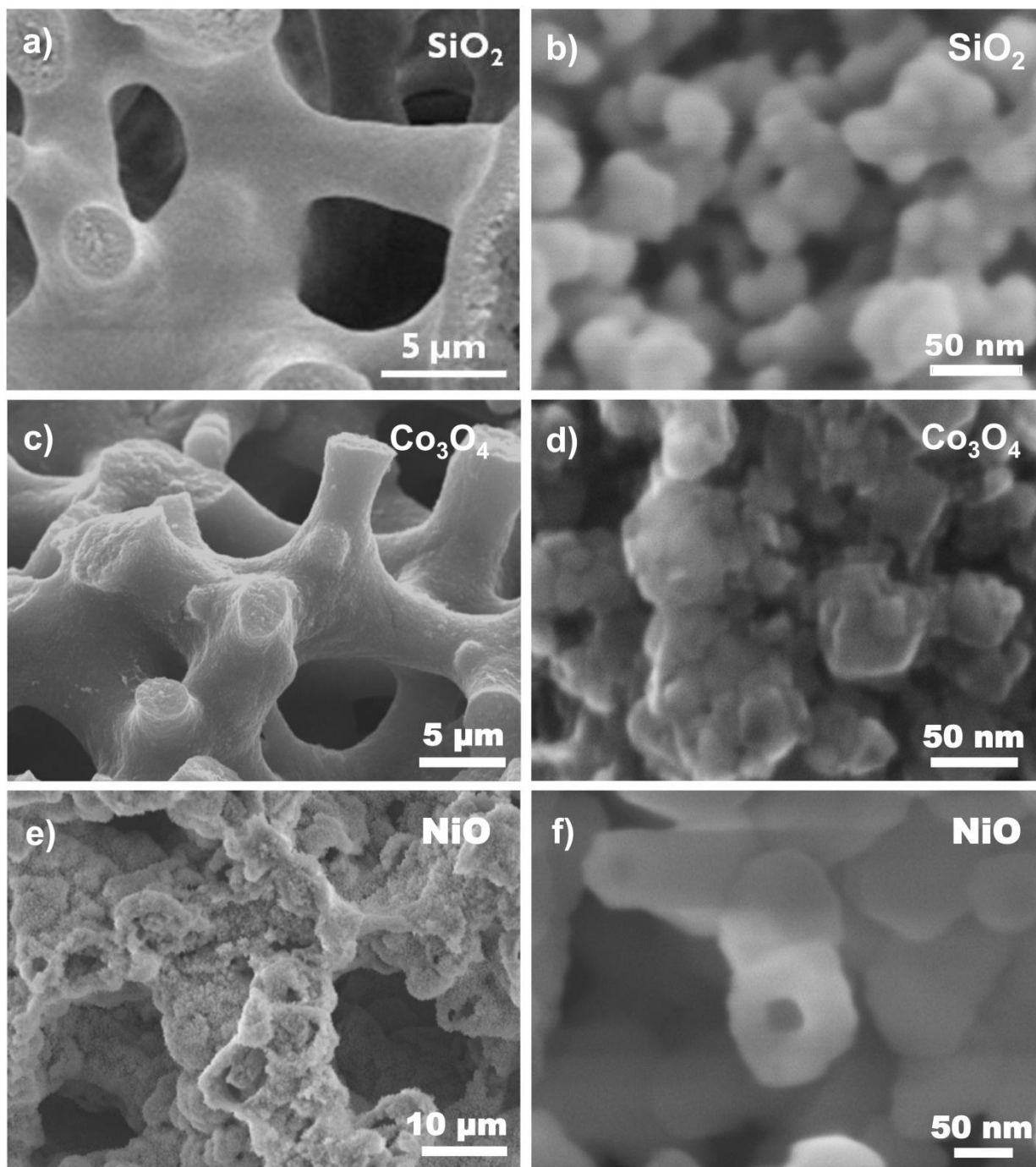


**Figure 4.2.** SEM Images of Silica (a) and (b), Cobalt Oxide (c) and (d), and Nickel Oxide (e) and (f) Monoliths at Micrometer and Nanometer Scales.

**Table 4.1. Nitrogen Sorption and X-ray Diffraction Data**

Sample	BET Surface Area		Mesopore Volume <sup>a</sup>		Total Pore Volume		NLDFT Pore Size	Crystallite Size
	(m <sup>2</sup> /g)	(m <sup>2</sup> /cm <sup>3</sup> )	(cm <sup>3</sup> /g)	(cm <sup>3</sup> /cm <sup>3</sup> )	(cm <sup>3</sup> /g)	(cm <sup>3</sup> /cm <sup>3</sup> )	(nm)	(nm)
SiO <sub>2</sub>	628	1382	0.56	1.24	1.27	2.79	4.4	-
Co <sub>3</sub> O <sub>4</sub> -SiO <sub>2</sub>	152.5	-	0.12	-	0.22	-	4.4	-
Co <sub>3</sub> O <sub>4</sub> -SiO <sub>2</sub> -A	156.6	-	0.13	-	0.21	-	4.4	-
Co <sub>3</sub> O <sub>4</sub>	140.7	860	0.15	0.94	0.38	2.32	6.1	14
Co <sub>3</sub> O <sub>4</sub> -A	106	648	0.14	0.83	0.31	1.89	6.6	-
Co-SiO <sub>2</sub>	75.9	-	0.05	-	0.10	-	3.2	-
Co-SiO <sub>2</sub> -A	65.1	-	0.04	-	0.09	-	3.2	-
Co	41.9	373	0.04	0.36	0.06	0.55	6.1	23
Co-A	37.0	329	0.04	0.37	0.08	0.74	5.9	-
NiO-SiO <sub>2</sub>	178.3	-	0.14	-	0.27	-	4.4	-
NiO-SiO <sub>2</sub> -A	140	-	0.12	-	0.24	-	4.4	-
NiO	32.2	215	0.03	0.18	0.06	0.38	3.8	16
NiO-A	41.4	276	0.03	0.22	0.06	0.43	3.2	19
Ni-SiO <sub>2</sub>	114.7	-	0.08	-	0.16	-	4.1	-
Ni-SiO <sub>2</sub> -A	86.8	-	0.06	-	0.11	-	3.8	-
Ni	13.7	122	0.02	0.16	0.05	0.45	6.1	27
Ni-A	18.8	168	0.02	0.20	0.04	0.36	6.1	-
Ag-SiO <sub>2</sub>	176	-	0.16	-	0.24	-	4.3	-
Ag	2.2	23.1	0.002	0.02	0.01	0.14	35	33

<sup>a</sup> the volumes at 0.6 and 0.8 P/P<sub>0</sub> were used to determine the relevant mesopore volumes. For silica and composites 0.6 P/P<sub>0</sub> was used. For replicas 0.8 P/P<sub>0</sub> was used. For the silica and composites the surfactant mesopores have a constant diameter of 4.4 nm, however because the silica wall thickness is variable the pore size distribution in the replicas is broader requiring a higher P/P<sub>0</sub> to capture the entirety of the distribution.

surfactant templated mesopores<sup>3</sup> and the second is attributed to the textural mesopores. The pore size distribution determined by NLDFT for the parent silica monolith is shown in Figure 4.5 and shows the presence of surfactant templated mesopores with a pore size distribution centered at 4.4 nm. There is also a broader peak due to textural mesopores in the range 10 to 60 nm. This is agreement with our previously published work.<sup>30,33</sup>

#### 4.4.2 Co<sub>3</sub>O<sub>4</sub> Monolith

Previous experiments revealed that decomposition under nitrogen flow gave significantly better replication than under air, both visually from SEM images and from higher BET surface area.<sup>35</sup> Hence, this method was used to produce the cobalt oxide replicas reported herein. Both XRD (Figure 4.4) and EDS confirmed pure, crystalline Co<sub>3</sub>O<sub>4</sub>. SEM analysis (Figure 4.2c) confirmed good replication of the silica macropores. Cross-sections through ligaments (Figure 4.2d) also showed complete replication throughout the ligaments with no voids in the ligament being observed. SEM (Figure 4.2d) also showed the presence of coarse agglomerates consisting of smaller aggregates 20-30 nm in diameter, similar to those seen in the parent silica (Figure 4.2b). The nitrogen physisorption isotherm and NLDFT pore size distribution for the Co<sub>3</sub>O<sub>4</sub> replica are given in Figure 4.5. The broader pore size distribution of the replica compared with the parent silica monolith is to be expected, since the pores in the silica were surfactant templated and so of very similar diameter. However, the wall thickness in the silica was variable, since the pores were not ordered. This has been observed for replication of similar silica monoliths in carbon and tin oxide.<sup>26,36</sup> In the replication process the template pores are expected to become filled with the cobalt oxide, while removal of the silica leaves variable spaces between the cobalt oxide nanostructures. The surface area for the cobalt replica (Table

---

<sup>3</sup> in the text that follows surfactant templated mesopores will be abbreviated as surfactant mesopores in the interest of brevity.

4.1) was lower on a per gram basis than that of the parent monolith:  $140 \text{ m}^2/\text{g}$  vs.  $628 \text{ m}^2/\text{g}$ . This is to be expected given the higher density of the  $\text{Co}_3\text{O}_4$  ( $6.11 \text{ g}/\text{cm}^3$ ) compared to silica ( $2.2 \text{ g}/\text{cm}^3$ ). A more useful comparison is on a surface area/volume basis comparing the surface area of the surfactant templated mesopores to the total surface area of the replica. The  $\text{Co}_3\text{O}_4$  replica had a surface area of  $860 \text{ m}^2/\text{cm}^3$  compared with that of the silica surfactant templated mesopores of  $925 \text{ m}^2/\text{cm}^3$ , as determined from the t-plot. While one might think that perfect replication should yield essentially the same surface area, this is not necessarily true since nanocasting produces a negative replica of the mesopore structure. The pore volume determined at relative pressures ( $P/P_0$ ) below 0.8 is significantly lower in the  $\text{Co}_3\text{O}_4$  replica than in the silica template. This could reflect either a less than perfect replication, or that the silica of the template occupies a smaller volume than the volume of the mesopores, or most likely a combination of both. We know from carbon replication of similar silica monoliths that the surfactant mesopore walls possess slightly less volume than the surfactant mesopores themselves; however, the loss in volume is not as large as what was observed here for the  $\text{Co}_3\text{O}_4$  replica. Even so, the decrease in total porosity for the replica compared to the silica template,  $0.47 \text{ cm}^3/\text{cm}^3$ , is mostly due to a decrease in porosity,  $0.30 \text{ cm}^3/\text{cm}^3$ , in the templated mesopore region.

In order to gain some insight into the nature of the replication process, nitrogen physisorption isotherms for silica- $\text{Co}_3\text{O}_4$  composites both before and after annealing at  $550 \text{ }^\circ\text{C}$  were obtained. These isotherms (Figure 4.S1) showed little difference in shape or volume of nitrogen adsorbed. Once the silica is removed, there is a larger difference between the two samples.  $\text{Co}_3\text{O}_4$  without annealing exhibits a larger volume of nitrogen adsorbed throughout the isotherm indicating that the annealing step causes a loss of surface area. Additionally, the pore size distribution for the non-annealed samples (Figure 4.5, and Figure 4.S1) is smaller and

narrower than that from the annealed samples. These observations indicate that significant sintering occurred during annealing.

#### 4.4.3 Cobalt Metal Monolith Synthesis

Figures 4.3a and 4.3b show SEM images of cobalt metal monoliths prepared by reduction under hydrogen/nitrogen. XRD (Figure 4.4) and EDS analysis confirmed that cobalt metal was produced. However, some cobalt oxide was present due to surface oxidation. SEM images of the cobalt metal show good macropore replication (Figure 4.3a). A cross section of a ligament revealed that the inside of the ligament is fairly dense (Figure 4.3b) similar to what was seen with cobalt oxide. However, unlike the cobalt oxide replicas, and the silica template, there are larger structures towards the edge of the ligament. We believe that these are produced by excessive sintering of the cobalt. EDS indicates that these structures are primarily cobalt rather than cobalt oxide, and so they are not produced by surface oxidation.

Nitrogen sorption (Figure 4.5 and Figure 4.S2) illustrates that nitrogen uptake takes place gradually across the entire adsorption branch of the isotherm indicative of a broad mesopore distribution. Significant hysteresis was seen between the adsorption and desorption branches followed by the sharp forced closure of the desorption branch, which can be seen at 0.4  $P/P_0$ . The pore size distribution (Figure 4.6) is broader than that of the silica template, as is expected from the discussion above, but is also broader than that in the  $\text{Co}_3\text{O}_4$  replica. Unlike any of the other composites, the cobalt-silica composites show no sign of unfilled silica surfactant mesopores. This indicates that the mesopores have been completely filled by Co, are entirely blocked off, or have been destroyed. The mesopore volume decreases significantly in the

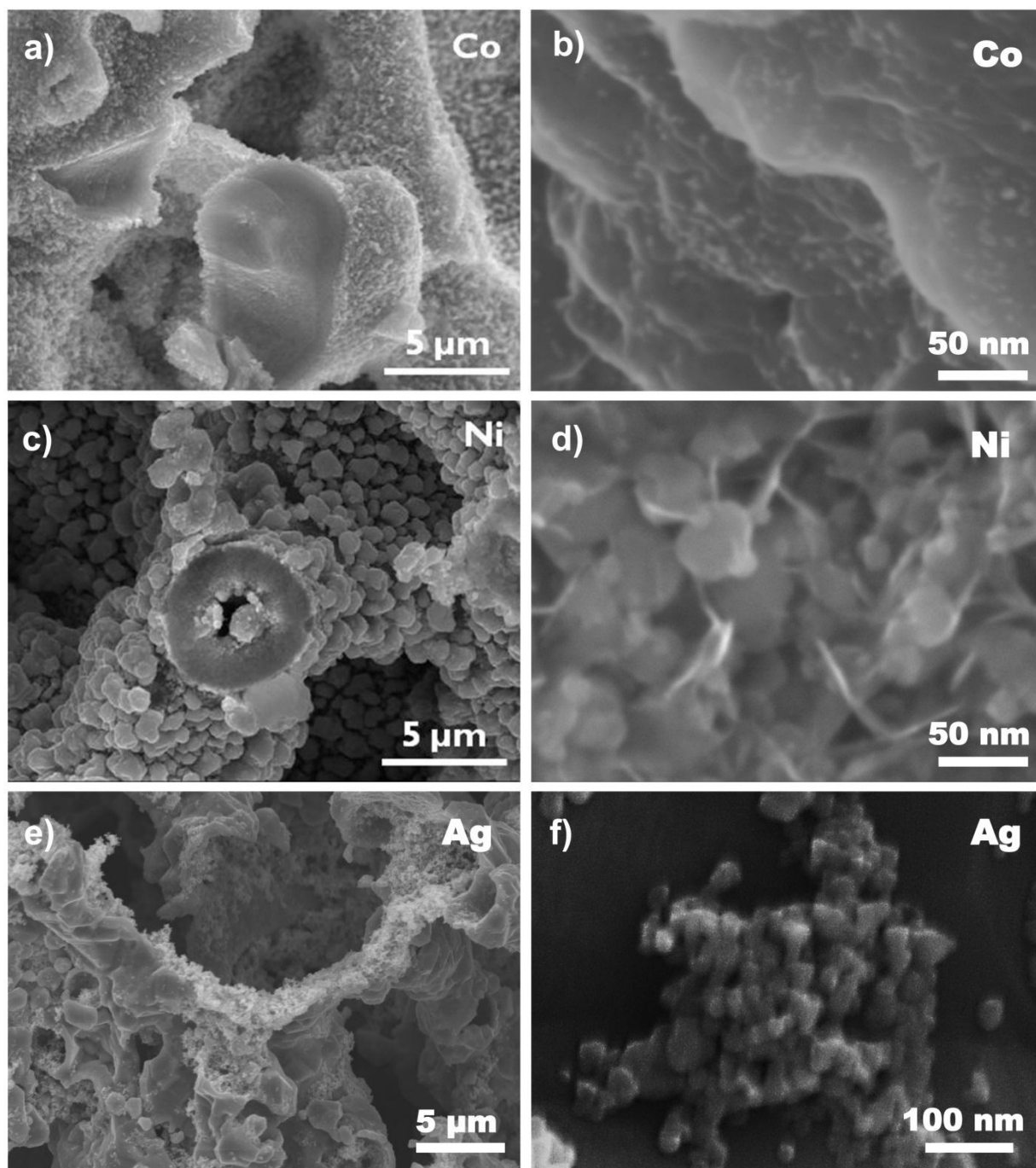


**Figure 4.3.** SEM Images of Nickel (a) and (b), Cobalt (c) and (d) and Silver (e) and (f) Replica Monoliths at Micrometer and Nanometer Scales.

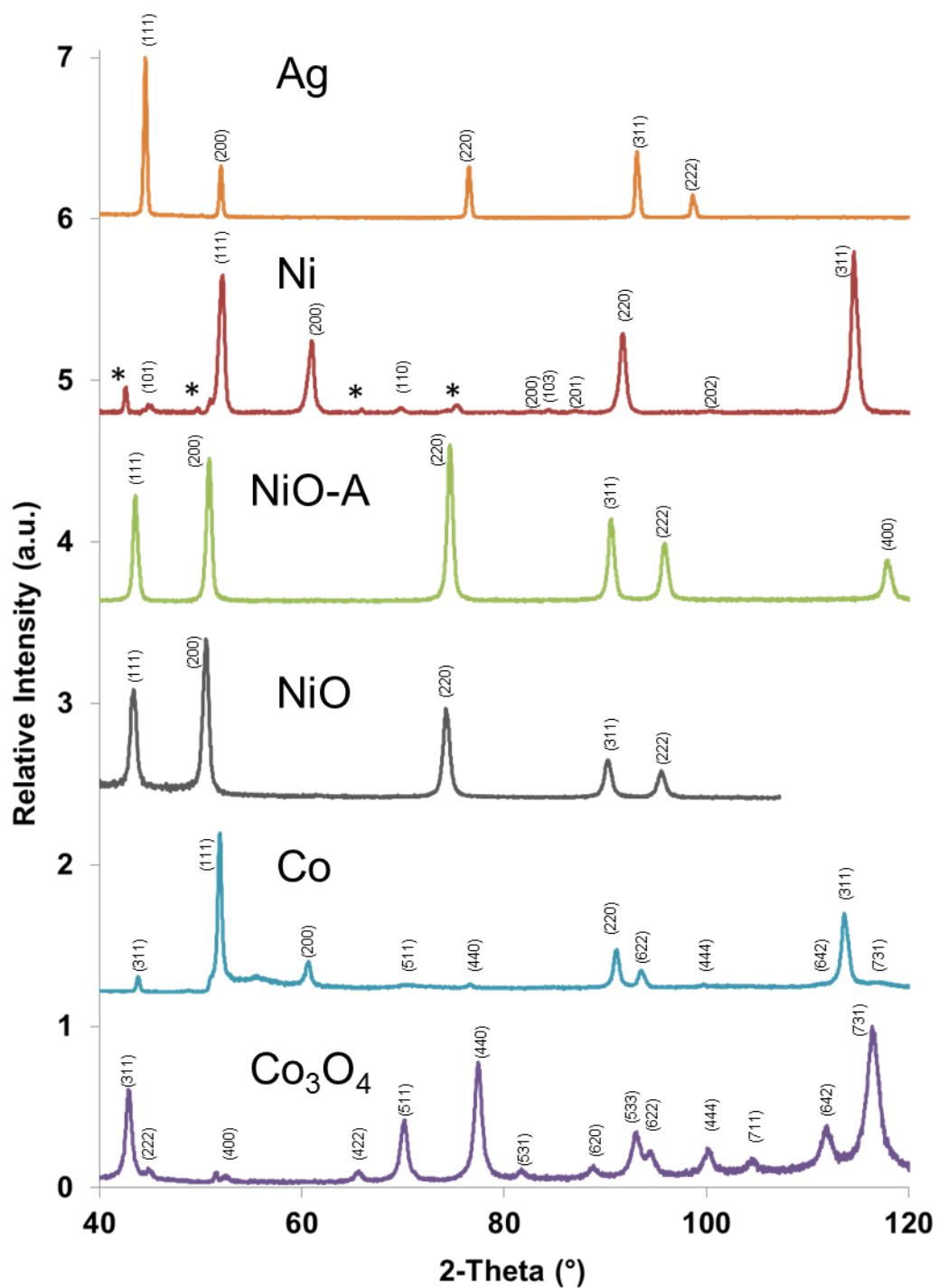
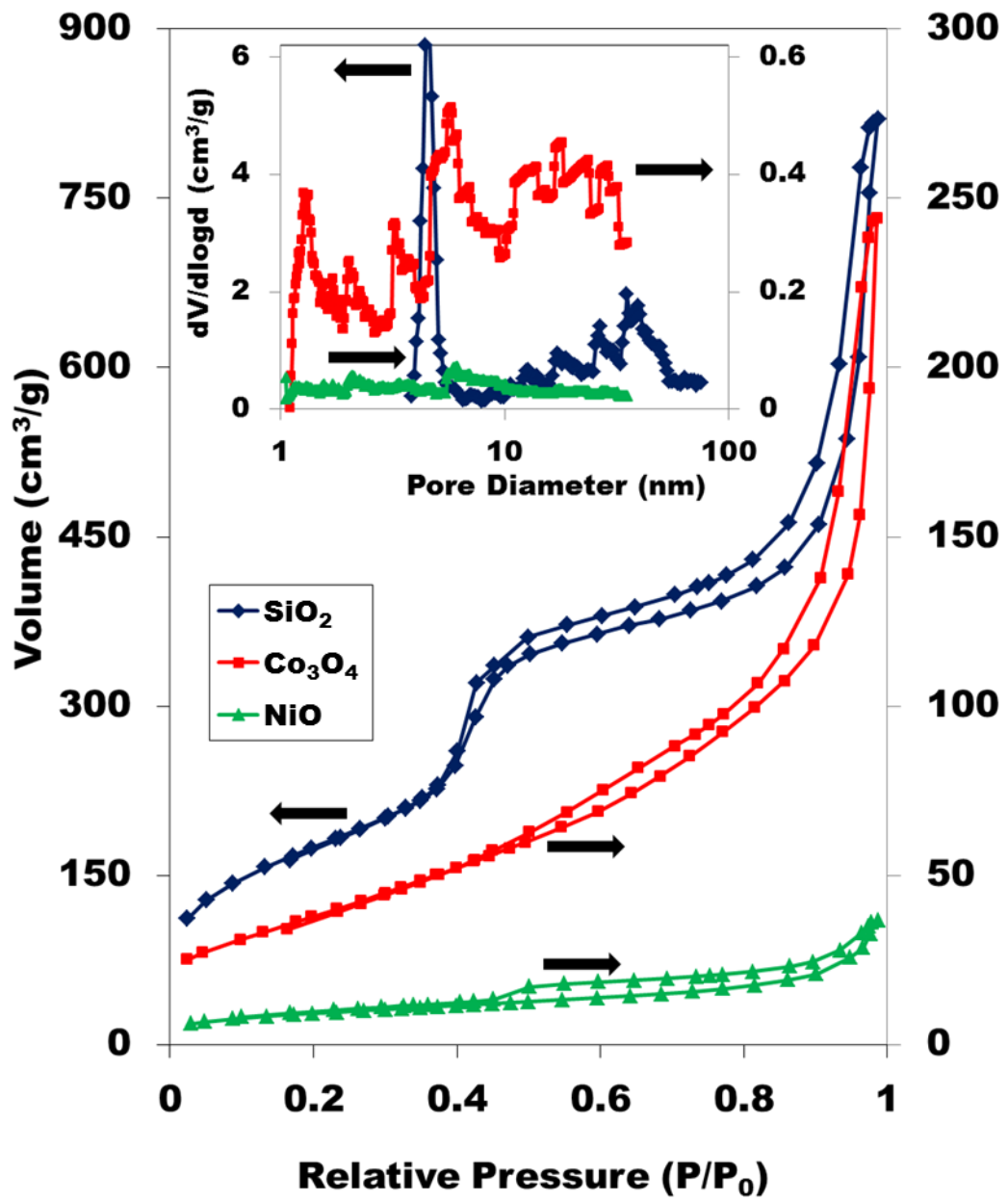


Figure 4.4. XRD of Replicas. (\*) indicate reflections from the sample holder.



**Figure 4.5.** Nitrogen Physisorption Isotherms and NLDFT Pore Size Distributions for Silica, Cobalt Oxide and Nickel Oxide Monoliths. Arrows point to axis.

composite and the sharp silica peak in the pore size distribution at 4.4 nm (Figure 4.6) appears to shift to 3.2 nm and broadens considerably (Figure 4.S2). Upon annealing, the surface area and pore volume decreased and the pore size distribution narrowed slightly when compared to the non-annealed composite. Once etched, the non-annealed cobalt monolith had a surface area of 42 m<sup>2</sup>/g and the annealed cobalt monolith has a slightly lower surface area of 37 m<sup>2</sup>/g. The sharp peak at 3.2 nm in the NLDFT pore size distribution of the composite (Figure 4.S2) disappears leaving a broad pore size distribution that begins at about 2 nm and extends to about 15 nm (Figure 4.6). The annealed cobalt sample exhibits a pore size distribution (Figure 4.S2) that begins at 3 nm and extends to 20 nm, and is slightly broader than that of the non-annealed sample. While the mesopore volume at 0.8 P/P<sub>0</sub> is similar for the 2 samples, the total pore volume after annealing and etching is notably higher (0.74 cm<sup>3</sup>/cm<sup>3</sup> in the annealed sample vs. 0.55 cm<sup>3</sup>/cm<sup>3</sup> in the non-annealed sample). This indicates that the higher total pore volume in the annealed sample is due to larger volumes of the larger pores.

#### 4.4.4 Synthesis of Nickel Oxide Monoliths

The nickel oxide monoliths produced by decomposing nickel nitrate at 250 °C were a black color consistent with the formation of a slightly non-stoichiometric nickel oxide.<sup>37</sup> After annealing the composite was observed to have become a green color, indicating the formation of the stoichiometric nickel (II) oxide. Removal of the silica by etching produced a free-standing monolith in the case of the non-stoichiometric nickel oxide as shown in Figure 4.1. The green stoichiometric nickel oxide did not produce a complete monolith after the silica was removed, breaking into a number of smaller pieces. For both the black and green nickel oxides, visual analysis showed that the color was constant throughout the entire volume of the sample.

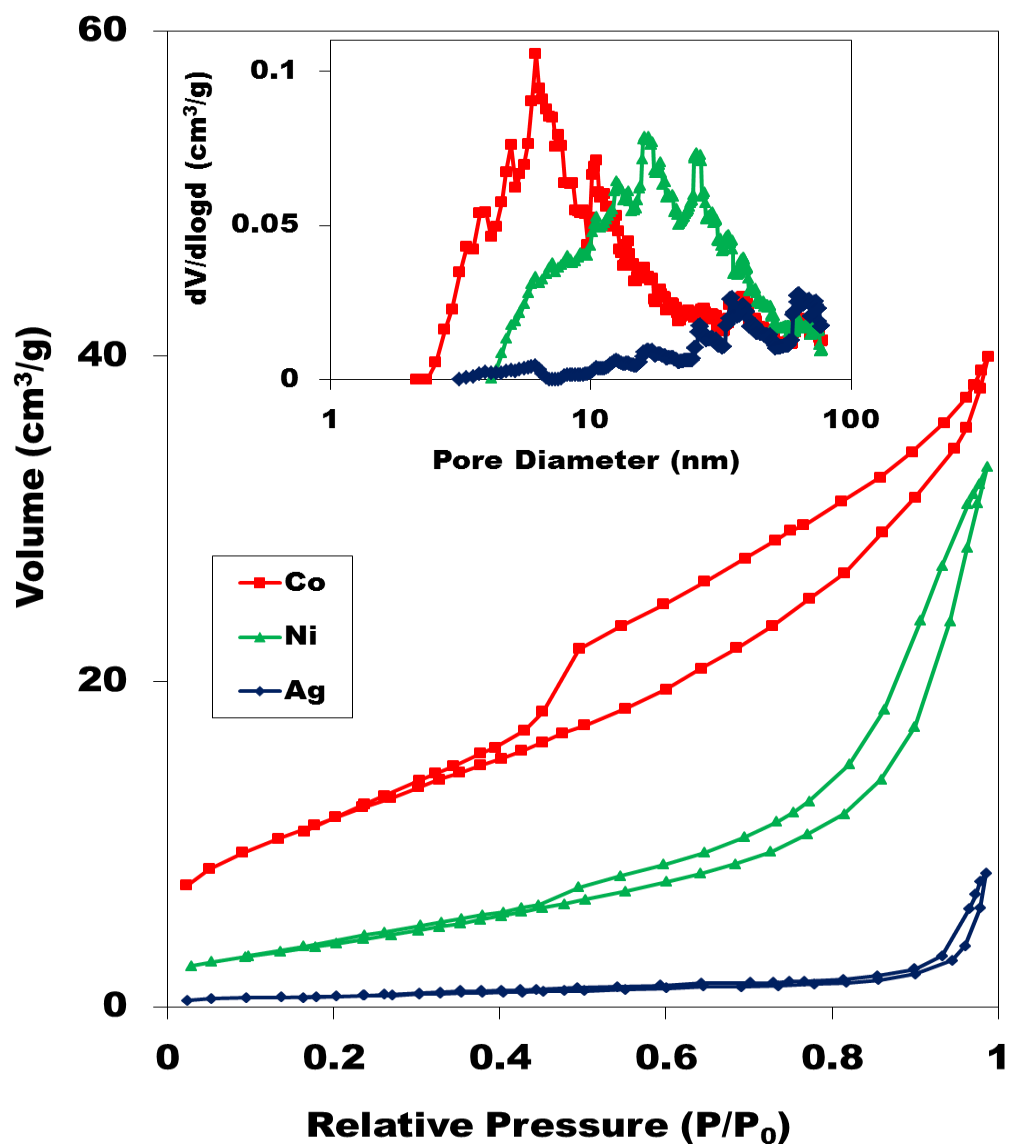


**Figure 4.6.** Nitrogen Physisorption Isotherms and NLDFT Pore Size Distributions for Cobalt, Nickel and Silver Monoliths.

XRD (Figure 4.4) and EDS from the black, non-stoichiometric nickel oxide indicate that pure nickel (II) oxide was produced and isolated. Analysis of the SEM image (Figure 4.2e) shows formation of a positive replica of the macropores. However, the nickel oxide surface appears much rougher than does that of the parent silica. Upon zooming in (Figure 4.2f), particles similar in shape to those seen in SEM images of the silica (Figure 4.2b) are apparent. Figure 4.5 shows the nitrogen physisorption isotherm and pore size distribution for nickel (II) oxide. The isotherm for NiO is clearly very different from that of silica and  $\text{Co}_3\text{O}_4$  in that there is very little increase in nitrogen adsorption until  $P/P_0$  reaches 0.8. Therefore, a pore size distribution without much small mesopore volume is expected. Given this difference in behavior, consideration of the isotherm behavior for the NiO/silica composites is instructive (Figure 4.S3). A priori, one would expect to see the same isotherm behavior with the NiO/silica composites as the cobalt oxide composites. However, before annealing, the nickel oxide was the black non-stoichiometric oxide which makes this comparison a little more difficult since the two replicas are chemically different. Even though an obvious color and reactivity difference was present, XRD data indicated that both nickel oxides had approximately the same bulk density. Upon comparing the composites, it appeared that less surfactant and textural mesopore volume were accessible after annealing. This was also observed in the NLDFT pore size distribution of the two composites (Figure 4.S3). Both composites have a sharp silica surfactant mesopore peak at 4.4 nm, but the non-annealed composite is broader at the base and has some microporosity. Once the composite was annealed, the pore size distribution became narrower and the microporosity disappeared. Both nickel oxides exhibit similar NLDFT pore size distributions. Interestingly, the mesopore volume, the total pore volume, and the BET surface area all increase

after the conversion to green NiO. Detailed consideration of these trends will be deferred until the discussion section.

#### 4.4.5 Synthesis of Nickel Monoliths

Nickel was formed by decomposing the nickel nitrate at 550 °C under H<sub>2</sub>/N<sub>2</sub>. XRD data (Figure 4.4) shows the presence of nickel peaks confirming the presence of nickel metal, but it also revealed peaks of nickel hydroxide. The presence of nickel hydroxide indicates that some nickel oxide was formed in the nickel/silica composite and the more concentrated potassium hydroxide etchant caused the formation of nickel hydroxide. EDS analysis supports these findings indicating the presence of nickel hydroxide based on the nickel:oxygen ratio observed. SEM (Figure 4.3c) shows that at the macropore scale there is reasonably good replication of the silica template, although as with cobalt and nickel oxide there is a difference in the surface morphology of the ligament when compared to the smooth surface of the parent silica. There appears to be growth of large platelets on the surface of the ligaments, which cannot be due to replication of the silica template as the silica does not possess these types of structures. The SEM image shows that the replication within a silica ligament is dense, although the center of the ligament shown does not appear to be completely replicated. At the textural mesopore level (Figure 4.3d) replication appears to be relatively complete. The platelets may correspond to nickel oxide or nickel hydroxide formation at the surface. This morphology has also been observed for nickel oxide prepared by other methods.<sup>38-40</sup>

The nitrogen physisorption isotherm (Figure 4.6) shows significantly less nitrogen adsorbed in comparison to nickel oxide and cobalt metal. The pore size distributions (Figure 4.6) show a significantly broader pore size distribution for the nickel than for cobalt. This is also

consistent with the surface area and the mesopore volumes (Table 4.1) which are also significantly lower for nickel than for cobalt.

The nitrogen physisorption isotherms of the nickel-silica composites before and after annealing exhibit interesting behavior (Figure 4.S4). The non-annealed nickel composite has an isotherm that shows a more gradual nitrogen uptake in the surfactant and textural mesopore regions than the parent silica. Once annealed, the nitrogen uptake in this region is even more gradual. The NLDFT pore size distributions for these two composites (Figure 4.S4) show a downward shift from that of the parent silica. For the non-annealed sample the peak occurs at 4.1 nm, while for the annealed sample the peak shifts down even further to 3.8 nm. After the silica is removed from the non-annealed sample, a very broad pore size distribution is observed from 3.8 nm to 35 nm. The surface area of this sample is 14 m<sup>2</sup>/g and the pore volume is 0.05 cm<sup>3</sup>/g. Interestingly, the etched sample that was annealed has an increased surface area of 19 m<sup>2</sup>/g with a pore volume of 0.04 cm<sup>3</sup>/g.

#### 4.4.6 Synthesis of Silver Monolith

XRD (Figure 4.4) and EDS analysis confirmed the presence of pure silver. SEM images (Figure 4.3e) confirmed approximate positive replication of the macropores. The macropore walls consisted of large sintered crystallites with small nanoparticles ranging from 20 to 50 nm in diameter inside the walls (Figure 4.3f). In contrast to the nickel and cobalt cases where the interior of the macropore walls appeared dense, in the case of silver the interior of the macropore walls appeared to be only partially replicated. The nitrogen physisorption isotherm of the silver composite (Figure 4.S5) showed that very little pore filling occurred. There was also no observed shift in pore size distribution. Annealing of the composite was attempted, but resulted in the excessive cracking of the silica monolith, limiting work to non-annealed samples. After

removal of the silica, the surface area obtained by nitrogen physisorption for the silver replica was  $2.2 \text{ m}^2/\text{g}$  with a pore volume of  $0.01 \text{ cm}^3/\text{g}$ . This low surface area may have been caused by excess sintering and further aggregation during the degassing process even though extensive efforts were made to minimize these effects. The density of silver metal is very high,  $10.5 \text{ g}/\text{cm}^3$ , and adjusting for this results in a surface area of  $23 \text{ m}^2/\text{cm}^3$  and  $0.14 \text{ cm}^3$  void volume per  $\text{cm}^3$  of silver.

#### **4.5 Discussion**

Significant differences in the fidelity of replication are observed between cobalt oxide and nickel oxide, between the different metals and between the metals and the oxides. For  $\text{Co}_3\text{O}_4$  the surface area, pore volume and SEM images all suggest that a very good replica of the silica template is formed. For nickel oxide the narrower pore size distribution and the shift to smaller average pore size suggest that at the mesopore level something other than true replication is occurring. For the metals, the replication appears to become steadily worse, in the order of cobalt, nickel and silver. These differences in behavior are not due to differences in amount of metal or metal oxide introduced to the silica template, as in each case the total amount added was only sufficient to fill the surfactant mesopores. Under the conditions presented here, except possibly for  $\text{Co}_3\text{O}_4$ , it does not seem that replication occurs in the classical sense of simply filling the smallest void space for all materials. These differences could be the results of loss of fidelity at a number of different points in the process: (1) solution infiltration, (2) movement of the nitrate salt/salt solution during the thermal decomposition, (3) movement of the metal or metal oxide formed during the decomposition and (4) movement of the metal or metal oxide during an annealing step. The factors affecting these processes will now be addressed.

#### 4.5.1 Solution Infiltration

It is generally assumed that in the nanocasting infiltration process the precursor solution is drawn into the surfactant mesopores by capillary action. Based on our previous work and that of many others,<sup>41</sup> we expect that the aqueous precursors would wet the silica surface well and so would fill the surfactant mesopores. The use of vacuum significantly accelerates the process of pore filling, and replicas prepared without this show clear evidence of unfilled surfactant mesopores. The high surface area of the cobalt oxide monolith also argues for the completeness of mesopore filling.

It would be expected that as the water is removed, the metal nitrate salts would be deposited within the surfactant mesopores. However, the drying and decomposition of metal nitrates can be a relatively complicated process which is still not completely understood. In this work the monoliths were heated directly to the decomposition temperature, bypassing a separate drying step.

#### 4.5.2 Thermal Decomposition

Nickel nitrate hexahydrate is reported<sup>42-46</sup> to go through a series of dehydration steps, and the mechanism of the decomposition is reported by a number of authors to depend upon the composition and pressure of the atmosphere that the decomposition is carried out under<sup>42, 43, 47-49</sup>. This sensitivity is highlighted in a recent report showing that even the shape of the container used for carrying out metal oxide replication of mesoporous silica can impact the nature of the products.<sup>32</sup> For nanocasting of nickel oxide in SBA-15 mesoporous silica particles Sietsma et al.<sup>47,48</sup> report that in air more extensive migration of nickel oxide out of the mesopores is observed. Decomposition under helium is reported to give less migration and particle growth, with decomposition under hydrogen or nitric oxide (NO) giving yet smaller nanoparticles.<sup>49</sup> The

impact of the various atmospheres on the decomposition products is consistent with the improvement being due to scavenging of oxygen which otherwise appears to be catalytic for nickel nitrate decomposition. The decomposition of cobalt and silver nitrates have not been as extensively studied, but variation in products for cobalt nitrate hexahydrate with heating rate was observed.<sup>50</sup> Furthermore, the observation of a container effect for nickel oxide, cobalt(III) oxide and a number of other metal oxides<sup>32</sup> suggests that atmosphere and mass transport will generally impact the decomposition of transition metal nitrates. For nanocasting into porous silica monoliths this effect could potentially be larger or smaller than for nanocasting of mesoporous particles, depending upon exactly how the particles or monoliths were placed in a container. The hierarchical nature of the pore structure in the monoliths will provide more efficient mass transport than in a powder sample of similar geometry. However, if the particles were spread in a thin layer then mass transport will be faster in the powder.

#### 4.5.3 Movement of Metal and Metal Oxides

The other factor that needs to be considered is that wetting of the silica surface by the metal or metal oxide becomes important if the metal or metal oxide is at a temperature where it is mobile. Although, the temperatures required to fully decompose the metal nitrates are significantly lower than the melting points of the metals and oxides, it is likely that they are sufficiently high for some transport of material to occur. Upon decomposition or reduction of a metal nitrate salt on a surface, in most cases, a very small particle of metal or metal oxide will form. Nanoparticles will become mobile and can migrate, sinter, agglomerate and melt at significantly lower temperatures than their bulk counterparts. The minimum temperature at which a nanoparticle can become mobile on a surface is referred to as the Hüttig temperature.<sup>51</sup> This temperature is approximately 0.3 times the melting point of the bulk substance in degrees

Kelvin and is dependent on particle size. Heating above this temperature allows for atomic migration which can lead to the nanoparticle growth via Ostwald ripening where larger particles begin to form at the expense of smaller nanoparticles. Heating at temperatures that are half of the bulk melting temperature in degrees Kelvin results in melting of the nanostructure surface. This is referred to as the Tammann temperature.<sup>51,52</sup> Collected in Table 4.2 are the bulk melting, Tammann, and Hüttig temperatures for the metals and metal oxides investigated in this study. Under these conditions, the interaction of the metals and metal oxides with the silica template, specifically the degree of wetting of the silica surface by the metal/metal oxide, becomes important. If the metal/metal oxide wets the surface, any metal/metal oxide close to the mesopore opening will be drawn inward via capillary forces upon heating. As more metal/metal oxide is added with successive infiltration cycles, growth will occur in the mesopores. On the other hand, for metals/metal oxides that do not wet silica, the reverse will occur. The metal nitrate salt will be deposited preferentially inside the mesopores, but after decomposition, capillary forces will tend to force the metal/metal oxides out of the surfactant mesopores into the larger textural mesopores and eventually into the macropores.

**Table 4.2.** Melting Temperatures

Material	T <sub>melt</sub> (°C)	T <sub>Tammann</sub> (°C)	T <sub>Hüttig</sub> (°C)	T <sub>used</sub> (°C)	σ <sub>m-g</sub> (J/m <sup>2</sup> )
Co <sub>3</sub> O <sub>4</sub>	900 <sup>d</sup>	314	79	250	1.96 <sup>b</sup>
Co	1495 <sup>d</sup>	611	257	400	1.99 <sup>c</sup>
NiO	1955 <sup>d</sup>	841	395	250	3.5 <sup>b</sup>
Ni	1455 <sup>d</sup>	591	245	350	1.895 <sup>c</sup>
Ag	962 <sup>d</sup>	345	98	250	0.976 <sup>c</sup>
SiO <sub>2</sub>	1610 <sup>d</sup>	669	292	-	0.557 <sup>c</sup>

<sup>b</sup>from reference (69) <sup>c</sup>from reference (55) <sup>d</sup>from reference (70)

If the wetting of the silica surface is not favored, the contact angle of the metal or metal oxide with the silica surface will be greater than 90°. Previously, contact angle studies have been carried out for molten metals on silica substrates.<sup>53</sup> Sangiorgi et al. reported that all the metals investigated in their study had contact angles greater than 90° on silica, with silver being the highest at 140° and cobalt and nickel having similar contact angles of approximately 120°.<sup>54</sup> This suggests that the annealing of cobalt, nickel and silver should result in migration of the metal from the mesopores to the macropores. This should be most pronounced for silver, which has the highest contact angle, and so presumably would have the strongest driving force. Additionally, silver has the lowest Hüttig and Tammann temperatures of the metals in this study, further predicting that it would be quite mobile at the reduction temperature of 250 °C (Table 4.2). In fact, the annealing temperature of 550 °C is over 200 degrees above the Tammann temperature for silver; the cracking observed after annealing would therefore appear to result from excessive particle growth.

While this information is not well documented for transition metal oxides on silica, it is generally believed that oxides wet other oxides reasonably well and result in contact angles of less than 90°. <sup>55</sup> A qualitative estimate can be made from the surface energies of the bulk silica and the metal oxide. The interfacial free energy for the metal or metal oxide in contact with the silica is given as ( $\sigma_{s-m}$ ):

$$\sigma_{s-m} = \sigma_{m-g} + \sigma_{s-g} - U_{s-m} \quad \text{Eq. 4.1}$$

where  $\sigma_{m-g}$  is the surface energy of the metal or metal oxide in the given gaseous atmosphere,  $\sigma_{s-g}$  is the surface energy of silica under the same atmosphere, and  $U_{s-m}$  is the chemical energy between the silica and metal or metal oxide per unit area at the interface adjusted for any strain energy due to mismatches in lattice spacing. The surface energies for silica, cobalt, nickel and

the appropriate oxides are given in Table 4.2. For good replication of the mesoporous template, the oxides should wet the silica surface to fill the mesopores. If it is assumed that the surface energy of the metal or metal oxide is not strongly affected by the presence of the atmosphere, then the total free energy of formation of such replica films on the silica surface ( $\sigma_f$ ) can be expressed as twice the free energy of the metal/metal oxide interface ( $\sigma_m$ ) minus the chemical energy of the silica-metal/metal oxide interaction ( $U_{s-m}$ ) as seen in Equation 4.2.<sup>56</sup>

$$\sigma_f = 2\sigma_m - U_{s-m} \quad \text{Eq. 4.2}$$

Formation of a chemical compound at the interface can lead to larger values for  $U_{s-m}$ . For nickel, cobalt and silver, the  $\sigma_m$  as given in Table 4.2 is generally large. If the interaction between the metal and the silica substrate is small, as is typical for most metals then the metal will not wet the silica substrate. As a result the contact angle will exceed 90°, and above the Hüttig temperature minimization of energy will push the metal out of the pores. For cobalt and nickel oxides the surface energies are also high (Table 4.2), but  $U_{s-m}$  would be expected to be higher. There is also the possibility of formation of silicates at the interface, which would aid in spreading of the oxide. The free energy of formation of nickel silicate ( $\text{Ni}_2\text{SiO}_4$ ) from NiO and silica is reported<sup>56</sup> to be -8.3 kJ/mol at 600 °C. Similarly the free energy of formation of cobalt silicate ( $\text{Co}_2\text{SiO}_4$ ) from silica and CoO is reported to be -14.3 kJ/mol at 550 °C. Formation of  $\text{Co}_2\text{SiO}_4$  from  $\text{Co}_3\text{O}_4$  supported on silica is reported<sup>57</sup> to occur at 800 °C, accompanied by spreading of the cobalt across the silica surface. Similarly spreading of nickel oxide particles on silica support is reported<sup>58</sup> to occur at 600 °C. This would suggest that at these temperatures the cobalt and nickel oxides wet the silica support, and/or that formation of silicates facilitates such spreading.

The cobalt oxide composite was heated above both the Hüttig and Tammann temperatures of  $\text{Co}_3\text{O}_4$ , but still retained a reasonably high surface area. This suggests that for

$\text{Co}_3\text{O}_4$  the cobalt oxide/silica interactions are favorable to  $\text{Co}_3\text{O}_4$  wetting the silica surface. Similar behavior for nickel oxide was expected. SEM images of the nickel oxide showed large particles that appear to be replicating mostly the textural mesopores. Nitrogen sorption of the annealed composite does exhibit some filling of the surfactant mesopores, but not total filling. The difference in behavior could be due to differences in the strength of the silica/oxide interactions, either directly or possibly mediated by formation of a surface cobalt silicate, similar to what we have observed for nanocasting in zirconia.<sup>35</sup> However, in that work we saw evidence for zirconium silicate formation based on the retention of silicon after etching as detected by EDS. In this study neither the cobalt oxide nor the nickel oxide monoliths showed any evidence for formation of surface silicates. Another factor may be the difference in atmosphere used for the nitrate decomposition. We have recently found a substantial difference in both the surface area and crystallite size between cobalt oxide decomposed under air versus nitrogen.<sup>35</sup> Nickel oxide was produced while heating under air flow while cobalt oxide was produced while heating under nitrogen. Decomposition under air was chosen, as it was unclear as to whether heating under nitrogen flow would produce the desired stoichiometric nickel (II) oxide. As shown in Equation 4.1, the atmosphere can impact the surface energy of the metal oxide, and so could also impact the extent of wetting of the silica surface.

#### 4.5.4 Metal Monolith Replication and Impact of Annealing

The nitrogen sorption isotherms taken before and after annealing of the cobalt-silica composites indicate that the decrease in pore volume occurs mostly in the surfactant mesopores. The overall shape of the isotherms is indicative of a broad mesopore size distribution. After silica removal, the sharp increase in nitrogen uptake around 0.9  $P/P_0$  of the annealed sample indicates more textural pore volume is made available through annealing. The mesopore volume

after etching was nearly the same between the two samples. All of this data is consistent with nanoparticle formation within the mesopores. Once the composite is heated above the Hüttig temperature for cobalt metal, these nanoparticles are able to move and sinter, which leads to a decrease in overall surface area by a small amount. The affinity of cobalt metal for silica compared to the oxide is much lower, allowing the metal nanoparticles to move more freely across the surface of mesopores and out into the textural mesopores/macropores. This is consistent with the observation (above) of coarsening of the ligament walls in cobalt. It is also consistent with work by Bore et al.<sup>59</sup> on migration of gold nanoparticles in mesoporous silica where the nanoparticles on annealing migrate out of the mesopores onto the exterior surface of the mesoporous silica particles.

There are a number of interesting observations concerning replication to give nickel monoliths. At one level, the lower surface area of nickel compared with that of nickel oxide, suggests that the poor wetting of the silica template is more important in impacting the fidelity of replication than the decrease in nickel nitrate mobility that would be expected from the use of hydrogen rather than air. Beyond this, upon examination of the isotherm and DFT pore size distribution for the non-annealed nickel-silica composite, a clear downward shift in the surfactant mesopore size distribution is seen, but unlike the cobalt composites, the distribution does not broaden extensively. After annealing, the pore size distribution shifted downward even further and the adsorption branch of the isotherm begins to flatten out. The surfactant mesopore volume of the annealed composite decreases considerably as does the textural pore volume and the BET surface area. After these samples were etched, the nickel sample that was annealed had a higher BET surface area than the sample that had not undergone annealing. Additionally, the mesopore volume was slightly higher in the annealed sample while the textural pore volume was lower.

When the nickel sample is annealed it appears that the nickel actually moves along the silica surface and sinters together wherever it is located in the pore system. This is indicated by the reduction in surface area in the composite and by both the reduction of surfactant mesopore and textural pore volume for the composite. Upon silica removal, the surface area of the annealed replicate is actually higher than that of the non-annealed sample. As discussed above it is likely that the nickel does not wet the silica, giving a driving force both for particle growth, and for migration of the nickel from the surfactant mesopores to the textural mesopores and to the macropores. Exactly this behavior has been observed for gold nanoparticles in mesoporous silica,<sup>59</sup> which migrate from the mesopores to the external surface of mesoporous silica particles. Further, the gold nanoparticles also grow into the walls of the mesoporous silica, crushing and disrupting the walls. Such growth could explain the observed downward shift in pore size distribution: as the silica walls are disrupted the average spacing between the nickel mesostructures being produced would decrease, leading to smaller pores on removal of the silica. While the surface area of the silver replica was the lowest of the monoliths in this study, the silver-silica composite does show a small sign of surfactant mesopore infiltration. The nitrogen sorption isotherm of the composite (Figure 4.S5) is similar to that seen in the nickel composite, where the surfactant mesopore region begins to show a more gradual adsorption of nitrogen. The NLDFT pore size distribution of the composite (Figure 4.S5) is shifted slightly downward. Upon annealing of this sample, the monoliths cracked. This is likely to be due to excessive agglomeration/growth of the silver within the macropores. The SEM image in Figure 4.3e shows that even after reduction at 250 °C, the sintering and agglomeration is already easily seen. This is not surprising when one considers the large contact angle of silver on silica measured by others and the low Hüttig temperature of silver, 98 °C. This suggests that to obtain improved

replication it will be necessary to work at a substantially lower temperature where the mobility of the silver would be lower.

#### 4.5.5 Metal Oxide Monolith Replication

Nanocasting of  $\text{Co}_3\text{O}_4$  appears to give good replication of the parent silica template, judging from the high surface area, which exceeds that reported in previous work.<sup>26</sup> The results for the nickel oxide indicate that the replication is not as conformal. The surface area is much lower, and the peak of the pore size distribution is shifted to a significantly lower value (3.8 nm) than is observed for  $\text{Co}_3\text{O}_4$  (6.1 nm). Annealing of the nickel oxide pushes the peak in the pore size distribution to a lower value still: 3.2 nm. It is possible that this is an artifact of the NLDFT fitting being used, as the kernel being used was developed for silica rather than for the metal oxides. However, pore size analysis using the BJH model<sup>60</sup> gives a similar result of a downward shift. This shift to lower values is accompanied by an increase in surface area on annealing, which is inconsistent with sintering and particle growth (although the average crystallite size seen in XRD does indeed increase). It is possible that these changes result from the conversion from the non-stoichiometric (black) nickel oxide to stoichiometric (green) nickel oxide, however the absence of detectable changes in the lattice spacing as determined by XRD does not appear to be consistent with the differences observed. Instead we believe that these anomalous results could reflect disruption/compression of the silica template during annealing, leaving smaller pores in the resulting nickel oxide. As discussed above such disruption of the silica template was observed by Bore et al.<sup>59</sup> for gold nanoparticles in a number of mesoporous silica templates, and appears to also be occurring for nickel metal. The dramatic difference in results for cobalt oxide, which gives excellent replication and nickel oxide which does not, appear not to be due to differences in wetting of the silica, which are likely to be relative small. Two possibilities would appear reasonable; the first that differences in the decomposition pathways in cobalt nitrate and nickel nitrate strongly impact precursor migration (out of the mesopores in the nickel oxide

case). The second possibility is that as the nickel oxide grows it disrupts the silica where growing cobalt oxide does not. Lu et al.<sup>13</sup> comment that different materials have preferred growth modes which may or may not match well with a given template structure. Cobalt oxide seems to tolerate a variety of mesopore geometries having been grown in a number of different templates by different groups.<sup>61-67</sup> We are only aware of one paper reporting the nanocasting of nickel oxide.<sup>68</sup>

#### **4.6 Conclusions**

Hierarchically porous silica monoliths have been successfully replicated in cobalt oxide, nickel oxide, cobalt, nickel, and silver via infiltration of aqueous nitrate solutions and thermal processing. This is the first detailed report of such replication for nickel oxide, nickel, cobalt and silver. SEM imaging of the replicas indicates that structures on the micrometer scale are successfully reproduced so that the resulting monoliths have high porosity. Nitrogen adsorption characterization is consistent with excellent replication of the mesostructure of the silica template for cobalt oxide, but lower fidelity in replicating nickel oxide, cobalt, nickel and silver. The trends in the surface area were explained using a comprehensive conceptual model of the processes involved in nanocasting metals and metal oxides. The trends are consistent with the non-wetting behavior of the metals on silica resulting in migration of the metal out of the mesopores of the silica template, as well as some disruption of the silica template by the growing nickel mesostructures. The behavior of nickel oxide, particularly after annealing is not well explained by the model, since nickel oxide is believed to wet silica at temperatures not much higher than used in this study. Such wetting would predict good replication. Some combination of two factors is believed to account for the differences in fidelity of replication between the nickel oxide and the cobalt oxide. The observed decrease in average mesopore size in the nickel

oxide, is consistent with disruption/compression of the mesoporous silica template by the growing nickel oxide, which is not observed for cobalt oxide. The pathways for the decomposition of the nickel and cobalt nitrate precursors are likely also different which would lead to differences in mobility of the precursors and intermediates during the thermal decomposition.

#### **4.7 Acknowledgements**

Primary support for this work was provided by NSF grant CHE-0719398 (MGB) and by the Academy of Finland 127919 (JHS). The use of the microscopes in the Central Analytical Facility of the University of Alabama is gratefully acknowledged.

This work was performed with co-authors Ms. Amy Grano, Professor Mika Lindén, Professor Jan-Henrik Smått, and Professor Martin Bakker.

## 4.8 References

- (1) Yamada, Y.; Tsung, C.-K.; Huang, W.; Huo, Z.; Habas, S.-E.; Soejima, T.; Aliaga, C. E.; Somorjai, G. A.; Yang, P. *Nat. Chem.* **2011**, *3*, 372-376.
- (2) Arico, A. S.; Bruce, P.; Scrosati, B.; Tarascon, J.-M.; Van Schalkwijk W. *Nat. Mat.*, **2005**, *4*, 366-377.
- (3) Dong W.; Dunn, B. in K.J. Klabunde and R.M. Richards (Editor), *Nanoscale Materials in Chemistry*, John Wiley & Sons, Hoboken, NJ, USA, 2009, p. 519-534.
- (4) Centi, G.; Perathoner, S. *Top. Catal.*, **2009**, *52*, 948-961.
- (5) Walcarius, A.; Kuhn, A. *Trend Anal. Chem.* **2008**, *27*, 593-603.
- (6) Banhart, J. *MRS Bull.* **2003**, 290-295.
- (7) Banhart, J. *Adv. Eng. Mat.* **2006**, *8*, 781-794.
- (8) Lui, Q. *Literature Review: Materials with Negative Poisson's Ratios and Potential Applications to Aerospace and Defence*, DSTO Defence Science and Technology Organization, Fishermans Bend, VIC, AU, 2006, p. 36.
- (9) Tappan, B. C.; Steiner, S. A.; Luther, E. P. *Angew. Chem. Int. Ed.* **2010**, *49*, 4544-4565.
- (10) Rolison, D. R.; Dunn, B. *J. Mater. Chem.* **2001**, *11*, 963-980.
- (11) Leventis, N. *Acc. Chem. Res.* **2007**, *40*, 874-884.
- (12) Stein, A.; Li, F.; Denny, N. R. *Chem. Mater.* **2008**, *20*, 649.
- (13) Lu, A.-H.; Zhao, D.; Wan, Y. *Nanocasting: A Versatile Strategy for Creating Nanostructured Porous Materials*, Royal Society of Chemistry, Cambridge, U. K., 2010.
- (14) Polarz, S.; Antonietti, M. *Chem. Comm.* **2002**, 2593-2604.
- (15) Caruso, R. A.; Antonietti, M. *Chem. Mater.*, **2001**, *13*, 3272-3282.
- (16) Yuan, Z. Y.; Ren, T.-Z.; Vantomme, A.; Su, B.-L. *Chem. Mater.* **2004**, *16*, 5096.
- (17) Ruzimuradov, O.; Hasegawa, G.; Kanamori, K.; Nakanishi, K. *J. Am. Ceram. Soc.* **2011**, *94*, 3335-3339.
- (18) Hasegawa, G.; Kanamori, K.; Nakanishi, K.; Hanada, T. *J. Am. Ceram. Soc.* **2010**, *93*, 3110-3115.

- (19) Konishi, J.; Fujita, K.; Oiwa, S.; Nakanishi, K.; Hirao, K. *Chem. Mater.* **2008**, *20*, 2165-2173.
- (20) Tokudome, Y.; Fujita, K.; Nakanishi, K.; Miura, K.; Hirao, K. *Chem. Mater.* **2007**, *19*, 3393-3398.
- (21) Numata, M.; Takahashi, R.; Yamada, I.; Nakanishi, K.; Sato, S. *App. Catal. A* **2010**, *383*, 66-72.
- (22) Liu, Z.; Sakamoto, Y.; Ohsuna, T.; Hiraga, K.; Terasaki, O.; Ko, C. H.; Shin, H. J.; Ryoo, R. *Angew. Chem. Int. Ed.*, **2000**, *39*, 3107-3110.
- (23) Shin, H. J.; Ryoo, R.; Liu, Z.; Terasaki, O. *J. Am. Chem. Soc.* **2001**, *123*, 1246-1247.
- (24) Shin, H. J.; Ko, C. H.; Ryoo, R. *J. Mater. Chem.* **2001**, *11*, 260-261.
- (25) Lee, K.; Kim, Y. H.; Han, S. B.; Kang, H.; Park, S.; Seo, W. S.; Park, J. T.; Kim, B.; Chang, S. *J. Am. Chem. Soc.* **2003**, *125*, 6844-6845.
- (26) Smått, J.-H.; Weidenthaler, C.; Rosenholm, J. B.; Lindén, M. *Chem. Mater.* **2006**, *18*, 1443-1450.
- (27) Lu, A.-H.; Smått, J.-H.; Lindén, M. *Adv. Funct. Mater.* **2005**, *15*, 865-871.
- (28) Smått, J.-H.; Spliethoff, B.; Rosenholm, J. B.; Lindén, M. *Chem. Comm.* **2004**, 2188-2189.
- (29) Taguchi, A.; Smått, J.-H.; Linden, M. *Adv. Mat.* **2003**, *15*, 1209-1211.
- (30) Maddox Sayler, F.; Bakker, M. G.; Smått, J.-H.; Lindén, M. *J. Phys. Chem. C* **2010**, *114*, 8710-8716.
- (31) Sayler, F. M.; Grano, A. J.; Scogin, W.; Sanders, P.; Smatt, J.-H.; Shaughnessy, K.; Bakker, M. G. *MRS Proceedings* **2012**, *1389*, g05-05.
- (32) Sun, X.; Shi, Y.; Zhang, P.; Zheng, C.; Zheng, X.; Zhang, F.; Zhang, Y.; Guan, N.; Zhao, D.; Stucky, G. D. *J. Am. Chem. Soc.* **2011**, *133*, 14542-14545
- (33) Smått, J.-H.; Schunk, S. A.; Lindén, M. *Chem. Mater.* **2003**, *15*, 2354-2361.
- (34) Ravikovitch, P. I.; Haller, G. L.; Neimark, A. V. *Adv. Colloid Interface Sci.* **1998**, *76-77*, 203-226.
- (35) Smått, J.-H.; Sayler, F. M.; Grano, A. J.; Bakker, M. G. *Adv. Eng. Mater.* **2012**, *14*, 1059-1073.

- (36) Lu, A. H.; Smått, J.-H.; Backlund, S.; Lindén, M. *Micro. Meso. Mater.* **2004**, *72*, 59-65.
- (37) Greenwood, N. N.; Earnshaw, A. *Chemistry of the Elements*, Elsevier, Oxford, 1997.
- (38) Zhang, Y.; Cao, X.; Yuan, H.; Zhang, W.; Zhou, Z. *Int. J. Hydrogen Energy*, **1999**, *24*, 529-536.
- (39) Meher, S. K.; Justin, P.; Rao, G. R. *Electrochim. Acta.* **2010**, *55*, 8388–8396.
- (40) Meher, S. K.; Justin, P.; Rao, G. R. *Nanoscale* **2011**, *3*, 683-692.
- (41) Roggenbuck, J.; Waitz, T.; Tiemann, M. *Micro. Meso. Mater.* **2008**, *113*, 575-582.
- (42) Brockner, W.; Ehrhardt, C.; Gjikaj, M. *Thermochim. Acta* **2007**, *456*, 64-68.
- (43) Llewellyn, P. L.; Chevrot, V.; Ragai, J.; Cerclier, O.; Estienne, J.; Rouquerol, F. *Solid State Ionics* **1997**, *101-103*, 1293-1298.
- (44) Mansour, S. A. A. *Thermochim. Acta* **1993**, *228*, 173-189.
- (45) Paulik, F.; Paulik, J.; Arnold, M. *Thermochim. Acta* **1987**, *121*, 137-149.
- (46) Estelle, J.; Salagre, P.; Cesteros, Y.; Serra, M.; Medina, F.; Sueiras, J. E. *Solid State Ionics* **2003**, *156*, 233-243.
- (47) Sietsma, J. R. A.; Meeldijk, J. D.; Versluijs-Helder, M.; Broersma, A.; van Dillen, A. J.; de Jongh, P. E.; de Jong, K. P. *Chem. Mater.* **2008**, *20*, 2921–2931.
- (48) Sietsma, J. R. A.; Friedrich, H.; Broersma, A.; Versluijs-Helder, M.; van Dillen, A. J.; de Jongh, P. E.; de Jong, K. P. *J. Catal.* **2008**, *260*, 227–235.
- (49) Wolters, M.; Munnik, P.; Bitter, J. H.; de Jongh, P. E.; de Jong, K. P. *J. Phys. Chem. C* **2011**, *115*, 3332-3339.
- (50) Ehrhardt, C.; Gjikaj, M.; Brockner, W. *Thermochim. Acta* **2005**, *432*, 36-40.
- (51) Moulijn, J. A.; van Diepen, A. E.; Kapteijn, F. *App. Catal. A* **2001**, *212*, 3-16.
- (52) Ruckenstein, E. in G.C. Kuszynski, A.E. Miller and G.A. Sargent (Editors), *Sintering and Heterogeneous Catalysis*, Plenum Press, New York, USA, 1984, p. 199-221.
- (53) Eustathopoulos, N.; Drevet, B. *Mat. Sci. Eng.* **1998**, *A249*, 176-183.
- (54) Sangiorgi, R.; Muolo, M. L.; Chatain, D.; Eustathopoulos, N. *J. Am. Ceram. Soc.* **1988**, *71*, 742-748.

- (55) Stevenson, S. A.; Dumesic, J. A.; Baker, R. T. K.; Ruckenstein E.(Editors), *Metal-Support Interactions In Catalysis, Sintering, and Redispersion*, Van Nostrand Reinhold Company, New York, USA, 1987.
- (56) Rog, G.; Kozłowska-Rog, A.; Bucko, M.; Głowacz, E. *J. Chem. Therm.* **2000**, *32*, 931-935.
- (57) Potoczna-Petru, D.; Krajczyk, L. *Cat. Lett.* **2003**, *87*, 51-56.
- (58) Nakayama, T.; Arai, M.; Nishiyama, Y. *J. Catal.* **1984**, *87*, 108-115.
- (59) Bore, M. T.; Pham, H. N.; Switzer, E. E.; Ward, T. L.; Fukuoka, A.; Datye, A. K. *J. Phys. Chem. B* **2005**, *109*, 2873-2880.
- (60) Barrett, E. P.; Joyner, L. G.; Halenda, P. P. *J. Am. Chem. Soc.* **1951**, *73*, 373-380.
- (61) Wang, Y. W.; Wu, Z. Y.; Wang, H. J.; Zhu, J. H. *Adv. Func. Mater.* **2006**, *16*, 2374-2386.
- (62) Ruplecker, A.; Kleitz, F.; Salabas, E.-L.; Schuth, F. *Chem. Mater.* **2007**, *19*, 485-496.
- (63) Wagner, T.; Roggenbuck, J.; Kohl, C.-D.; Forba, M.; Tiemann, M. in D. Zhao, S. Qiu, Y. Tang and C. Yu (Editors), *Recent Progress in Mesoporous Materials*, Elsevier, 2007, p. 347-350.
- (64) Tuysuz, H.; Lehmann, C. W.; Bongard, H.; Tesche, B.; Schmidt, R.; Schuth, F. *J. Am. Chem. Soc.* **2008**, *130*, 11510–11517.
- (65) An, Z.; He, J.; Shu, X.; Wu, Y. *Chem. Comm.* **2009**, 1055–1057.
- (66) Zheng, M.-B.; Cao, J.; Liao, S.-T.; Liu, J.-S.; Chen, H.-Q.; Zhao, Y.; Dai, W.-J.; Ji, G.B.; Cao, J.-M.; Tao, J. *J. Phys. Chem. C* **2009**, *113*, 3887-3894.
- (67) Wang, Y.; Wang, Y.; Ren, J.; Mi, Y.; Zhang, F.; Li, C.; Liu, X.; Guo, Y.; Guo, Y.; Lu, G. *J. Solid State Chem.* **2010**, *183*, 277-284.
- (68) Yue, W.; Zhou, W. *Chem. Mater.* **2007**, *19*, 2359-2363.
- (69) Navrotsky, A.; Ma, C.; Lilova, K.; Birkner, N. *Science* **2010**, *330*, 199-201.
- (70) Lide, D. R. *CRC Handbook of Chemistry and Physics: A Ready-reference Book of Chemical and Physical Data*, CRC Press, London, UK, 2004.

4.9 Supplemental Information

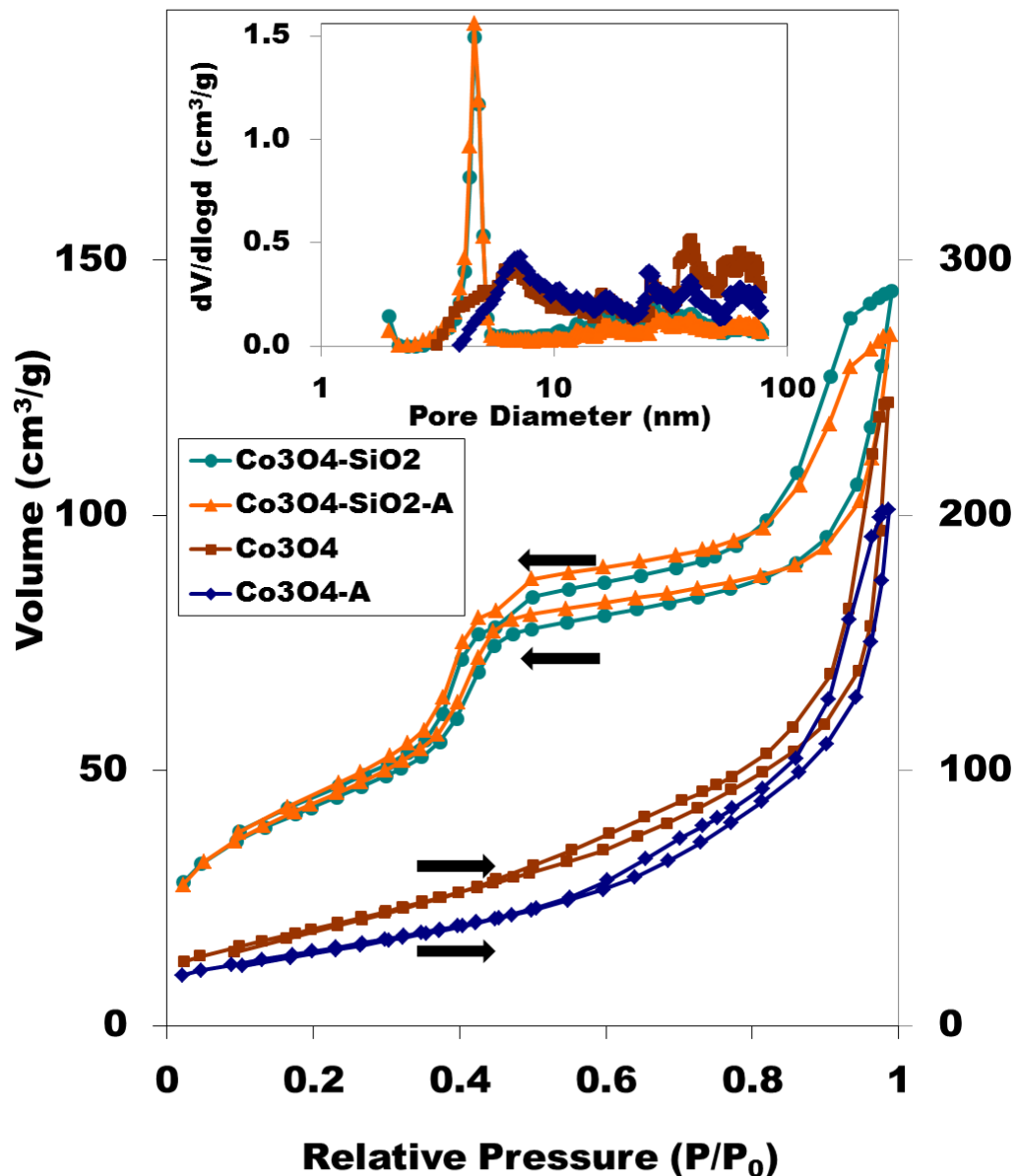


**Figure 4.S1.** Nitrogen Sorption Isotherms and NLDFT Pore Size Distributions for Cobalt Oxide Composites and Replicas Before and After Annealing.

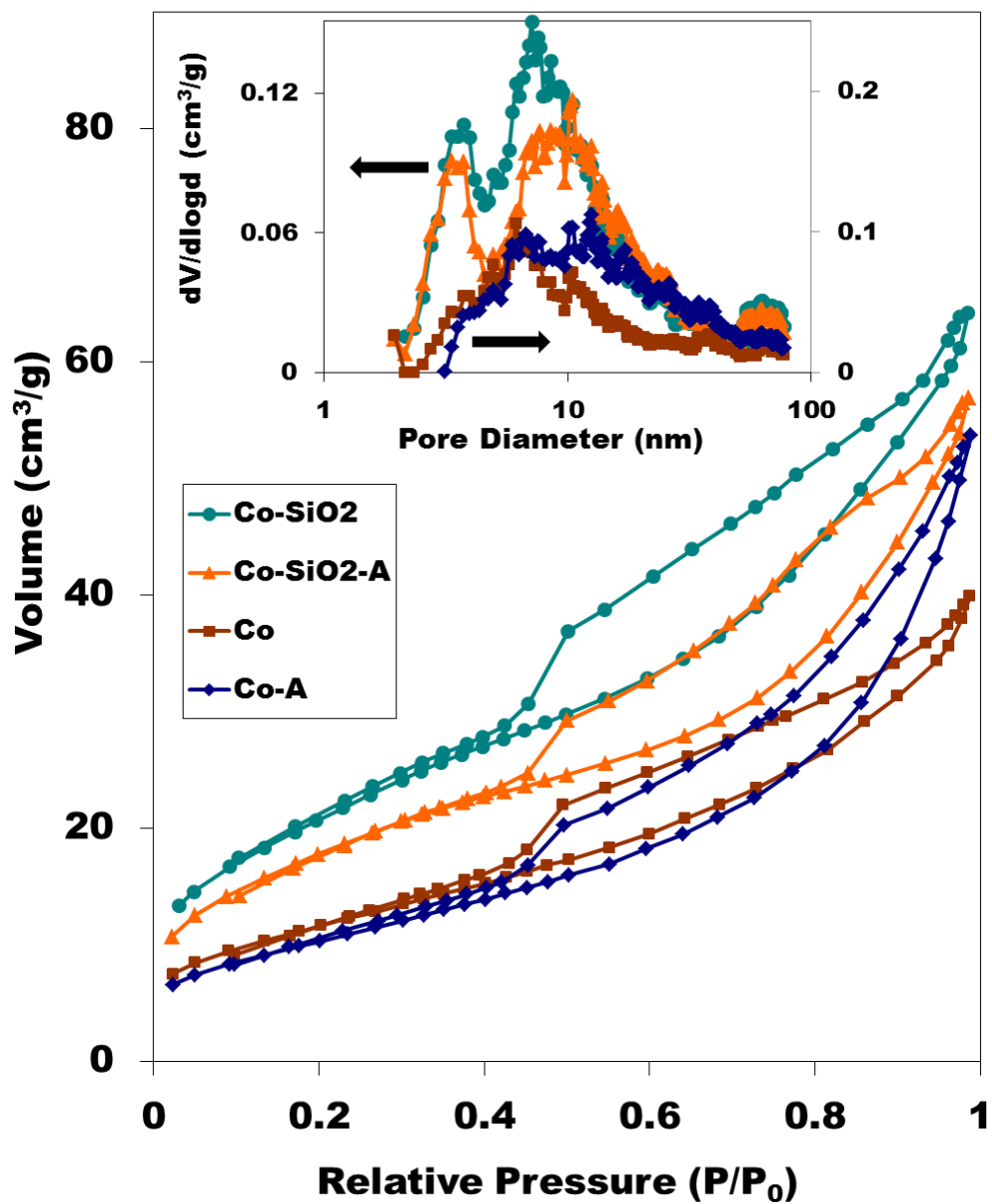


**Figure 4.S2.** Nitrogen Sorption Isotherms and NLDFT Pore Size Distributions for Cobalt Metal Composites and Replicas Before and After Annealing.

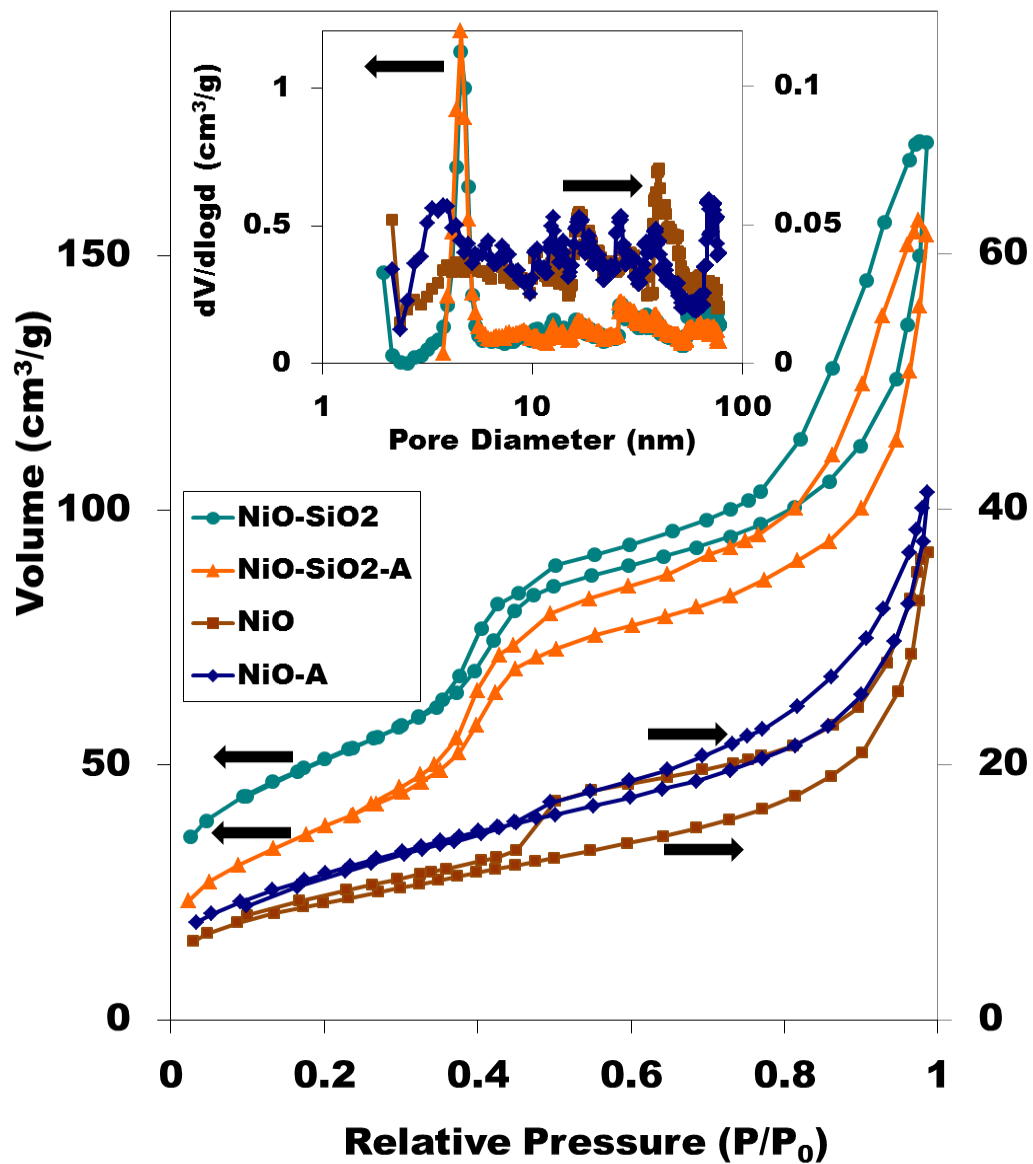


**Figure 4.S3.** Nitrogen Sorption Isotherms and NLDFT Pore Size Distributions for Nickel Oxide Composites and Replicas Before and After Annealing.

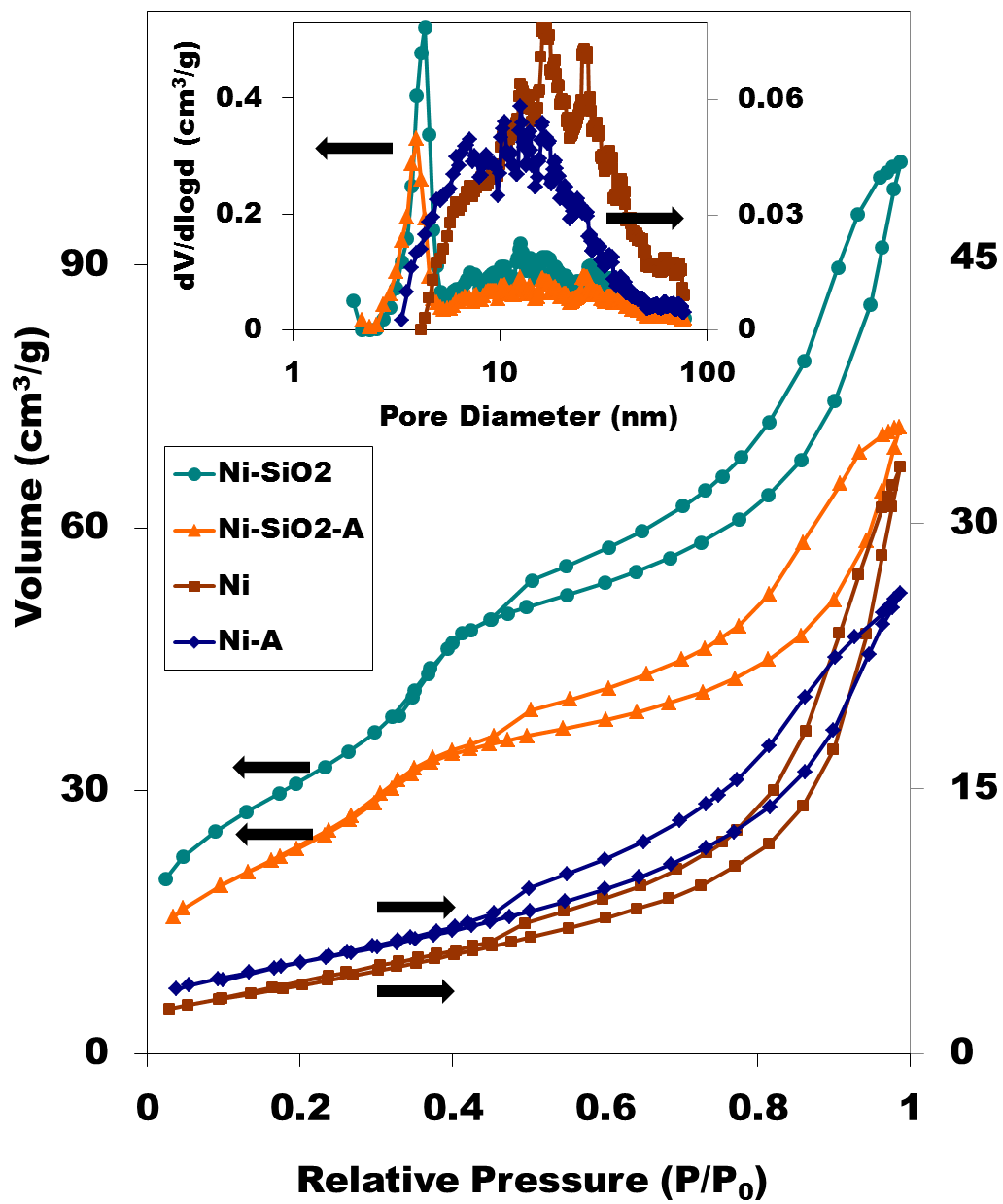


**Figure 4.S4.** Nitrogen Sorption Isotherms and NLDFT Pore Size Distributions for Nickel Metal Composites and Replicas Before and After Annealing.

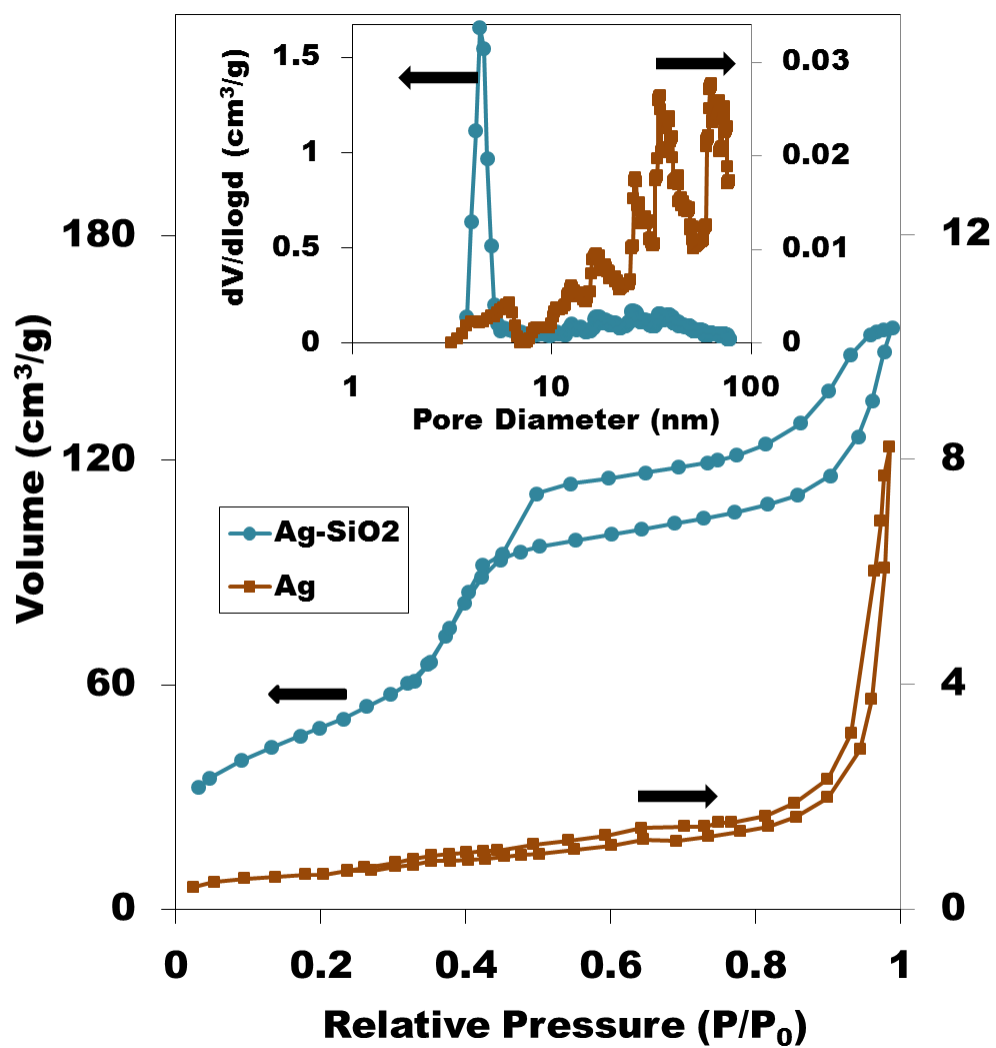


**Figure 4.S5.** Nitrogen Sorption Isotherms and NLDFT Pore Size Distributions for Silver Composite and Replica.

## Chapter 5

### Formation of Hierarchically Porous Metal Oxide and Metal Monoliths by Nanocasting into Silica Monoliths

#### 5.1 Abstract

The formation of hierarchically porous metal and metal oxide monoliths by replication of hierarchically porous silica templates is reviewed. The various factors that impact the structure and properties of the synthesized materials are discussed and illustrated by the formation of new  $\alpha$ -Fe<sub>2</sub>O<sub>3</sub>, ZrO<sub>2</sub>, nickel, silver and silver silicate porous monoliths. The impact of the atmosphere is addressed in the formation of Co<sub>3</sub>O<sub>4</sub> and silver monoliths. For Co<sub>3</sub>O<sub>4</sub> formation of the monolith under vacuum, air, argon or nitrogen was found to dramatically change the structure of the final material. For silver, decomposition of the silver nitrate under air resulted in porous monoliths composed of silver silicates. Decomposition of silver nitrate under vacuum produced monoliths for which the chemical composition of the monolith was predominantly silver on the exterior of the monolith consisted of silver silicates in the interior of the monolith.

#### 5.2 Introduction

Porous materials, particularly those with bicontinuous porosity, are central to a number of important application areas including heterogeneous catalysis<sup>1,2</sup> and separations.<sup>3-6</sup> When the material is electrically conducting or semiconducting such porous electrodes are central to electrochemical sensors, supercapacitors, electrocatalysis and as electrodes in advanced batteries.<sup>7-9</sup> If the material displays ionic conduction rather than electronic conduction, these materials are a key component of fuel cells. All these applications require a large interfacial surface area, and efficient transport of reactants and products between the exterior and interior of the material. To meet these two requirements, a bicontinuous macropore network is needed.

And this network needs to be either formed from mesopores or it could be covered with which is covered with or formed from mesopores with pore size on the 1-10 nanometer length scale to generate the necessary high surface area. A number of synthetic approaches to preparing such structures have been developed. For instance, the group of Su et al. has developed a synthetic pathway where hierarchically porous metal oxides can spontaneously be formed using the self-assembly of nanoparticles around surfactant micelles.<sup>10,11</sup> However, this method has fairly poor morphology control and is not generally well suited for formation of large (mm-cm) pieces; often referred to as “monoliths”. A number groups have used colloidal crystal templating; self-assembly of polymer or silica beads to give a relatively hard template into which precursor solutions can be infiltrated to create a macroporous structure in metals, and metal oxide materials (also known as 3DOM materials).<sup>12-15</sup>

Infiltration of a sol-gel precursor including a surfactant as template can be used to induce ordered mesopores in the macropore walls of these materials.<sup>16</sup> Major drawbacks of this approach are the expense of the polymeric beads for macroscopic pieces, and the presence of constrictions in the macropore network. A number of other methods of producing hierarchically porous materials have been developed using microemulsions,<sup>17,18</sup> bicontinuous polymer foams,<sup>19</sup> salt crystals,<sup>20</sup> bacteria,<sup>21</sup> butterfly wings,<sup>22</sup> cellulose,<sup>23,24</sup> sugars,<sup>25</sup> or ice<sup>26</sup> as templates for macrostructure, and foaming of the sol-gel silica.<sup>27</sup>

These methods of forming macropores can be coupled with addition of surfactants or block copolymers to template mesopores. Liquid-solid phase separation induced by chemical reaction has also been used to produce bicontinuous silica macrostructures,<sup>28</sup> and extended to zirconia,<sup>29</sup> titania,<sup>29,30</sup> alumina<sup>31</sup> and calcium, barium and strontium titanates.<sup>32</sup> This process is an example of spinodal decomposition, in which spontaneous fluctuations in local composition

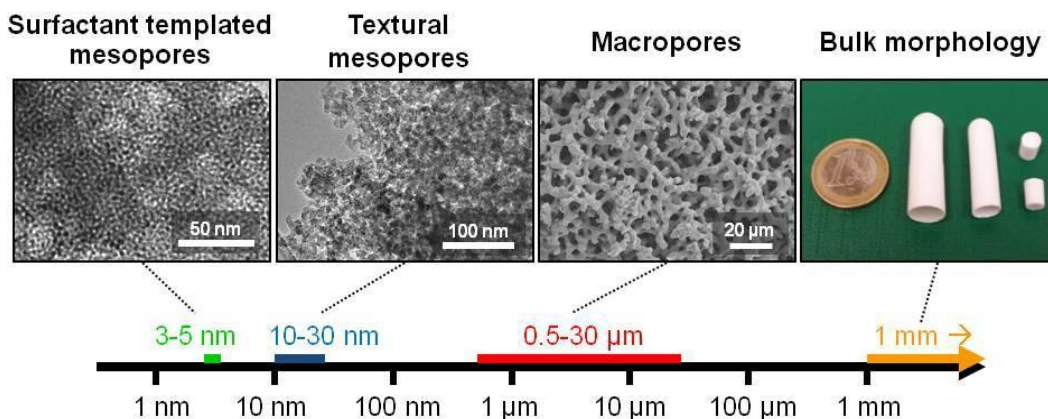
are amplified to produce phase separation at a number of length scales.

This paper focuses on the formation of sol-gel derived hierarchically porous monoliths prepared by such phase separation induced processes, and their conversion to other materials with related structures by "nanocasting": infiltration of various solution or gas phase precursors which react to produce other materials within the monolith. This approach has been used to make hierarchically porous  $\text{MnO}_2$ ,  $\text{Mn}_2\text{O}_3$ ,  $\text{Co}_3\text{O}_4$ ,  $\text{SnO}_2$ <sup>33,34</sup> and carbon<sup>35,36</sup> monoliths with well-developed porosity at micrometer length scales and reasonable surface areas of up to  $40 \text{ m}^2/\text{g}$  for metal oxides and  $>1000 \text{ m}^2/\text{g}$  for carbon. The template for these materials was one that did not include a surfactant and so only provided textural mesopores. Such monoliths as referred to as being "monomodal". For silica monoliths containing surfactant mesopores ("bimodal" monoliths) the surfactant mesopores provides higher surface areas, which if well replicated would result in higher surface area in the nanocast replicas. In this contribution we explore the use of bimodal rather monomodal silica templates and we (1) survey the various methods and materials developed for producing the original monoliths, (2) outline the nanocasting approach when applied to monoliths including a discussion of the various factors that impact the quality of nanocast material and (3) give representative examples of the approach to produce new materials including hierarchically porous iron oxide, zirconium oxide, nickel oxide and the first reports of hierarchically porous metal and metal silicate monoliths formed by nanocasting.

### 5.2.1 Formation of Porous Silica and Metal Oxide Monoliths by Spinodal Decomposition

Various hierarchically porous silica and metal oxide monolith can be formed by the use of sol-gel processes in which organic precursors react with water to produce monomeric forms of silica or the metal oxide. These monomeric forms condense to give oligomers which continue to grow and give solid material. The hydrolysis produces an alcohol as a by-product and this

together with the water will phase separate from the growing inorganic component as the polymerization reaction proceeds. Often a high molecular weight polymer such as polyethylene oxide<sup>37</sup> or polyethylene glycol<sup>38</sup> is added to improve the phase separation and to control the length scale of the macropore network. This approach has been used to form porous monoliths of titania,<sup>39</sup> zirconia,<sup>29,30</sup> aluminas,<sup>31,40</sup> and of mixed oxides of titania with barium, strontium and calcium.<sup>32</sup> A related approach is to add a monomer such as furfuryl alcohol which will itself undergo polymerization as the phase separation occurs.<sup>41</sup> Including surfactants<sup>38,42</sup> or block copolymers<sup>43</sup> in the synthesis mixture can give silica monoliths that are macroporous and mesoporous with a narrow range of pore sizes. Whereas the addition of a cationic surfactant give disordered networks of pores, the block copolymer templated materials can have highly ordered pores.<sup>44,45</sup> Scheme 5.1 shows SEM images of porous silica monoliths that display the typical network of macropores, it can be seen that the macropore networks are generated by silica ligaments, where the ligaments are formed by agglomeration of smaller particles.



**Scheme 5.1.** The Hierarchical Nature of the Monolithic Silica Templates Used in This Study.

The particles themselves can be mesoporous (having pores in the 3–10 nm) range, and the regions where the particles are in contact also generates voids on the 10–50 nm range depending

upon the sizes of the particles. We will use the term "surfactant" mesopores to designate mesopores generated by an added charged or non-ionic surfactant, and "textural" mesopores to designate those mesopores generated by contact of silica particles.

Typically the surfactant mesopores have a constant diameter throughout a monolith, where the diameter of the mesopores is determined by the chain length of the hydrophobic portion of the surfactant, whereas the textural mesopores will have a broader range of diameters.

To summarize; these cationic surfactant templated hierarchically porous monoliths have controllable porosity of three different forms on three different length-scales: surfactant templated pores with 3–5 nm diameter, textural mesopores of 10–30 nm scale, and macropores controllable between 0.5 and 30  $\mu\text{m}$ . Surface areas for these materials are typically 600–1100  $\text{m}^2/\text{g}$ , or, adjusting for the density of silica (2.2  $\text{g}/\text{mL}$ ), 1300–2500  $\text{m}^2/\text{mL}$ . These materials can be fabricated as large monolithic pieces, with dimensions of 1–20 cm.

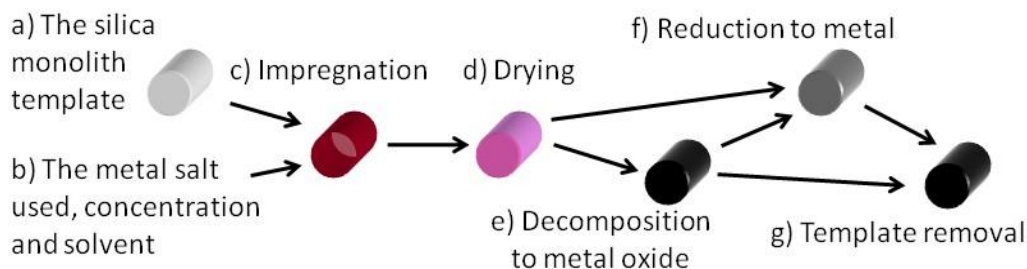
Instead of a cationic surfactant, a non-ionic block copolymer can also be used.<sup>44,46</sup> Where cationic surfactants produce disordered arrays of pores, block copolymers can produce highly ordered arrays of mesopores with diameters in the range 6–9 nm. The resulting silica then also has micropores (< 1 nm) that bridge the ordered mesopores. These porous materials therefore have porosity controllable on 4 length scales; <1 nm, 3–10 nm, 10–50 nm and 500 nm–30  $\mu\text{m}$ .

Although the block copolymer templated materials have considerable promise as templates for synthesis of large pieces of highly ordered nanomaterials, this is still a largely unexplored field, and so these materials will not be discussed further.

### 5.2.2 Nanocasting to Form Other Hierarchically Porous Materials

An overview of the replication process is given in Scheme 5.2: a solution of the precursor is added to a silica monolith, solvent is removed by evaporation/heating and the precursor is then

decomposed to the metal oxide or metal. This process is repeated as often as necessary to build up the desired structure. Capillary forces generally favor filling of the smallest mesopores first,



**Scheme 5.2.** An Overview of the Different Steps That are Involved in the Nanocasting Process.

so that in some cases the textural mesopores are not filled. This process therefore forms a negative replica of the mesopores and a positive replica of the macropores. The details of the processing significantly impact the properties of the final product and will be discussed in the order in which the processes are carried out. Although the focus will be on monolithic materials, there is a large body of work on nanocasting into mesoporous silica particles<sup>47-50</sup> and such work will be discussed where it has potential impact on nanocasting into monoliths.

Metal nitrate salts are widely used in nanocasting because of the high solubility in aqueous solution and the relatively easy decomposition to the metal oxide. Other metal salts including chlorides<sup>31,51-53</sup>, carbonate<sup>53</sup> and acetates<sup>54</sup> have also been used, and we will discuss examples in which aqueous nickel acetate is used to produce nickel and in which aqueous zirconium sulfate is used as precursor to form zirconia. For monoliths, capillary forces will favor filling of the mesopores over the macropores, and so by adding a volume of solution that matches the volume of the mesopores, infiltration of solution can be limited to the mesopores. This approach is sometimes termed "incipient wetness" and is also used for nanocasting into mesoporous silica particles. A variation on this approach is to use a solution which is not

saturated and then let evaporation concentrate the precursors into the mesopores since evaporation will occur preferentially from the macropores. This does require careful control of the starting concentration as salt deposition can occur into the macropores if the solution reaches saturation concentration while there is still solution in the macropores. This leads to significant filling of the macropores as seen in some of our earlier work on manganese oxides.<sup>34</sup> Because of the very significant differences in effective density between even the most concentrated aqueous solutions and the final metal oxide or metal, a number of infiltration cycles are necessary. For metal oxides this is typically 4–6 and for the metals it may be as high as 8–12.

A newer approach that can significantly decrease the number of infiltration cycles uses metal nitrate hydrate melts which have a significantly higher metal concentration than is attainable from saturated aqueous solutions. A number of metal nitrate hydrates have low melting points well below their decomposition temperatures, and so modest heating is sufficient to allow them to form a liquid that can penetrate into the mesopores. This process has recently been applied by a number of groups to nanocasting into mesoporous silica particles,<sup>55-57</sup> and we have also successfully applied it to nanocasting into silica monoliths.

The thermal decomposition of the precursor produces either a metal oxide or a metal depending upon the metal and on the atmosphere used. Transition metals decomposed under air, oxygen or inert atmospheres typically give metal oxides. Decomposition under hydrogen can produce transition metals, particularly noble metals.<sup>58</sup> The high surface area of the resulting metal monoliths tends to make them very reactive, which can be advantageous for catalytic applications,<sup>59</sup> but also means that the material oxidizes rapidly in air. A detailed study of the impact of gas atmosphere is included below. The temperature at which the decomposition reaction is carried out and the length of time at elevated temperatures both critically impact the

structure and properties of the final material. This can be understood in context of the Tammann and Hüttig temperatures and the wetting of the silica template by the metal oxide or metal being formed. The Hüttig temperature is the temperature at which atoms at defects become mobile, and the Tammann temperature is the temperature at which atoms in the bulk become mobile.<sup>60</sup> The Hüttig temperature is estimated to be approximately one third the Kelvin melting point of the material, and the Tammann temperature approximately half the Kelvin melting point. If the metal or metal oxide wets the silica (i.e. adhesion is stronger than cohesion), the metal or metal oxide will spread across the silica giving good replication of the silica template structure. If on the other hand a metal or metal oxide does not wet silica, then Ostwald ripening will occur at temperatures for which the metal or metal oxide is mobile. This will tend to favor migration of the metal or metal oxides out of the smaller mesopores into the larger mesopores, and the macropores, resulting in a decrease in surface area and loss of the nanostructure. This can be seen clearly in Figure 5.1 which shows the growth of silver crystallites within the macropores.

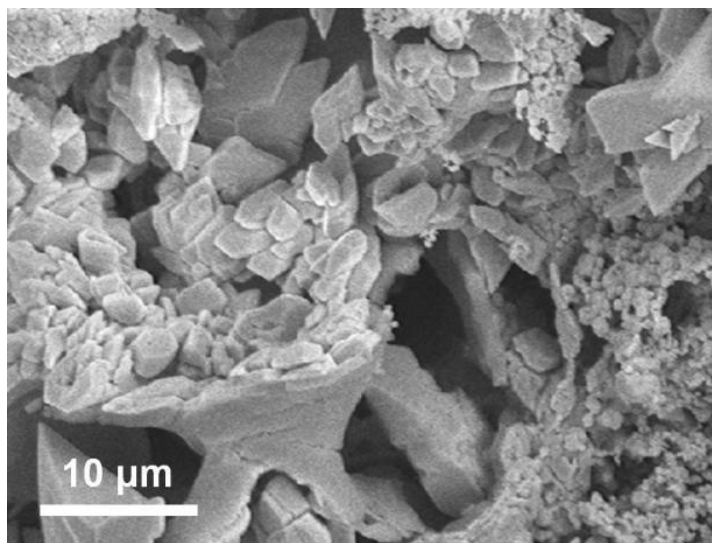


**Figure 5.1.** SEM Image of a Silica Monolith with Silver Crystallites in the Macropore Structure.

The wetting of the silica template by the metal oxide or metal can be evaluated from the contact

angle between the metal oxide or metal and silica surface. Unfortunately, most metals do not wet silica and so minimizing the time the sample spends at elevated temperature coupled with a slow decomposition will tend to give the best final structure. There is little data available on the contact angles between metal oxides and silica. Our experience indicates that most metal oxides can give reasonable replicas suggesting that they wet silica sufficiently well that Ostwald ripening is slow.

Despite the potentially negative impact on surface area and nanostructure replication of allowing significant migration of metal or metal oxide within the silica template, it may be desirable to allow such migration to improve the mechanical stability of the resulting monolithic material. If all the metal or metal oxide is confined to the surfactant mesopores and the smaller textural mesopores the replica may be continuous, but not sufficiently mechanically robust to survive subsequent processing and handling. The coefficients of thermal expansion of the largely amorphous silica template monolith and of the metal or metal oxide replica are likely to be significantly different, producing stresses in the materials as they cool. This often leads to fracturing of the material, sometimes in the parent silica monoliths, at other times after the silica is removed. A thermal annealing step may therefore be desirable to minimize these stresses.

A further consideration in the thermal processing of the material results from interaction of the silica matrix with the incorporated metal or metal oxide. It is often tacitly assumed that the silica matrix is inert, playing no role other than acting as a mold, however at elevated temperatures there is reason to believe that metals can be incorporated into the mesoporous silica walls to form metal silicates. This has been inferred for decomposition of cobalt acetate in mesoporous silica,<sup>61</sup> and a surface layer of silicon bonded to zirconium dioxide is inferred for nanocasting of  $ZrO_2$  into mesoporous silica, based on FTIR spectra.<sup>53</sup> We report below

observation of zirconium silicate and silver silicates.

Nanocasting into mesoporous silica is also a route to mixed metal oxides. The interest here is primarily in magnetic materials such as (1) ferrites:  $MFe_2O_4$  where  $M =$  zinc,<sup>62</sup> manganese,<sup>63</sup> nickel,<sup>57,63,64</sup> cobalt,<sup>63-66</sup> copper<sup>57,63</sup> and magnesium<sup>64</sup> (2) strontium hexaferrite<sup>67</sup> (3)  $NiCo_2O_4$  spinel<sup>68,69</sup> and (4) copper doped cerium oxide<sup>57</sup> for solid oxide fuel cell applications.

After nanocasting the silica needs to be removed. This is done by etching away the silica with either an aqueous hydroxide solution or aqueous hydrogen fluoride. Not all nanocast materials are stable in one of these solutions. For instance, zinc oxide is soluble in both etching solutions. One method of overcoming this limitation is to use a double nanocasting procedure involving first making a carbon replica of mesoporous silica particles, etching away the silica, and then nanocasting zinc oxide into the mesoporous carbon, followed by removal of the carbon to make mesoporous zinc oxide.<sup>70,71</sup> Other examples are copper oxide and copper which we have successfully nanocast into mesoporous silica monoliths, but again both dissolve on etching of the silica.

After etching of the silica to leave the mesoporous nanocast material, further transformations are possible with retention of structure if carried out carefully. Examples are reduction by glycol of particles of mesoporous  $Co_3O_4$  to  $CoO$ <sup>72</sup> and the reduction by hydrogen of  $\alpha$ - $Fe_2O_3$ , to  $Fe_3O_4$  and then oxidation under air to  $\alpha$ - $Fe_2O_3$ .<sup>73</sup> Again we are not aware of any examples of such transformations being carried out on monolith materials. We report here on the first such example in which hierarchically porous nickel oxide monoliths are reduced to nickel.

## 5.3 Experimental

### 5.3.1 Preparation of Hierarchically Porous Silica Monoliths

Hierarchically porous silica monoliths were prepared according to previously described

procedures.<sup>28,38</sup> In the preparation of monoliths with a monomodal mesopore size distribution, polyethylene glycol (PEG, MW: 35 000 g/mol) was used to induce the macroporosity.<sup>38</sup> These samples are denoted SiO<sub>2</sub>-M1 and SiO<sub>2</sub>-M2 depending on the PEG amount (4.7 wt% and 5.3 wt%, respectively). Monoliths with a bimodal mesoporosity were produced by using a combination of PEG and hexadecyltrimethylammonium bromide (C<sub>16</sub>TAB) or PEG and octadecyltrimethylammonium bromide (C<sub>18</sub>TAB) as structure directing agents.<sup>38</sup> These samples are denoted SiO<sub>2</sub>-B1 (9 wt% C<sub>16</sub>TAB), SiO<sub>2</sub>-B2 (7 wt% C<sub>18</sub>TAB), and SiO<sub>2</sub>-B3 (9 wt% C<sub>18</sub>TAB). A more detailed description can be found in the Supporting Information.

### 5.3.2 Preparation of Co<sub>3</sub>O<sub>4</sub> Monoliths (Varying the Gas Atmosphere)

Silica monoliths with a bimodal mesopore size distribution (SiO<sub>2</sub>-B1) were used as templates for Co<sub>3</sub>O<sub>4</sub> monoliths. The silica monoliths were impregnated with a 58 wt% aqueous solution of Co(NO<sub>3</sub>)<sub>2</sub> · 6H<sub>2</sub>O (98%, Fluka) under vacuum. After soaking for 1 h, the monoliths were rolled on copier paper to remove excess solution. Impregnated monoliths were then heated to 150 °C at a rate of 2 °C/min and held at 150 °C for 10 hours under stagnant air, argon flow, nitrogen flow or vacuum. These steps were repeated twice. The monoliths were then calcined at 550 °C for 6 hours under the mentioned atmospheres with a ramp rate of 1 °C/min, except for the vacuum sample which was calcined under stagnant air. The silica template was removed with 4 M aqueous NaOH (2 x 24 h treatments at 90 °C). Co<sub>3</sub>O<sub>4</sub> monoliths were then rinsed with deionized water and dried at 90 °C.

### 5.3.3 Preparation of Fe<sub>2</sub>O<sub>3</sub> Monoliths

Silica monoliths with bimodal mesopore size distribution (SiO<sub>2</sub>-B2) were used as templates for Fe<sub>2</sub>O<sub>3</sub> monoliths. Silica monoliths were soaked in a 87 wt% aqueous solution of Fe(NO<sub>3</sub>)<sub>3</sub> · 9H<sub>2</sub>O (98+%, Alfa Aesar) at 75 °C until they appeared translucent, approximately 24

hours. Excess solution was removed and they were dried and the salt decomposed in air at 150 °C for 10 hours. Impregnation of iron nitrate and decomposition was repeated twice for these samples. The sample was then calcined in air at 550 °C for 6 hours with a ramp rate of 1 °C/min. The silica was removed by etching in 3 M KOH overnight. Monoliths were then rinsed with deionized water and dried at 90 °C.

#### 5.3.4 Preparation of ZrO<sub>2</sub> Monoliths

Silica monoliths with monomodal mesopore size distribution (SiO<sub>2</sub>-M1 and SiO<sub>2</sub>-M2 described above) were used as templates in the preparation of hierarchically porous ZrO<sub>2</sub> monoliths. The monoliths were impregnated with a 50 wt% aqueous solution of Zr(SO<sub>4</sub>)<sub>2</sub> · 4H<sub>2</sub>O (98+%, Alfa Aesar) under vacuum. After soaking for 1 h, the monoliths were carefully wiped with a paper tissue to remove excess solution and dried at 40 °C for 24 h. The impregnation and drying procedure was repeated once after which the samples were calcined in air 2 h at 750 °C (heating ramp 1 °C/min) to fully decompose the sulfate to the oxide (which occurs at 720 °C for the pure salt). In order to obtain a mechanically stable ZrO<sub>2</sub> replica the impregnation-drying-impregnation-drying-calcination cycle was carried out 4 times in total. In a final step, the silica template was removed by etching the composite monoliths in 1 M aqueous NaOH solution (24 h at 90 °C). The monoliths were then washed thoroughly with water and acetone and finally dried at 40 °C for more than 24 h.

#### 5.3.5 Preparation of Ag Monoliths

Silica monoliths with a bimodal mesopore size distribution (SiO<sub>2</sub>-B3) were soaked in melted AgNO<sub>3</sub> (99.9 %, Alfa Aesar) at 400 °C until the salt had visibly wet the entire monolith, approximately 1 hour. Excess salt was removed and the monoliths were heated to 450 °C and held for 1 hour in either air or under vacuum to decompose the salt. The composite was cooled

and the silica was removed with 3 M aqueous KOH solution overnight. Monoliths were then rinsed with deionized water and dried at 80 °C under vacuum.

### 5.3.6 Preparation of NiO and Ni Monoliths

Silica monoliths with a bimodal (B1) mesopore size distribution were used as templates for the preparation of nickel oxide monoliths. The monoliths were impregnated via incipient wetness with 0.7 M aqueous nickel acetate (98 %, Aldrich). After drying, the monoliths were heated under air to 400 °C for 5 hours to decompose the salt. This procedure was repeated 8 times to obtain a stable replica. The silica template was then removed with 4 M NaOH for 48 hours, rinsed with water to remove excess salt, and then dried at 40 °C. The nickel oxide replicas were then heated under a reducing atmosphere (5% H<sub>2</sub> in N<sub>2</sub>) to 240 °C, at a ramp of 1 °C/min to reduce the monoliths to nickel metal. These samples are designated Ni-B1-post-H<sub>2</sub>.

In situ reduction under hydrogen was also carried out. Silica monoliths possessing a bimodal pore size distribution (SiO<sub>2</sub>-B2) were impregnated with a 57 wt% Ni(NO<sub>3</sub>)<sub>2</sub> · 6H<sub>2</sub>O (98 %, Alfa Aesar) solution under vacuum. Excess solution was removed and monoliths were heated at 150 °C for 10 hours, ramped to 350 °C at a rate of 2 °C/min, and held at 350 °C for 5 hours under 5% hydrogen in nitrogen flow. Samples were cooled and infiltration and reduction cycles were repeated 4 times. Samples were etched with aqueous 3 M KOH, rinsed with deionized water, and dried at 80 °C under vacuum. These samples are designated Ni-B2-H<sub>2</sub>.

### 5.3.7 Characterization Methods

Scanning electron microscopy/electron dispersive spectroscopy (SEM/EDS) measurements were carried out on a JEOL 7000 SEM or a JEOL JSM-6335F equipped with Oxford EDS detectors, while the transmission electron microscope images were taken with a Hitachi HF2000 TEM instrument, equipped with a cold field emission gun. Nitrogen

physisorption measurements were conducted on a Nova 2200e or an Autosorb-1 instrument (both from Quantachrome), as well as an ASAP 2010 instrument (from Micromeritics). In the pore size calculations, mainly the BJH model based on the desorption branch was used, with the exception for the silica monoliths where the NLDFT method was used for pores smaller than 6 nm (kernel for cylindrical pores using the adsorption branch). X-ray diffraction (XRD) patterns were measured on either a Bruker D2 Phaser system or a Bruker AXS D8 Discover instrument (both using X-ray copper sources). Crystallite sizes were estimated from the XRD measurements by applying the Scherrer equation<sup>85</sup> using the Topas software provided from Bruker. FT-Raman spectroscopy was carried out on a Bruker FRA 106 instrument.

## 5.4 Results and Discussion

### 5.4.1 SiO<sub>2</sub> Template Monoliths

In this study, we used hierarchically porous silica monoliths in the nanocasting process to form metal oxides and metals of similar structure. The starting monolith monolithic pieces (cylinders of about 5 mm diameter and 10 mm length) were designed to all have interconnected macropores with pore diameters in the range of 1-15  $\mu\text{m}$  (similar to the ones shown in Scheme 1).<sup>74</sup> Furthermore, as evident from the pore size distribution plot derived from nitrogen physisorption in Figure 5.2, the monoliths where only polyethylene glycol (PEG) was used as structure directing agent (samples SiO<sub>2</sub>-M1 and SiO<sub>2</sub>-M2), have only a monomodal textural porosity centered around 20 nm. When adding a surfactant (C<sub>n</sub>TAB: C<sub>n</sub>H<sub>2n+1</sub>N(CH<sub>3</sub>)<sub>3</sub>Br) to the reaction mixture, another set of pores with a pore diameter close to 4 nm is induced in the final monoliths. The abundance and size of these surfactant templated mesopores can be controlled by the amount added and the chain length of the hydrocarbon moiety of CTAB, respectively. Thus, by changing the surfactant from C<sub>16</sub>TAB to C<sub>18</sub>TAB, the size can be increased from 4.3

nm to 4.6 nm (Table 5.1). Both the textural and the surfactant templated mesopores are depicted in Scheme 5.1. The original isotherm data can be found in the supporting information, while the specific surface areas, pore volumes and pore sizes for the samples are summarized in Table 5.1.

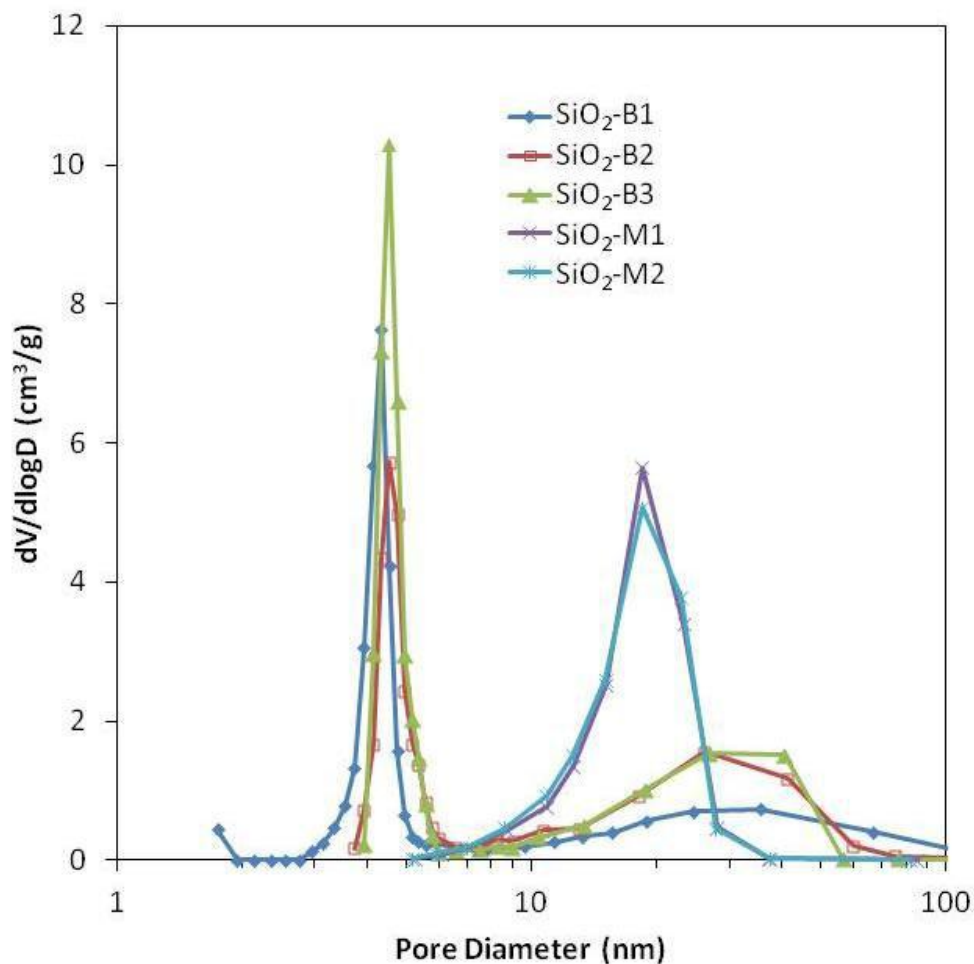


**Figure 5.2.** Pore Size Distribution Plots of the Different Silica Monoliths Used as Templates in This Study. For pore sizes smaller than 6 nm, NLDFT has been used to determine the size distribution (kernel for cylindrical pores using the adsorption branch), while for larger pores the BJH model based on the desorption branch has been applied.

**Table 5.1. Replica Monoliths. Summary of textural properties of the starting silica monoliths and the different replica samples.**

**Silica template monoliths**

Sample	BET	BET	Mesopore	Mesopore	Mesopore		Crystal
	Surface	Surface			Diameter	Size	
	Area	Area <sup>a</sup>	Volume	Volume <sup>a</sup>	Surf	Text	Diameter
	[m <sup>2</sup> /g]	[m <sup>2</sup> /cm <sup>3</sup> ]	[cm <sup>3</sup> /g]	[cm <sup>3</sup> /cm <sup>3</sup> ]	[nm]	[nm]	[nm]
SiO <sub>2</sub> -B1	833	1830	0.95	2.09	4.3 <sup>b</sup>	~30 <sup>c</sup>	-
SiO <sub>2</sub> -B2	643	1410	1.31	2.88	4.5 <sup>b</sup>	~30 <sup>c</sup>	-
SiO <sub>2</sub> -B3	742	1630	1.43	3.14	4.6 <sup>b</sup>	~30 <sup>c</sup>	-
SiO <sub>2</sub> -M1	264	581	1.13	2.49	-	19	-
SiO <sub>2</sub> -M2	267	587	1.16	2.55	-	19	-

**Replica monoliths**

Sample	BET	BET	Mesopore	Mesopore	Mesopore		Crystal
	Surface	Surface			Diameter	Size	
	Area	Area <sup>a</sup>	Volume	Volume <sup>a</sup>	Small	Large	Diameter
	[m <sup>2</sup> /g]	[m <sup>2</sup> /cm <sup>3</sup> ]	[cm <sup>3</sup> /g]	[cm <sup>3</sup> /cm <sup>3</sup> ]	[nm]	[nm]	[nm]
Co <sub>3</sub> O <sub>4</sub> -B1-Stag	68.8	420	0.20	1.22	10	~40 <sup>c</sup>	
Co <sub>3</sub> O <sub>4</sub> -B1-N <sub>2</sub>	89.5	547	0.19	1.17	7.2	~40 <sup>c</sup>	
Co <sub>3</sub> O <sub>4</sub> -B1-Ar	95.4	583	0.19	1.15	6.4	~40 <sup>c</sup>	
Co <sub>3</sub> O <sub>4</sub> -B1-Vac	25.1	153	0.12	0.73	-	19	
Fe <sub>2</sub> O <sub>3</sub> -B2	65.3	342	0.12	0.61	11	-	17.1
SiO <sub>2</sub> /ZrO <sub>2</sub> -M1	133	-	0.30	-	6.7	15	
ZrO <sub>2</sub> -M1	97	551	0.22	1.26	8.5	-	
ZrO <sub>2</sub> -M2	84	477	0.21	1.19	8.5	-	12.5
Ag-B3-Air	17.9	-	0.09	-	-	~30 <sup>c</sup>	
Ag-B3-Vac	94.7	-	0.34	-	-	23	28 <sup>d</sup>
NiO-B1	37.7	182	0.09	0.44	-	20	
Ni-B1-post H <sub>2</sub>	10.7	95	0.07	0.62	-	~40 <sup>c</sup>	21.5
Ni-B2-H <sub>2</sub>	21.8	194	0.08	0.71	-	~30 <sup>c</sup>	

<sup>a</sup> The surface areas and the pore volume values have been adjusted for the bulk densities: 2.2 g/cm<sup>3</sup> for SiO<sub>2</sub>, 6.11 g/cm<sup>3</sup> for Co<sub>3</sub>O<sub>4</sub>, 5.24 g/cm<sup>3</sup> for Fe<sub>2</sub>O<sub>3</sub>, 5.68 g/cm<sup>3</sup> for ZrO<sub>2</sub>, 6.67 g/cm<sup>3</sup> for NiO, and 8.91 g/cm<sup>3</sup> for Ni. The bulk densities for the SiO<sub>2</sub>/ZrO<sub>2</sub> composite and the silver samples are uncertain and so a meaningful mesopore volume cannot be calculated.

<sup>b</sup> NLDFT pore size distribution (adsorption model for cylindrical pores).

<sup>c</sup> Gas adsorption is less sensitive for mesopores above ~20 nm, so these pore diameters are approximate.

<sup>d</sup> Measured on the Ag metal peaks.

#### 5.4.2 Co<sub>3</sub>O<sub>4</sub> Monoliths (Varying the Gas Atmosphere)

Figure 5.3 shows SEM images of the macropore walls for nanocast cobalt oxide samples decomposed under vacuum and different gaseous atmospheres. The scale of all four images is the same, and it is clear that the macropore structure is retained. The nature of the atmosphere does produce differences in sample morphology as can be seen clearly from comparison of the images. The most apparent difference is in the sample decomposed under vacuum, Co<sub>3</sub>O<sub>4</sub>-B1-Vac, in which the image is dominated by spherical structures of 400-500 nm in diameter. These structures are not replicas of the original silica template, and are much larger than the length scale of structures in the samples prepared under air, nitrogen or argon. For these latter samples, the size of the features decreasing in going from stagnant air (130±30 nm) to argon (100±15 nm) to nitrogen (70±10 nm). A comparison with the SEM image of the parent silica monolith (Scheme 5.1) shows that the typical feature size is closer to 20 nm. The nitrogen adsorption data is summarized in Table 5.1, and the pore size distribution is given in Figure 5.4.

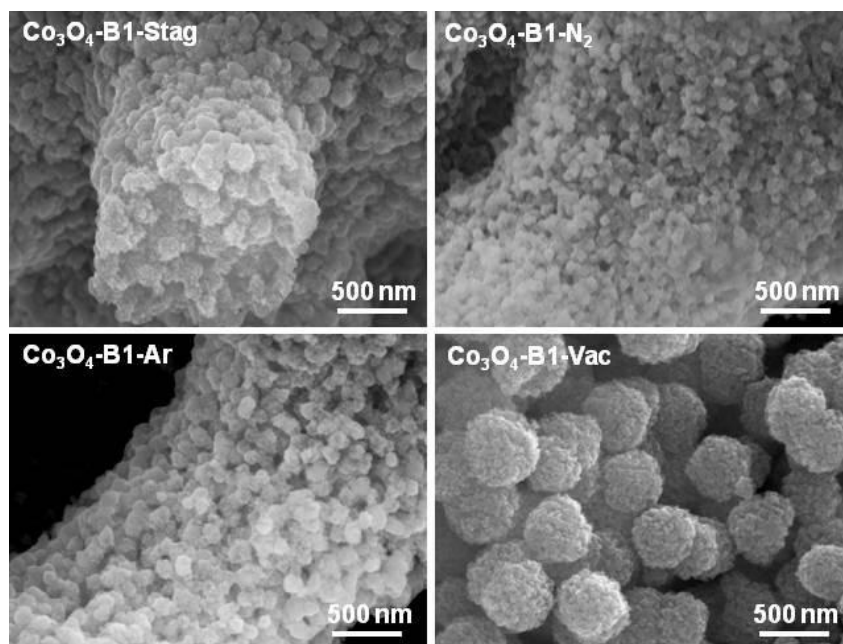


**Figure 5.3.** SEM Images Showing the Influence of the Morphology of the Co<sub>3</sub>O<sub>4</sub> Macropore Walls by Different Gas Atmospheres (stagnant air, N<sub>2</sub> flow, Ar flow and vacuum).

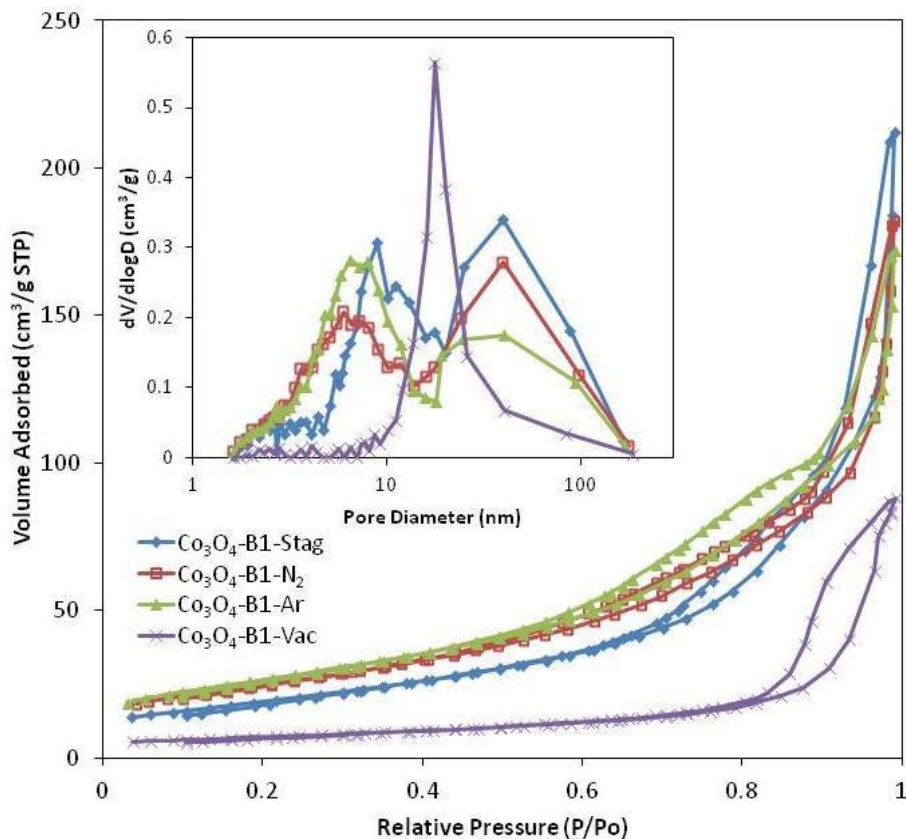


**Figure 5.4.** Nitrogen Physisorption Isotherms of  $\text{Co}_3\text{O}_4$  Replicas Prepared under Different Gas Atmospheres. Inset: The corresponding BJH pore size distribution plots (desorption branch).

The difference between the evacuated sample and the other three samples is striking. The surface area of sample  $\text{Co}_3\text{O}_4\text{-vac}$  is barely one third of the next lowest, and the pore size distribution shows only a single peak at approximately 20 nm. This peak is not from interparticle pores produced by contact of the 400-500 nm aggregates seen in Figure 5.3, but instead is likely to be produced by replication of the textural mesopores present in the silica template. The other samples not only have much higher surface areas, but also have bimodal pore size distributions. A more detailed analysis of the pore size distributions shows clear differences in the other three samples, with the sample decomposed under stagnant air showing a lower surface area, a larger average mesopore size (10 nm) and a proportionately larger volume

of pores in the 40 nm size region. The argon and nitrogen samples are more similar, with the sample decomposed under argon having a somewhat higher total surface area than the sample decomposed under nitrogen, more pores in the 4–10 nm range and proportionately fewer pores in the 20–100 nm range.

A bimodal pore size distribution in the replica monoliths is expected if the replication of the silica templates was perfect. However, even for the inert gas atmospheres which give the smallest pores, the pore size distributions actually produced are on length scales that suggest that the replication was less than perfect.

In forming a replica, capillary forces will initially confine the solution to the smallest pores: the surfactant mesopores. If the replication process is perfect and controlled to replicate only the surfactant mesopores then on removal of the silica template, the distribution of textural mesopores should be largely unchanged. The distribution of the surfactant mesopores on the other hand is expected to change. The surfactant mesopores have a narrow pore size distribution, but they are not ordered, and so the thickness of the silica walls is variable, leading to a broader pore size distribution, as is observed for carbon replicas.<sup>75</sup> The differences in the pore size distributions of both the textural mesopores, and the mesopores resulting from replication of the surfactant mesopores can best be explained by differences in mobility of the cobalt nitrate, cobalt nitrate decomposition products and cobalt oxide during the decomposition process, and potentially the interactions with the silica template. If the energy of adhesion of nanocast materials to silica is lower than the cohesive energy of the material then the enthalpy of the system can be minimized by particle growth leading to Ostwald ripening. This provides a natural driving force for material to move from the surfactant mesopores to the larger textural mesopores and then into the macropores. Although little information is available on the nature

of the interactions between nitrate salts, their decomposition products, and transition metal oxides and silica, empirical evidence from nanocasting a range of metal and metal oxide systems<sup>34,76</sup> is consistent with neither metals nor metal oxides wetting silica particularly well. Extended periods above the Hüttig temperature of cobalt oxide will therefore provide greater opportunity for migration of the cobalt oxide from the surfactant mesopores into the textural mesopores, and for migration within the textural mesopores to decrease the surface curvature.

The nature of the atmosphere can impact the replication process at multiple steps. Decomposition of nickel nitrate under an atmosphere of NO is reported<sup>77,78</sup> to significantly impact the surface area of nickel catalyst by altering the decomposition mechanism. Under oxygen atmosphere sintering of the nickel oxide is reported, with migration of the nickel oxide from within mesoporous silica particles to the exterior surface. These authors advocate keeping the concentrations of oxygen and NO<sub>2</sub> gas, a decomposition product, at low levels. The observation of lower surface area and larger pore sizes for stagnant air compared to flowing nitrogen and argon are very consistent with this result. However this does not explain the result for decomposition under vacuum in which the concentration of oxygen and the other decomposition products would also be very low. This sample was decomposed at 150 °C under vacuum, but calcined under stagnant air at 550 °C to improve the mechanical stability of the monolith. The large difference in structure between this sample and that decomposed only under stagnant air, indicates that the key effect here is the absence of gas during the decomposition process rather than the absence during the higher temperature calcination step. Since even the presence of chemically inert gases has a considerable impact this cannot be a purely chemical effect. One possible mechanism is a purely physical one. During the decomposition considerable gas evolution occurs, this gas must move out of the mesopores where the bulk of

the material is located out into the macropores. Under vacuum there is a larger pressure difference providing more impetus to move un-decomposed cobalt nitrate as well as already formed cobalt oxide. A second possibility is that the presence of a gaseous atmosphere shifts the decomposition equilibria, slowing them down and giving more time for the gas evolved to slowly diffuse out into the macropores, or favoring the formation of decomposition products which are less mobile at 150 °C. The use of vacuum during the decomposition of silver nitrate (below) produces substantial changes in the nature of the final product, suggesting that possible shifts in chemical equilibria are distinctly possible.

#### 5.4.3 Fe<sub>2</sub>O<sub>3</sub> Monoliths

Figure 5.5 shows SEM images from the iron oxide monolith Fe<sub>2</sub>O<sub>3</sub>-B2 prepared by nanocasting using iron nitrate. The macrostructure is clearly well replicated, and the presence of features on the 100 nm length scale on the surface of the macropore walls indicates that the growth of iron oxide in this system is consistent with what is seen for cobalt oxide synthesized under air. XRD (Figure 5.6) shows clearly peaks from  $\alpha$ -Fe<sub>2</sub>O<sub>3</sub> with no significant peaks from other crystalline phases. The broad background observed in Figure 5.6 results from X-ray luminescence from the copper X-ray source used. The average crystallite size is 17 nanometer, which is significantly larger than the 4.5 nanometer pore diameter of the mesopores in the parent silica monolith. The pore size distribution in Figure 5.7 shows a peak at approximately 10 nm which is similar to that observed for nickel oxide using the same template (below), but significantly larger than that observed for cobalt oxide. The surface area to volume ratio is lower than that for cobalt oxide and zirconia but higher than observed for nickel oxide.

We believe that these results are consistent with significant migration of the iron oxide out of the surfactant mesopores into the textural mesopores. The melting point of  $\alpha$ -Fe<sub>2</sub>O<sub>3</sub> is

1565 °C, giving a Tammann temperature of 646 °C. This is significantly higher than 550 °C the temperature at which the sample was calcined. But this is higher than the Hüttig temperature so we would expect some migration to occur. The Tammann and Hüttig temperatures for  $\text{Fe}_2\text{O}_3$  are higher than those of  $\text{Co}_3\text{O}_4$ , so other factors such as wetting and extent of pore filling must also be contributing to the lower surface area compared to  $\text{Co}_3\text{O}_4$ .

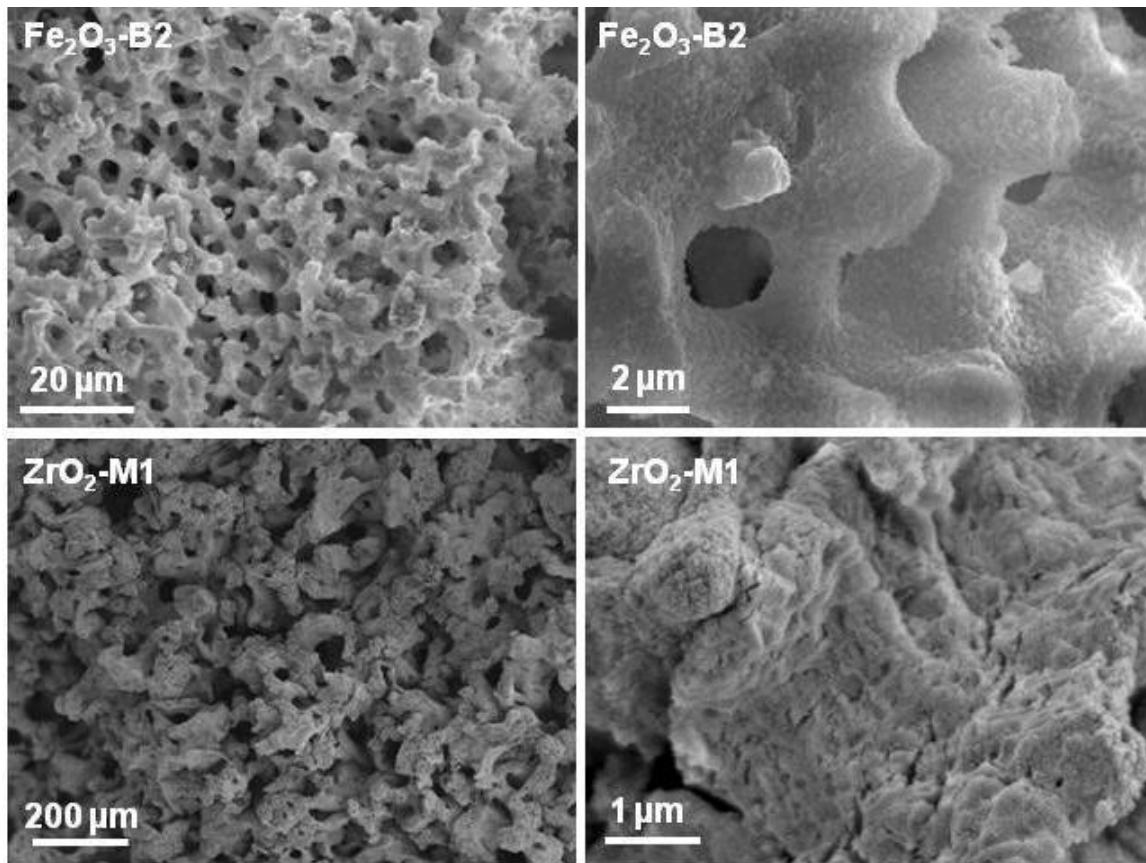


**Figure 5.5.** SEM Images of Samples  $\text{Fe}_2\text{O}_3\text{-B2}$  and  $\text{ZrO}_2\text{-M1}$ .

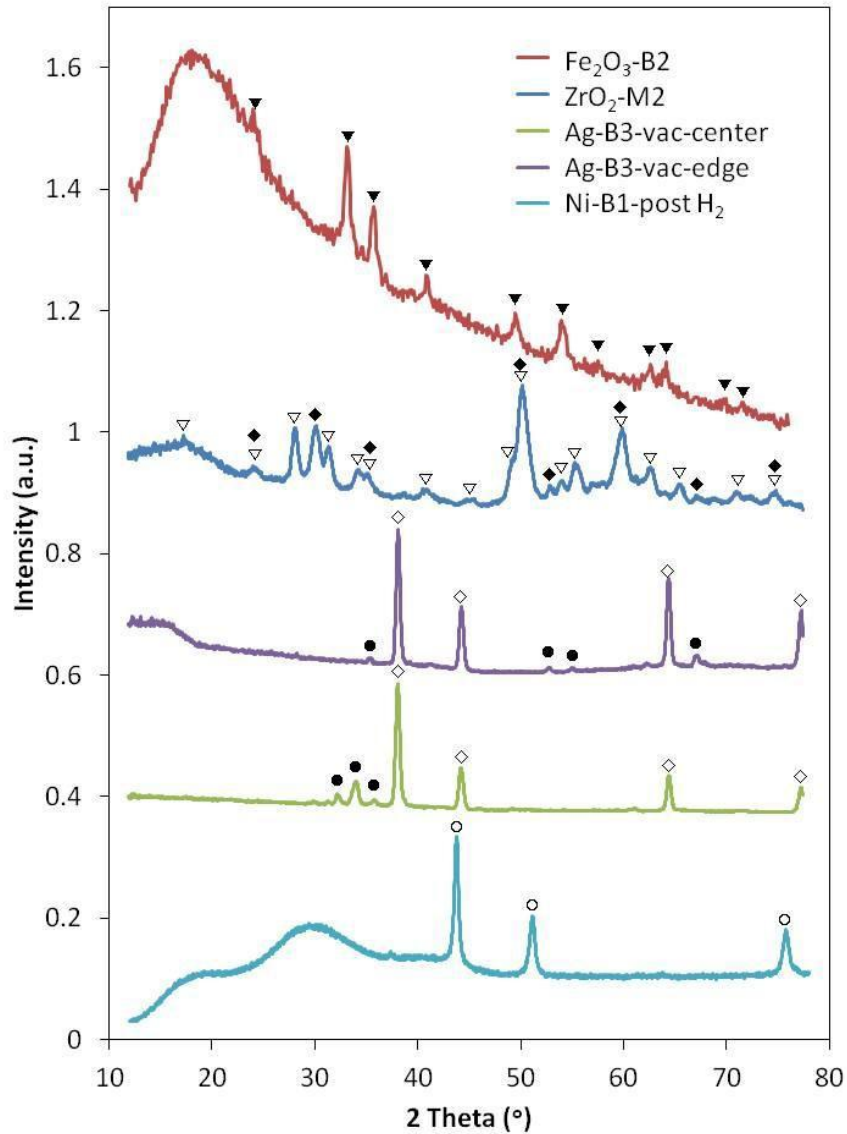


**Figure 5.6.** XRD Measurements of Fe<sub>2</sub>O<sub>3</sub>, ZrO<sub>2</sub>, Ag and Ni Monoliths. The symbol (▼) indicates reflections from  $\alpha$ -Fe<sub>2</sub>O<sub>3</sub> (hematite), while in sample ZrO<sub>2</sub>-M2 both monoclinic ZrO<sub>2</sub> (▽) and orthorhombic or tetragonal ZrO<sub>2</sub> (◆) phase can be seen. Mainly metallic Ag peaks (◇) can be seen at the edge of the Ag-B3-vac monoliths, while at the center additional silver silicate peaks can be seen (●). For Ni-B1-postH<sub>2</sub>, the peaks are from metallic nickel (○). The broad peaks below 40° are the sample holder.

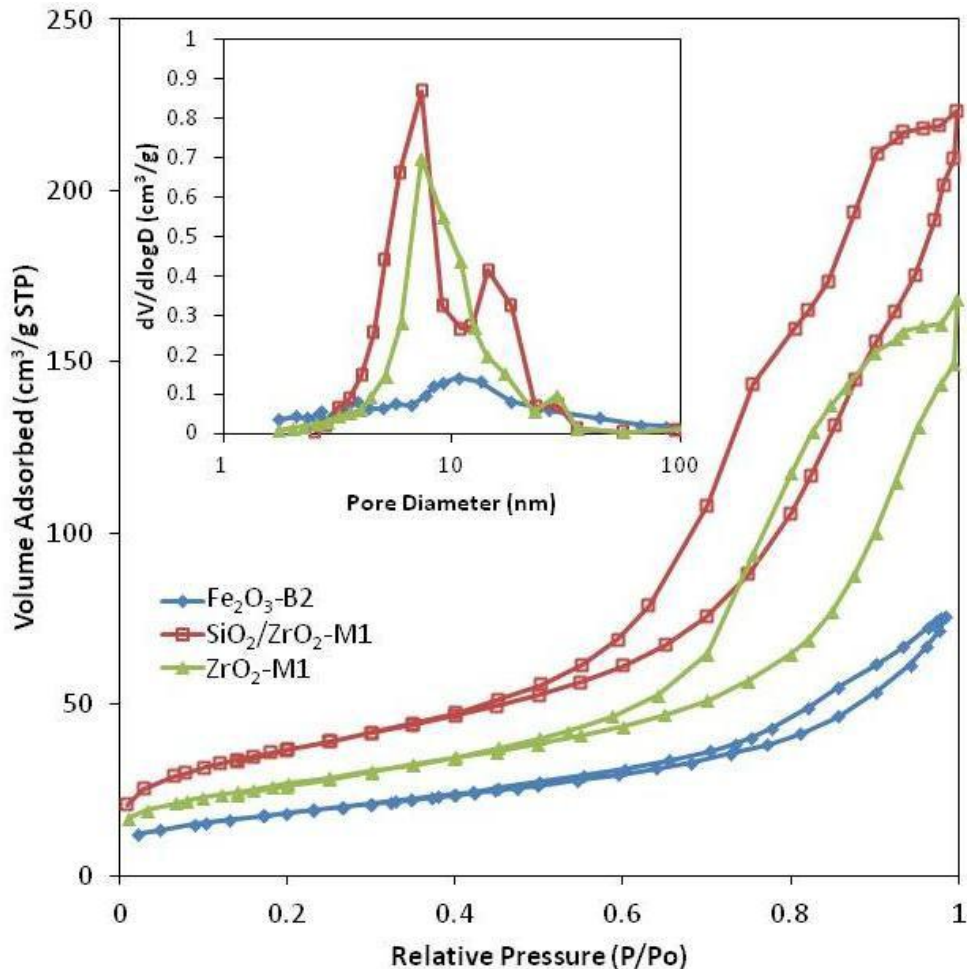


**Figure 5.7.** Nitrogen Physisorption Measurements on the  $\text{Fe}_2\text{O}_3$ -B2 Replica, the  $\text{SiO}_2/\text{ZrO}_2$ -M1 Composite and the  $\text{ZrO}_2$ -M1 Replica Monoliths.

#### 5.4.4 $\text{ZrO}_2$ Monoliths

Hierarchically porous  $\text{ZrO}_2$  monoliths with stable monolithic structures could be prepared by using  $\text{Zr}(\text{SO}_4)_2 \cdot 4\text{H}_2\text{O}$  as precursor salt, which is evident from Figure 5.8. Previous attempts to use aqueous solutions of  $\text{ZrOCl}_2$  or  $\text{ZrO}(\text{NO}_3)_2$  as  $\text{ZrO}_2$  precursors lead to severe cracking of the monolith structure during the impregnation/drying/calcination stages, which may result from faster reaction kinetics and a strong interaction between the Zr species and the  $\text{SiO}_2$  template. These effects can also be observed (although to a lesser degree) for the  $\text{ZrO}_2$  monoliths prepared with the zirconium sulfate salt as the silica template is removed by chemical etching in  $\text{NaOH}$ .

After being etched, the  $\text{ZrO}_2$  monoliths shrink to some extent upon the final drying step (for sample M1 5.0% and for M2 3.8%), due to the removal of the rigid silica scaffold. The improved mechanical strength of the composites when using zirconium sulfate as precursor can probably be ascribed to the high decomposition temperature needed before the oxide is formed ( $\sim 720^\circ\text{C}$  for the pure salt). In addition, when calcining  $\text{Zr}(\text{SO}_4)_2$  at  $750^\circ\text{C}$ , the  $\text{ZrO}_2$  formed is more dense and has a more rigid structure that can withstand shrinkage better. Several repeated impregnation steps also helps to improve the mechanical stability of the zirconia replica.

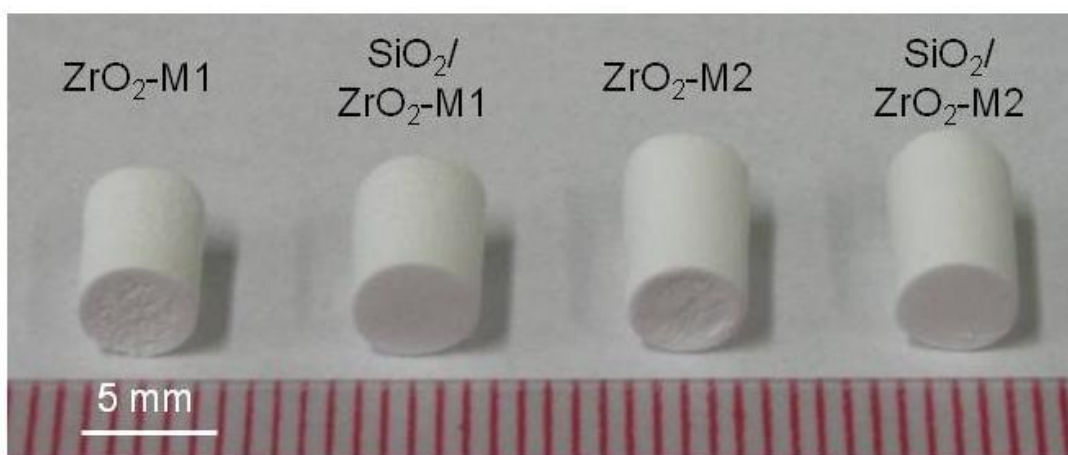


**Figure 5.8.** Photograph Showing Etched ( $\text{ZrO}_2$ ) and Non-Etched ( $\text{ZrO}_2/\text{SiO}_2$ ) Composites.

From the SEM images in Figure 5.5, it is evident that the macropore structure of the  $\text{ZrO}_2$  replica is not as well defined as in the starting silica monoliths, although one can clearly see that the structure is made up of interconnected macropores. The flow characteristics of these materials are still expected to be suitable for applications in catalysis.<sup>79</sup>

Nitrogen physisorption isotherms of the starting silica template together with the  $\text{SiO}_2/\text{ZrO}_2$  composite and the  $\text{ZrO}_2$  replica are shown in Figure 5.7, while the extracted textural properties are listed in Table 5.1. The original silica monolith shows a narrow pore size distribution around 20 nm, which is still present to a less extent in the composite monolith.

Interestingly a new set of pores appears in this sample at around 8 nm. The precise origin of these pores is still unclear. The  $\text{ZrO}_2$  replica also shows a BET surface area close to that of the silica template ( $551 \text{ m}^2/\text{cm}^3$  vs.  $581 \text{ m}^2/\text{cm}^3$ ). Generally nanocast replicas have lower surface areas than the parent silica templates, which suggests that the induced pores do contribute significantly to the total surface area.

The structure on the nanometer length scale was further investigated by TEM (Figure 5.9). From these images it is clear the macropore walls are built up of loosely aggregated particles ( $11 \pm 2 \text{ nm}$ ) that appear to be single crystallites based on the crystal fringes that can be observed at higher magnifications. No internal particle porosity can be observed suggesting that the introduced porosity observed in the nitrogen physisorption data probably originates from the interparticle voids seen in the TEM images.

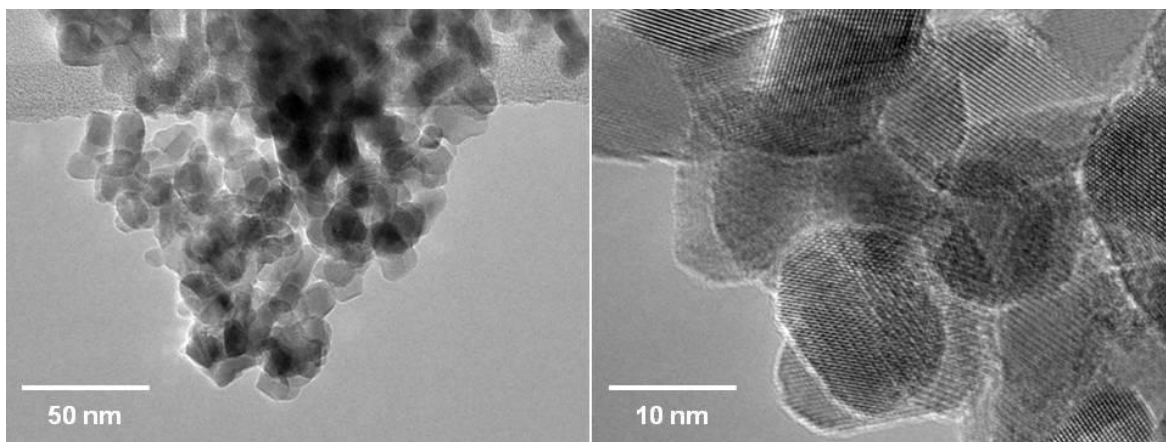


**Figure 5.9.** TEM images of sample  $\text{ZrO}_2$ -M2 at different magnifications showing the particles and the crystal fringes.

In order to shed some light on the chemical composition of the  $\text{ZrO}_2$  replica monoliths various characterization techniques were used, for instance EDS to estimate the remaining Si content in the replica monoliths (results not shown). From these measurements it was clear that the replicas still contain fairly high concentrations of silicon:  $\sim 7 \text{ at-\% Si}$  in  $\text{ZrO}_2$ -M1 and  $\sim 8 \text{ at-\%}$

in ZrO<sub>2</sub>-M2. The silicon that remains is not associated with undissolved template, as the dissolution times used were sufficient to completely dissolve the silica template in all the other samples. Liu and Baker reported the formation of zirconium silicate when they nanocast zirconia into mesoporous silica particles,<sup>53</sup> which suggests that this could also be the cause for the retained silicon. This is consistent also with our observation of the formation of silver silicates (below).

The XRD plot in Figure 5.6 shows that the replica structure consists of a mixture of monoclinic ZrO<sub>2</sub> and tetragonal ZrO<sub>2</sub> (or orthorhombic ZrO<sub>2</sub> which would give almost the same peaks). However, there is no evidence of any crystalline phases of mixed Si-Zr oxides (for instance ZrSiO<sub>4</sub> = zircon), although a broad diffraction peak between 10–20° 2θ would indicate an amorphous phase. The monoclinic ZrO<sub>2</sub> peak at ~28° 2θ was used to determine the crystallite size by the Scherrer equation and the size was estimated to be ~12.5 nm which corresponds quite well to the TEM images.

FT-Raman spectroscopy gave further information about the crystalline structure of the ZrO<sub>2</sub> replica monoliths (Figure 5.10). Here again the conclusion was that the samples are mixtures of monoclinic and tetragonal ZrO<sub>2</sub>, while no peak from zirconium silicate can be detected. The presence of both m-ZrO<sub>2</sub> and t-ZrO<sub>2</sub> is typical for calcinations at temperatures between 400 and 800 °C, where the transition from the tetragonal to the monoclinic form is evident with increasing temperature.<sup>80,81</sup> The peak at 1063 cm<sup>-1</sup> typically appears for small crystallites or grain sizes (< 20 nm) and the ratio between the S1063 and C475 peaks can be used to estimate the grain size. In this case it is about 15 nm which corresponds well with both the XRD and TEM results.

The absence of peaks from zirconium silicate in the XRD is not particularly surprising as

XRD requires that there be some minimum crystallinity in the material. Liu and Baker in their work on nanocasting of zirconia into mesoporous silica particles<sup>53</sup> were also not able to detect any XRD peaks due to scattering from the zirconium silicate. They believed this was because the zirconium silicate was formed only at the surface of the silica and that this was not a bulk phase. In the absence of XRD peaks for  $ZrSiO_4$  they relied on careful comparison of the Raman spectrum of their silica matrix in the presence and absence of added zirconia to identify the zirconium silicate phase. From their work it is clear that the peaks for zirconium silicate would be undetectable in our Raman spectrum (Figure 5.10) as they would be masked by the zirconia peaks.

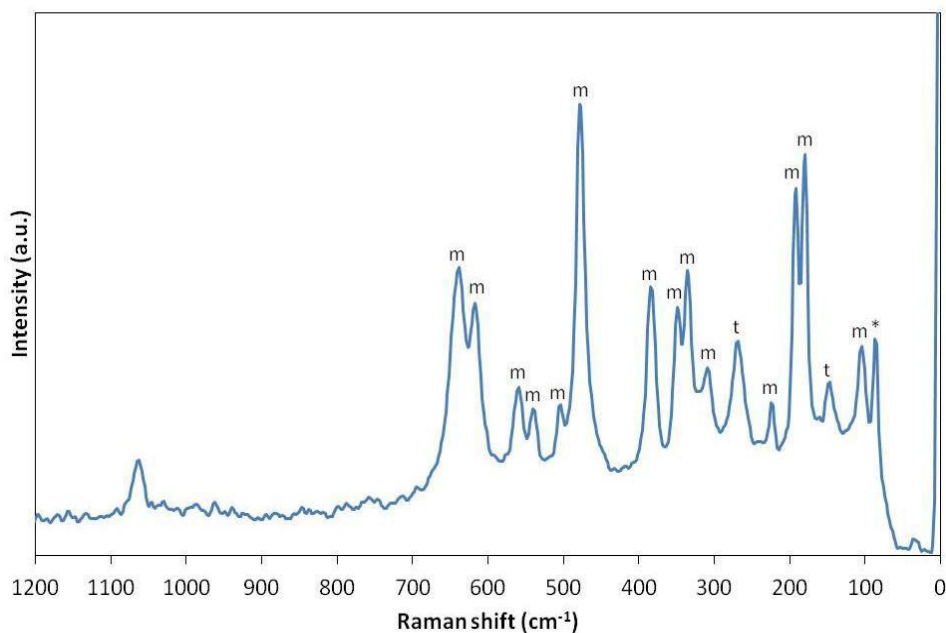


**Figure 5.10.** FT-Raman Measurement of Sample  $ZrO_2$ -M2 Showing Both Monoclinic (m) and Tetragonal (t) Peaks (\* previously observed ambiguity).

#### 5.4.5 Ag Monoliths

The silver monoliths produced by decomposition of silver nitrate under vacuum and under air were both a flat grey color on the exterior. Visual inspection of the interior however showed significant differences between the two samples. The sample prepared under vacuum,

Ag-B3-vac was spatially inhomogeneous. A cross-section showed that the flat grey color extended only ca. 1 mm into the monolith. The center 2 mm of the sample was a dark pink/orangey red in color. The samples impregnated under air appeared homogeneous under visual inspection of cross-sections. Figure 5.11 and Figure 5.1 show SEM images taken from the exterior region of the monolith decomposed under vacuum. The EDS (shown in supporting information) gives a composition which is 80 atomic% silver. The XRD (Figure 5.6) also shows that the dominant peaks for this region are from metallic silver. The morphology of the material (Figure 5.1 and Figure 5.11) is consistent with that of agglomerated silver. The decomposition was carried out at 450 °C. This exceeded the Hüttig temperature for silver, and so sintering and particle growth of the silver crystallites are expected. The XRD for the center of sample Ag-B3-vac is quite different from that of the exterior of the monolith. Peaks due to metallic silver are clearly present, however there are also a number of other peaks, a set of which agree well with a silver silicate of composition  $\text{Ag}_{10}\text{Si}_4\text{O}_{13}$ . The inhomogeneous nature of the sample in this area is clearly seen in Figure 5.11, which shows a cross-section of a ligament showing two very different morphologies, a very smooth central core surrounded by a shell of material with coarser

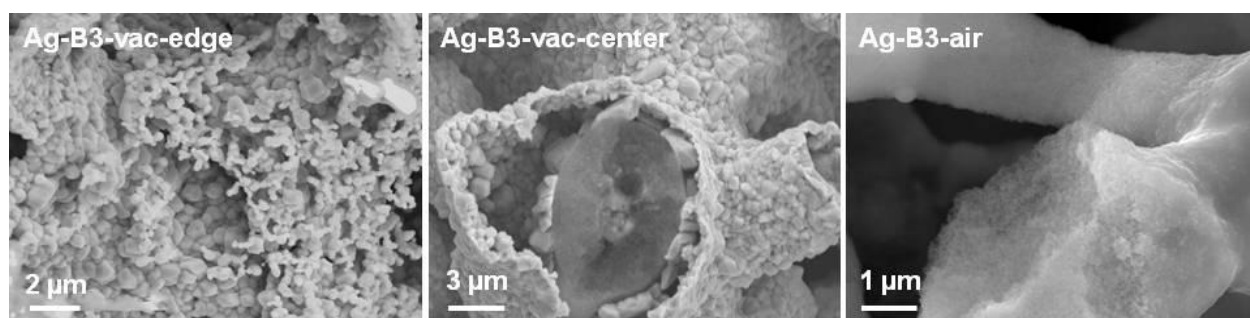


**Figure 5.11.** SEM images (from left to right) from the center portion of Ag-B3-vacuum, the exterior portion of Ag-B3-vacuum, and Ag-B3-air.

structures. The composition of these two phases from EDS is significantly different (supporting information) with the shell having an atomic composition: Ag 10%: Si 26%: O 64%, and the

core having a composition: Ag 66%: Si 6%: O 28%.

Figure 5.11 also shows a typical SEM image of the sample decomposed under air, sample Ag-B3-air. The observed morphology is relatively smooth at the micrometer length scale and consists of smaller features more typical of other nanocast samples such as Fe<sub>2</sub>O<sub>3</sub> above. This morphology is consistent throughout sample Ag-B3-air. The XRD data for this does show the presence of metallic silver, but also shows the presence of a number of other peaks. The composition estimated by EDS varies from 8 to 15% silver and 10 to 21% silicon. The surface area of the two monoliths is also very different. Sample Ag-B3-vac has a surface area of 94.7 m<sup>2</sup>/g compared to 17.9 m<sup>2</sup>/g for sample Ag-B3-air, with a mesopore volume three times higher. To the best of our knowledge the formation of silver silicates from mesoporous silica has not been previously reported. The formation of Ag<sub>2</sub>SiO<sub>3</sub> is reported to be thermodynamically unfavorable for bulk materials, but becomes favorable for mixtures of silver and silica nanoparticles with diameters less than 20 nm.<sup>82</sup> Similarly the formation of Ag<sub>6</sub>Si<sub>2</sub>O<sub>7</sub> is reported to occur at the interface between silica nanoparticles and amorphous silica.<sup>83</sup> The formation of silver silicates within our mesoporous silica templates is consistent with both these reports.

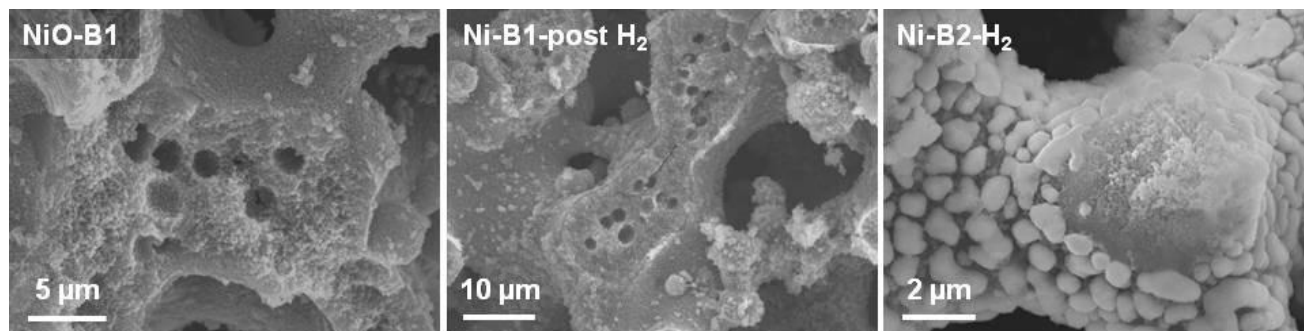
We believe that the spatial variations in composition, and the impact of atmosphere can be explained by assuming that the decomposition of the silver nitrate to silver and growth of silver nanoparticles is in competition with formation of silver silicates. The presence of air could well modify the decomposition pathway for the silver nitrate, as is known to occur for other metal nitrates.<sup>78</sup> Under vacuum the decomposition products would be more quickly carried away and so the reduction would occur more rapidly. The data from the sample decomposed under vacuum suggests that in the core of the monolith the transport of decomposition products is too slow to produce complete conversion to the metallic silver. Although these types of spatially

heterogeneous structures have not previously been reported in silica monoliths, a comparable effect has been reported for nanocasting of iron oxide into mesoporous silica particles where the shape of the container impacted the size and morphology of the resulting mesoporous iron oxide particles.<sup>84</sup> This model is also broadly consistent with the impact of different gas atmospheres on  $\text{Co}_3\text{O}_4$  monolith formation discussed above, although the exact chemical pathways must be significantly different given the formation of silicates in the case of silver but not cobalt.

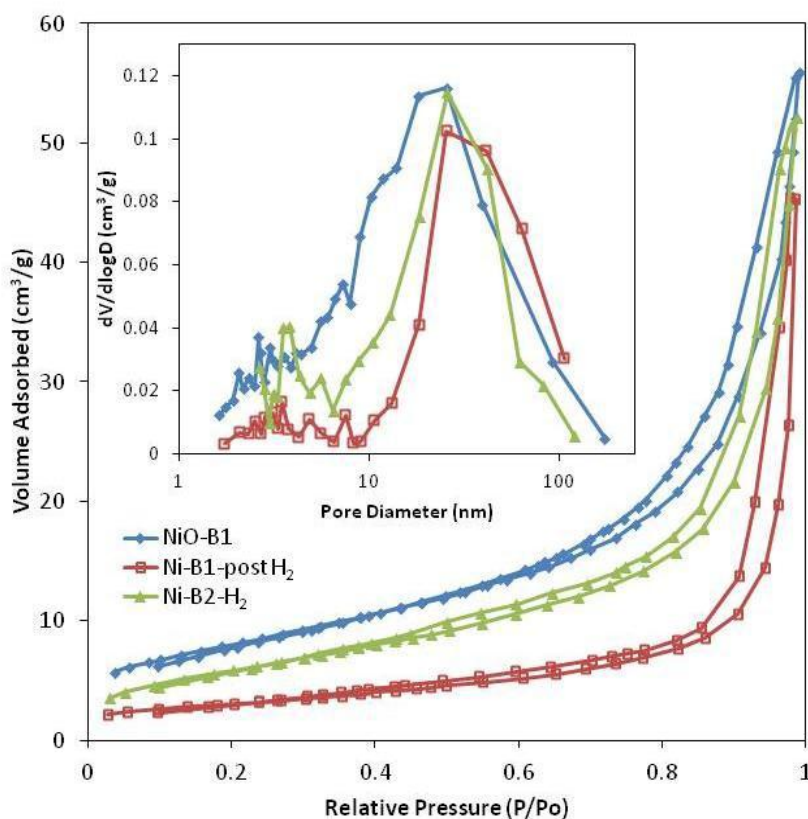
#### 5.4.6 Nickel Oxide and Nickel Monolith

Figure 5.12 shows an SEM image of a nickel oxide monolith (sample NiO-B1) produced from decomposition of nickel acetate after removal of the silica template. The reduction of this sample by hydrogen gas leads to the nickel monolith Ni-B1-post $\text{H}_2$  with the SEM image shown in Figure 5.12. XRD shows (Figure 5.6) that the reduction is largely complete, although EDS data from the sample indicates that surface oxidation occurs relatively quickly. A comparison of the SEM images at multiple length scales indicates that the reduction retains the structure down to a length scale of 50-100 nm, however comparison of the nitrogen adsorption isotherms suggests that there is some loss of structure on reduction as indicated by the drop in surface area/volume from  $182 \text{ m}^2/\text{cm}^3$  for the nickel oxide sample NiO-B1 to  $95 \text{ m}^2/\text{cm}^3$  in the resulting nickel sample Ni-B1-post  $\text{H}_2$ . This is also reflected in the pore size distribution where the nickel oxide has a peak in the pore size distribution at around 20 nm, this peak shifts and broadens in the nickel (Figure 5.13). This is not surprising as we would expect that the elevated temperatures associated with the hydrogen reduction would allow for some migration of the nickel, resulting in smoothing out of the highest curvature surfaces and a resultant decrease in surface area. The 0.5–1 micrometer voids that can be seen in the SEM images of NiO-B1 and Ni-B1-post $\text{H}_2$  are almost certainly a result of similar voids that were present in the parent silica monolith. We

believe that these voids are the result of air bubbles present during the sol-gel processing that produced the silica monoliths.



**Figure 5.12.** SEM images from left to right of nickel oxide sample NiO-B1, nickel sample Ni-B1-post- H<sub>2</sub> and nickel sample Ni-B2-H<sub>2</sub>.



**Figure 5.13.** Nitrogen Physisorption of Nickel Oxide and Nickel Monoliths (a) Nickel Oxide, (b) Nickel sample Ni-B2-post-H<sub>2</sub> and (c) nickel sample Ni-B2-H<sub>2</sub>.

Figure 5.12 shows an SEM image of nickel (Ni-B1-H<sub>2</sub>) made by an alternative route using a different template that does not contain voids in the ligament. This sample was

synthesized from aqueous nickel nitrate solution, with the decomposition at each step being carried out under hydrogen. Hydrogen is believed to reduce the mobility of the nickel during the decomposition of nickel nitrate by scavenging the oxygen formed in the reaction and preventing this causing further decomposition.<sup>78</sup> Formation by this pathway leads to a surface/volume ratio which is significantly higher. The pore size distribution is also centered at a slightly lower pore diameter. Although it is tempting to conclude that the in situ hydrogen reduction did result in better retention of structure, the two samples were produced from different monoliths using different precursors and different procedures. Sample SiO<sub>2</sub>-B1 used a lower concentration of a shorter chain surfactant, leading to smaller pores (4.3 nm for SiO<sub>2</sub>-B1 cf. 4.5 nm for SiO<sub>2</sub>-B2) and a smaller mesopore volume (2.09 cm<sup>3</sup>/cm<sup>3</sup> for SiO<sub>2</sub>-B1 cf. 2.88 cm<sup>3</sup>/cm<sup>3</sup> for SiO<sub>2</sub>-B2). Sample Ni-B1-postH<sub>2</sub> was made by "incipient wetness" in air using an acetate precursor. This means that only enough solution was added to completely fill the surfactant mesopores. Sample Ni-B2-H<sub>2</sub> was made using nickel nitrate under vacuum infiltration. We believe this method leads to faster filling of the surfactant mesopores.

Overall the use of bimodal rather than monomodal silica templates does appear to produce an enhancement in the surface area of the nanocast metal oxides, but the extensive migration of materials from the surfactant mesopores into the textural mesopores is such that the potentially accessible surface area is not fully realized.

#### 5.4.7 Impact of Monolith Type

The greater surface area available from the bimodal monoliths Si-B1, Si-B2 and Si-B3 would be expected to be translated into a similarly higher surface area in the nanocast replicas. Although there are no direct comparisons in this work between the same material nanocast into monomodal and bimodal templates comparison with our previously published work<sup>34</sup> and the

results in Table 1 does allow some observations to be made. The different molar masses of the different nanocast material makes comparison of the surface area/gram misleading. Surface area per volume of nanocast material ( $\text{m}^2/\text{cm}^3$ ) is a more meaningful comparison. On this basis the previously reported<sup>34</sup> surface area for  $\text{Co}_3\text{O}_4$  from a monomodal template would have a value of  $247 \text{ m}^2/\text{cm}^3$  (based on a density of  $\text{Co}_3\text{O}_4$  of  $6.11 \text{ g}/\text{cm}^3$ ). This is less than half the best value in Table 5.1. This difference is in-line with results from  $\text{SnO}_2$  (based on a density of  $\text{SnO}_2$  of  $6.95 \text{ g}/\text{cm}^3$ ) which increases from  $250 \text{ m}^2/\text{cm}^3$  for a monomodal template to  $490 \text{ m}^2/\text{cm}^3$  for a bimodal template.<sup>34</sup> It is more difficult to discern any trends in the results as a function of metal oxide, as the values for  $\text{ZrO}_2$  nanocast in monomodal templates are comparable to those for  $\text{Co}_3\text{O}_4$  from bimodal templates and significantly higher than that observed for  $\text{Fe}_2\text{O}_3$  and  $\text{NiO}$ . However, considerable zirconium silicate formation at the interface between the zirconia and the silica template occurred in this sample, and so the higher surface area may well reflect this phenomenon. Silver monoliths on the other hand do not show a similarly high surface area, but in this case bulk silver silicate formation is believed to have occurred, implying large scale movement of materials which would allow considerable Ostwald ripening to have occurred.

## 5.5 Conclusions

The use of hierarchically porous silica as templates for nanocasting to produce hierarchically porous metals and metal oxides as a general method to make these classes of materials has been demonstrated by synthesis of nickel oxide,  $\alpha\text{-Fe}_2\text{O}_3$ ,  $\text{ZrO}_2$ , nickel and silver monoliths. The details of the processes used in converting the silica template to the replica monolith have a significant impact on the structure and properties of the final material. This was illustrated by the effect of carrying out the processes under vacuum or under different gases on  $\text{Co}_3\text{O}_4$  and silver monoliths. In the case of the silver monoliths the atmosphere impacts not

simply the structure of the material, but also the composition of the material, and the composition as a function of location in the monolith. We have also demonstrated that metal silicates can be formed at relatively modest temperatures within mesoporous silica templates, which appears to have received little attention within the nanocasting field.

## **5.6 Acknowledgements**

Support for this work was provided by NSF CHE-0719398 (MGB) and by the Academy of Finland 127919 (JHS). Electron microscopy was carried out in the Central Analytical Facility at The University of Alabama. Mika Lindén (University of Ulm) is gratefully acknowledged for valuable discussion, as are Mikael Järn (Åbo Akademi University) for SEM measurements ( $\text{SiO}_2$  and  $\text{ZrO}_2$ ) and Bernd Spliethoff (MPI, Mülheim an der Ruhr) for TEM measurements ( $\text{SiO}_2$  and  $\text{ZrO}_2$ ). Ms. Keana Graves ( $\text{Fe}_2\text{O}_3$ ), Ms. Alison Hu (Ni and NiO) and Ms. Elizabeth Junkin ( $\text{Co}_3\text{O}_4$ ) provided technical assistance with sample preparation.

This work was performed with co-authors Ms. Amy Grano, Professor Jan-Henrik Småt, and Professor Martin Bakker.

## 5.7 References

- (1) Kadib, A. E.; Chimenton, R.; Sachse, A.; Fajula, F. O.; Galarneau, A.; Coq, B. *Angew. Chem. Int. Ed.* **2009**, *121*, 5069.
- (2) Sachse, A.; Galarneau, A.; Fajula, F. O.; DiRenzo, F.; Creux, P.; Coq, B. *Micro. Meso. Mater.* **2011**, *140*, 58.
- (3) Jiang, Z.; Smith, N. W.; Liu, Z. *J. Chromatogr. A* **2011**, *1218*, 2350.
- (4) Miller, S. *Anal. Chem.* **2004**, *76*, 99A.
- (5) Unger, K. K.; Skudas, R.; Schulte, M. M. *J. Chromatogr. A* **2008**, *1184*, 393.
- (6) Guiochon, G. *J. Chromatogr. A* **2007**, *1168*, 101.
- (7) Winter, M.; Brodd, R. J. *Chem. Rev.* **2004**, *104*, 4245.
- (8) Long, J. W.; Dunn, B.; Rolison, D. R.; White, H. S. *Chem. Rev.* **2004**, *104*, 4463.
- (9) Rolison, D. R.; Long, J. W.; Lytle, J. C.; Fischer, A. E.; Rhodes, C. P.; McEvoy, T. M.; Bourg, M. E.; Lubers, A. M. *Chem. Soc. Rev.* **2009**, *38*, 226.
- (10) Yuan, Z. Y.; Ren, T.-Z.; Vantomme, A.; Su, B.-L. *Chem. Mater.* **2004**, *16*, 5096.
- (11) Vantomme, A.; Leonard, A.; Yuan, Z. Y.; Su, B.-L. *Coll. Surf. A* **2007**, *300*, 70.
- (12) Lytle, J. C.; Stein, A. *Annual Review of Nano Research*, Vol. 1 (Eds: G. Cao, C. J. Brinker), World Scientific, **2006**, 1.
- (13) Stein, A.; Li, F.; Denny, N. R. *Chem. Mater.* **2008**, *20*, 649.
- (14) Dziomkina, N. V.; Vancso, G. J. *Soft Matter* **2005**, *1*, 265.
- (15) Antonietti, M.; Berton, B.; Goltner, C.; Hentze, H.-P. *Adv. Mat.* **1998**, *10*, 154.
- (16) Li, F.; Wang, Z.; Ergang, N. S.; Fyfe, C. A.; Stein, A. *Langmuir* **2007**, *23*, 3996.
- (17) Carn, F.; Colin, A.; Achard, M.-F.; Deleuze, H.; Sellier, E.; Birot, M.; Backov, R. *J. Mater. Chem.* **2004**, *i*, 1370.
- (18) J. J. Chui, D. J. Pine, S. T. Bishop, B. F. Chmelka, *J. Catal.* **2004**, *221*, 400.
- (19) Maekawa, H.; Esquena, J.; Bishop, S.; Solans, C.; Chmelka, B. F. *Adv. Mat.* **2003**, *15*, 591.

- (20) Zhao D. Y.; Yang P. D.; Chmelka B. F.; Stucky, G. D. *Chem. Mater.* **1999**, *11*, 1174.
- (21) Davis, S. A.; Burkett, S. L.; Mendelson, N. H.; Mann, S. *Nature* **1997**, *385*, 420.
- (22) Mille, C.; Tyrode, E. C.; Corkery, R. W. *Chem. Comm.* **2011**, *47*, 9873.
- (23) Caruso, R.A.; Antonietti, M. *Adv. Funct. Mater.* **2002**, *12*, 307.
- (24) Caruso, R. A.; Schattka, J. H. *Adv. Mat.* **2000**, *12*, 1921.
- (25) Walsh, D.; Arcelli, L.; Ikoma, T.; Tanaka, J.; Mann, S. *Nat. Mat.* **2003**, *2*, 386.
- (26) Nishihara, H.; Mukai, S. R.; Yamashita, D.; Tamon, H. *Chem. Mater.* **2005**, *17*, 683.
- (27) Suzuki, K.; Ikari, K.; Imai, H. *J. Mater. Chem.* **2003**, *13*, 1812.
- (28) Nakanishi, K. *J. Porous. Mat.* **1997**, *4*, 67.
- (29) Konishi, J.; Fujita, K.; Oiwa, S.; Nakanishi, K.; Hirao, K. *Chem. Mater.* **2008**, *20*.
- (30) Konishi, J.; Fujita, K.; Oiwa, S.; Nakanishi, K.; Hirao, K. *Mater.* **2006**, *18*, 864.
- (31) Tokudome, Y.; Fujita, K.; Nakanishi, K.; Miura, K.; Hirao, K. *Chem. Mater.* **2007**, *19*, 3393.
- (32) Ruzimuradov, O.; Hasegawa, G.; Kanamori, K.; Nakanishi, K. *J. Am. Ceram. Soc.* **2011**, *94*, 3335.
- (33) Smått, J.-H.; Spliethoff, B.; Rosenholm, J. B.; Lindén, M. *Chem. Comm.* **2004**, 2188.
- (34) Smått, J.-H.; Weidenthaler, C.; Rosenholm, J. B.; Lindén, M. *Chem. Mater.* **2006**, *18*, 1443.
- (35) Taguchi, A.; Smatt, J.-H.; Linden, M. *Adv. Mat.* **2003**, *15*, 1209.
- (36) Lu, A.-H.; Smått, J.-H.; Lindén, M. *Adv. Funct. Mater.* **2005**, *15*, 865.
- (37) Nakanishi, K.; Komura, H.; Takahashi, R.; Soga, N. *Bull. Chem. Soc. Jpn.* **1994**, *67*, 1327.
- (38) Smått, J.-H.; Schunk, S. A.; Lindén, M. *Chem. Mater.* **2003**, *15*, 2354.
- (39) Konishi, J.; Fujita, K.; Nakanishi, K.; Hirao, K. *Chem. Mater.* **2006**, *18*, 6069.
- (40) Murai, S.; Fujita, K.; Iwata, K.; Tanaka, K. *J. Phys. Chem. C* **2011**, *115*, 17676.

- (41) Drisko, G. L.; Zelcer, A. E.; Luca, V.; Caruso, R. A.; Soler-Illia, A. *Chem. Mater.* **2010**, *22*, 4379.
- (42) Nakanishi, K.; Sato, Y.; Ruyat, Y.; Hirao, Y. *J. Sol-Gel Sci. Tech.* **2003**, *26*, 567.
- (43) Sato, Y.; Nakanishi, K.; Hirao, Y.; Jinnai, J.; Shibayama, M.; Melnichenko, Y. B.; Wignall, G. D. *Coll. Surf. A* **2001**, *187*, 117.
- (44) Amatani, T.; Nakanishi, K.; Hirao, K.; Kodaira, T. *Chem. Mater.* **2005**, *17*, 2114.
- (45) Zhong, H.; Zhu, G.; Wang, P.; Liu, J.; Yang, J.; Yang, Q. *J. Chromatogr. A* **2008**, *1190*, 232.
- (46) Brandhuber, D.; Torma, V.; Raab, C.; Peterlik, H.; Kulak, A.; Husing, N. *Chem. Mater.* **2005**, *17*, 4262.
- (47) Lu, A.-H.; Zhao, D.; Wan, Y. *Nanocasting: A Versatile Strategy for Creating Nanostructured Porous Materials*, Vol. 11, Royal Society of Chemistry, Cambridge, U. K., 2010.
- (48) Lu, A.-H.; Schuth, F. *Adv. Mat.* **2006**, *18*, 1793.
- (49) Yang, H. F.; Zhao, D. Y. *J. Mater. Chem.* **2005**, *15*, 1217.
- (50) Tiemann, M. *Chem. Mater.* **2008**, *20*, 961.
- (51) Bao, R.; Jiao, K.; He, H.; Zhuang, J.; Yue, B. *Studies Surf. Sci. Catal.* **2007**, *165*, 267.
- (52) So, B. G.; Shon, J. K.; Yu, J.; Joo, O.-S.; Kim, J. M. *Prog. in Meso. Mater.* **2007**, 309.
- (53) Liu, B.; Thornton-Baker, R. *J. Mater. Chem.* **2008**, *18*, 5200.
- (54) Wang, Y. M.; Wu, Z. Y.; Wang, H. J.; Zhu, J. H. *Adv. Funct. Mater.* **2006**, *16*, 2374.
- (55) Yue, W.; Zhou, W. *Chem. Mater.* **2007**, *19*, 2359.
- (56) Yue, W. B.; Zhou, W. Z. *Studies Surf. Sci. Catal.* **2007**, *170*, 1755.
- (57) Yen, H.; Seo, Y.; Guillet-Nicolas, R.; Kaliaguinec, S.; Kleitz, F. *Chem. Comm.* **2011**, *47*, 10473.
- (58) Bakker, M. G.; Warke, V. *Nanowire Research Progress*, (Ed: X. Xue), Nova Science Publishers, Hauppauge, NY **2008**, *15*.
- (59) Sayler, F. M.; Grano, A. J.; Scogin, W.; Sanders, P.; Smatt, J.-H.; Shaughnessy, K.; Bakker, M. G. *MRS Proceedings*, **2012**, *1389*, g05-05.

- (60) Moulijn, J. A.; van Diepen, A. E.; Kapteijn, F. *App. Catal. A* **2001**, *212*, 3.
- (61) Martinez, A.; Lopez, C.; Marquez, F.; Diaz, I. *J. Catal.* **2003**, *220*, 486.
- (62) Liu, S.; Yue, B.; Jiao, K.; Zhou, Y.; He, H. *Materials Letters* **2006**, *60*, 154.
- (63) Valdes-Solis, T.; Tartaj, P.; Marban, G.; Fuertes, A. B. *Nanotech.* **2007**, *18*, 145603.
- (64) Gu, M.; Yue, B.; Bao, R.; He, H. *Mater. Res. Bull.* **2009**, *44*, 1422.
- (65) Tuysuz, H.; Lehmann, C. W.; Bongard, H.; Tesche, B.; Schmidt, R.; Schuth, F. J. *Am. Chem. Soc.* **2008**, *130*, 11510.
- (66) El-Sheikh, S. M.; Harraz, F. A.; Hessien, M. M. *Mat. Res. Chem. Phys.* **2010**, *123*, 254.
- (67) Eliseev, J. *Magn. Magn. Mat.* **2005**, *106*, 290-291.
- (68) Cabo, M. E.; Pellicer, E.; Rossinyol, E.; Castell, O.; Surinach, S.; Baro, M. D. *Cryst. Growth Des.* **2009**, *9*, 4814.
- (69) Cabo, M. E.; Pellicer, E.; Rossinyol, E.; Estrader, A.; Lopez-Ortega, A.; Nogues, J.; Castell, O.; Surinach, S.; Baro, M. D. *J. Mater. Chem.* **2010**, *20*, 7021.
- (70) Polarz, S.; Orlov, A. V.; Schuth, F.; Lu, A.-H. *Chem. Eur. J.* **2007**, *13*, 592.
- (71) Waitz, T.; Tiemann, M.; Klar, P. J.; Sann, J.; Stehr, J.; Meyer, B. K. *Appl. Phys. Lett.* **2007**, *90*, 123108.
- (72) Tuysuz, H.; Liu, Y.; Weidenthaler, C.; Schuth, F. *J. Am. Chem. Soc.* **2008**, *130*, 14108.
- (73) Jiao, F.; Jumas, J.-C.; Womes, M.; Chadwick, A. V.; Harrison, A.; Bruce, P. G. *J. Am. Chem. Soc.* **2006**, *128*, 12905.
- (74) Smått, J.-H.; Schunk, S. A.; Lindén, M. *Chem. Mater.* **2003**, *15*, 2354.
- (75) Lu, A.-H.; Smått, J.-H.; Backlund, S.; Lindén, M. *Micro. Meso. Mater.* **2004**, *72*, 59.
- (76) Haffer, S.; Waitz, T.; Tiemann, M. *J. Phys. Chem. C* **2010**, *114*, 2075.
- (77) Sietsma, J. R. A.; Meeldijk, J. D.; Versluijs-Helder, M.; Broersma, A.; van Dillen, A. J.; de Jongh, P. E.; de Jong, K. P. *J. Catal.* **2008**, *260*, 227.
- (78) Sietsma, J. R. A.; Friedrich, H.; Broersma, A.; Versluijs-Helder, M.; van Dillen, A. J.; de Jongh, P. E.; de Jong, K. P. *Chem. Mater.* **2008**, *20*, 2921.

- (79) Tidahy, H. L.; Siffert, S.; Lamonier, J.-F.; Zhilinskaya, E. A.; Aboukais, A.; Yuan, Z.-Y.; Vantomme, A.; Su, B.-L.; Canet, X.; De Weireld, G.; Frere, M.; N'Guyen, T. B.; Giraudon, J.-M.; Leclercq, G. *App. Catal. A* **2006**, *310*, 61.
- (80) Li, C.; Li, M. *J. Raman Spectrosc.* **2002**, *33*, 301.
- (81) Siu, G. G.; Stokes, M. J.; Liu, Y. *Phys. Rev. B* **1999**, *59*, 3173.
- (82) De, J.; Umarji, A. M.; Chattopadhyay, K. *Mat. Sci. Eng.* **2007**, *449-451*, 1062.
- (83) Cai, W.; Zhang, L. *Appl. Phys. A* **1998**, *66*, 419.
- (84) Sun, X.; Shi, Y.; Zhang, P.; Zheng, C.; Zheng, X.; Zhang, F.; Zhang, Y.; Guan, N.; Zhao, D.; Stucky, G. D. *J. Am. Chem. Soc.* **2011**.
- (85) Langford, J. I.; Wilson, A. J. C. *J. Appl. Crystallogr.* **1978**, *11*, 102.

## 5.8 Supporting Information

In the preparation of monoliths with a monomodal mesopore size distribution, polyethylene glycol (PEG, MW: 35,000 g/mol) was used to induce the macroporosity. First, PEG was dissolved in H<sub>2</sub>O and HNO<sub>3</sub> (30%). TEOS was then added, and the solution was stirred until a clear and homogeneous solution was obtained. The H<sub>2</sub>O/HNO<sub>3</sub>/TEOS/PEG(35,000) molar ratio in the final sol was 14.7:0.25:1:6.9x10<sup>-4</sup> (sample SiO<sub>2</sub>-M1) and 14.7:0.25:1:7.8x10<sup>-4</sup> (SiO<sub>2</sub>-M1). Monoliths with a bimodal mesoporosity were produced by using a combination of PEG and hexadecyltrimethylammonium bromide (C<sub>16</sub>TAB) or PEG and octadecyltrimethylammonium bromide (C<sub>18</sub>TAB) as structure directing agents.<sup>38</sup> These samples are denoted SiO<sub>2</sub>-B1 (9 wt% C<sub>16</sub>TAB), SiO<sub>2</sub>-B2 (7 wt% C<sub>18</sub>TAB), and SiO<sub>2</sub>-B3 (9 wt% C<sub>18</sub>TAB). The solutions were portioned into micro-titer plates and were allowed to gel and age for 72 h at 40 °C. Solvent exchange in a 1 M NH<sub>4</sub>OH solution for 24 h at 90 °C was performed to increase the stability of the monoliths and to adjust the textural mesopore size. The monoliths were subsequently dried at 40 °C for 72 h and finally calcined at 550 °C for 5 h with a heating ramp of 1 K/min.

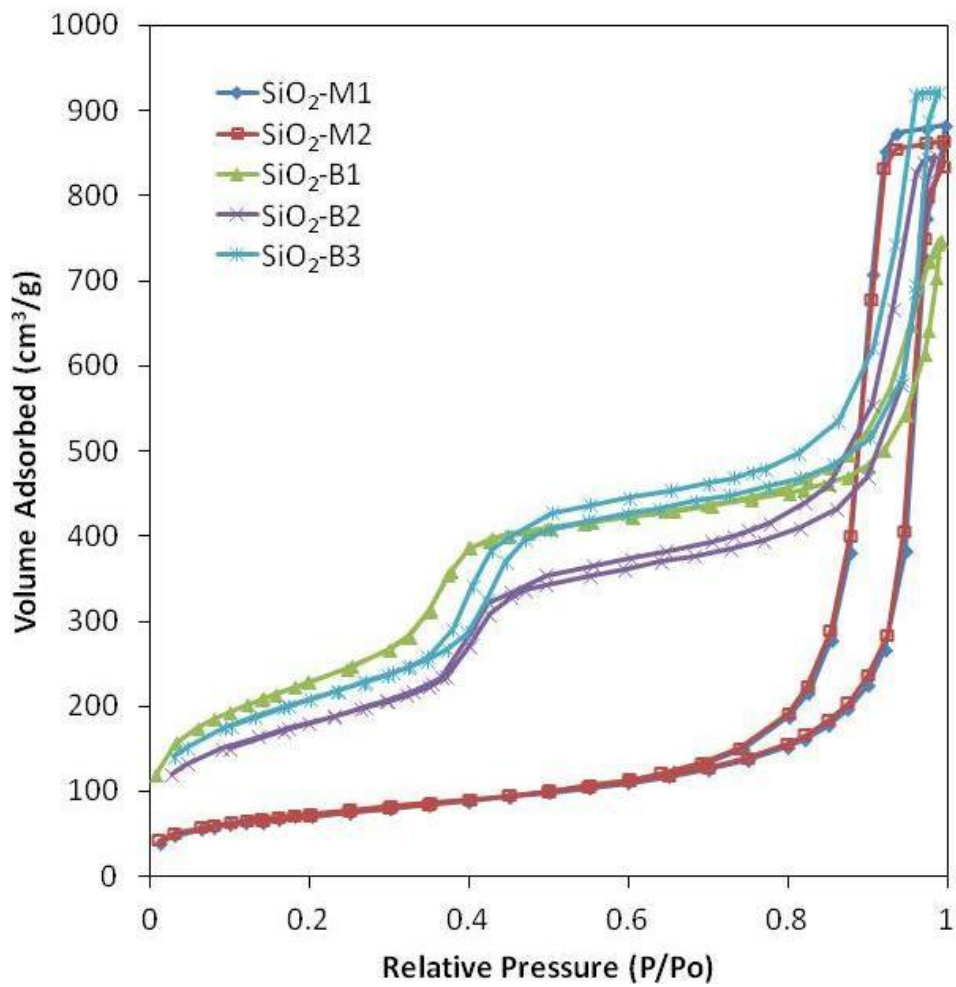


**Figure 5.S1.** Nitrogen physisorption isotherms of the different silica templates used in this study.

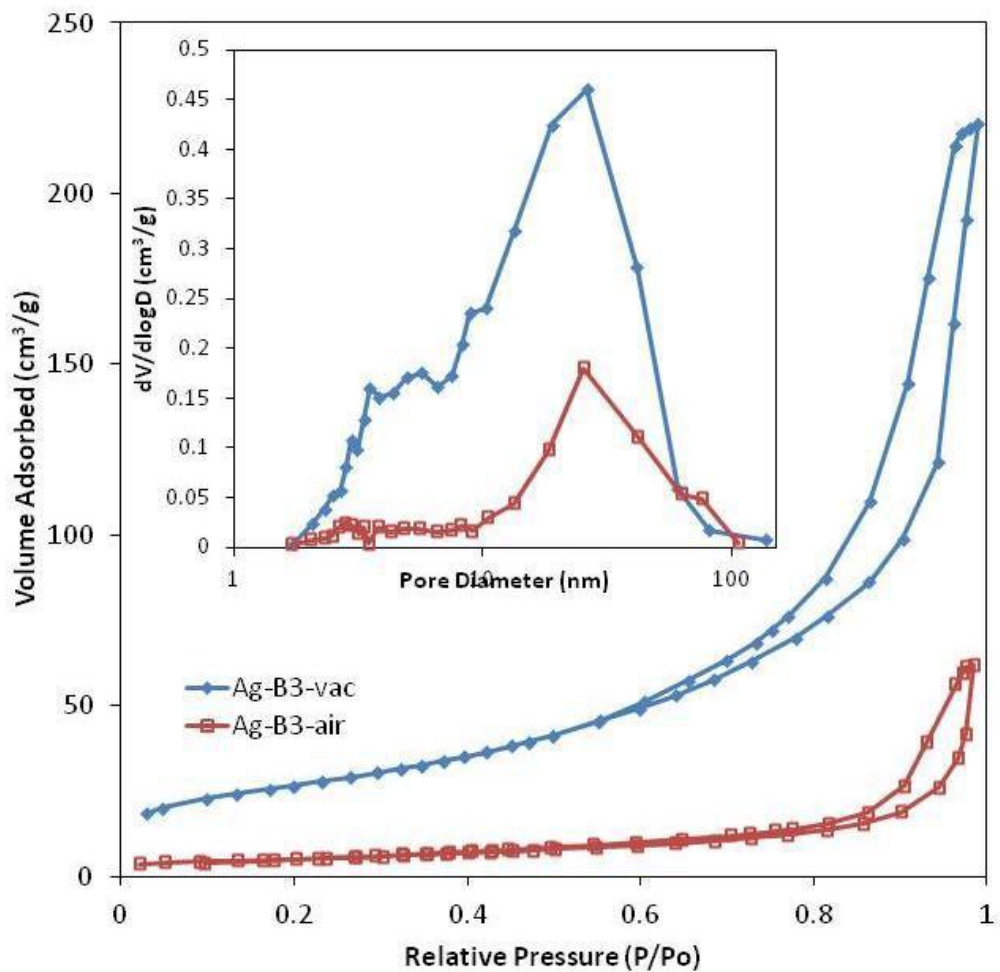


**Figure 5.S2.** Nitrogen physisorption results of Ag-B3-air and Ag-B3-vac samples.

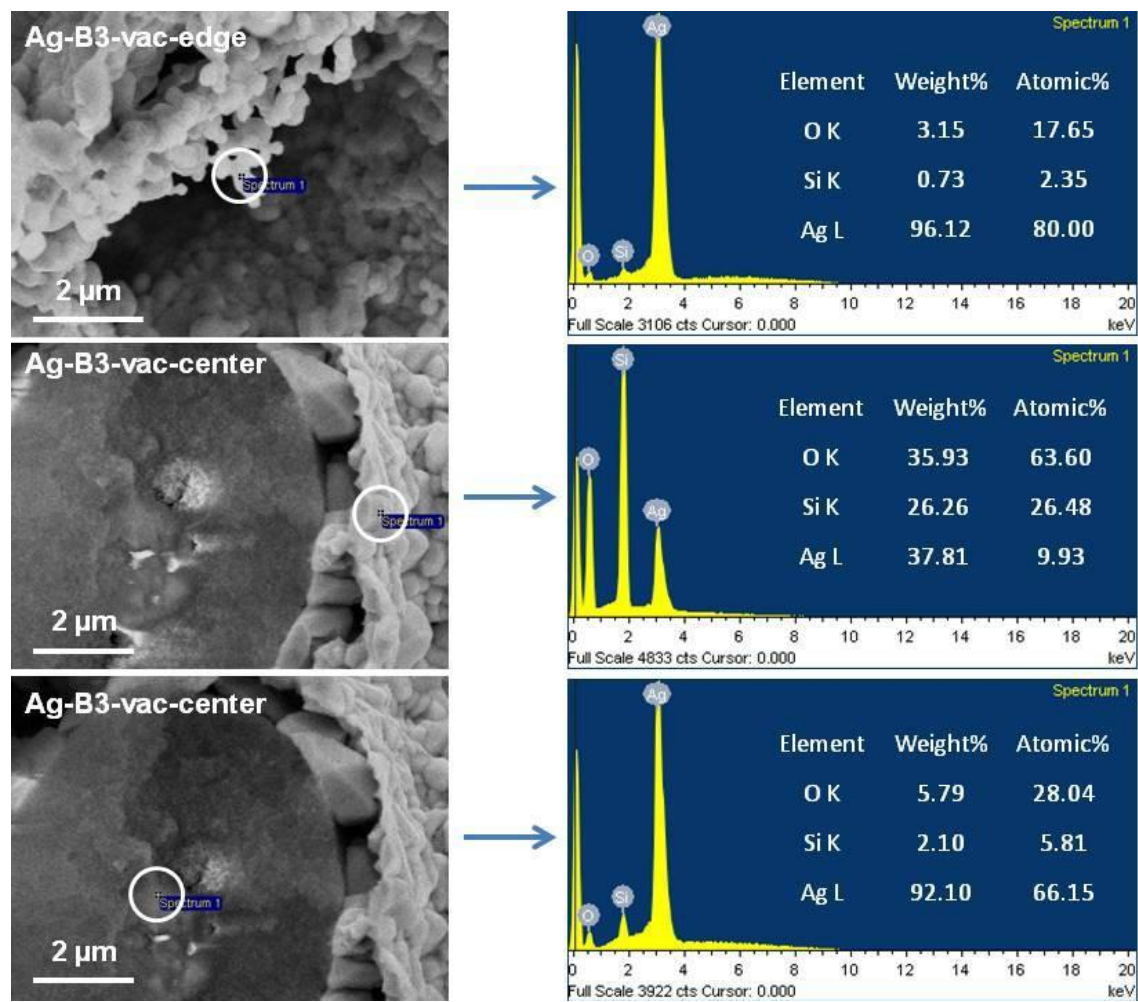


**Figure 5.S3.** EDS results for the different silver samples. The area sampled is indicated in the SEM images on the left hand side.

## Chapter 6

### Formation and Applications of Hierarchically Porous Carbon, Metals and Metal Oxides Formed by Nanocasting

#### 6.1 Abstract

Hierarchically porous materials are of interest in a wide range of applications. If the materials are electronic or ionic conductors such materials are of interest as electrodes for use in fuel cells, flow batteries, electrocatalysis, and pseudo/supercapacitors. We have demonstrated the synthesis of hierarchically porous carbon, metal and metal oxide monoliths. Hierarchically porous silica with porosity at three length scales: 0.5-30 micrometer, 200-500 nm, and 3-8 nm, is used as a template to form these materials. The porosity of the silica template is produced by spinodal decomposition (0.5-30 micrometer), particle agglomeration (200-500 nm) and addition of surfactant or block copolymer (3-8 nm). Nanocasting: replication of all or part of the structure via one of a number of chemical replication techniques has been used to produce the carbon, metal oxide and metal replicas. The final surface areas of the materials can be as high as 1200 m<sup>2</sup>/g for carbon replicas, and > 300 m<sup>2</sup>/cm<sup>3</sup> for metals and metal oxides. The use of the nanocasting technique allows for formation of materials that are compositionally or spatially heterogeneous.

We report here results on the synthesis and characterization of hierarchically porous monoliths of carbon and nickel and the use of some of these monoliths in catalysis and electrochemical capacitors.

#### 6.2 Introduction

Hierarchically porous materials are of interest in a wide range of applications, such as fuel cells, catalysts, sensors and energy storage. The ability to control the spatial composition

and the structure and scale of the pores in the material significantly impacts the properties of the materials. We have been developing methods that use hierarchically porous silica monoliths prepared by sol-gel processes as the starting point to synthesize a range of other hierarchically porous materials including metal oxides<sup>1</sup>, metals and carbon<sup>2</sup> by "nanocasting"<sup>3</sup>: using the silica as a sacrificial template. This contribution will focus on two applications of such materials: nickel metal based hydrogenation and the functionalization of hierarchically porous carbon as current collector for manganese dioxide and iron oxide electrodes for use in aqueous supercapacitors. The former serves as a test case for evaluating the reactivity and stability of porous nickel monoliths, the latter are of interest because the electrode pair manganese dioxide/iron oxide has high charge storage capacity and optimal electrode potentials for use with aqueous electrolytes. The nanostructured nature of the current collector is expected to produce very high charge/discharge rates.

## **6.3 Experimental**

### **6.3.1 Synthesis of Monolithic Silica Templates, Nickel and Carbon Monoliths**

Hierarchically porous silica monoliths were prepared using sol-gel processes in which polyethylene glycol of 35,000 molecular weight was included during formation of the sol to assist with the spinodal decomposition to give macropores in the silica.<sup>4</sup> For the samples used to make nickel catalysts 7 wt% of the cationic surfactant  $C_{18}H_{37}N(CH_3)_3Br$  was added during the monolith synthesis. This caused the formation of disordered mesopores having a diameter of 4 nm.<sup>4</sup>

Hierarchically porous nickel monoliths were produced by solution infiltration of nickel nitrate hydrate at 70 °C followed by reduction with either 5% hydrogen/95% nitrogen or methanol. This process was repeated three times to completely fill the mesopores in the

material. The sample was then etched with 3 M potassium hydroxide solution to dissolve away the silica, leaving porous nickel monoliths. The resulting monoliths were then characterized by nitrogen gas adsorption to determine surface area and with SEM to confirm the hierarchically porous nature of the material.

Carbon replicas were produced by a one step process in which the silica monoliths were added to a solution of furfuryl alcohol, oxalic acid and trimethylbenzene. This solution polymerizes within the silica template. After heating to complete the polymerization and evaporate any remaining solvent the silica/hydrocarbon composite is heated under nitrogen at 850 °C to convert the hydrocarbon polymers into a conducting carbon. The silica is then removed by etching in 3 M potassium hydroxide solution. The resulting material was imaged by

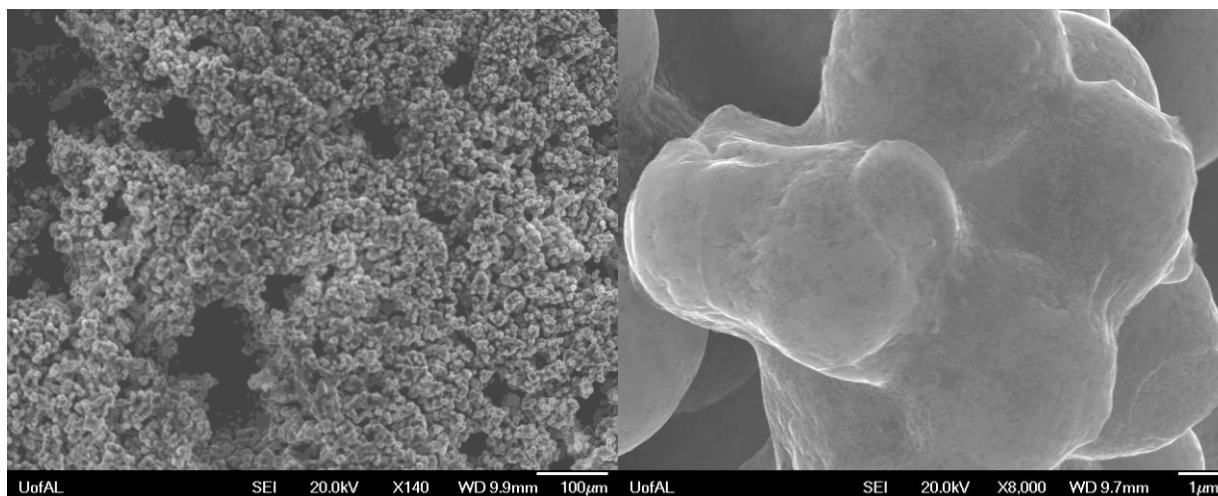


**Figure 6.1.** SEM Images of Hierarchically Porous Carbon Monoliths Produced by "Nanocasting" into Porous Silica Templates.

electron microscopy. Representative images are shown in Figure 6.1. The carbon replicas are seen to be porous at the 5-10 micrometer length scale, and also have mesopores with a range of pore sizes between 4-50 nm. These carbons are typically also microporous: having pores with diameters <1 nm.

### 6.3.2 Catalysis Experiments

The catalytic activity of the nickel monoliths was evaluated for the reduction of cyclohexanone to cyclohexanol by 2-propanol. Reactions were carried out in 20 mL vials under nitrogen, under conditions similar to those reported by Mabane et al.<sup>5</sup> except as noted below. The mass of nickel catalyst was determined, and sufficient cyclohexanone added to give a 2:5 ratio of cyclohexanone to catalyst. Five milliliters of 2-propanol was added to each vial which was then sealed and the reaction allowed to proceed for 18 hours. The extent of conversion to cyclohexanol was determined by NMR spectrometry. Comparison reactions were run against Raney® nickel catalyst obtained from Sigma-Aldrich. Raney® nickel is a sponge metal catalyst made by the microphase separation of aluminum and nickel alloy. The aluminum can be dissolved by leaching away the aluminum with base and then a drop of HCl is added to the reaction to neutralize the excess base. Since the silica was also etched away from the nickel monolith with base, the comparison experiments were carried in a similar manner in which a drop of concentrated HCl was used to neutralize the reaction.

### 6.3.3 Preparation of Porous Electrodes

The electroless deposition of the manganese dioxide onto the carbon monolith was carried out by soaking in 0.1 M aqueous  $\text{Na}_2\text{SO}_4$  for 1 hour, then soaking overnight in aqueous 0.1 M  $\text{NaMnO}_4$  and 0.1 M  $\text{Na}_2\text{SO}_4$ . The samples were then thoroughly rinsed with distilled water and dried overnight at 50 °C. The electrochemical characterization of these monoliths was done using a solution of 1.5 M LiOH and 5.6 M KOH as the electrolyte. The manganese dioxide coated monoliths were soaked in the electrolyte for 1 hour and excess solution was removed. The monolith was then wrapped in a piece of carbon fabric, attached to a potentiostat using a

gold clip, and placed in the hydroxide solution. A high surface area platinum basket was used as the counter electrode.

Deposition of iron oxide onto the carbon monoliths was carried out using a modified literature procedure<sup>6</sup> by soaking in 9 M aqueous KOH solution for 24 hours. The monoliths were then soaked for 2 hours in a solution of 0.025 M  $K_2FeO_4$  in 9 M KOH. The  $FeO_x$  coated carbon monoliths were then rinsed thoroughly with distilled water and dried overnight at 50 °C under vacuum. Electrochemical characterization of these samples was done using a solution of 2.5 M  $Li_2SO_4$  and 0.5 M  $Na_2B_4O_7$  in  $H_2O$  as the electrolyte. Prior to the electrochemical characterization,  $FeO_x$  coated monoliths were soaked with the electrolyte for 1 hour and then excess solution was removed. The monolith was then wrapped in a piece of carbon fabric and attached to a potentiostat using a gold clip and the cyclic voltammogram was run using the 2.5 M  $Li_2SO_4$ /sodium tetraborate electrolyte solution.

## **6.4 Results and Discussion**

### **6.4.1 Catalysis**

Raney® Nickel gives 96% conversion of cyclohexanone to cyclohexanol after 18 hours without stirring. The best value found for a nickel monolith was 80% conversion for a nickel monolith produced by methanol reduction. This was after the addition of a drop of concentrated hydrochloric acid. For nickel monoliths reduced under hydrogen the highest conversion obtained was 69%, again after addition of a drop of concentrated hydrochloric acid. It is not clear from our experiments if the hydrochloric acid played a significant role for the nickel monoliths. The addition of hydrochloric acid to Raney® nickel is important as this dissolves away any excess aluminum leaving clean high surface area nickel. For surfaces that are already nickel the hydrochloric acid may act to dissolve surface nickel oxide. The difference in

reactivity between the hydrogen reduced and methanol reduced monoliths is not surprising. The hydrogen reduction leaves atomic hydrogen adsorbed on the nickel surface, which reacts with oxygen when the sample is exposed to air, producing a nickel oxide coated surface. We believe that the methanol reduction produces less surface oxide, which results in higher catalytic activity.

The surface area of the nickel monoliths is approximately two-thirds that of the Raney® nickel on a per gram basis, and so we believe that the larger amount of a cleaner nickel surface for the Raney® nickel would be expected to produce a more reactive surface. We would anticipate for a reaction carried out under hydrogen gas, which would reduce surface nickel oxide to reactive nickel, the nickel monolith would have a reactivity closer to that of the commercial product.

#### 6.4.2 Porous Electrodes

Figure 6.2 shows SEM images of manganese dioxide grown onto hierarchically porous carbon monoliths. The bright areas on the left hand image are manganese dioxide as confirmed by electron dispersive spectroscopy. Cyclic voltammetry (Figure 6.3) shows that the bulk of the capacitance for this electrode in fact comes from carbon, and that only a small amount of capacitance is added by the manganese dioxide coating. The very high surface area of the carbon monolith will give rise to strong electric double layer capacitance, which produces the high observed capacitance. The SEM images indicate that only a relatively thin coating of manganese dioxide is formed on the carbon. This could well reflect a combination of poor penetration of the hydrophobic carbon monolith by the permanganate solution, coupled with limited reactivity and adhesion.

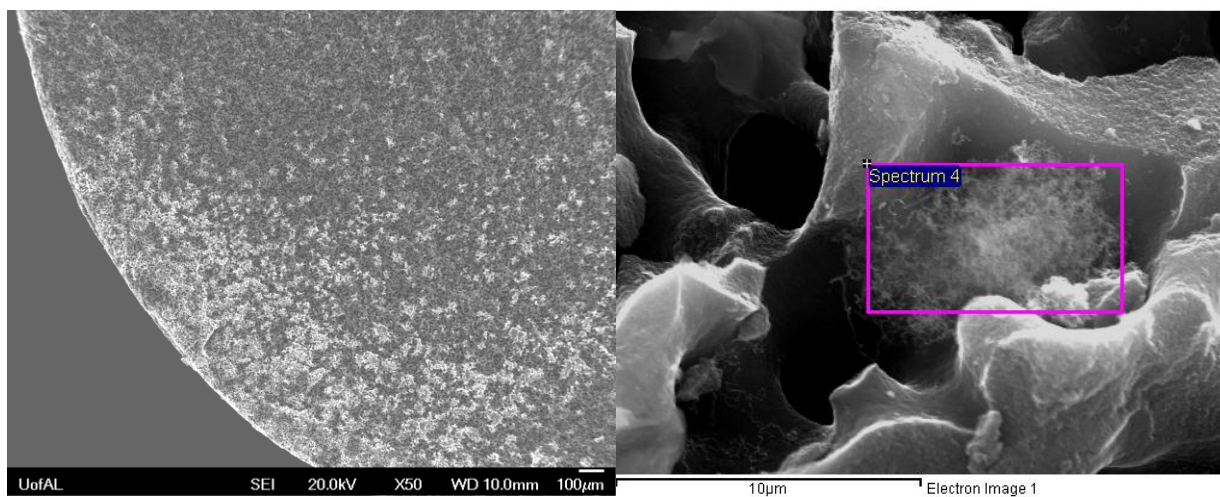


**Figure 6.2.** SEM Images of Manganese Dioxide Coated Hierarchically Porous Carbon Monoliths.

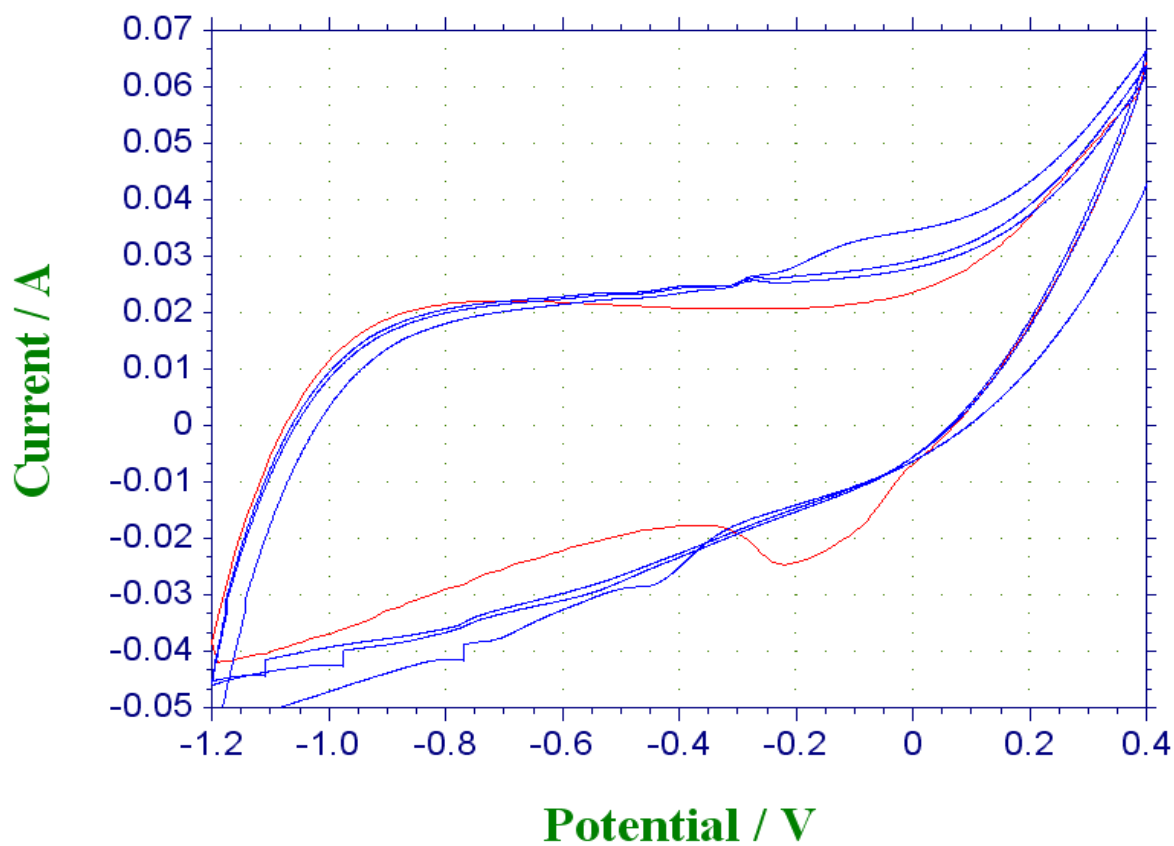


**Figure 6.3.** Cyclic Voltammogram of Bare Carbon Monolith (blue traces) and Manganese Dioxide Coated Carbon Monolith (red trace).

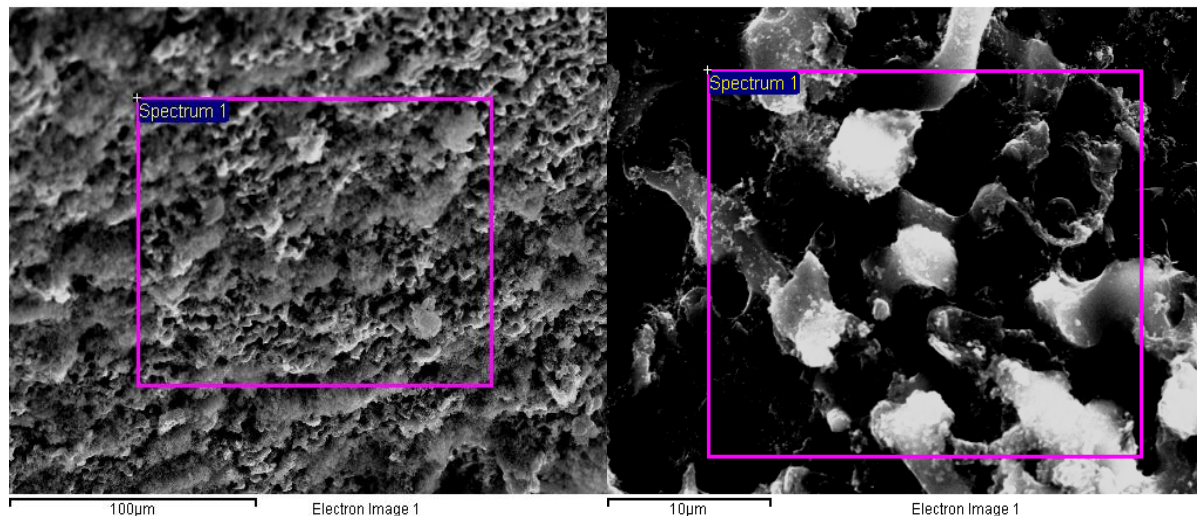


**Figure 6.4.** SEM Images of Carbon Monoliths Coated with Iron Oxide. The iron oxide is the white areas in the right hand image. Box show where EDS data was collected confirming the presence of iron oxide.

The electroless deposition of iron oxide onto the carbon monolith produced a 24% increase in the weight of the monolith. Figure 6.4 shows SEM images of carbon monoliths coated with iron oxide. The presence of the iron oxide is indicated by the white areas in the images which are believed to be due to build up of charge on the iron oxide induced by the insulating nature of the coating. EDS measurements are consistent with the formation of a significant layer of iron oxide. The cyclic voltammetry (Figure 6.5) is also consistent with the growth of a significantly thicker film, showing significant Faradaic peaks added to the underlying electric double layer capacitance of the carbon monolith.

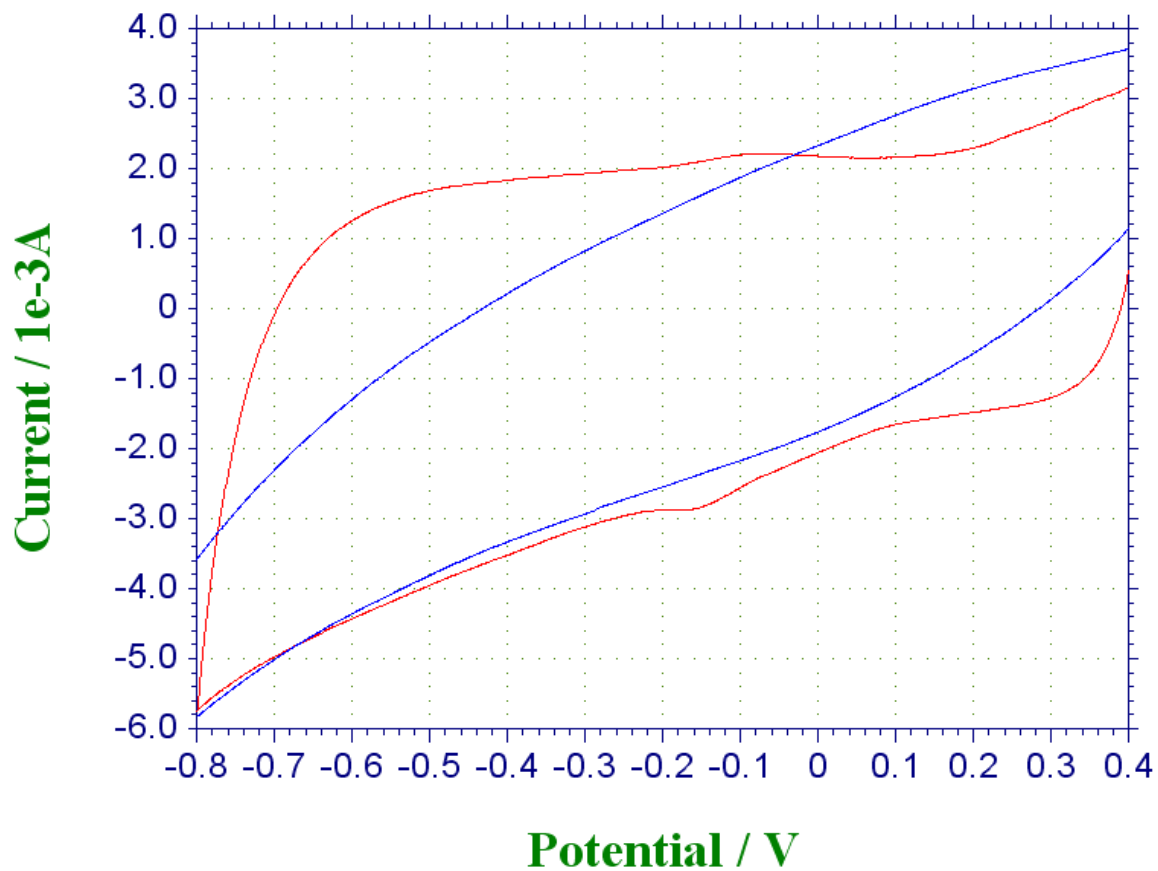


**Figure 6.5.** Cyclic Voltammogram of Bare Carbon Monolith (blue) and Iron Oxide Coated Carbon Monolith (red).

## 6.5 Conclusions

We have successfully prepared hierarchically porous nickel monoliths by nanocasting into silica templates and demonstrated that they are catalytically active for hydrogenation reactions with activities only somewhat below that of commercial catalysts. Electroless deposition of manganese dioxide and iron oxides onto hierarchically porous carbon monoliths produces electrodes with electroactivity. Unfortunately, these monoliths did not exhibit superior or equivalent activity when compared to commercial capacitors. A thin film geometry may enhance activity and this will be explored.

## **6.6 Acknowledgements**

Primary support for this work was from NSF CHE-0719398 (MGB), and by summer research positions provided by NSF CHE 1004098 (PS) and Department of Energy DE-FG02-08ER46499 (WS). The Electron Microscopy was carried out at the Central Analytical Facility of the University of Alabama.

This work was performed with co-authors Ms. Amy Grano, Mr. William Scogin, Ms. Pasha Sanders, Professor Jan-Henrik Smått, Professor Kevin Shaughnessy, and Professor Martin Bakker.

## 6.7 References

- (1) Smått, J.-H.; Weidenthaler, C.; Rosenholm, J. B.; Lindén, M. *Chem. Mater.* **2006**, *18*, 1443-1450.
- (2) Lu, A.-H.; Smått, J.-H.; Lindén, M. *Adv. Funct. Mater.* **2005**, *15*, 865-871.
- (3) Lu, A.-H.; Zhao, D.; Wan, Y. *Nanocasting: A Versatile Strategy for Creating Nanostructured Porous Materials*; Royal Society of Chemistry, Cambridge, U. K., 2010.
- (4) Smått, J.-H.; Schunk, S. A.; Lindén, M. *Chem. Mater.* **2003**, *15*, 2354-2361.
- (5) Mebane, R. C.; Holte, K. L.; Gross, B. C. *Synth. Comm.* **2007**, *37*, 2787-2791.
- (6) Sassin, M. B.; Mansour, A. N.; Pettigrew, K. A.; Rolison, D. R.; Long, J. W. *ACS Nano* **2010**, *4*, 4505-4514.

## Chapter 7

### Application of 3-D Hierarchically Porous Silver, Cobalt Oxide and Zinc Oxide Monoliths to Chromatographic Separations

#### 7.1 Abstract

Hierarchically porous silica monoliths were introduced into liquid phase chromatography at the beginning of the last decade. The high surface area, high void volume and bicontinuous nature of the porosity of the materials are significant advantages over existing chromatographic supports and have resulted in rapid acceptance of these materials into the chromatography market.

We report here on the synthesis of 3-D porous sterling silver, cobalt oxide and zinc oxide monoliths, their materials characterization, fabrication as liquid chromatographic columns and initial chromatographic characterization. The, as prepared, columns gave very low back pressure, consistent with the bicontinuous nature of the columns. Cobalt oxide and zinc oxide both demonstrated retention of a number of nitrogen heterocycles, providing the basis for molecular separation.

#### 7.2 Introduction

Monolithic columns have been of interest in chromatography for many years, but it has only been with the development of monolithic silica columns in the late '90s<sup>1</sup> and their commercialization in the last decade<sup>2</sup> that this approach has had a major impact.<sup>3-5</sup> Monolithic silica columns are approximately six times faster than equivalent packed particle columns for many separations.<sup>3-5</sup> Materials other than silica are of interest to give enhanced separations, and monolithic zirconium oxide<sup>6</sup> and titanium dioxide<sup>7,8</sup> columns have been reported. Particularly for protein separations, there is considerable interest in broadening the range of materials

available for larger diameter, semi-preparative columns. It is known that many metal oxides can retain adsorb molecules, providing the basis for chromatographic separations, and so we have been interested in expanding the range of available materials to other metal oxides and to metals.

### 7.3 Experimental

Hierarchically porous silica monoliths were prepared using sol-gel processes in which polyethylene glycol of 35,000 molecular weight was included during formation of the silica sol to assist with the spinodal decomposition to give macropores in the silica.<sup>9</sup> Cationic surfactants can be added during the monolith synthesis to form mesopores.<sup>9</sup> Cobalt oxide, sterling silver and zinc oxide columns were made by replicating monolithic silica columns using “nanocasting”,<sup>10</sup> specifically, solution infiltration of nitrate salts followed by decomposition of the nitrate to oxide or the reduced metal. The cobalt oxide column was produced as  $\text{Co}_3\text{O}_4$  using a silica monolith template which included 9 wt%  $\text{C}_{18}\text{H}_{37}\text{N}(\text{CH}_3)_3$  bromide, which produces a network of mesopores with diameter ca. 4 nm. The sterling silver and zinc oxide columns were produced from a silica template that did not contain added surfactant and so did not have such a mesopore network. The procedure for making the metal oxide is in general similar to that reported in earlier work.<sup>11</sup> Figure 7.1 shows an SEM image of the cobalt oxide replica. The completed monolith was then placed into heat shrink tubing, and the heat shrink heated to produce a conformal coating. The monolithic column inside the heat shrink was put into stainless steel tubing and epoxy poured in between the stainless steel tube and the exterior of the heat shrink to stabilize the column and prevent any solvent bypassing the column. Stainless steel column end fittings were then attached to form a complete chromatography column (Figure 7.2). Due to thermal stress during the nanocasting considerable cracking of the monoliths occurred both during processing and after etching, this limited the overall length of the columns.

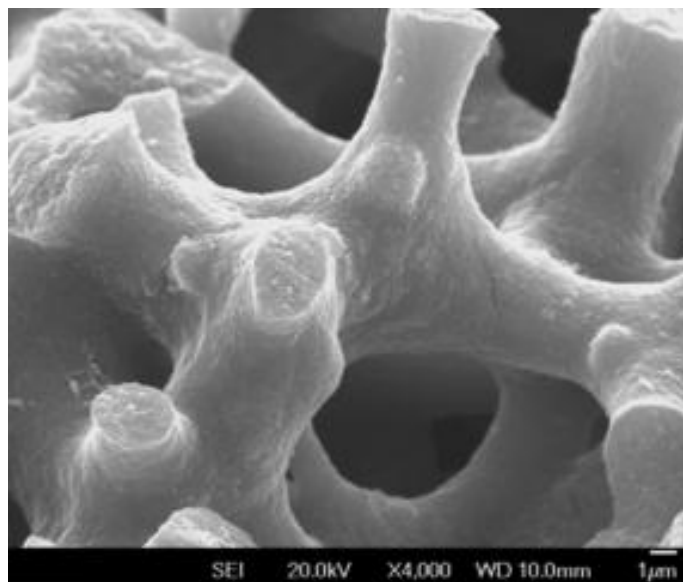


**Figure 7.1.** SEM Image of Cobalt Oxide Produced by Nanocasting into a Monolithic Silica Template.



**Figure 7.2.** Completed Chromatography Column Incorporating Monolithic Cobalt Oxide. Arrow indicates direction of solvent flow.

This was minimized by annealing the cobalt oxide to allow some movement of the cobalt oxide and so relieve the mechanical stress. The cobalt oxide and zinc oxide columns produced were 5 cm in length with a diameter of 5 mm. The sterling silver column was 10 cm in length and 5 mm in diameter.

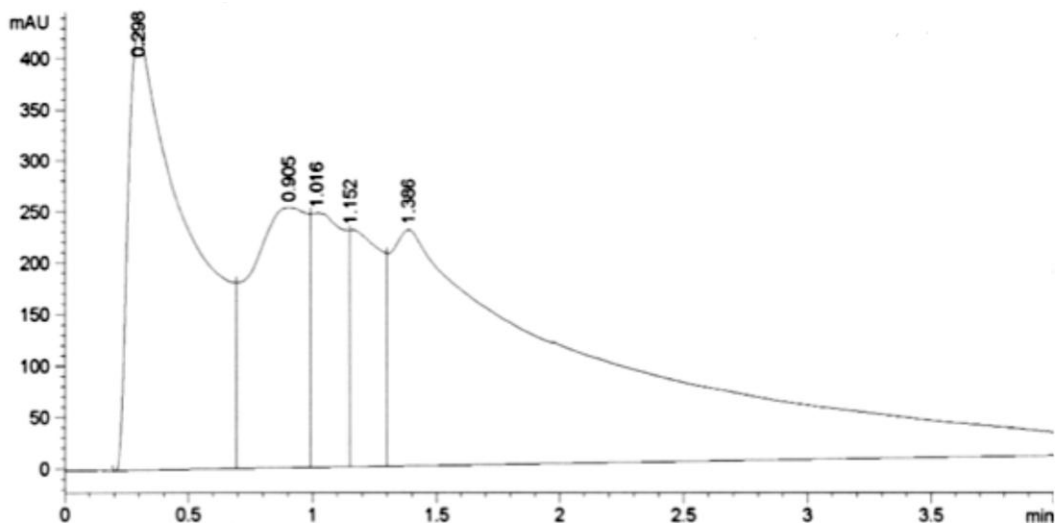
Chromatographic separations were carried using an Agilent HPLC system with UV detector operating at 254 nm. The Phenomenex® standard used was a polar/non-polar standard solution consisting of uracil (0.1 mg/mL), acetophenone (0.22 mg/mL), benzene (9.42 mg/mL), toluene (9.42 mg/mL), and naphthalene (9.42 mg/mL) in acetonitrile.

#### **7.4 Results and Discussion**

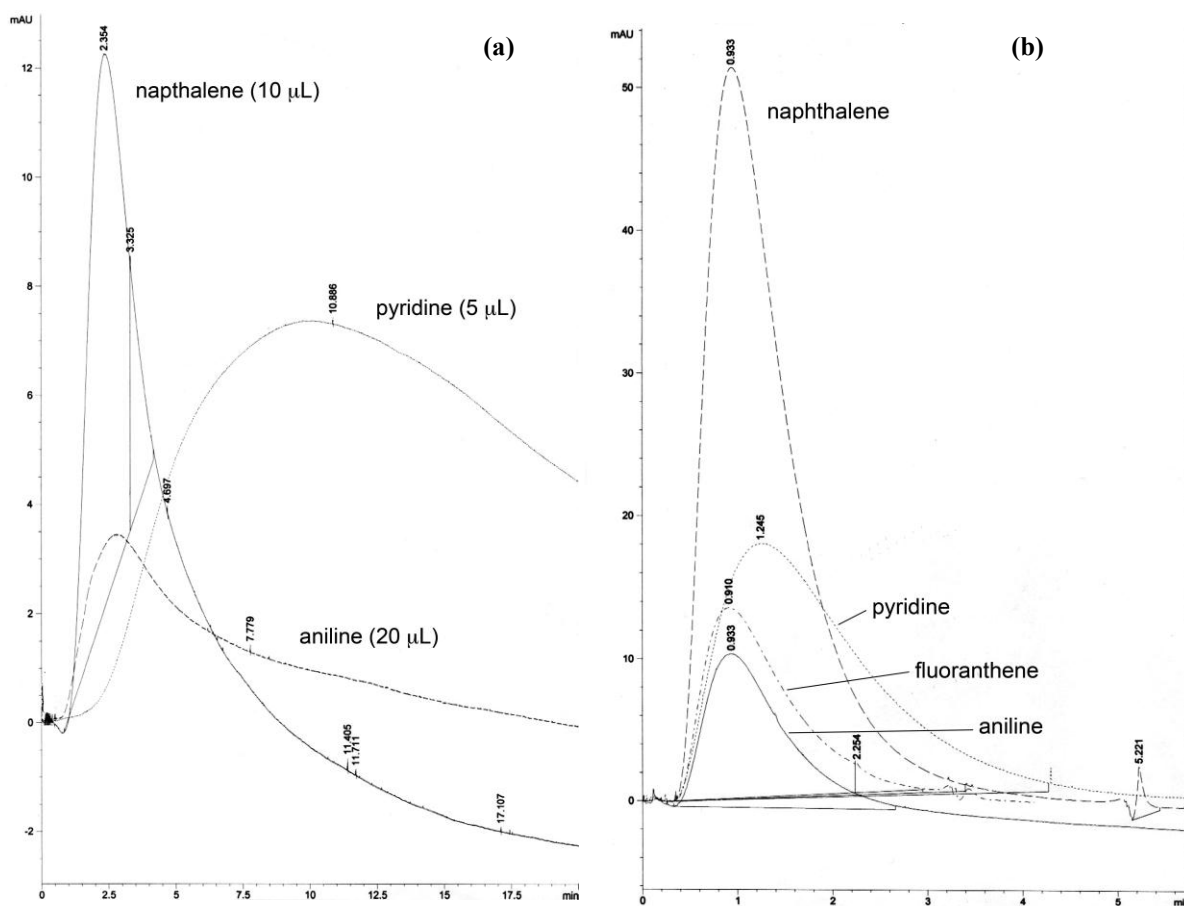
Effective chemical separations using chromatography require minimization of “dead-space”: void space that the solution flows through. In order to reduce dead-space, the metal and metal oxide columns were packed in heat-shrink, and then an epoxy sealant was used to remove voids between the exterior of the heat-shrink and the stainless steel outer jacket. Unfortunately, it was determined that the epoxy used was not chemically resistant to the acetonitrile solvents which are commonly used in chromatography and this led to a number of artifact peaks before the problem was identified. The sealant was inert to water and alcohols and so these or very dilute acetonitrile/water solutions were used in the work reported here.

Figure 7.3 shows a chromatogram for a Phenomenex® standard solution composed of a mixture of hydrophilic and hydrophobic components on the sterling silver column. Some separation of the components is apparent, although the peaks for the various analytes are not completely resolved.

Figure 7.4 shows composites of a number of individual chromatograms of naphthalene, aniline and pyridine adsorbed on a cobalt oxide column, and of naphthalene, aniline, fluoranthene and pyridine in 50% water/50% methanol, showing that under the conditions used these analytes are retained on the column. To the best of our knowledge this is the first example of the demonstration of retention of any analytes on sterling silver, cobalt oxide or zinc oxide.



**Figure 7.3.** Chromatogram of a Standard Solution from Phenomenex<sup>®</sup> on a Sterling Silver Column using a 20% Water: 80% Methanol Eluent.



**Figure 7.4.** Chromatograms on (a) Cobalt Oxide and (b) Zinc Oxide Columns. Analytes and injection volumes as indicated. Eluent was 50% water: 50% methanol.

Analytes traveling through a column undergo a series of adsorption/desorption events on the column and separation occurs when different analytes spend different amounts of time adsorbed on the column. The greater the number of adsorption/desorption events a molecule undergoes in passing through the column the more efficient the separation is. This is often described by the theoretical plate height, or the number of theoretical plates in a column. This can be estimated by the square of the ratio of time taken for an analyte to travel through the column to the width of the chromatographic peak. For pyridine in 1:1 water:methanol solution, at a flow rate of 20 cm/s one equilibration occurs in 1.6 mm. To further characterize the chromatographic properties of the column, a series of measurements of peak width/retention time vs. flow velocity were made for aniline. The peak width, column height and retention time are used to determine the theoretical plate height for a given column.<sup>4</sup> Konishi et al. report theoretical plate heights of 2600-13000/m for various organophosphates on titanium dioxide columns.<sup>12</sup> Our value of 600/m is significantly lower, but we have not yet optimized the separations in terms of eluent and analyte. Such optimization is likely to result in significant improvement.

The plate height changes as a function of flow velocity, as shown in Figure 7.5. The fitted line in Figure 7.5, is the best fit to the Van Deemter equation:

$$H = A + \frac{B}{u} + Cu \quad \text{Eq. 7.1}$$

Where H is the plate height, u is the flow velocity and A, B and C are constants determined by the column, eluent and analyte. The best fitted line gives the A term as effectively zero, B=0.9565 and C=0.0021. The A term is referred to as "eddy diffusion", and accounts for differences in the paths that different analyte molecules take through the column. The

observation that our value for A is zero, or close to zero, indicates that the column is relatively homogeneous.

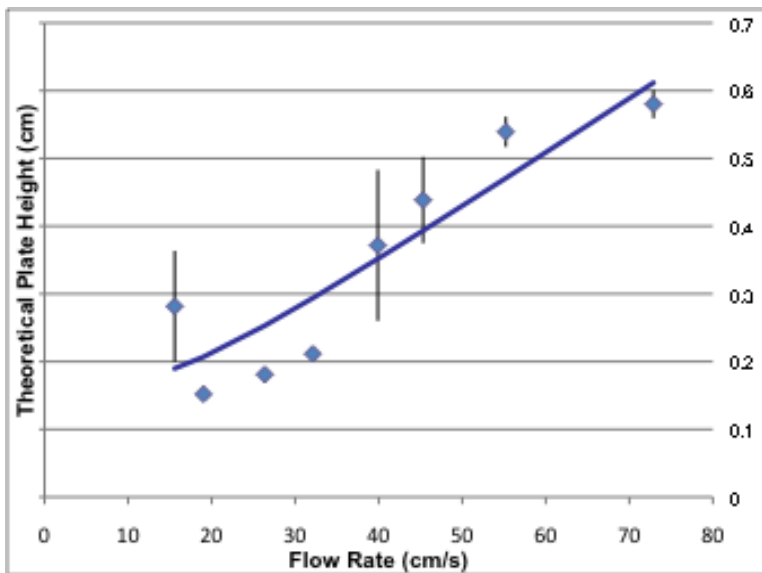


**Figure 7.5.** Van Deemter Plot of Pyridine Retention on Cobalt Oxide.

We also observe very low back pressures, generally less than 1 bar, consistent with very efficient flow through our monoliths.

Although we have successfully demonstrated retention of a number of analytes on new oxide chromatographic media, and shown that the media have the low resistance to flow expected from monolithic media, there are still a number of technical issues to be addressed before these media can be of commercial interest. In particular the aspect ratio of the columns needs to be improved before they can successfully be used. The experiments were performed on 5 mm diameter and 5 cm long columns. A more typical semi-preparative column would be 10-15 cm long for this diameter. We are able to make silica monoliths with these dimensions, however the higher the aspect ratio of the template used, the more liable the column is to crack due to the thermal stresses of the replication process. We believe that more careful control of the

temperature, perhaps including further annealing during the replication process will result in higher aspect ratio columns.

## **7.5 Conclusions**

We have successfully produced chromatographic columns based on sterling silver, cobalt oxide, and zinc oxide and demonstrated that they have good flow characteristics and are capable of retaining common small molecules.

## **7.6 Acknowledgements**

Primary support for this work was from NSF CHE-0719398 (MGB). Support for the chromatography experiments by the University of Alabama College of Arts and Sciences is gratefully acknowledged. The electron microscopy was carried out at the Central Analytical Facility of the University of Alabama.

This work was performed with co-authors Ms. Amy Grano, Professor Susanne Wiedmer, Professor Jan-Henrik Smått, and Professor Martin Bakker.

## 7.7 References

- (1) Nakanishi, K. *J. Porous. Mat.* **1997**, *4*, 67-112.
- (2) Leinweber, F. C.; Lubda, D.; Cabrera, K.; Tallarek, U. *Anal. Chem.* **2002**, *74*, 2470-2477.
- (3) Miller, S. *Anal. Chem.* **2004**, *76*, 99A-101A.
- (4) Guiochon, G., *J. Chromatogr. A* **2007**, *1168*, 101-168.
- (5) Unger, K. K.; Skudas, R.; Schulte, M. M. *J. Chromatogr. A* **2008**, *1184*, 393-415.
- (6) Konishi, J.; Fujita, K.; Oiwa, S.; Nakanishi, K.; Hirao, K. *Chem. Mater.* **2008**, *20*.
- (7) Konishi, J.; Fujita, K.; Nakanishi, K.; Hirao, K. *Chem. Mater.* **2006**, *18*, 6069-6074.
- (8) Konishi, J.; Fujita, K.; Oiwa, S.; Nakanishi, K.; Hirao, K. *Mater.* **2006**, *18*, 864-866.
- (9) Smått, J.-H.; Schunk, S. A.; Lindén, M. *Chem. Mater.* **2003**, *15*, 2354-2361.
- (10) Lu, A.-H.; Zhao, D.; Wan, Y. *Nanocasting: A Versatile Strategy for Creating Nanostructured Porous Materials*, Royal Society of Chemistry, Cambridge, U. K., 2010.
- (11) Smått, J.-H.; Weidenthaler, C.; Rosenholm, J. B.; Lindén, M. *Chem. Mater.* **2006**, *18*, 1443-1450.
- (12) Konishi, J.; Fujita, K.; Nakanishi, K.; Hirao, K.; Morisato, K.; Miyazaki, S.; Ohira, M. *J. Chromatogr. A* **2009**, *1216*, 7375-7383.

## Chapter 8

### Conclusions and Future Work

#### 8.1 Conclusions

Nanocasting into mesoporous silica monoliths provides a general method to produce a number of different hierarchically porous, high surface area metal and metal oxide monoliths. In Chapter 2, electrochemical methods for measuring the connectivity of mesoporous, monolithic silica were developed. These measurements offer a quick and inexpensive alternative to neutron scattering and TEM tomography experiments that are otherwise required to determine connectivity at the nanometer scale. The results showed that mesoporous silica monoliths produced with 7 wt% C<sub>18</sub>TAB as the meso-porogen generated a highly connected mesopore system. Generally, this particular type of silica monolith was used as the sacrificial nanocasting template to produce the materials presented throughout the remainder of this work.

In Chapters 3-5, these silica monoliths are shown to be ideal templates for nanocasting to produce high surface area metal and metal oxide monoliths. Chapter 3 disclosed these factors in a patent application which include controlling the metal salt solution, impregnation method, temperature, atmosphere, and etchant. Examples of hierarchically porous copper, cobalt, nickel, sterling silver, nickel oxide and cobalt oxide monoliths are shown that illustrate the value of monitoring each of these factors. Chapter 4 provided an in-depth discussion of the scientific basis for how the temperature, atmosphere and precursors impact the structure and nature of the hierarchically porous metal and metal oxides produced. This was illustrated with nickel, cobalt, silver, nickel oxide, and cobalt oxide monoliths. Chapter 5 further emphasized the significance atmosphere by presenting experiments where cobalt oxide (Co<sub>3</sub>O<sub>4</sub>) monoliths were generated under vacuum, air, argon, and nitrogen. Argon was found to produce the best silica replica in the

case of cobalt oxide. Chapter 5 also illustrated the consequences of excess heat and possibly mass transport limitations by showing evidence for the formation of silver and zirconium silicates when the intended products were silver metal and zirconium oxide.

Chapters 6 and 7 demonstrated that these materials can be applied to various applications. In chapter 6, the catalytic activity of a nickel monolith was compared to that of Raney® nickel in the hydrogenation of cyclohexanone to cyclohexanol. It was found that the Raney® nickel was a better catalyst, producing 96% conversion while the nickel monolith reduced with methanol yielded 80% conversion. In chapter 7, monolithic cobalt oxide ( $\text{Co}_3\text{O}_4$ ), zinc oxide and sterling silver were utilized as chromatography columns. While the sterling silver monolith did show some evidence of separating a hydrophobic/hydrophilic standard mixture though unresolvable, the zinc oxide and cobalt oxide columns could only demonstrate retention of various analytes. A van Deemter plot was constructed using the cobalt oxide column and pyridine as the analyte. It was determined that all columns needed to be longer and possibly smaller in diameter in order to enhance separations.

In conclusion, a robust method for producing monolithic high surface area metals has been explored. This method has been able to produce materials with unique properties not seen elsewhere in the literature. Several applications were explored for these materials including catalysis and liquid chromatography. While the materials did show promise in each of these areas, without optimization the results were still below other commercial materials suggesting a need for further optimization of both the synthesis of the materials along with their use in applications.

Some of these synthesis methods have been recorded on video and are available upon request from Professor Martin Bakker at The University of Alabama Department of Chemistry.

## 8.2 Future Work

Future work includes producing higher fidelity metal replicas and using them in catalytic and chromatographic applications. Now that all the factors controlling replication have been identified, improved nickel metal monoliths should be prepared. These higher surface area nickel monoliths may show interesting results as a replacement for Raney® nickel. The improved synthesis will be achieved by using a reductant other than methanol or hydrogen, such as hydrazine, to allow reduction of the nickel salt to occur at a lower temperature. If the temperature at which reduction occurs is decreased, excess migration and sintering of the nickel metal can be avoided, thereby increasing the fidelity of the replica. This more accurate replica will have higher surface area and thus be more catalytically active. Also reusability of this high surface area monolithic nickel will be investigated and compared to that of Raney® nickel, which is difficult to reuse due to the very fine powder form it exists in.

Additionally, much more characterization of these unique metal and metal oxide as stationary phases is required. The sterling silver column is of particular interest to the field of electrochemical chromatography. Electrochemical chromatography works by applying a potential directly to the separations column which effectively changes the nature of the stationary phase and therefore the retention time of the analyte. This field shows promise in more complex separations such as enantiomeric separations. The sterling silver monolithic column presented in this dissertation is an ideal candidate for an electrochemical chromatography column as it is highly electrically conductive and it unlikely to adsorb analytes as strongly as competing monolithic carbon columns. When sterling silver is nanocast, it is fairly straightforward to increase the length of this column in order to enhance separations. Therefore, the aspect ratio (length:width) of the column can be optimized without much difficulty. Furthermore, silver does

not corrode like many other metals and it is much less expensive than palladium or platinum. While separations of small molecules and enantiomers will be investigated, larger molecules including proteins, lipids and viruses will also be examined since silver is known to interact with biological molecules.

In addition to future work on applications, the metal monoliths produced could be further characterized by using techniques and instruments not available to the researcher. Mechanical strength measurements of the replicated monoliths could determine the amount of force needed to crush and/or stretch the monoliths. Solid state nuclear magnetic resonance could also be performed on the monoliths made of spin 1/2 nuclei, such as iron and silver, to better determine if impurities exist and if the metal is completely reduced. Finally, analysis using a Plasma FIB/SEM, such as TESCAN's FERA3 XMH Plasma FIB-FESEM, could allow better determination of both the macroscopic and nanoscopic distribution of the material across the length and the width of the monolith.